Measurement of the J/ψ elliptic flow in Pb-Pb collisions at $\sqrt{}$sNN=5.02TeV with the muon spectrometer of ALICE at the LHC

Audrey Francisco

UNIVERSITE MATIERE BRETAGNE MOLECULES LOIRE ET MATERIAUX

IMT Atlantique
Bretagne-Pays de la Loire
École Mines-Télécom

THESE DE DOCTORAT DE

L'ÉCOLE NATIONALE SUPERIEURE MINES-TELECOM ATLANTIQUE
BRETAGNE PAYS DE LA LOIRE - IMT ATLANTIQUE
COMUE UNIVERSITE BRETAGNE LOIRE

ECOLE DOCTORALE N° 596
Matière, Molécules, Matériaux
Spécialité : Physique Subatomique et Instrumentation Nucléaire

Par

Audrey FRANCISCO

Measurement of the J/ψ elliptic flow in Pb-Pb collisions at $\sqrt{s_{NN}}$=5.02TeV with the muon spectrometer of ALICE at the LHC

Thèse présentée et soutenue à Nantes le 24 Septembre 2018
Unité de recherche : SUBATECH— UMR6457
Thèse N° : 2018IMTA0087

Composition du Jury :

Président :	Pol-Bernard GOSSIAUX	Professeur, IMT-Atlantique
Examinateurs :	Javier CASTILLO CASTELLANOS	Chercheur-Ingénieur, CEA
	Manuel CALDERON DE LA BARÇA SANCHEZ	Professeur, University of California Davis
	Marielle CHARTIER	Professeur, University of Liverpool
	Silvia NICCOLAI	Directeur de Recherche CNRS, Univ. Paris-Sud/Paris-Saclay
Dir. de thèse :	Gines MARTINEZ GARCIA	Directeur de Recherche CNRS, SUBATECH
Co-dir. de thèse :	Laurent APHECETCHE	Chargé de Recherche CNRS, SUBATECH
	Guillaume BATIGNE	Maître-Assistant, IMT-Atlantique

Remerciements

"There's nothing you can do that can't be done / Nothing you can sing that can't be sung / Nothing you can say, but you can learn how to play the game / It's easy / All you need is love."

— John Lennon, Magical Mystery Tour (The Beatles)

Cette page est dédiée à tous ceux qui ont croisé mon chemin. Merci pour votre aide, votre confiance, vos encouragements, vos conseils, votre temps et votre inspiration.
Mes pensées s'orientent vers mes proches. Par pudeur et par souci de concision, je ne m'adresserai pas individuellement à chacun d'entre vous mais soyez assurés de ma reconnaissance. Je citerai ici mon cher directeur de thèse, l'ensemble du groupe plasma, le laboratoire Subatech, notamment les services administratifs et informatiques, les membres de la collaboration ALICE, plus spécialement le groupe PWG-DQ et les équipes des upgrades ITS et MFT, et enfin mon jury de thèse, pour cette tâche chronophage.
Merci également à tous les yeux qui ont brillé en m'écoutant.
Enfin, merci à ceux qui ont renforcé ma détermination par leurs douces objurgations et lassitudes, vous ne mesurerez jamais l'importance de votre contribution.
Je souligne aussi le soutien et l'acceuil de la région Pays de la Loire, du CNRS, de l'IMT Atlantique, du laboratoire Subatech, de l'Université Bretagne-Loire, de la collaboration ALICE et du CERN qui ont permis la réalisation de cette thèse.

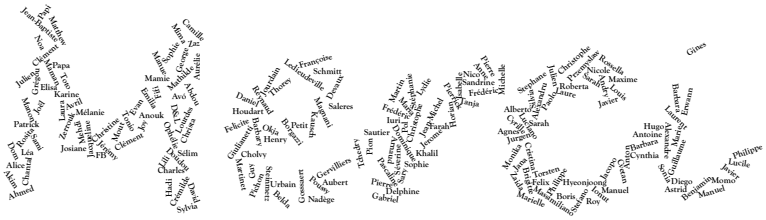

À l'attention de mon entourage non-physicien :
Le terme *« gypsy »* ou *« gipsy »* est un mot anglais souvent désigné sous le terme de *« gens du voyage »* en France. Il fait généralement référence à une communauté d'individus dont le mode de vie a une origine nomade, bien que beaucoup soient aujourd'hui sédentaires. Le terme englobe plusieurs populations d'origines éthniques et de cultures différentes. Cette thèse ne raconte pas leur histoire.

INTRODUCTION

Significant investments have been made to study the properties of the strong interaction, responsible for the stability of nuclei. Several experimental facilities and experiments have been devoted to the creation and observation of a deconfined state of matter, the Quark Gluon Plasma (QGP), where elementary building blocks of nuclei evolve quasi-freely. Heavy-ion collisions are unique tool to investigate this primordial state of the Universe and test Quantum ChromoDynamics (QCD) predictions. The A Large Ion Colliding Experiment (ALICE) experiment is a dedicated apparatus at the Large Hadron Collider (LHC).

The lifetime of the created QGP is very short (~5–10 fm/c) and makes it impossible to observe it directly. Various observables are therefore measured to extract information about the deconfined state. Among them, anisotropic flow provides very useful results to extract the thermal properties of the system. Bound states of heavy quarks have been identified as ideal probes of the ALICE several decades ago. This thesis contains two parts: the measurement of the J/ψ elliptic flow in Pb–Pb collisions at $\sqrt{s_{\rm NN}} = 5.02$ TeV with the ALICE detector and the characterisation of CMOS sensors for the Muon Forward Tracker upgrade.

The first chapter of this thesis of offers a general introduction to the Quark-Gluon Plasma and its study through heavy-ion collisions. The second chapter describes the ALICE detector, dedicated to heavy-ion collision studies, and its future upgrade with details on the Muon Forward Tracker and the work performed for the characterisation study of the sensors. Chapter three is an overview of collective phenomena in the QGP with a summary of the main observations from A–A collisions, a brief discussion of the small-system results and a dedicated section on heavy flavours. The relevance of quarkonium states in the study of A–A collisions is discussed in chapter four. Experimental results and theoretical description of heavy-quark bound states are presented. The analysis performed during this thesis is detailed in the chapter 5. The J/ψ elliptic flow analysis was performed at forward rapidity in Pb–Pb collisions at $\sqrt{s_{\rm NN}} = 5.02$ TeV through the dimuon decay channel. The measurement was performed using the Event Plane method (using either the $\langle v_2 \rangle$ or the $d{\rm N}/d\Delta\phi$ technique) and the Scalar Product method. The azimuthal dependence of J/ψ production is also investigated here for the first time. The results are discussed in the chapter 6 by comparing it to other measurements and theoretical predictions (when available) and drawing the conclusions about charm-quark flow at LHC. Future prospectives with the ALICE detector upgrade are also proposed here. The last chapter is a general conclusion over quarkonium results and the results obtained during this thesis.

CONTENTS

CHAPTER 1

INTRODUCTION TO THE QUARK-GLUON PLASMA

"Only the most naive questions are truly serious."

— Milan Kundera, The Unbearable Lightness of Being

Heavy-ion collisions aim to study hadronic matter at high-energy densities. In this regime, QCD predicts a transition towards a deconfined state of matter, the QGP. This first chapter is a short introduction to color deconfinement, its evolution and endorsed probes for its study.

1.1 A deconfined state of matter

1.1.1 Quantum ChromoDynamics

The most successful theory to describe matter and its non-gravitational interactions is the **Standard Model of Particle Physics**. This relativistic quantum field theory is based on the gauge symmetry $SU(3)_C \times SU(2)_L \times U(1)_Y$ to describe each interaction. Elementary particles (see Fig. 1.1) are divided into fermions, with half-integer spin and following the Fermi–Dirac statistics, and bosons, with zero or integer spin and following the Bose-Einstein statistics. Fermions are categorised into **quarks**, building blocks of hadrons and mesons, and leptons, insensitive to the strong interaction, along with their associated anti-particles. Fundamental interactions are mediated through the exchange of bosons: the photon for the electromagnetic interaction, the **gluon** for the strong interaction, the massive Z and W bosons for the weak interaction, and the Higgs boson for mass through the Higgs-Englert-Broot mechanism.

Within the Standard Model, **Quantum Chromodynamics** (QCD) [GW73, GW74] is the theory of the strong interaction. Since not only quarks but also the strong-force mediator, the gluon, carry a color charge (red, blue, green, and corresponding anti-charges), the strong interaction is a non-abelian gauge theory with an SU(3) symmetry group. The QCD coupling constant α_s is represented on Fig. 1.2 as a function of the momentum transfer Q. The strong force is a short-distance interaction (large Q^2) as it becomes stronger at large distances (small Q^2). perturbative QCD (pQCD) can be applied at high-momentum transfer ($Q > \Lambda_{QCD} \sim 200\,\text{MeV}$) but calculations do not converge in the regime $Q < \Lambda_{QCD}$. Because of the self-interaction of the gluon, the creation of new quark-anti-quark pairs will be energetically favoured to increasing the distance between bound quarks. This property is known as **confinement** and translates into the impossibility to observe a single-color carrier. However, the decrease of the interaction strength at short distances (high-energy

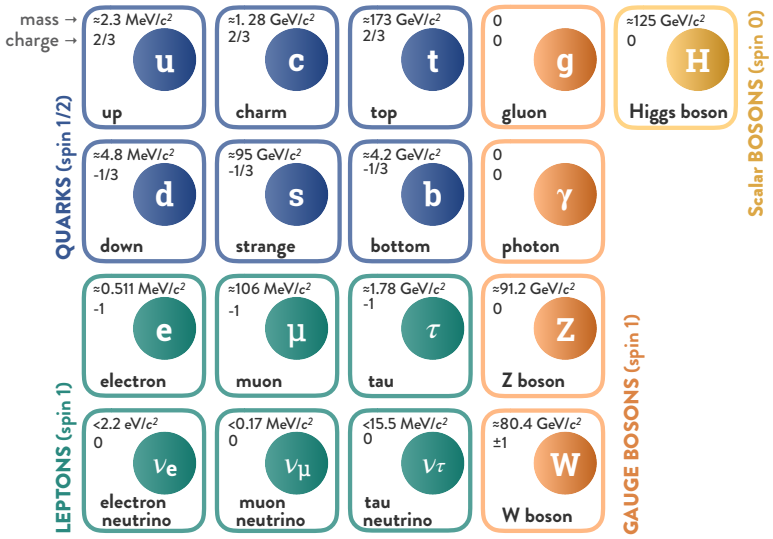

Figure 1.1 – Standard-model particles

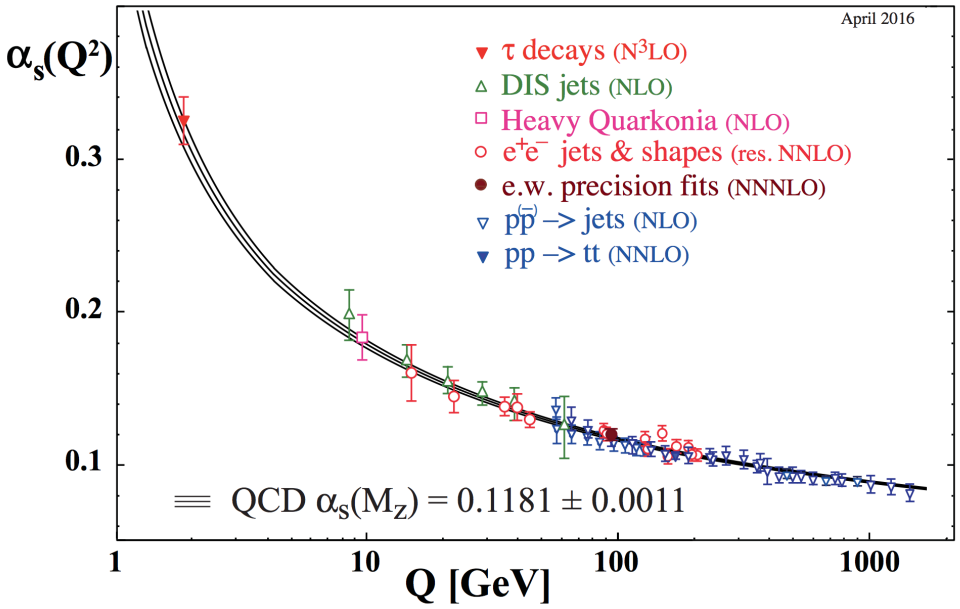

Figure 1.2 – Evolution of the strong coupling constant α_s as function of the the energy scale Q [eaPDGte]

densities) should enable the formation of a **new state of matter** where quarks and gluons, together referred to as **partons**, would evolve towards the **asymptotically free** region: **the quark-gluon plasma** [CP75b, Shu78].

1.1.2 The phase transition

A deconfined state can only be formed in the regime of high-energy density and temperature [CP75a]. The nature and the order of the phase transition from hadronic matter to a quark-gluon plasma (QGP) is still debated today. The phase diagram of matter is presented on Fig. 1.3 as a function of temperature and chemical potential (μ_B). At low temperature and μ_B, matter can be represented as a gas of hadrons. For a given μ_B, the phase transition occurs when the temperature reaches the critical temperature $T_c|_{\mu_B}$. Lattice-

QCD calculations predict a smooth crossover transition at zero chemical potential around 155 MeV [FJ16]. A phase transition should occur for positive chemical potential from a critical point [FK04]. In the high μ_B region, a color superconducting state is expected to form [ASRS08].

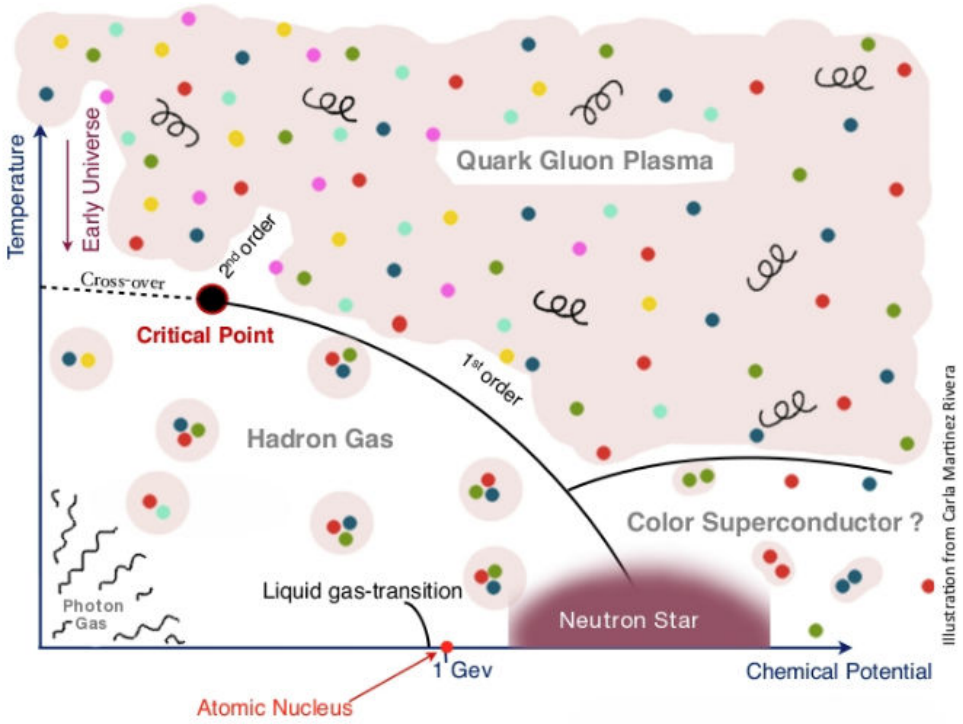

Figure 1.3 – Sketch of the phase diagram of hadronic matter

While the QGP may have existed a few millionths of a second after the Big Bang, it can only be observed today through **ultra-relativistic heavy-ion collisions**. Such a state might also be found inside the core of neutron stars [CP75b]. In the context of recent gravitational-wave observations generated by the merger of two neutron stars [A+16a], the study of their properties could be useful to extract information on the state of the matter [AFJ+11, HLPS10, HLPS13].

1.2 Heavy-ion collisions

Ultra-relativistic heavy-ion collisions provide a unique opportunity to study matter properties at **extreme energy densities**. Considerable theoretical and experimental investments were supported in the last 30 years to create and understand deconfined matter. Powerful machines have been developed both at the Brookhaven National Laboratory (BNL) in the USA, with the AGS Alternating Gradient Synchrotron (AGS) and now Relativistic Heavy-Ion Collider (RHIC), and at Centre Européen pour la Recherche Nucléaire (CERN) in Switzerland with the Super Proton Synchrotron (SPS) and the LHC (Large Hadron Collider).

If the temperature and the energy density reached during the collision are high enough, a deconfined state could form. At the LHC, it is expected at lower μ_B than the critical point. The created hot medium can be referred to as a *fireball*. The evolution of the fireball is described through successive stages within the Bjorken [Shu78, Bjo83] scenario.

1.2.1 The Bjorken scenario

Before colliding, ultra-relativistic nuclei are Lorentz-contracted and therefore seen as flat instead of spherical in the center-of-mass system. The collision schematics is illustrated on Fig. 1.4 with (Right) or without (Left) the formation of a QGP. In the case where a phase transition occurs towards a deconfined state, its evolution follows several phases:

Pre-equilibrium state: If the crossing time of the nuclei is smaller than the time scale of the strong interaction $\tau_{\text{strong}} \sim 1/\Lambda_{\text{QCD}} \sim 1\,\text{fm}/c$, parton interactions generate particles after the nuclei have already crossed each other. The crossing time is computed from the nucleus radius R and the Lorentz factor γ as $\tau_{\text{cross}} = 2R/\gamma$. In Pb–Pb collisions at $\sqrt{s_{\text{NN}}} = 5.02\,\text{TeV}$, $\gamma \sim 2700$ and $R_{^{208}\text{Pb}} \sim 6.62\,\text{fm}$. Bjorken also assumes a uniform distribution of the particle multiplicity as a function of the rapidity. Multiple partonic interactions with high-momentum transfer are occuring. The system is in a pre-equilibrium state where inelastic scatterings possibly lead to **thermalisation**.

QGP phase and longitudinal expansion: If the energy density of the volume filled with particles is high enough, a deconfined state is formed. The formation of the QGP can be estimated as the time scale of the strong interaction and its size around 10–20 fm. After thermalisation, the QGP is expected to evolve like a fluid and is described through relativistic hydrodynamics. The QGP phase is estimated to survive between $\sim$ 5–10 fm/c. The system expands first longitudinally then in 3-dimensions.

Mixed phase: As the medium expands and cools down, partons hadronise and the system enters a mixed phase of hadron gas and QGP.

Hadronic gas: Once all quarks hadronise into partons, the expanding system can be described as a gas of hadrons.

Freeze-out: When the particle density is sufficiently low, interactions stop. The *chemical freeze-out* is reached when inelastic interactions cease and the relative abundances of hadrons are fixed. The *kinetic freeze-out* refers to the end of all elastic interactions and when particle momenta are fixed. The system keeps on expanding as particles travel in the vacuum.

In the case where the system size is too small or the number of participants too low, no QGP is formed. The non-equilibrium state will then evolve towards a hadronic gas after partons hadronise.

Several collision properties affect the system formation and evolution. The **energy of the collision** (denoted $\sqrt{s_{\text{NN}}}$ in the center-of-mass system) affects the initial energy density of the QGP. The size, and therefore the nature, of the colliding nuclei (mainly Pb–Pb, S–U at SPS, Au–Au, Cu–Cu, U–U at RHIC, and Pb–Pb, Xe–Xe at the LHC) also impacts the number of participants in the collision. The **number of participants** $\langle N_{\text{part}} \rangle$, which corresponds to the number of nucleons participating in the collision, provides an equivalent reference. Alternatively, experiments use the **centrality** observable of the collision. It refers to the overlap region of the two colliding nuclei. Head-on, *central* collisions typically involve more nucleons than **peripheral** collisions. The centrality is computed from the impact parameter b of the collision, the distance between the centres of the nuclei. The ALICE collaboration estimates the centrality of collisions from the Glauber model [MRSS07] from the collision volume and by describing nucleus-nucleus collisions as the superposition of independent binary nucleon-nucleon collisions. The full description of the method can be found at [A+13b]. The system geometry can be studied through measurements with respect to the **symmetry plane of the collision**, referred to as reaction plane (see Sec. 3).

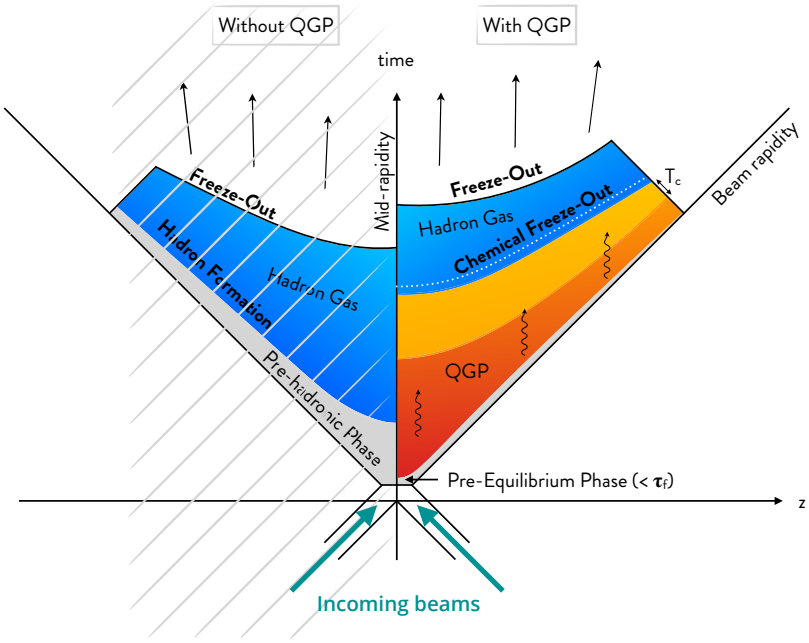

Figure 1.4 – Space-time evolution of the system formed during heavy-ion collisions

1.2.2 Experimental signatures of the QGP

Because of the short lifetime of the deconfined state, **no direct observation** of it can be performed. The properties of the system must be inferred from the final-state particles reaching the detectors. This specificity of heavy-ion physics creates a strong mutual dependence between theory and experiment as no conclusions can be drawn from observations alone. A wide range of probes have been proposed for the study and the characterisation of the QGP. Probes are usually divided according to their momentum scale into soft or hard probes.

Soft probes correspond to relatively small-momentum interactions and are the most abundant particles. They are produced along different stages of the collision and form the bulk of the expanding fireball. The study of soft probes provides information on the **collective behaviour** and **thermodynamical properties of the medium** (see Sec. 3). Within the statistical-model approach, the relative yields of light particles allow to extract the temperature and the chemical potential of the freeze-out stage [ABMS09]. **Strangeness enhancement** was among the first signatures of a QGP formation [RM82], as strange quarks should be abundantly produced during the deconfined stage. Recent observations [A$^+$17c] suggest that strangeness enhancement is rather an indicator of the system equilibrium.

The production of **hard probes** involves larger momentum scales and is therefore occurring during the most energetic interactions, at the beginning of the collision. The modification of parton showers in the medium and the suppression of back-to-back correlations, known as **jet quenching**, was first observed at RHIC [A$^+$03a]. The measurement of **heavy-flavours** is also a key tool for the characterisation of the medium, further details can be found in Sec.4.1.

A single probe on its own cannot lead to the conclusion that a QGP has formed, as it might be independently explained by several models diverging on its interpretation. Only a **set of concomitant results** can help understanding the medium formed during the collision. This thesis focuses on bound states of heavy quarks.

CHAPTER 2

STUDYING EXPERIMENTALLY THE QGP WITH ALICE

> "In this world, there are things you can only do alone, and things you can only do with somebody else. It's important to combine the two in just the right amount."
>
> — Haruki Murakami, After Dark

The conditions for the formation of a QGP are experimentally created through collisions of ultra-relativistic heavy ions. The chapter gives a brief description of the ALICE detector at the LHC which is dedicated to the study of heavy-ion collisions.

2.1 The LHC collider

The LHC [BCL+04] is currently the world's largest and most powerful particle accelerator. Based at CERN, it lies in a 50–100 m-deep tunnel beneath the Franco-Swiss border near Geneva in Switzerland. The first beam was steered at the end of 2008 in the 27-kilometres ring of superconducting magnets.
The LHC is optimised to deliver **proton or ion beams**. Protons are extracted from hydrogen gas by applying an electric field to strip electrons. The beam then goes trough a complex of accelerators to gain more and more energy. The injection chain is illustrated on Fig. 2.1. Protons are first accelerated to the energy of 50 MeV via two linear accelerators (LINear ACcelerator (LINAC)-3 and LINAC-4). The beams reach the energy of 1.4 GeV in the Proton Synchrotron Booster (PSB)), 25 GeV in the Proton Synchrotron (PS) and 450 GeV in the SPS, which injects to the LHC. Ion beams can also be injected to the SPS, then to the LHC, after being stripped out of their electrons and accelerated through LINAC-3, Low-Energy Injector Ring (LEIR) and PS. Lead (^{82}Pb), or more recently Xenon (^{54}Xe), ions are injected and collided at the LHC. A ultra-high vacuum is required in the two beam pipes of the LHC where beams circulate in opposite directions and collide at six different locations corresponding to dedicated experiments:

, designed to study the properties of the QGP through heavy-ion collisions,

A Toroidal Lhc ApparatuS (ATLAS) and Compact Muon Solenoid (CMS) , general-purpose detectors, mainly investigating physics beyond the standard model through pp collisions

Large Hadron Collider beauty (LHCb) , designed to study the asymmetry between matter and anti-matter by focusing on beauty measurements

Large Hadron Collider forward (LHCf) , focusing on cosmic-ray physics

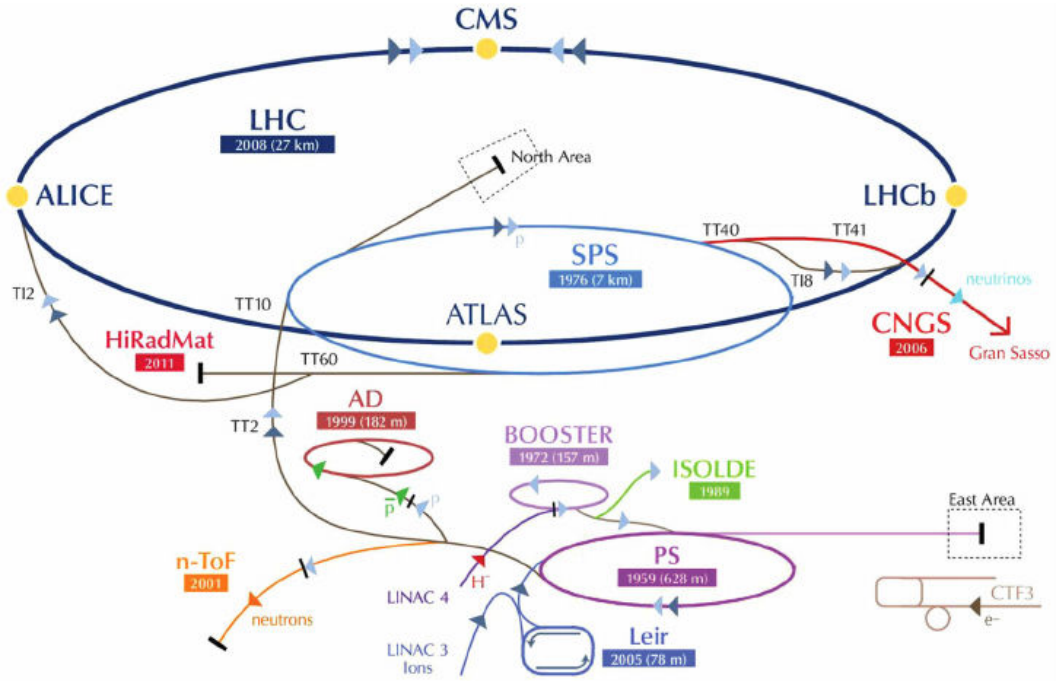

Figure 2.1 – CERN's accelerator complex

TOTal cross section, Elastic scattering and diffraction dissociation Measurement at the LHC (TOTEM) focusing on proton physics.

The ATLAS, CMS and LHCb experiments have also a dedicated heavy-ion program and provide complementary observations to the A Large Ion Colliding Experiment (ALICE) results.

2.2 The ALICE detector

ALICE is the only **heavy-ion dedicated experiment at the LHC**. The Letter of Intent [CER93] for the detector was submitted 25 years ago to the CERN LHC Committee, completed a few years later with several addenda formulated as technical propositions, including the Muon Spectrometer [CER96] in 1996 to study quarkonia via their dimuon decays. The collaboration gathers today over 1800 members in 42 countries.

This section describes the detector status during LHC run II and focuses on the sub-detectors involved in the J/ψ v_2 analysis at forward rapidity. The 10000-ton apparatus is composed of a central detector system at mid-rapidity and a muon arm at forward rapidity. The detector is made of several specific sub-detectors for the detection and the tracking of particles and decay products produced during the collision (see illustration on Fig. 2.5). For a full description of the ALICE detector, please refer to [A$^+$08]. A review of the detector performances is also available here [A$^+$14g].

2.2.1 The ITS

The ITS is a cylindrical vertex detector located around the beam pipe at the Interaction Point (IP). The reconstruction of primary vertices (and secondary if the decay length is larger than the 100 µm resolution of the detector) is performed by tracking particles through the 6 silicon layers divided into three sub-systems (see Fig.2.2). The two innermost layers compose the Silicon Pixel Detector (SPD), the two middle ones form the Silicon Drift Detector (SDD) and the two outermost layers compose the Silicon Strip Detector (SSD). The ITS provides also an extended tracking with respect to the central-barrel for low-p_{T} tracks. The detector covers the pseudorapidity range $|\eta| < 0.9$.

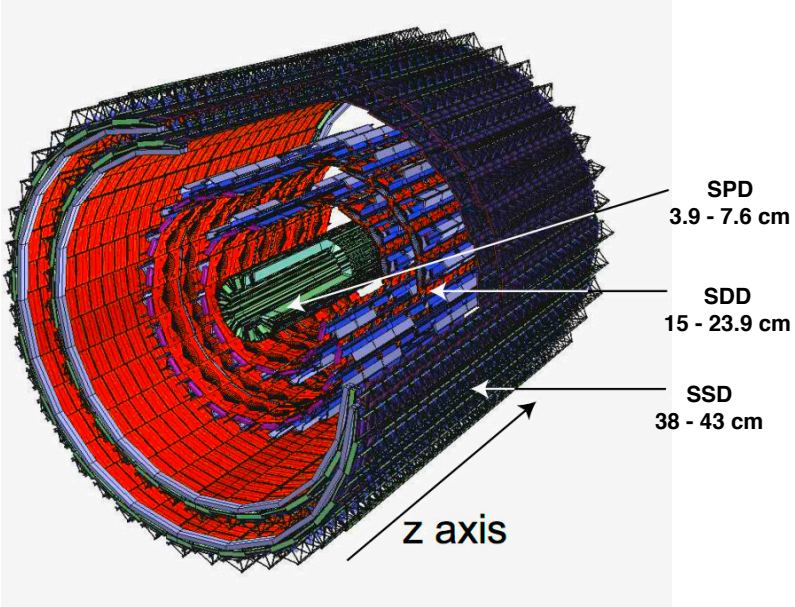

Figure 2.2 – The Inner Tracking System (ITS)

2.2.2 ZDC

The ZDC detector [CER99] consists of two types of calorimeters. Two sets of quartz-fiber hadronic calorimeters, proton ZDCs (ZP) and neutron ZDCs (ZN), are located on both

sides of the IP at z ± 116 m and measure the energy of spectator nucleons in order to determine the centrality of the collision. Two electromagnetic calorimeters (ZEM) at forward rapidity (at 7 m from the IP) provide an additional discrimination between the most central and peripheral events where the detected number of spectators crossing the hadronic calorimeters can be fairly similar due to the fragmentation of the nuclei.

2.2.3 The V0

The V0 detector [CER04] consists of two arrays of scintillators perpendicular to the beam direction and located asymmetrically on each side at z = 340 cm (VZERO-A (V0A)) and z = -90 cm (VZERO-C (V0C)) of the IP. Both arrays are divided into four rings, each segmented into eight sectors. The V0 provides rejection of beam-gas events by measuring the time-of-flight difference between both arrays, and it is therefore used as a minimum-bias trigger. In addition, the detector can also provide an estimation of the luminosity, particle multiplicity, collision centrality, and event plane direction.

2.2.4 The T0

The T0 detector [CER04] has a similar geometry to the V0 as it is composed of two arrays of detectors (T0A and T0C) located on both sides of the IP next to the V0 detectors (z = 350 cm and z = -70 cm). The arrays are made of 24 Cherenkov counters with a good time resolution (better than 50 ps), providing the collision signal for the Time Of Flight (TOF) detector, a precise determination of the vertex position (within 1.5 cm), an estimation of the particle multiplicity and a minimum-bias trigger.

2.2.5 The TPC

Tracking and particle identification at mid-rapidity are performed in the TPC [CER00]. The TPC is located around the ITS (between z = ± 250 cm) and consists of a cylindrical volume (87 < r < 247 cm) filled with a $Ne - CO_2$ (90–10 %) gas mixture for precise momentum and dE/dx measurements of charged particles (see Fig. 2.3). The drift cage is completed by two read-out planes on the end caps. The active drift volume is divided by the central high-voltage electrode providing a field of 400 V/cm.

2.2.6 The muon arm

The Muon Spectrometer is a forward detector designed to detect muons with a polar angle of 171° < θ < 178° with respect to the beam axis and in the pseudo rapidity coverage -4 < η < -2.5. The main physics motivations are the study of open heavy flavours, quarkonia, electroweak bosons and low-mass mesons. The detector consists of a frontal absorber, ten planes of tracking chambers, a dipole magnet, a second absorber and 4 planes of trigger chambers as illustrated on Fig. 2.4.

The frontal absorber was developed to shield the spectrometer from the flux of charged hadrons and minimise the muonic background from π and K decays. It is located at 90 cm from the interaction point with a length of 4.13 m (~ 10 interaction lengths). Its composition was optimised to reduce multiple scatterings which affect the mass resolution of the spectrometer. Therefore, low-Z materials (Carbon) were chosen for the closest layers to the vertex and high-Z materials (Lead and polyethylene) at the rear end. The middle layers

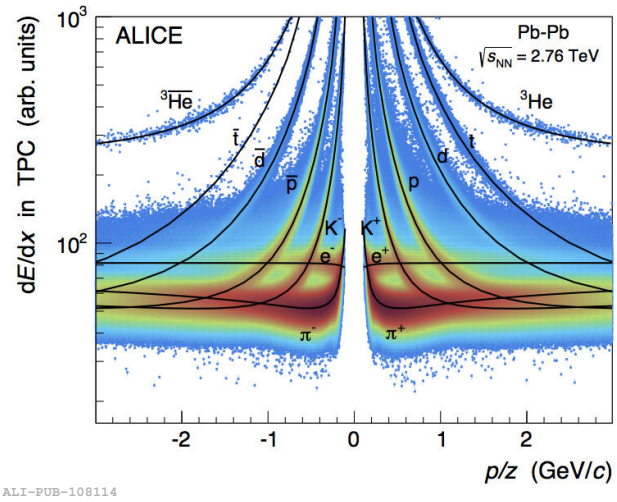

Figure 2.3 – Specific energy loss (dE/dx) in the TPC versus rigidity (momentum/charge) in 0–80 % Pb–Pb collisions at $\sqrt{s_{NN}}$ = 2.76 TeV. The solid lines represent a parametrisation of the Bethe-Bloch curve. Figure taken from [A+16i]

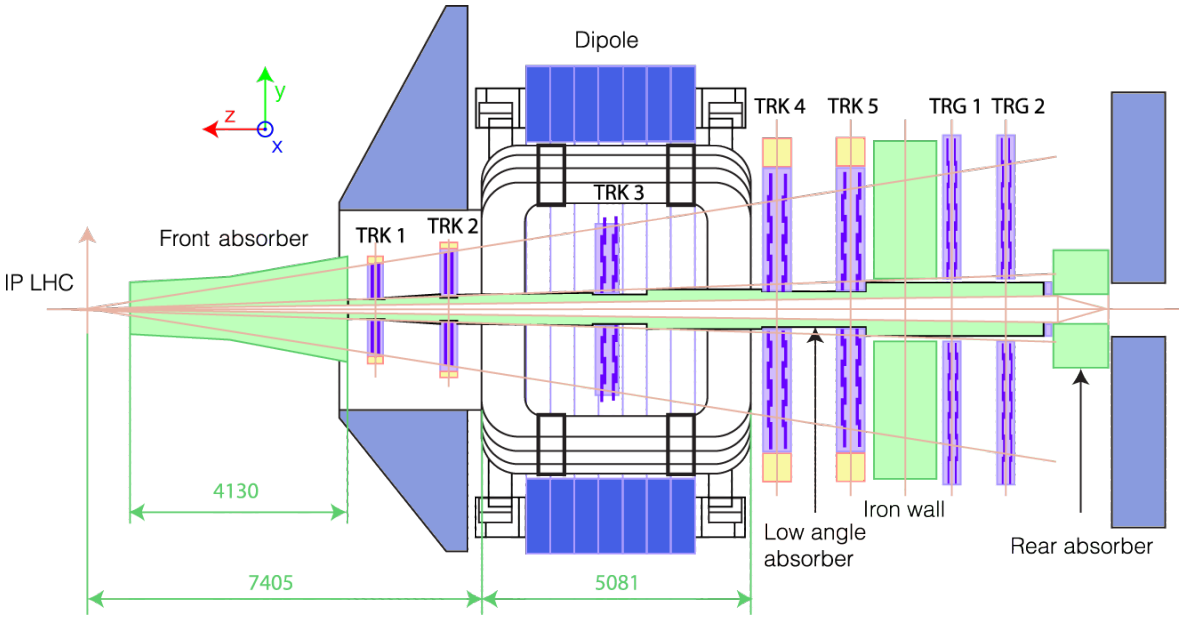

Figure 2.4 – Layout of the Muon Spectrometer in the (z,y) plane (Distances in mm). Figure taken from [CER13a]

are made of concrete.

The tracking chambers consist of ten high-granularity Multi-Wire-Proportional Chambers (MWPC) filled with a gas mixture of Argon (80%) and CO_2 (20%). The chambers are arranged in five stations between z = -5.2 m and z = -14.4 m, achieving a spatial resolution of 100 µm in the bending plane.

The dipole magnet, covering the middle tracking station, provides an integral field of 3 T m creating a magnetic field perpendicular to the beam axis, for particle momentum and charge determination.

The second absorber is a 1.2 m-long iron wall (~ 7 interaction lengths) located after

the tracking chamber. Its purpose is to shield the trigger system from energetic hadrons and secondary particles.

The trigger system is made of four planes of 18 Resistive Plate Chamber (RPC) arranged in two stations (MT1 and MT2). The system triggers events containing at least one muon with a p_{T} above an adjustable threshold.

2.2.7 Triggering System and Data Acquisition

The Central Trigger Processor (CTP) is a three-level architecture which triggers data acquisition system. It selects potentially interesting events and deals with detector latencies. Depending on the physics program, trigger classes are defined as the logical combination of several detector inputs. The first trigger inputs (L0) are sent by fast trigger detectors 1.2 µs after the collision (V0, T0, SPD, ElectroMagnetic Calorimeter (EMCal), PHoton Spectrometer (PHOS), and Muon Trigger (MTR)). If the conditions of the trigger class are fulfilled, the CTP sends a signal to the corresponding readout detectors. The second level (L1) corresponds to trigger inputs issued after some online calculations. The signal is issued with latency of 6.5 µs due to the computation time in the Transition Radiative Detector (TRD) and EMCal and the propagation times to the ZDC. The final level decision (L2) is taken about 100 µs after the collision corresponding to the TPC drift time. Detector data are sent subsequently to the ALICE Data AcQuisition (DAQ) system and to the High Level Trigger (HLT). The HLT filters and compresses data from a fast online reconstruction and the LHC bunch filling scheme. If all selection requirements are met, the event is registered to Permanent Data Storage (PDS). Recorded events are then processed and reconstructed after passing quality assurance to be ready for data analysis.

Several trigger classes are included in this analysis. The CMUL triggers are selected for J/ψ measurement via dimuon reconstruction. The other triggers are mainly used for normalisation purposes, as well as flow vector measurement and calibration.

Minimum Bias (MB) *(CINT7-B-NOPF-MUFAST)*, defined as a logical AND of a signal in the V0A and a signal in the V0C

Dimuon unlike *(CMUL7-B-NOPF-MUFAST)*, requiring at least two opposite-sign muons above the low-p_{T} muon track cut $\mathrm{p}_{\mathrm{T}}^{\mathrm{trigger}} > 1\,\mathrm{GeV}/c$

Dimuon like *(CMLL7-B-NOPF-MUFAST)*, requiring at least two same-sign muons above the low-p_{T} muon track cut $\mathrm{p}_{\mathrm{T}}^{\mathrm{trigger}} > 1\,\mathrm{GeV}/c$

MUSPB *(CINT7-B-NOPF-CENT)*, defined as the combination of the single muon trigger and a logical OR of a signal in the V0A and a signal in the V0C

The **physics selection** is an offline selection of events based on timing information from the V0 detectors and the ZDC to reduce beam-induced background.

Figure 2.5 – The ALICE apparatus and its subdetectors

2.3 The Muon Forward Tracker upgrade

The ALICE detector is preparing for a challenging **upgrade of several sub-systems** during the next shutdown [A+14d]. The strategy is aligned with the LHC luminosity increase of Pb–Pb collisions. The future interaction rate is foreseen to reach 50 kHz in Pb–Pb collisions, corresponding to an instantaneous luminosity of $\mathscr{L} = 6\,\mathrm{cm}^{-1}\,\mathrm{s}^{-2} \times 10^{27}\,\mathrm{cm}^{-1}\,\mathrm{s}^{-2}$, and 200 kHz in pp and p–Pb collisions. To make the most of this unprecedented operating conditions and enable the read-out of all interactions, several improvements and modifications of the current ALICE detector will be addressed. The upgrade consists of:

- a **smaller beam pipe**, reducing the radius from 29.8 mm down to 19.2 mm
- **two new high resolution silicon trackers** based on Complementary Metal–Oxide–Semiconductor (CMOS) sensors
  - the current **ITS** covering the mid-rapidity region will be replaced with seven layers of sensors for an improved tracking efficiency and resolution, particularly at low p_{T}, and an increased read-out rate [A+14c]
  - a new tracker will be installed at forward rapidity to add vertexing capabilities to the current Muon Spectrometer: **the Muon Forward Tracker** [CER13a, CER15]
- the replacement of the existing wire chambers in the TPC with **Gas Electron Multiplier (GEM)** detectors and a new pipelined read-out electronics to operate in continuous mode [CER13b]
- an **upgraded read-out electronics** of the TRD, TOF detector, and the Muon Spectrometer [AKR]
- a **new integrated online-offline computing system** (O^2) to handle the expected 3.4 TB/s data flow and 100 GB/s data-to-storage rate [BKVV15] as detector read-out will be activated either by a minimum bias trigger or in a continuous mode.

The upgrade will significantly **expand the current capabilities of the apparatus**. A total of 10 nb^{-1} Pb–Pb collisions is expected to be collected. The statistical gain combined with the enhanced capabilities of the detector will enable to address the next physics program of ALICE, focusing on **high-precision measurements of rare processes at low p_{T}**.

This section focuses on the Muon Forward Tracker upgrade and specifically on the characterisation of the detector sensor performed as part of this thesis.

2.3.1 Physics motivations

The addition of the Muon Forward Tracker (MFT) aims to **fully exploit the kinematic range of the Muon Spectrometer** by addressing several intrinsic limitations. The physics program focuses on charmonium dynamics, heavy quark thermalisation and energy loss in the QGP, beauty physics and the study of chiral symmetry breaking and restoration through low-mass vector mesons. Currently, multiple scatterings in the frontal absorber and the distance of the spectrometer to the collision point smear out information on the primary vertex. The accessible track resolution by extrapolating from the spectrometer to match the MFT reconstructed tracks before the frontal absorber would benefit the study of open heavy flavours, quarkonium states and low mass dimuons.

The MFT upgrade project aims to address the current design limitations of the Muon Spectrometer:

- the background level in both single-muon and dimuon analyses by rejecting muons coming from semi-muonic decays of pions and kaons (particularly significant for low masses and at low p_T)
- the inclusive charmonium production by providing a reliable separation of prompt and non-prompt J/ψ production down to zero p_T
- open heavy flavour study down to $p_T \sim 2\,\mathrm{GeV}/c$ by separating charm and beauty components without relying exclusively on model assumptions
- the poor angular resolution for low masses (ω, ϕ mesons).

More details can be found in the Letter of Intent [CER13a] and the Technical Design Report [CER15] of the MFT.

2.3.2 Overview of the detector

General layout and environment

The MFT will stand **between the interaction point and the frontal absorber** of the muon arm by surrounding the beam pipe (Fig.2.6). It consists of two half-cones made of 5 half-disks along the beam axis. The pseudo-rapidity acceptance will cover $3.6 < \eta < 2.45$.

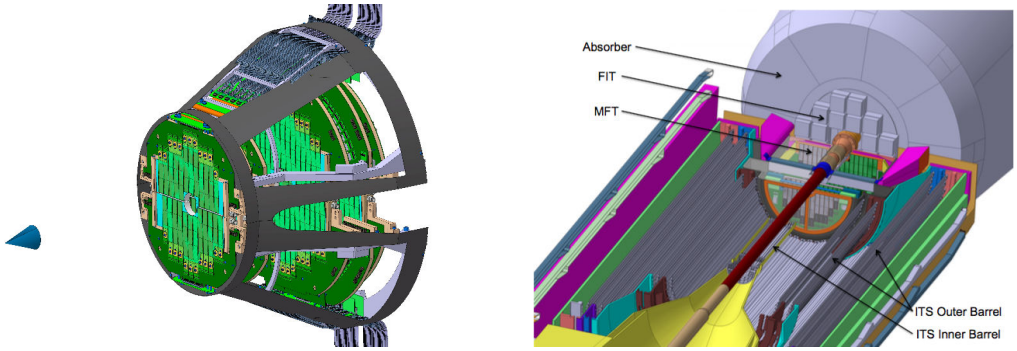

Figure 2.6 – MFT layout and position within the ALICE apparatus [CER15]

The detection sensors are soldered on vertical mechanical ladder structures with aluminium strips to a flex printed circuit. Each half-disk contains 2 detection planes (front and back) and consists of 24 to 34 sensor ladders, a disk support, two PCB Printed Circuit Board (PCB) disks and a disk spacer. The geometrical characteristics of the MFT half-disks are reported in Tab. 2.1.

The highest hit density was estimated about 12.9 particles/mm^2 from central Pb–Pb collisions at $\sqrt{s_{\mathrm{NN}}} = 5.5\,\mathrm{TeV}$. The accumulated radiation level over operation is expected to reach up to $5.91 \times 10^{12}\,\mathrm{MeV\,n_{eq}/cm}$ of non-ionizing energy loss and 380 krad of total ionizing dose, including a safety factor of ten.

Detector technology

To achieve the objectives of the physics program, the future MFT sensors must fulfil several specifications, reported in Tab. 2.2, established from Monte-Carlo simulations. To meet with the required low-material budget, the sensors are thinned down to 50 µm.

Half-Disk	0	1	2	3	4	Full MFT
Inner radius (mm)	25.0	25.0	25.0	38.2	39.2	-
Outer radius (mm)	92.6	98.0	104.3	130.1	143.5	-
z-position (mm)	460	493	531	687	768	-
No. sensors	64	64	76	112	132	896
No. ladders	24	24	26	32	34	280

Table 2.1 – Geometrical details of the MFT half disks (radius, position, number of sensors and number of ladders), table taken from [CER15]

Detection: Given the similar requirements of the ITS upgrade, the same sensor was selected, with a common R&D and characterisation effort between both ITS and MFT teams. In addition, the MFT sensors will cover a much smaller surface (0.4 m^2) compared to the upgraded ITS (10.3 m^2).

Parameter	value
spatial resolution	5 µm
pixel pitch	25 µm
detection efficiency	> 99.5 %
integration time	20 µs
sensor thickness	50 µm
power dissipation	<150 mW/cm^2

Table 2.2 – MFT sensor requirements

Many tracking devices involve silicon microstrip and pixel sensors with read-out electronics based on **CMOS technology**. The technology shows great features in terms of granularity, material thickness, read-out speed, power consumption and radiation hardness. CMOS Monolithic Active Pixel Sensor (MAPS) integrate **both sensor and read-out electronics into a single detection device**, allowing **interface optimisation between the sensor and the read-out electronics**. The main advantage with respect to hybrid pixels is the **lower material budget and power consumption** but the radiation tolerance is limited. MAPS pixel have already been implemented on a large scale with the Solenoidal Tracker At RHIC (STAR) PXL detector at RHIC in 2015 and research has been conducted for many years on this technology. The more restrictive requirements of the ITS/MFT detectors do not allow to use the same sensors as STAR, and a new chip was thus developed.
The TowerJazz 0.18 µm CMOS Imaging Sensor Process was selected for the future sensors. The technology offers several advantages, starting with the **high resistivity** (> 1 kΩcm) p-type epitaxial layer that provides an efficient charge collection and an improved radiation tolerance through the possibility of applying a **reverse substrate bias** to the collection diode. A schematic cross section is illustrated on Fig. 2.7. Charged particles passing through the epitaxial layer produce electron-hole pairs along their path through many scattering processes in the absorbing material. In the case of charged particles heavier than the electron, the mean rate of energy loss is described by the Bethe-Bloch formula. The energy loss is a discrete stochastic process depending on the particle type and momentum. The formula can be corrected with additional terms such as density and shell corrections.

Created charges in the sensor volume are collected by the n-well diode electrodes (the depletion volume is represented in white on the schematic cross section).

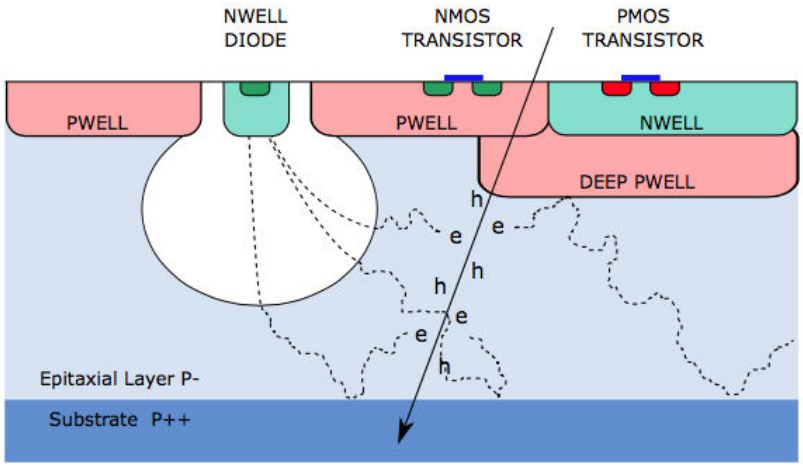

Figure 2.7 – Schematic cross section of a CMOS pixel sensor using TowerJazz 0.18 µm CMOS Imaging Process, figure taken from [A+14d]

The deep p-wells shielding p-channel Metal Oxide Semiconductor (PMOS) transistors together with the 6 metal layers allow the integration of the front-end circuitry with a very low-power consumption (<40 mW/cm^2). The pixel chip consists of 512 rows x 1024 columns of 27 x 29 µm^2 charge collection diodes on a single silicon die of about 15 mm× 30 mm.

Front-end electronics: The surface electronics performs signal amplification, digitisation and zero-suppression. The schematics of the matrix is illustrated on Fig. 2.8 with successive zooms onto the chip regions.

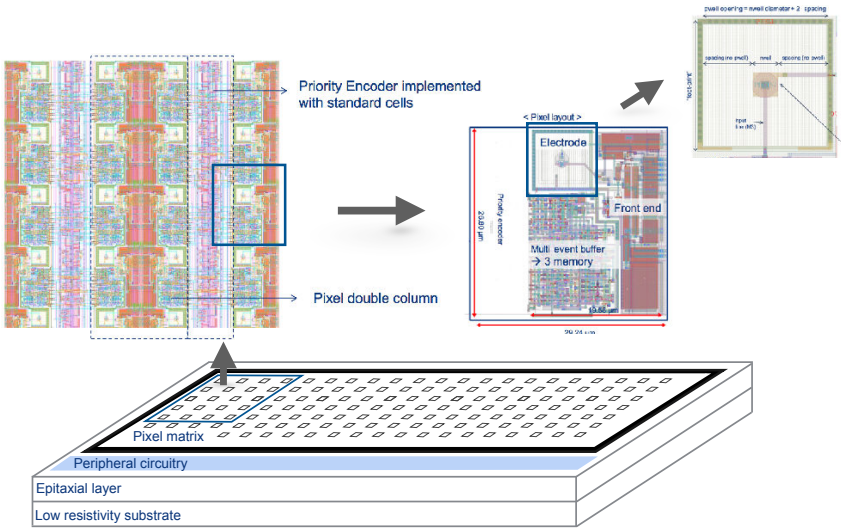

Figure 2.8 – Layout of the final pixel matrix (Bottom), zoom over several pixels (Top Left), the pixel region (Middle) and the pixel geometry (Top Right)

The output signal is the PIX_OUT_B node which is high in static behaviour and becomes active when driven low. The dynamic behaviour of the analogue front-end can be described as follows: a charge collection in the diode D_1 (alternatively a charge injection through the

capacitance C_{inj}) causes a potential drop at the IN node. The circuit is then divided into a *gain* stage and a *discrimination* stage. The increase of source-to-gate voltage generates an additional current to flow through the PMOS cascade (M_1,M_2) from the current source I_{BIAS}, charging the OUT node. The node is restored as the voltage becomes close to the gate potential V_{CASN} of the M_4 transistor and reduces its conductance. Thus the value of the V_{CASN} voltage sets the baseline of the OUT potential. The current I_{THR} will therefore flow through the CURFEED node, opening the M_3 transistor and discharging the OUT node. The duration of the restoration process and the pulse shape can be adjusted with the I_{THR} current. A clipping mechanism was added to limit the pulse duration. Then the transistor M_7 becomes conductive again and the CURFEED node is also restored. During the time laps where the OUT potential is larger than the critical voltage of the M_7 n-channel Metal Oxide Semiconductor (NMOS) transistor, the latter becomes conductive. If the current from the bottom line (V_{SSA}) exceeds the I_{DB} current, the PIX_OUT_B will be driven low and becomes high again once the OUT node is discharged.

The front-end electronics is completed by a novel read-out approach, faster than the traditional rolling shutter architecture.

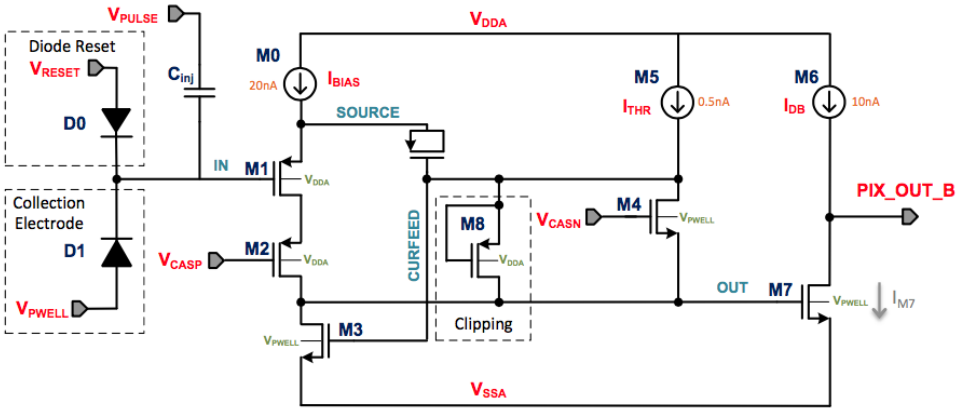

Figure 2.9 – Schematic drawing of the analogue front-end of the Prototype ALPIDE-3 (pALPIDE-3) chip

Diode geometry and reset mechanisms: Different geometries for the n-well collection diode were investigated with small-scale prototypes. Several diameters and spacings between the n-well and p-well with the selected octagonal shape were tested for the full-scale Prototype ALICE PIxel DEtector (pALPIDE) prototypes. Both distances are illustrated on Fig. 2.10 for both reset mechanisms. The front-end presents two implementations depending on the reset of the collection diode.

Read-out: A novel Address Encoder Reset Decoder (AERD) asynchronous circuit was implemented with respect to the traditional rolling-shutter architecture to achieve the low-power consumption, fast read-out and short integration time requirements. The AERD read-out is data-driven and is based on priority logic, reading only the hit pixels. It is arranged in double columns inside the matrix (see Fig. 2.11) and pixel outputs are treated by successive four-input blocks. This architecture loops over all hit pixels, and then encodes, propagates, and resets their addresses to the chip periphery, ensuring data-compression before storing information in the chip memory.

Data acquisition can be performed either in a **triggered or a continuous integration mode** (see illustration on Fig. 2.12). In the triggered case, each trigger signal opens an

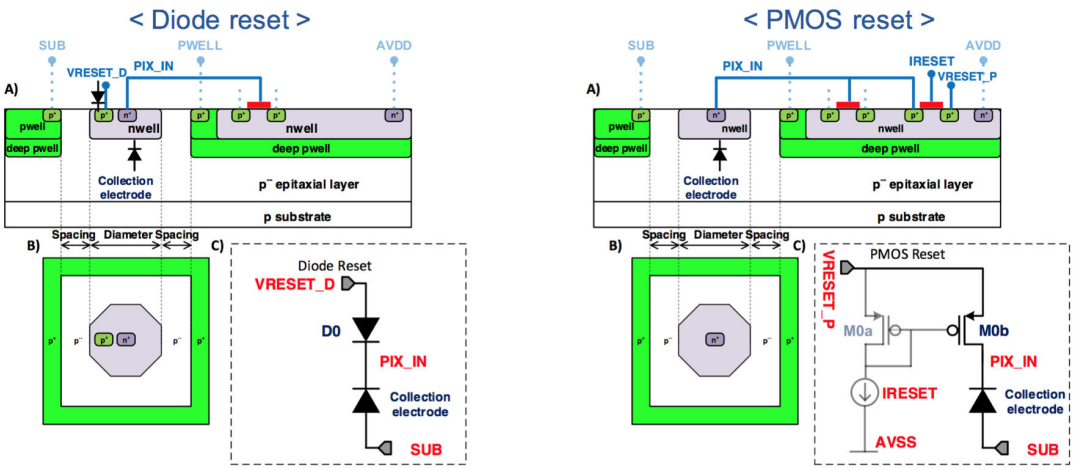

Figure 2.10 – Schematic view of a pALPIDE collection diode with a diode (Left) or PMOS (Right) reset mechanism

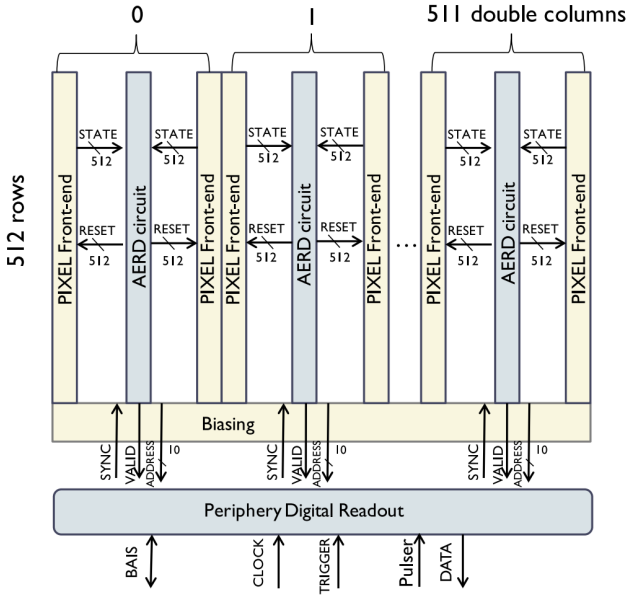

Figure 2.11 – Structure of the ALICE PIxel DEtector (ALPIDE) AERD circuit, figure taken from [Y+15]

acquisition window. Upon the end of the fixed-duration window (~ 250 ns), the read-out of the pixel matrix is initiated and data are transferred to the memory blocks. In the continuous integration mode, the trigger is asynchronous from physics events. The acquisition window stays open between signals that trigger the matrix read-out.

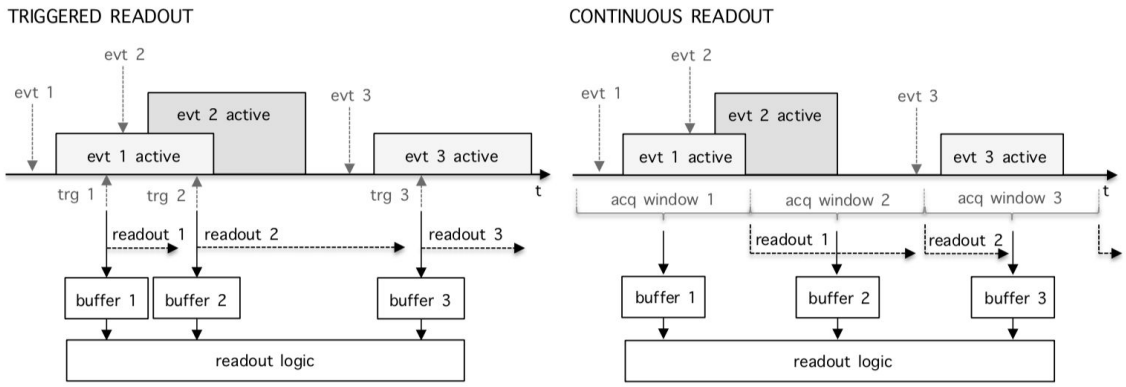

Figure 2.12 – Illustration of the triggered (Left) and continuous integration (Right) read-out modes with three in-pixel memory cells, figure taken from [Szc16]

2.4 CMOS prototype characterisation

The final sensor was the result of several years of R&D design and an extensive characterisation campaign.

2.4.1 Measurement techniques

About 300 prototypes were tested, both in the laboratory for **setting optimisation** and pulse-shape measurements and under **test beams** in several facilities for measurements of spatial resolution, detection efficiency, noise, charge collection efficiency, chip-by-chip variation effects and other external parameters (temperature, track multiplicity, irradiation, etc...).

Laboratory measurements

After production, the chips are checked for faults and characterised to find their optimal operation settings. Chips are wire-bonded to carrier boards and connected to read-out DAQ boards with usb ports for readout and control functionality (see Fig. 2.13).

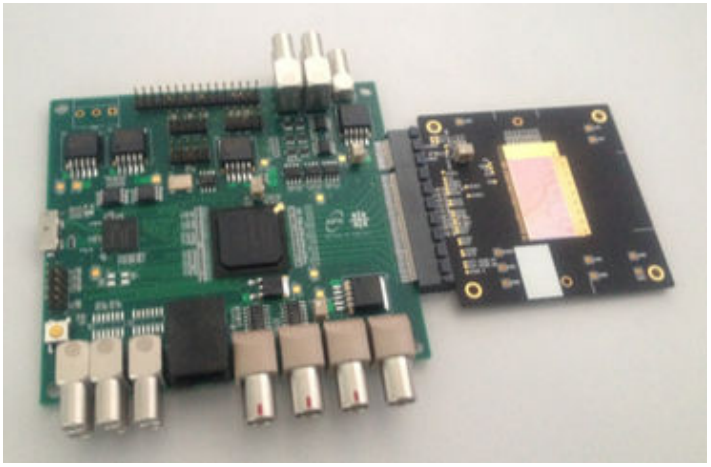

Figure 2.13 – DAQ read-out board connected an ALPIDE chip

Each test is performed on the pixel level, the sector level, and over several chips to

extract average values. The *AlpideAnalysis* software was developed to perform tests and analyse the results. Examples of tests are:

- **Threshold and temporal noise**: A charge can be injected into the preamplifier of each pixel by applying a voltage step to the injection capacitance (C_{inj}). The injected charge is increased to find the threshold to fire the pixel. The pixel noise is the width of the charge step (yellow width on Fig. 2.14, Left). Threshold variations between pixels are taken into account by performing threshold tests over several pixels for each sector of a prototype (see Fig. 2.14, Right). Several parameters affects the pixel

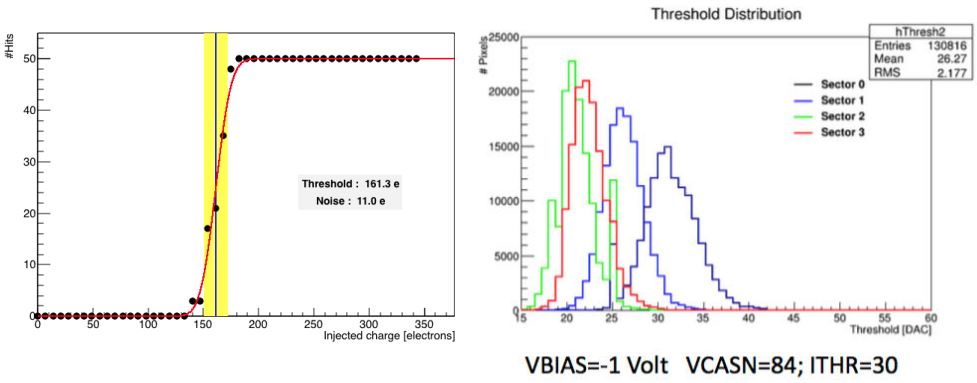

Figure 2.14 – (Left) Illustration of a threshold scan: number of hits as a function of the injected charge for a single pixel (black points) with a fit (red line), (Right) Example of threshold distribution for 1 % of pixels inside each sector of an pALPIDE-3 chip

response, all were studied to find the optimal values. For example, pixel threshold and temporal noise depend on the values of the I_{THR} current and the V_{CASN} voltage. Fig. 2.15 illustrates the dependency on a 2D-map for a given sector.

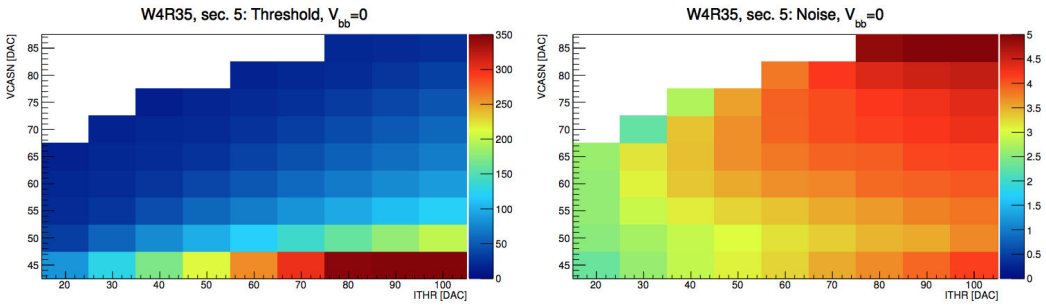

Figure 2.15 – Example of 2D-maps of treshold (Left) and noise (Right) dependence versus the I_{THR} and V_{CASN} parameters

- **Pulse shape**: The strobe delay with respect to charge injection affects the hit-detection probability. By scanning the pulse shape dependence as a function of the injected charge and the strobe delay, several characteristic parameters can be extracted.

- **Noise occupancy**: Some tests were conducted to measure the fake-hit rate of the matrix. Masking a small fraction of noisy pixels reduces significantly the total fake-hit rate.

- **Charge collection efficiency** using radioactive sources.

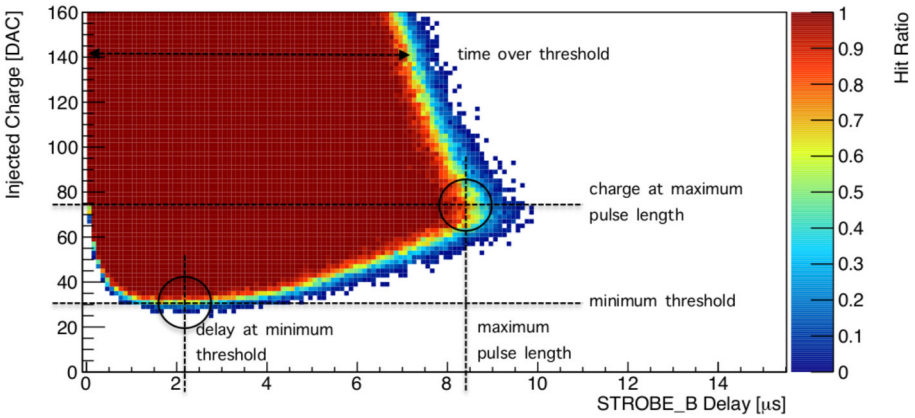

Figure 2.16 – Example of 2D-pulse-shape scan with definition of characteristic parameters

Test beam campaign

After optimisation of the pixel settings, the chip performances were tested into several test-beam facilities, namely Beam Test Facility (BTF) in Frascati (450 MeV e^- beam), Deutsches Elektronen-Synchrotron (DESY) in Hamburg (5 GeV e^- beam), Pohang Accelerator Laboratory (PAL) in Pohang (60 MeV e^- beam), Synchrotron Light Research Institute (SLRI) in Nakhon Ratchasima (1 GeV e^- beam), PS at CERN (6 GeV π^- beam),SPS at CERN (120 GeV π^- beam) and U—120M in Řež (300 MeV proton beam). Seven chips are placed inside an experimental setup, named telescope, holding the chips in place. The middle three chips are tested (denoted Device Under Test (DUT)) and the others are used for the alignment. The telescope is illustrated on Fig. 2.17 containing chips connected to their DAQ boards. The beam configuration is set up and monitored with scintillators.

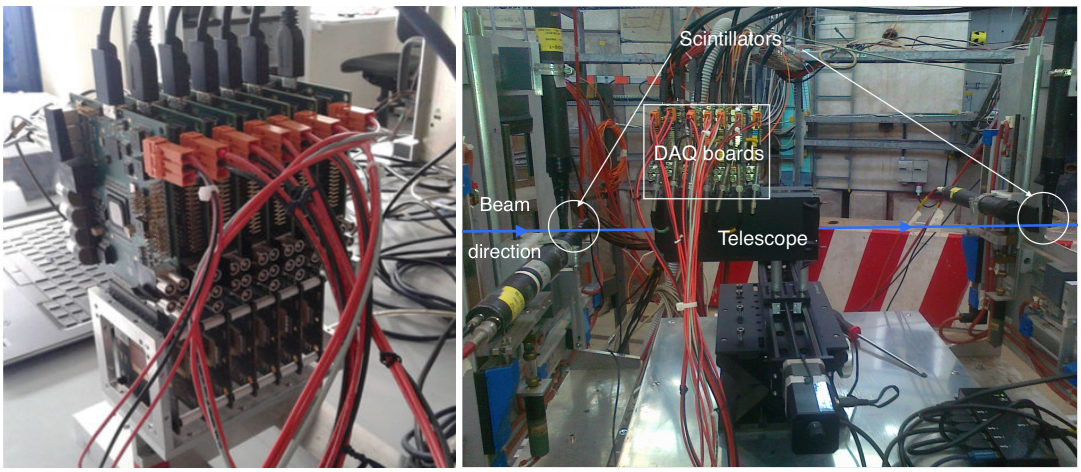

Figure 2.17 – (Left) Layout of the telescope and (Right) setup for test beam at PS (CERN)

Data were analysed within the EUTelescope framework (designed and supported by the DESY collaboration).This group of processors is used for DUT measurements and provides a full-featured infrastructure for analysis and reconstruction of data taken with pixel beam telescopes. The test-beam analysis was oriented towards detection efficiency, noise occupancy, spatial resolution, and cluster size. Examples can be found on Fig. 2.18.

Other systematic studies were conducted. For example chip fluctuations were investigated both through laboratory and test beam measurements to ensure a realistic description of the chip characteristics. The temperature dependency of the signal response

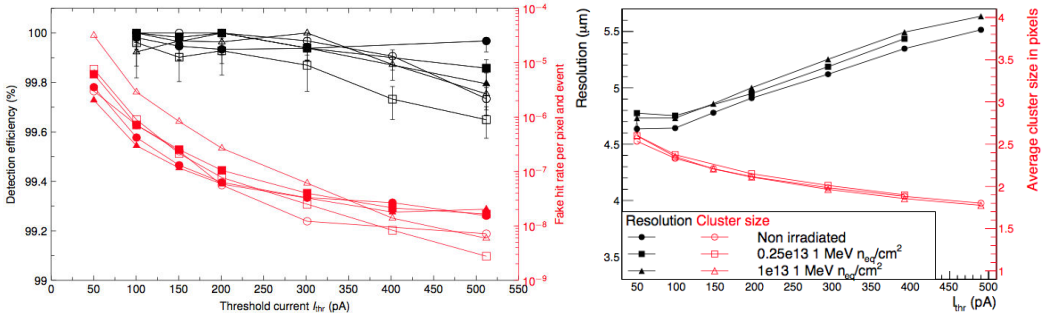

Figure 2.18 – (Left) Detection efficiency (in black, legend on the left) and fake hit rate (in red, legend on the right), (Right) spatial resolution (in black, legend on the left) and cluster size (in red, legend on the right) of ALPIDE chips with different irradiation levels

was also characterised since the temperature of the chip rises during its operation to reach ~ 25–30 °C. Some tests were also carried out with a cooling system on the chip and no major variation was observed. The impact of dead pixels inside a matrix on the chip performances was also studied, masking a few noisy pixels was very successful and allows to significantly improve the overall performances of the chip. Applying back-bias voltage (up to $V_{bb} = -6$ V) also significantly improves the performances of the sensor (new chips do not require to apply back-bias but a larger margin of operation is available, which might be exploited after irradiation).

2.4.2 ALPIDE prototypes

Several prototypes were developed to test and optimize the features of the final sensors. Full-scale prototypes were produced from 2014 (Prototype ALPIDE-1 (pALPIDE-1), Prototype ALPIDE-2 (pALPIDE-2) and pALPIDE-3). Tests were also conducted on irradiated chips to study the long-term behaviour of the chip in the expected radiation environment inside the ALICE detector. A complete description of the characterisation can be found at [vHKR15, RSM16, VKSGO17, BAB16].

pALPIDE-1

The pixel matrix is divided into 4 sectors of 256x512 pixels with different spacing and/or reset mechanisms. The chip is 28.7 mm by 14.3 mm and its total thickness approximates 50 µm depending on the epitaxial layer. About 130 pALPIDE-1 prototypes were produced and tested with different epitaxial layer thickness. Increasing the epitaxial thickness enlarges the volume for charge generation (higher number of e–h pairs) but this also implies a larger diffusion volume. In terms of noise occupancy and detection efficiency, the sector 0 falls behind the others. The enhancing parameters are the diode reset and the larger spacing.

pALPIDE-2

In parallel, a second full-scale prototype was tested, featuring the final interface, the high-speed link excepted. To give more space for in-pixel circuitry, the pixel size was reduced. The matrix is divided into four sectors with different spacings, input transistor sizes and reset mechanisms (see Tab. 2.4). Different epitaxial layer properties (thickness) were tested. Pixels with a wider input transistor exhibit a lower fake-hit rate. The required performances after irradiation are met when applying back bias for 25 µm– and 30 µm–thick epitaxial

Sector	Nwell diameter	Spacing	Pwell	Reset
0	2 µm	1 µm	4 µm	PMOS
1	2 µm	2 µm	6 µm	PMOS
2	2 µm	2 µm	6 µm	diode
3	2 µm	4 µm	10 µm	PMOS

Table 2.3 – pALPIDE-1 sectors

layers. Comparisons of the different sectors show that larger spacing and input transistor are beneficial.

Sector	Spacing	Input transistor	Reset
0	2 µm	small	PMOS
1	2 µm	large	PMOS
2	4 µm	small	PMOS
3	4 µm	small	diode

Table 2.4 – pALPIDE-2 sectors

pALPIDE-3

The last prototype was dedicated to the optimisation of the front-end electronics (see Tab. 2.5). The characterisation focused on 18–25 µm thickness. From the results of the previous prototypes, the sectors 3, 5 and 7 were specifically investigated, in particular for back bias performances. The decision criteria were the detection efficiency with respect to fake-hit-rate and the pulse shape. The chip contains the final high-speed connection and the three in-pixel hit buffers. A second version (Prototype ALPIDE-3b (pALPIDE-3b)) was produced with an increased input size and V_{CASP} transistors to reduce the Random Telegraph Signal (RTS) noise.

Sector	M3, M5, M6, M8	M9	M6 Clipping	M1 Bulk	Reset	Spacing
0	optimized	yes	diode conn.	AVDD	diode	2 µm
1	optimized	no	diode conn.	AVDD	diode	2 µm
2	previous	no	diode conn.	AVDD	diode	2 µm
3	optimized	yes	VCLIP	AVDD	diode	2 µm
4	optimized	yes	VCLIP	SOURCE	diode	2 µm
5	optimized	yes	VCLIP	SOURCE	diode	3 µm
6	previous	no	diode conn.	AVDD	PMOS	2 µm
7	optimized	yes	VCLIP	AVDD	PMOS	2 µm

Table 2.5 – pALPIDE-3 sectors

The final sensor

The pixel characterisation for the future ITS/MFT detectors was conducted over several months through small-scale and full-scale prototypes. A deep understanding of the parameters influencing the chip behaviour – both from the collecting diode geometry, the epitaxial layers properties, and the front-end electronics – was achieved. The performances from all full-scale prototypes fall within the detector requirements, in particular in terms of detection efficiency, noise occupancy, spatial resolution and cluster size, even after irradiation. The recommendations for the final sensor correspond to the sector 5 of the 18 µm pALPIDE-3 chip with a diode reset, a 3 µm– spacing and optimized transistors. The pixels have a large margin to operate with a back-bias at $V_{bb} = -3$V where the pulse shape length is around ~ 8–10 µs and test beam results show a very low fake-hit rate.

CHAPTER 3

ELLIPTIC FLOW

"You live as long as you dance."

— Rudolph Nureyev

Studies of collective phenomena have greatly contributed to the description of the system created during high-energy nucleus-nucleus collisions. If the system is strongly interacting, a **local thermal equilibrium** should be established and maintained so that the fireball evolution may be described as a **fluid** undergoing **collective motion** [A+05b] with a **short thermalisation time**. The collective expansion of the created hot and dense matter is developed from the initial pressure gradients and is particularly sensitive to the interactions among constituents [Oll92]. One of the major and most suprising discoveries in the field is the quantitative good description of heavy-ion collisions by **relativistic hydrodynamics** [RZ06], allowing to access the **shear viscosity** of the medium. An excellent review of elliptic flow measurements from AGS to the first LHC run is available at [Sne11].

This chapter focuses on elliptic flow measurements. Heavy-ion collisions exhibit sizeable azimuthal anisotropy coefficients, usually attributed to collective phenomena. Initially associated to light flavours, these observations have recently been extended to the heavy-flavour sector. More surprising are the similar features observed in smaller collision systems, where no QGP is expected to form.

3.1 Azimuthal asymmetry

Anisotropic flow is the **system response to the initial collision geometry** as the two nuclei collide. The final azimuthal anisotropies in the momentum distributions are thought to originate from the initial spatial asymmetry of the system and are developed through multiple interactions between the medium constituents at an early stage in the system evolution. The collision geometry varies with the impact parameter of the nuclei. In non-central collisions the overlap region of the two colliding nuclei is azimuthally asymmetric. The symmetry plane of the initial geometry, referred to as **reaction plane**, is spanned by the impact parameter vectors and the beam direction, as illustrated on Fig. 3.1. The initial geometry of the system is almond-shaped, and as it expands and cools down, the pressure gradients drive it towards a more symmetric shape (cf Fig. 3.2).

The particle momentum distribution with respect to the reaction plane can be decomposed into a Fourier series [VZ96] as:

$$\mathrm{E}\frac{d^3\mathrm{N}}{d^3p} = \frac{1}{2\pi}\frac{d^2\mathrm{N}}{p_\mathrm{T}dp_\mathrm{T}dy}\{1+\sum_{n=1}^{\infty}2v_n\cos(\mathrm{n}(\phi-\Psi_\mathrm{RP}))\}. \tag{3.1}$$

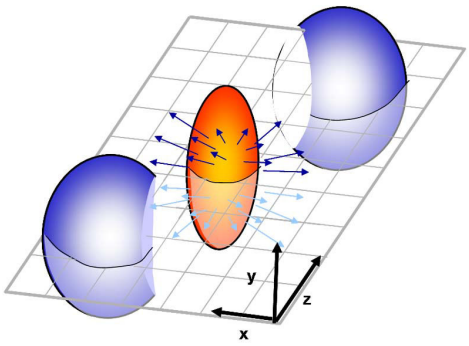

Figure 3.1 – Illustration of the reaction plane

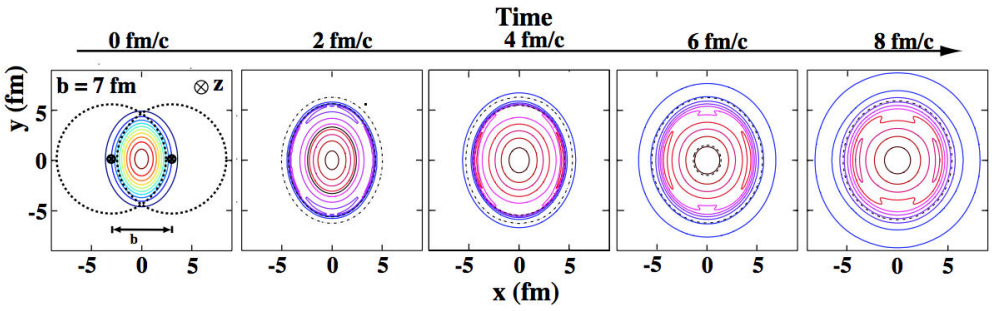

Figure 3.2 – Time evolution of the transverse energy-density profile for non-central heavy-ion collisions [KH03]

For each flow harmonic, the corresponding n^{th} flow coefficient can be experimentally measured as the average over all particles in all events $v_n = \langle \cos[n(\phi - \Psi_{RP})] \rangle$. The first coefficient corresponds to the direct flow and the second coefficient is called the **elliptic flow**. The v_2 coefficient is positive in the case where the in-plane region contains more particles in the final particle distribution than the out-of-plane region. Higher harmonics are related to fluctuations in the initial parton distributions inside the nuclei, including the triangular coefficient v_3. Event-by-event fluctuations are studied through odd harmonics (v_3 and v_5).
The second harmonic is particularly sensitive to the equation-of-state, transport properties and early times of the system due to the geometry of the collision. Particle anisotropy can also have a non-collective origin. For example high-p_T particles traverse a longer distance moving out-of-plane than in-plane, thus out-of-plane particles should experience more scattering and energy loss.

3.2 Observations in A–A collisions

Experimental observations of elliptic flow were first performed at the BNL AGS [B+94, B+97], at the CERN SPS [A+03d], and at RHIC [A+01a] and are addressed by all the current heavy-ion physics programs. Flow studies usually focus on its dependence on centrality, particle transverse momentum, and mass. This section highlights some of the main results in A–A collisions.

The comparison of flow measurements at different facilities as a function of the **collision energy** is illustrated on Fig. 3.3 for semi-central collisions (integrated over the 20–30 % centrality range), where elliptic flow typically reaches its maximum value. The comparison of low-momentum elliptic flow measurements of charged particles [A+01a, B+02, A+01b]

suggests a continuous increase of the v_2 amplitude from RHIC to LHC energies. An increase of about 30 % is observed for charged particle v_2 from RHIC to LHC [A+10] (mainly originating from the harder p_T spectra) with a smooth transition and a smaller enhancement from $\sqrt{s_{NN}} = 2.76$ TeV to $\sqrt{s_{NN}} = 5.02$ TeV [A+16b]. At low collision energies, where the nuclei crossing time is larger and compares to the expansion time of the system, the final anisotropy is affected by the spectator nucleons which disfavour the in-plane region [GKS+89].

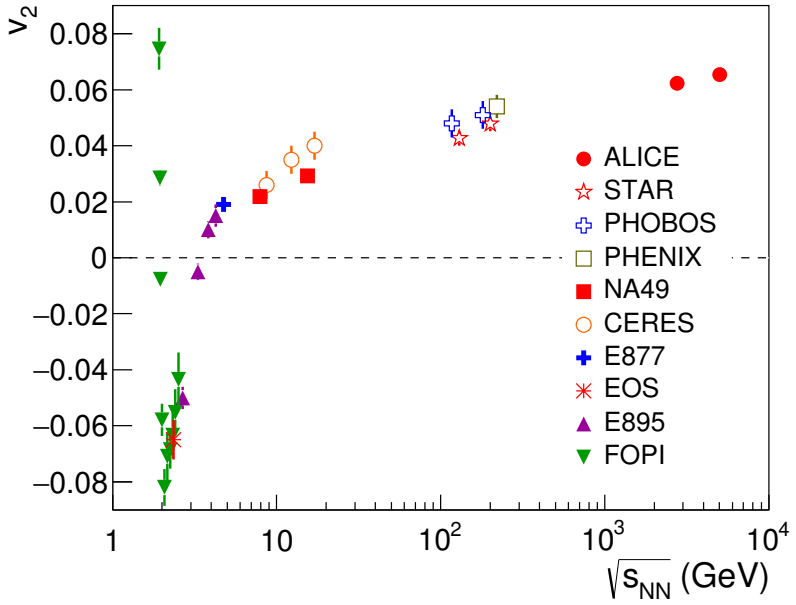

Figure 3.3 – Integrated elliptic flow measurement for semi-central collisions as a function of the collision energy[A+16b] from the Heavy Ion Synchrotron to the LHC

The **centrality dependence** of the elliptic flow is illustrated on Fig. 3.4 for charged particles in Pb–Pb collisions at the LHC [A+16b]. An increase from central to peripheral collisions is observed, with a maximum value in the 40–50 % centrality class, followed by a gentler decrease for more peripheral collisions. This observation is consistent with the picture of an azimuthal anisotropy originating from the initial geometry of the overlap region. The asymmetry is indeed boosted for peripheral collisions compared to central ones up to a limit where the number of participants in the collision becomes too low.

Depending on the p_T range, two main characteristic behaviours are observed and can be explained in the coalescence picture [Mol04]. Fig.3.5 represents elliptic flow measurements of ALICE at $\sqrt{s_{NN}} = 2.76$ TeV for several identified particles in semi-central collisions. Similar observations can be extracted from results at $\sqrt{s_{NN}} = 5.02$ TeV [A+18c].
For the vast majority of the particles (produced roughly for p_T below 2–3 GeV/c), particle flow is ordered as a function of the particle mass. This characteristic mass dependence, or **mass ordering**, was observed very early (E877 at the AGS [B+99] and NA49 at the SPS [A+04b]), studied in detail for elliptic flow (Pioneering High Energy Nuclear Interaction eXperiment (PHENIX) [A+07c, A+12d] and STAR [A+07a, A+05a]) and later for higher coefficients (STAR [A+13e], PHENIX [Gu13], ALICE [A+16h]).
At intermediate p_T particles tend to group according to their number of constituent quarks, this observation being commonly referred to as the **number of constituent quark scaling**. This behaviour can be explained with an elliptic flow developed at the partonic level and a

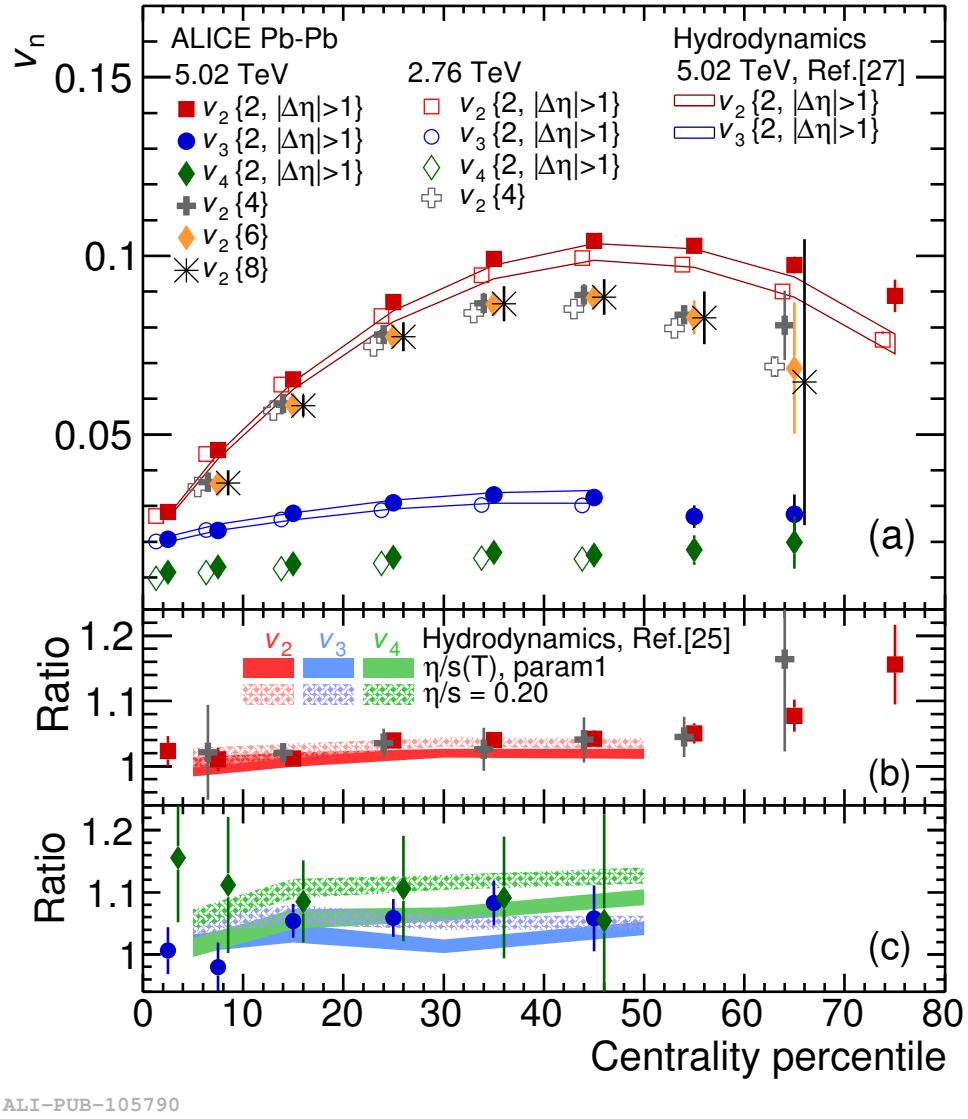

Figure 3.4 – (Top) Flow coefficients v_n as a function of event centrality (integrated over $0.2 < p_{\mathrm{T}} < 5.0\,\mathrm{GeV}/c$) measured in Pb–Pb collisions at $\sqrt{s_{\mathrm{NN}}} = 2.76\,\mathrm{TeV}$ and $\sqrt{s_{\mathrm{NN}}} = 5.02\,\mathrm{TeV}$ by ALICE using multi-particle correlations with x cumulants ($v_n\{x\}$), Calculations from hydrodynamic models [NHLO16, NEPT16] are presented. (Bottom) Ratios of v_n coefficients between both data samples [A$^+$16b]

baryon/meson splitting occurring during the hadronisation stage.
More recently, ALICE measurements at $\sqrt{s_{\mathrm{NN}}} = 5.02\,\mathrm{TeV}$ suggest an approximate power law scaling of each flow charmonic, in the form $v_n(p_{\mathrm{T}}) \sim p_{\mathrm{T}}^{n/3}$ below $2\,\mathrm{GeV}/c$ and close to $v_n(p_{\mathrm{T}}) \sim p_{\mathrm{T}}^{n}$ above [A$^+$18f].

The **pseudorapidity dependence** of the elliptic flow is shown on Fig. 3.6 for charged particles in Pb–Pb collisions at $\sqrt{s_{\mathrm{NN}}} = 2.76\,\mathrm{TeV}$ and Au–Au collisions at $\sqrt{s_{\mathrm{NN}}} = 200\,\mathrm{GeV}$. The maximum value is reached for central rapidities and the anisotropy becomes less pronounced as we move towards forward/backward rapidities, with a delta up to 30 %. This observation may originate from spectators around the collision creating density gradients of matter distribution [LFLHA16].

The large azimuthal anisotropies in particle spectra observed in A–A collisions at RHIC and LHC energies can be reproduced by hydrodynamic calculations assuming a

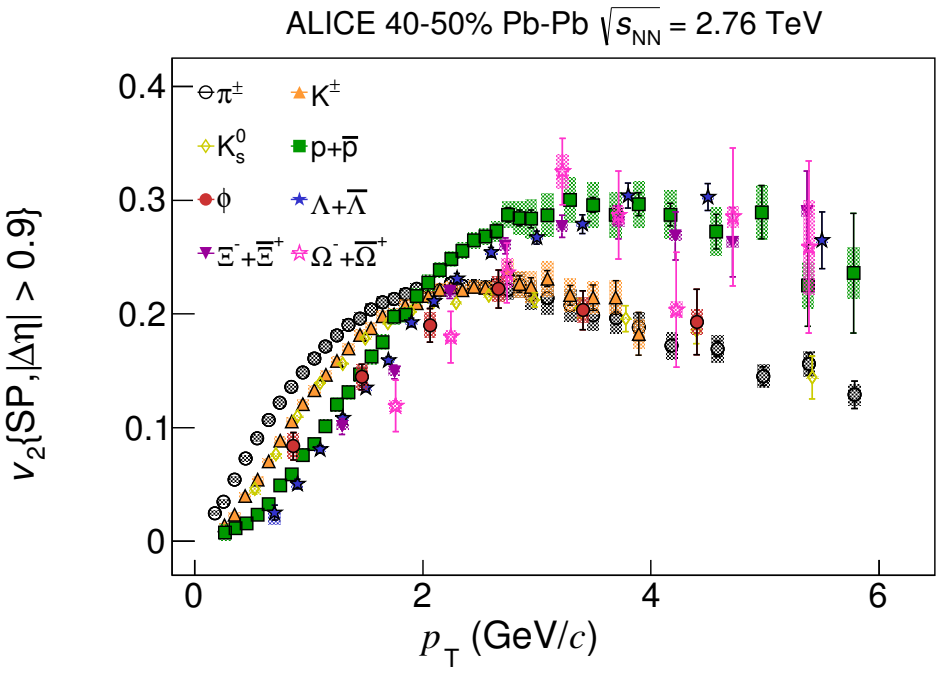

ALI-PUB-82660

Figure 3.5 – The p_T-differential v_2 measured by ALICE for different particle species in the 40–50 % centrality range of Pb–Pb collisions at $\sqrt{s_{NN}} = 2.76$ TeV [A+15b]

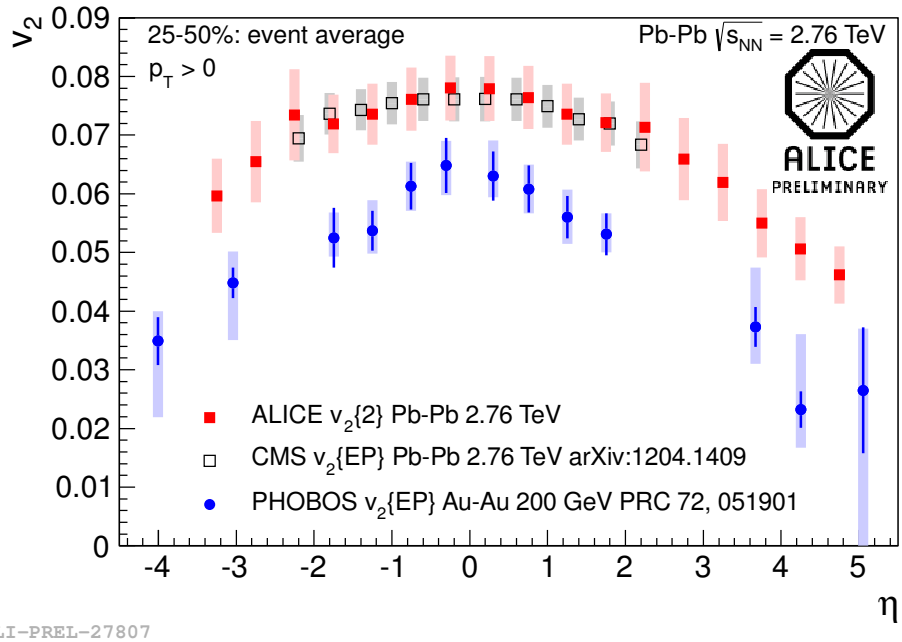

ALI-PREL-27807

Figure 3.6 – Pseudorapidity dependence of the elliptic flow measured by ALICE [A+16j] and CMS [S+17] in Pb–Pb collisions at $\sqrt{s_{NN}} = 2.76$ TeV and by PHOBOS [B+05] in Au–Au collisions at $\sqrt{s_{NN}} = 200$ GeV

rapid thermalisation of the system and a very small viscosity of the interacting medium. From quantum mechanics principles, strong-coupling calculations [KSS05] based on the anti-de Sitter/conformal field theory (AdS/CFT) conjecture[Mal99] estimate the lowest shear-viscosity-to-entropy-density ratio $\frac{\eta}{s}$ at $\frac{\hbar}{4\pi}$ [PSS01]. Flow-coefficient and correlation measurements demonstrated that the QGP produced at RHIC and LHC is close to this lower

bound [LR08, NBZ11, SHHS11], which indicates that the hot matter produced in heavy-ion collisions behaves *de facto* as a nearly **perfect fluid**. A review is available here [Cre11].
While pure hydrodynamical models can describe particle spectra in the p_{T} regime below ~ 2 GeV/c (corresponding to the majority of particles from the bulk), hybrid models combining hydrodynamics calculations and hadronisation modeling, such as hadronic cascade or quark coalescence, are required to reproduce experimental data [Huo03] at higher p_{T}. An easy introduction to relativistic hydrodynamics can be found at [Oll08].

3.3 Heavy-flavour results

Heavy quarks experience the same medium as light quarks, yet their flow might be different if restrained by their **larger mass**. A major understanding of heavy-quark physics would be the answer to **whether a local equilibrium is reached** and if heavy and light quarks follow the same hydrodynamical evolution in the medium. Because the bulk completely thermalises, the spectra of hadrons made of light quarks reflect the medium expansion properties. Yet information about the interaction history is lost. In contrast, **heavy quarks carry information about interactions in the medium** and keep it through the hadronisation stage. In comparison to the large abundances of light flavours in the QGP, only a small number of charm quarks is produced in a single collision. Moreover, because of the large charm mass, the elliptic flow of hadrons containing charm quarks is qualitatively different than that of hadrons made of light quarks [LM03].
Studies of heavy-flavour elliptic flow are particularly interesting since **degrees of interaction and thermalisation** of heavy quarks in the medium can be extracted. The comparison to transport-theory based models would in principle give access to **transport coefficients** and to the quantification of quark interactions and diffusion inside the expanding fireball. The heavy-quark spectrum is modified by radiative and collisional energy-loss processes. The greater the interaction strength of heavy quarks with the medium constituents, the smaller the spatial diffusion coefficient and the larger the elliptic flow developed by heavy quarks [RvH10]. At low p_{T}, heavy quarks might experience the system evolution, while losing or gaining energy by interacting with the medium constituents [GKR04] and recombine with lighter quarks. High-p_{T} heavy quarks are not expected to be sensitive to pressure gradients from the bulk. Even so, a small anisotropy is expected from the path length differences through the asymmetric fireball [Shu02]. The next paragraphs highlight a few experimental results of heavy-flavour flow.
The observation of "non-photonic" electrons, originating mainly from semi-leptonic decays of charm and bottom mesons, exhibits a sizeable elliptic flow in Au–Au collisions at $\sqrt{s_{\mathrm{NN}}} = 200$ GeV by PHENIX. The observations are compatible below $p_{\mathrm{T}} \sim 2$ GeV/c with theoretical predictions including charm flow and comparable with π and K results [But06, A$^+$05d, A$^+$11b]. The measurement is presented on Fig. 3.7. More theoretical predictions investigating several values of heavy-quark-gluon scattering cross section can be found in [Mol07].

Forward- and mid-rapidity measurements of single-lepton decays of heavy-flavour hadrons at $\sqrt{s_{\mathrm{NN}}} = 2.76$ TeV [A$^+$16f, A$^+$16e] also suggest that heavy quarks follow the bulk expansion. These observations are compatible with theoretical calculations testing charm interactions with the medium constituents as illustrated on Fig. 3.8. The azimuthal anisotropy of heavy-flavour electrons has also been measured in Pb–Pb collisions at $\sqrt{s_{\mathrm{NN}}} = 5.02$ TeV (cf Fig. 3.9), and exhibits compatible values with $\sqrt{s_{\mathrm{NN}}} = 2.76$ TeV results.

Direct measurements of open-heavy-flavour hadrons are challenging due to the high

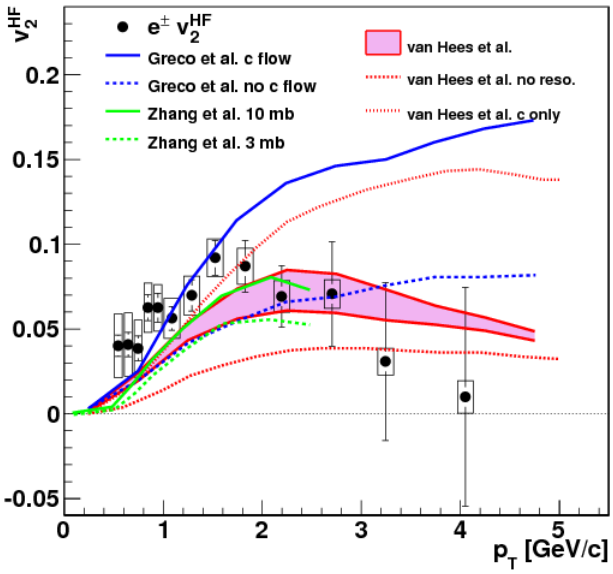

Figure 3.7 – Heavy-flavour electron v_2 measured by PHENIX in Au–Au collisions at $\sqrt{s_{NN}} = 200$ GeV [A+11b] compared with two scenarii for charm-quark interactions in theoretical models [GKR04, ZCK05, vHGR06, vHMGR08]

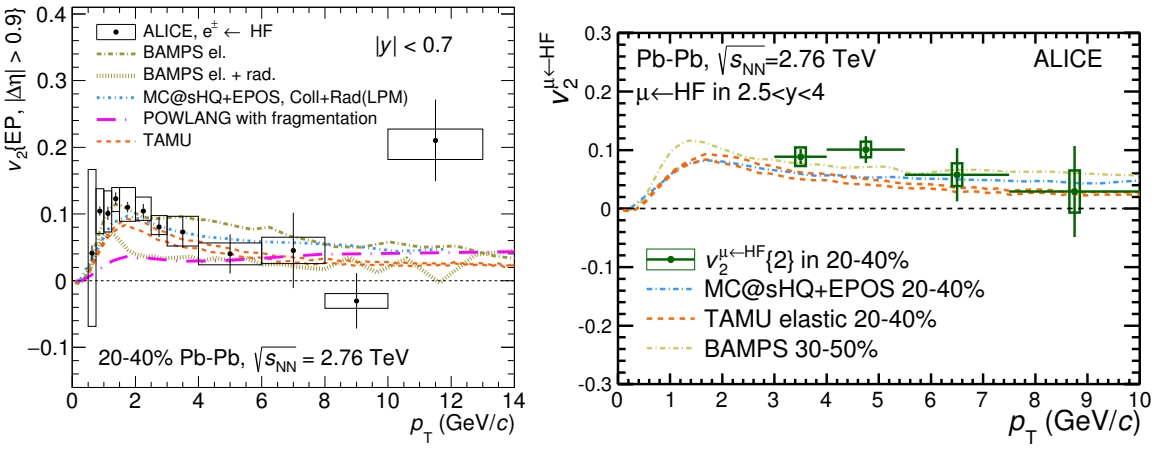

Figure 3.8 – Elliptic flow measurements in Pb–Pb collisions at $\sqrt{s_{NN}} = 2.76$ TeV by ALICE for heavy-flavour (Left) electrons [A+16e] and (Right) muons [A+16f] in semi-central collisions (20–40 % centrality class) compared to theory predictions

background in the hadronic channel. Prompt D^0, D^+, and D^{*+} azimuthal anisotropies measured by ALICE at $\sqrt{s_{NN}} = 2.76$ TeV [A+14e] and $\sqrt{s_{NN}} = 5.02$ TeV [A+18e] with an extended p_T range are presented on Fig. 3.10. Substantial v_2 coefficients are observed for both collision energies, similar to π measurements. Several model predictions are compared to the results, providing a fair description of the measurements with a spatial diffusion coefficient, close to the critical temperature, around $2\pi T D_s(T) \sim 1.5 - 7$.

Recent measurements at $\sqrt{s_{NN}} = 5.02$ TeV [A+18e] are twice more precise than previous $\sqrt{s_{NN}} = 2.76$ TeV results. Comparing the elliptic flow of D^0, D^+, and D^*_+ mesons allows one to investigate the hadronisation of charm quark with lighter quarks. D_s was also measured for the first time, allows one to study charm-coupling and hadronisation processes [HFR13]. Detailed results for each measured D meson (D^0, D^+, D^{*+}, and D_s^+) and their charge conjugates are shown on Fig.3.11. The amplitude of the elliptic flow is similar for D mesons with or without strange content although associated uncertainties are quite significant for D_s mesons. A large significance of positive v_2 was also observed for D^0 mesons at RHIC

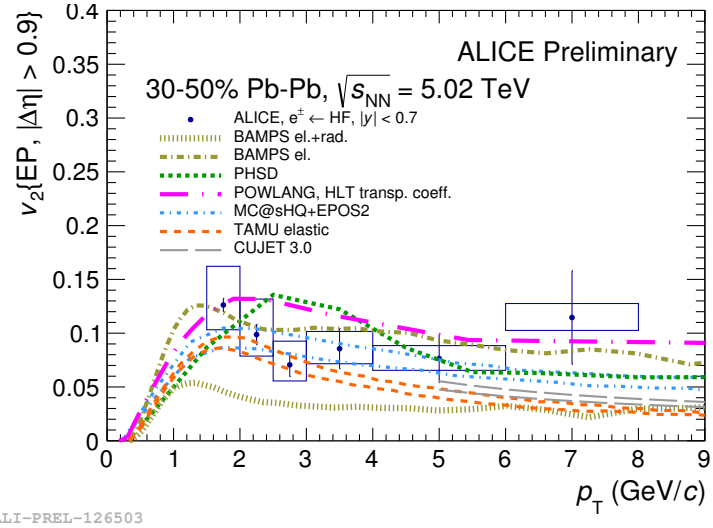

Figure 3.9 – Elliptic flow measurements for heavy-flavour electrons in Pb–Pb collisions at $\sqrt{s_{NN}} = 5.02$ TeV by ALICE

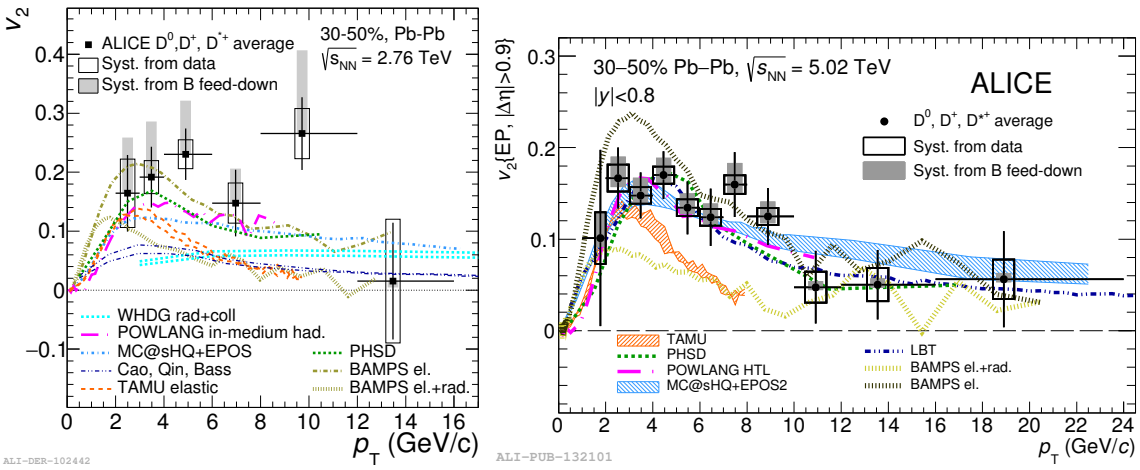

Figure 3.10 – Elliptic flow measurements in Pb–Pb collisions at $\sqrt{s_{NN}} = 2.76$ TeV by ALICE [A+14e] and $\sqrt{s_{NN}} = 5.02$ TeV for D mesons in semi-central collisions (30–50 % centrality class)

energy by the STAR collaboration [A+17f]. Transport models including interactions with the expanding medium provide a good description of the measurement but face a real challenge in simultaneously describing the high-p_T yield suppression.

Since the elliptic flow of charmed hadrons results from the interplay between the charm- and light-quark distributions, then hadron elliptic flow can be predicted from partonic flow using hadronisation models (e.g. independent fragmentation or coalescence). Flow predictions for several charmed hadrons in the coalescence picture are shown on Fig. 3.12 in solid red lines, considering either a zero partonic-charm flow (labelled with $v_{2c} = 0$) or the limit where charm flow is the same as that for light quarks (unlabelled). The dashed green curves illustrate the hadronic-flow evolution when considering a linearly increasing light-quark flow which saturates for $p_T > p_0$, while solid red lines correspond to a quark-flow following Molnar's parton transport model [MG02]. In return, charm-quark elliptic flow can be inferred from that of charmed-hadron measurements [LM03].

In a scenario where no charm interactions occur in the medium, D-meson elliptic flow could arise from the v_2 of the light component. However, this effect could only contribute to open-heavy-flavour flow at low p_T since the transverse momentum of the final particle

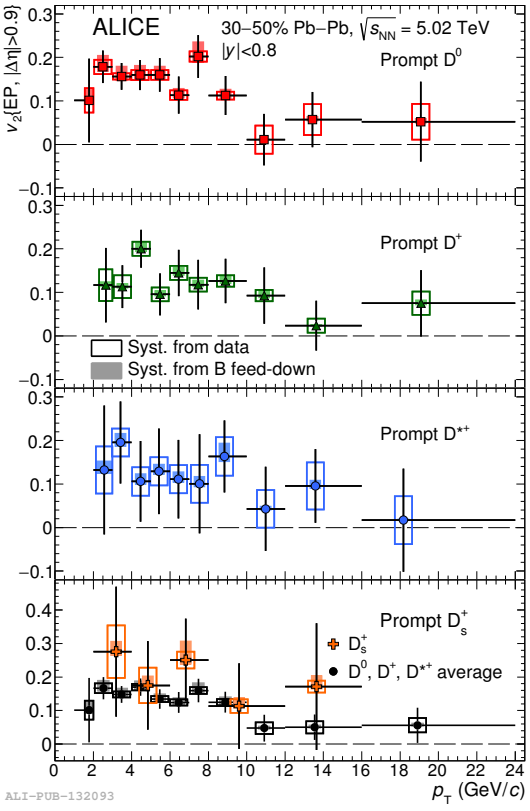

Figure 3.11 – Elliptic flow measurements in Pb–Pb collisions at $\sqrt{s_{NN}} = 5.02$ TeV by ALICE for D^0, D^+, D^{*+}, and D_s^+ mesons as a function of p_T in semi-central collisions (30–50 % centrality class)

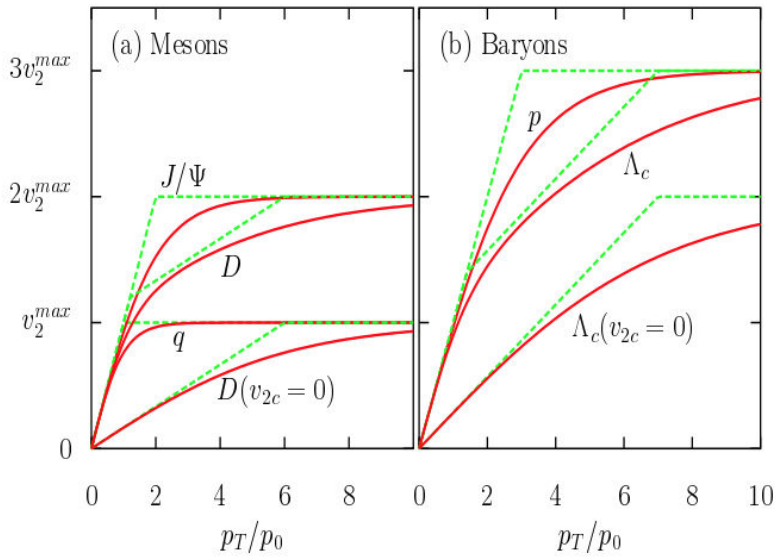

Figure 3.12 – Comparison of elliptic-flow p_T evolution for charm quarks, mesons and baryons [LM03] at RHIC with zero charm v_2 (labelled with $v_{2c} = 0$) or the same flow for charm and light quarks (unlabelled). Green dashed curves correspond to a linear light-quark flow increase with a saturation above $p_T > p_0$ and solid red lines correspond to a light-quark flow following Molnar's parton transport model [MG02]

is nearly given by the heavy quark. In addition, the flow of (re)generated J/ψ should be null under this hypothesis. In contrast, if charm quarks thermalise in the medium then both D-meson and (re)generated-J/ψ flow should be maximal and converge towards the

same upper limit. The comparison of theoretical calculations based on coalescence with or without charm thermalisation is given on Fig. 3.13 for Au–Au collisions at $\sqrt{s_{NN}} = 200\,GeV$. The input parametrisations show that the charm-quark v_2 saturates at the same value as the one of light quarks. The predictions for D-mesons considering either a complete thermalisation of charm quarks or no re-interactions with the medium differ by a factor 2 above $p_T > 1.5\,GeV/c$. The J/ψ v_2 originates only from charm quarks and only (re)generated J/ψ are considered here. The v_2 increase as a function of p_T is delayed for the J/ψ compared to the D-meson but saturates faster and around the same value.

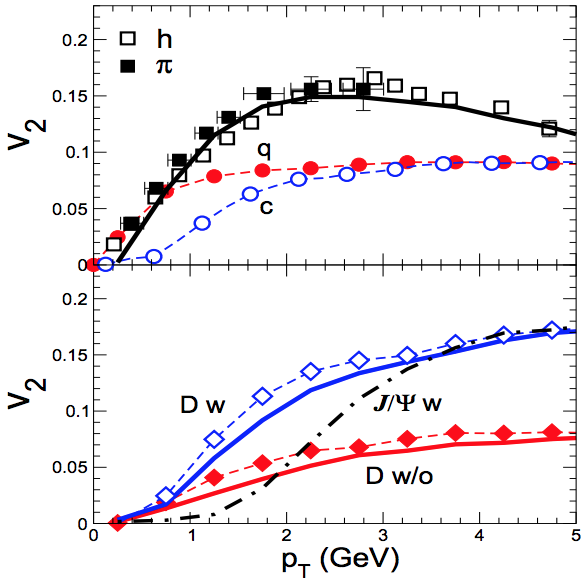

Figure 3.13 – Elliptic flow predictions in Au–Au collisions at $\sqrt{s_{NN}} = 200\,GeV$ [GKR04] for (Top) π (solid line) in a coalescence plus fragmentation model, compared to π(filled squares) [Esu03] and charged particles (open squares) [A+03b] measured by PHENIX, input parametrisations for light (filled red circles) and charm quarks (open blue circles) are also given, (Bottom) D-mesons using pQCD charm-quark distributions (lower solid line) and for thermal+flow c-quark spectra at T_c (upper solid line) with respective decay electrons (diamonds), and J/ψ mesons (dash-dotted line) in the full thermalisation scenario

A recent approach [NHR18] addresses charm thermalisation by investigating the influence of thermal-charm production in the equation of state (light, strange, and with/without charm) from lattice QCD calculations [BFH+14, B+16] and predicts corresponding flow harmonics in the soft sector from RHIC to LHC energies for various systems (Xe–Xe, Au–Au and Pb–Pb). An example of calculations compared to ALICE charged-hadrons measurements in Pb–Pb collisions at $\sqrt{s_{NN}} = 5.02\,TeV$ is represented on Fig. 3.14. Predictions including thermal charm (EoS2+1+1) might offer a better description of experimental measurements than calculations with light- and strange-quark thermalisation only (EoS2+1), as seen for the 30–40 % centrality bin. Although only charm quarks from thermal production are considered, the approach shows that thermalised charm quarks could influence the thermodynamic properties of the QGP, and proposes a new test based on soft-probe measurements. Much more charm quarks are initially produced and could also modify the system equilibrium.

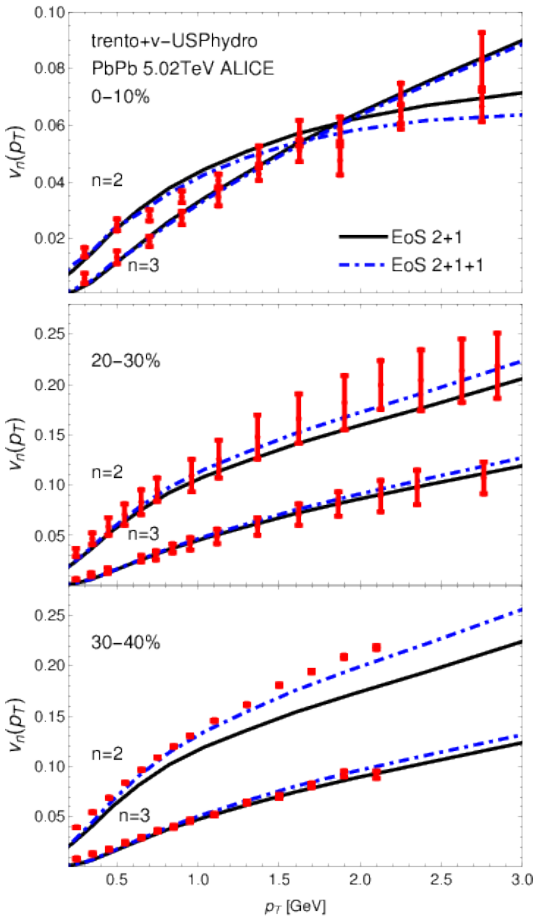

Figure 3.14 – $v_n(p_T)$ calculations of [NHR18] in Pb–Pb collisions at $\sqrt{s_{NN}} = 5.02$ TeV for charged particles for the 2+1-flavour [BFH+14] and 2+1+1-flavour [B+16] equations of state, compared to the experimental data from ALICE [A+16b, A+18f]

3.4 Collectivity in small systems

If the origin of collectivity in large collision systems seems to be well understood, the observations in pp and p–Pb collisions – where no QGP is expected – revealed surprising similarities with Pb–Pb collisions, even if the system geometry and size are different. The first observation of the **ridge**, a characteristic structure emerging from bi-dimensional correlations of particle pairs as a function of their relative azimuthal angle and pseudorapidity, in pp collisions by the CMS experiment [K+10], triggered many new studies. Signs of collective expansion are observed in **high multiplicity** pp **and** p–Pb **collisions**, where the multiplicity becomes comparable to peripheral Pb–Pb collisions. Several measurements of flow harmonics are available. In small systems, the subtraction of the non-flow contribution, consisting of correlations not related to the system collectivity (e.g. jets, resonance decays,..), is particularly critical.

As in Pb–Pb collisions, a clear **mass ordering** of the v_2 coefficients is observed below $p_T < 2.5$ GeV/c and particles seem to group into baryons and mesons afterwards. From high- to low-multiplicity events, these features persist but become less pronounced (see Fig. 3.15). An approximate scaling by the number of constituent quarks seems to hold among the three centrality classes [Pac18].

The heavy-flavour sector also exhibits signs of collective behaviour in the asymmet-

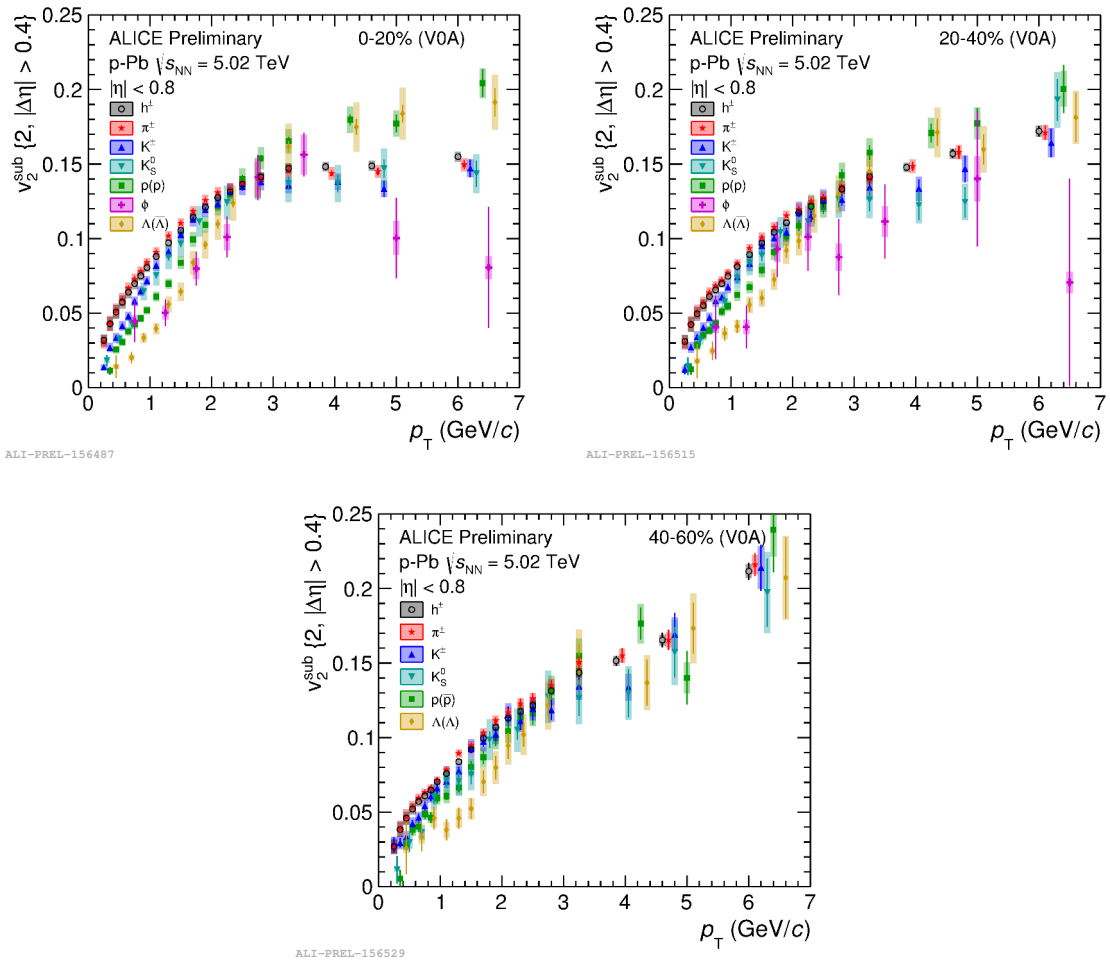

Figure 3.15 – Elliptic flow coefficients vs p_T of identified hadrons measured by ALICE in p–Pb collisions at $\sqrt{s_{NN}} = 5.02$ TeV for (left to right) 0–20 %, 20–40 % and 40–60 % centrality ranges

ric p–Pb collision system. Fig. 3.16 shows the v_2 measurements of heavy-flavour decay electrons measured by ALICE at mid-rapidity in p–Pb collisions at $\sqrt{s_{NN}} = 5.02$ TeV. A significant elliptic flow is observed and compared to charged particles (dominated by light-flavour hadrons) and inclusive muons at forward rapidity, mostly coming from heavy-flavour hadron decays above $p_T > 2$ GeV/c. Results for open-heavy-flavour mesons show similar observations. Recent measurements of prompt D^0 mesons by CMS (see Fig. 3.17) also indicate that collective behaviour extends to heavy flavours. However, the comparison to other light-flavour hadrons shows a lower anisotropy for charmed mesons. If the elliptic flow originates from partonic interactions, the latter observation might possibly reflect a weaker interaction of charm quarks with the medium.

The origin of azimuthal anisotropies in small systems is not fully understood yet. Initial and **final state effects** could play a role but different underlying mechanisms could also be involved. These results also question the interpretation of flow in Pb–Pb collisions. The study of intermediate systems would certainly help to identify the origin of collective results in small systems.

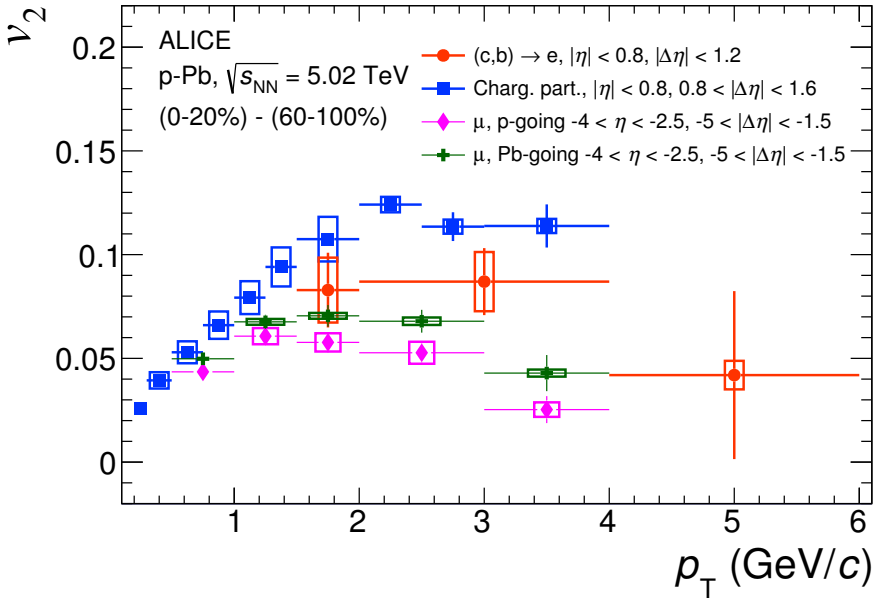

Figure 3.16 – Elliptic flow of HF electrons and inclusive muons compared to charged particles in p–Pb collisions at $\sqrt{s_{NN}} = 5.02$ TeV measured by CMS [A+18d]

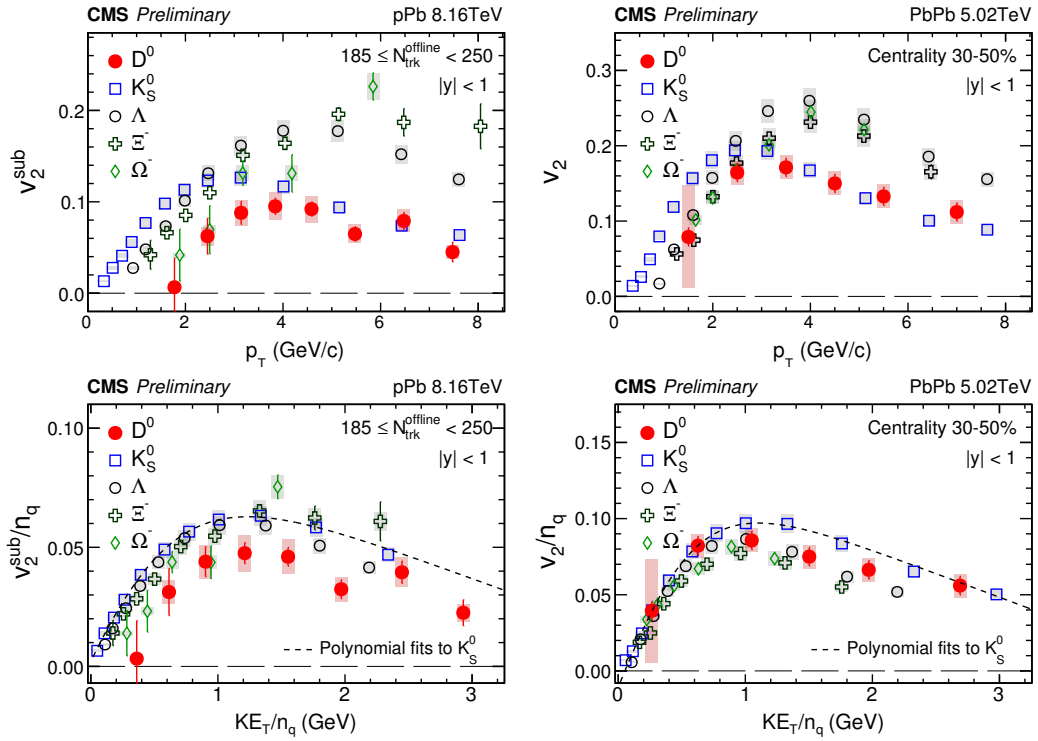

Figure 3.17 – Prompt D^0 elliptic flow in (Left)p–Pb collisions at $\sqrt{s_{NN}} = 8.16$ TeV compared to (Right)Pb–Pb collisions at $\sqrt{s_{NN}} = 5.02$ TeVmeasured by CMS. (Bottom) Results normalised by the number of constituent quarks [CMS18a]

CHAPTER 4

BOUND STATES OF HEAVY QUARKS AS A PROBE OF THE QGP

"Each colour lives by its mysterious life."

— Wassily Kandinsky

4.1 Relevance of heavy quarks in the QGP study

Heavy quarks are produced during the **early stages** of the collision, through hard-scattering partonic interactions. These short-distance processes involve high-energy transfer and take place prior to the QGP formation ($\tau_{QGP} \sim 0.3\,\mathrm{fm}/c$ [A+05c]). Their time scale is in general shorter than the QGP thermalisation, the formation time of a $c\bar{c}$ pair being roughly estimated as $\tau_f \sim \frac{1}{2m_c} \sim 0.1\,\mathrm{fm}/c$. Open and hidden heavy-flavours constitute therefore a sensitive tool to probe the medium as they experience its whole evolution while interacting with its constituents.

Bound states of heavy quarks ($Q\bar{Q}$), called **quarkonia**, are especially relevant to extract the properties of the medium, and quarkonium studies in heavy-ion collisions have been going on for thirty years. Because of the large mass of the constituents ($m_c \simeq 1.3\,\mathrm{GeV}$ and $m_b \simeq 4.2\,\mathrm{GeV}$), quarkonia can be described as **non-relativistic systems**. Relativistic corrections are indeed limited and quantum physics provides a good description of quarkonium spectroscopy. Hence **effective theoretical approaches** can be applied to describe the evolution of the $Q\bar{Q}$ pair into the physical quarkonium state. Furthermore, the same number of heavy quarks per binary collision is expected to be produced in pp and A–A collisions. Heavy-quark annihilation rate is believed to be negligible [BM07]) and no thermal production is expected at the LHC [ZKL08]. Heavy-quark number is thus conserved throughout the partonic and hadronic phases of the collision. The sequential suppression of the quarkonium states, by colour screening or by dynamic partonic interactions, was originally suggested as a signature of the QGP. Later, a (re)generation of quarkonia by (re)combination of deconfined quarks and anti-quarks was also predicted, mainly affecting charmonia. Today, their production mechanism is still not settled, and many effects of the medium with or without the formation of a QGP are not completely understood yet.

This thesis focuses on charmonium states made of charm and anti-charm quarks. The next section introduces some aspects of quarkonium physics, a detailed review can be found at [A+16k].

4.2 Charmonium production

4.2.1 Spectroscopy

The charmonium family comprises several bound states with different quantum numbers. The charm–anti-charm mesons have relatively long decay lifetime compared to the QGP lifetime of about 20 fm. Since their mass is less than two times the mass of the lightest meson with a single charm quark (the open-charm D meson, $m_{\mathrm{D}} \simeq [1.9-2.0]\mathrm{GeV}/c^2$), $\mathrm{D\bar{D}}$ decays are forbidden. Other strong decays are also suppressed by the OZI rule. Masses and binding energies (ΔE) of the main charmonia are summarised in Tab. 4.1.

state	η_c	J/ψ	χ_{c0}	χ_{c1}	χ_{c2}	ψ(2S)
Mass [GeV/c^2]	2.98	3.10	3.42	3.51	3.56	3.69
ΔE [GeV]	0.75	0.64	0.32	0.22	0.18	0.05

Table 4.1 – Mass and binding energy of charmonium states [Sat06]

The different states of the $\mathrm{c\bar{c}}$ pair can be described as solutions in the vacuum of the Schrödinger equation with an effective Cornell potential V:

$$\mathrm{V}(r) = \sigma r - \frac{\alpha}{r}. \tag{4.1}$$

The first term σr describes the non-perturbative confinement at long distance with a strength $\sigma = 0.2$ GeV^2 [MP08]. The second one is a perturbative Coulomb-like interaction and dominates at short distance. The coupling coefficient $\alpha \sim \frac{\pi}{12}$ can be obtained from lattice calculations [NS02].

Quarkonia dominantly decay via the electromagnetic- or strong-interaction decays. The transitions of the different resonances within the charmonium family are illustrated in Fig. 4.1. The first charmonium observation was that of the vector ground state J/ψ , which

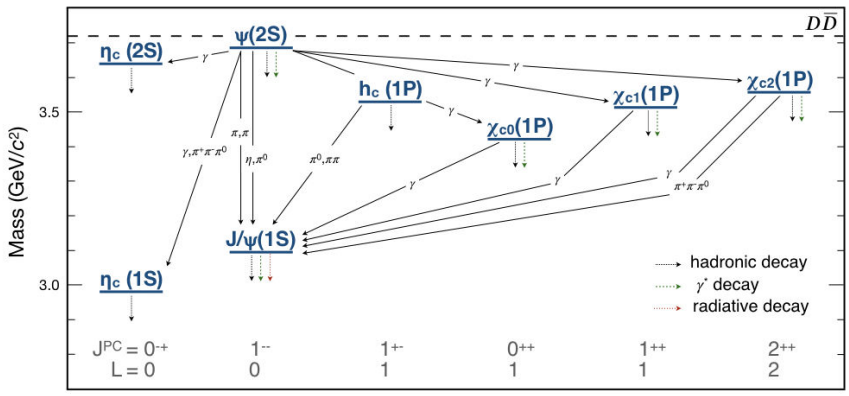

Figure 4.1 – Spectroscopic scheme of charmonium states as a function of the state mass and quantum numbers

was discovered simultaneously at the Stanford Linear Accelerator Center (SLAC) [A$^+$74b] and at BNL in 1974 [A$^+$74a]. Few measurements are available for the η_c [A$^+$15a, A$^+$17a], the lightest charmonium state. However, a very abundant literature exists for the J/ψ state. Its

lifetime ($\tau_{J/\psi} \sim 215\,\mathrm{fm}/c$) is indeed much larger than the η_c($\tau_{\eta_c} \sim 6\,\mathrm{fm}/c$), mainly because the 2-gluon decay is forbidden for the J/ψ and its di-lepton decay channel has a larger branching ratio.

Several states decay to lower-mass charmonia. Two sources of charmonium production must therefore be distinguished: the **direct production** where the state is formed at the initial stage of the collision and the **feed-down** contribution from excited states. Both contributions are referred to as the **prompt production**. Other processes can form charmonia, in particular b-hadrons decays are an important source of production, commonly called **non-prompt contribution**. Since beauty hadrons decay via weak interactions, the resulting non-prompt quarkonia will originate from a displaced decay vertex with respect to the main interaction vertex. In pp collisions at $\sqrt{s} = 7\,\mathrm{TeV}$ at the LHC, around ~60 % of J/ψ states come from direct production, ~24 % from χ_c [A+12b] and ψ(2S) decays [A+12a] and ~ 9 % originate from B hadron decays [A+11a].

4.2.2 pp collisions: stringent pQCD test and A–A reference

The formation of a quarkonium state can be factorised into two processes involving two different energy scales: the formation of the $Q\bar{Q}$ pair and its hadronisation into the quarkonium bound state. The creation of a $c\bar{c}$ pair is a partonic process requiring a minimum energy $Q \geq 2m_c \gg \Lambda_{QCD}$ hence perturbative QCD can be applied. Fig. 4.2 shows the leading order of production processes. The binding of the $Q\bar{Q}$ pair into the physical quarkonium state is usually described by effective theories from non-perturbative QCD.

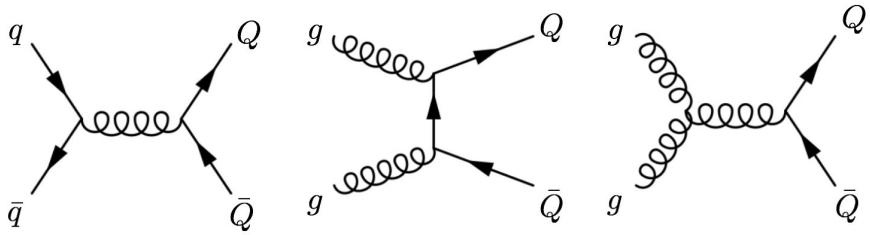

Figure 4.2 – Feynman diagrams for $Q\bar{Q}$ pair production at leading order through quark annihilation (left) and gluon fusion (middle and right)

Several approaches have been carried out to describe quarkonia production. Most of theoretical descriptions are based on the factorisation of these two energy scales and mainly differ in their hadronisation process and how the color of the $Q\bar{Q}$ pair is treated. The theoretical descriptions most commonly found in the literature are the color-evaporation model [Fri77, Hal77, AEGH97], the color-singlet model [BR81, CL96], and the color-octet model [BBL95] based on the effective Non Relativistic QCD (NRQCD) theory. Measurements in pp collisions provide an excellent opportunity to test theory models since the system can be considered as the QCD vacuum. It is also the unique way to obtain a reference for the study of cold nuclear and **hot medium effects** on quarkonium production.

4.3 Charmonium production in heavy ion collisions: probing the QGP

In nucleus-nucleus collisions the production of quarkonia is affected by the so-called hot medium effects, related to the presence of the LHC, but also by **Cold Nuclear Matter**

(CNM) effects, caused by the nuclear environment. While the former effects are present in high-energy A–A collisions, the latter are studied in p–A collisions. CNM modify the production of charmonia with or without the formation of a deconfined medium. Since it could also significantly affect the quarkonium production in A–A collision, an accurate description is required to quantify these effects.

4.3.1 Cold nuclear matter effects

The presence of cold nuclear matter can affect quarkonium production before the formation of the pair (initial-state effects) or after the pair is formed (final-state effects). Measurements in p–A (or d–A [A$^+$13f, A$^+$13g, A$^+$14j]) collisions provide the largest source of information on CNM effects since no QGP is expected to form. Recent measurements for quarkonia in p–Pb collisions can be found in [A$^+$14f, A$^+$14h, A$^+$15d, A$^+$15c, A$^+$18g] with ALICE, in [A$^+$14a, A$^+$14b] with LHCb, and in [C$^+$14] with CMS. More recently, the rising interest in ultra-peripheral nucleus–nucleus collisions revealed that the process of quarkonium photo-production is also a great probe of CNM effects [Kla02, A$^+$09b].
Effects include, but are not limited to:

- modification of parton distribution functions [Arm06, EPS09, Vog10] (depending on the x-value: shadowing, anti-shadowing, EMC)
- gluon saturation within the Color Glass Condensate approach [FW13a, FW13b]
- coherent parton energy-loss in cold matter [APS11, AP13, AKPR13, PK15]
- interactions of the $Q\bar{Q}$ pair with the nucleus (nuclear absorption) [AT08, LVW09] or surrounding partons (comovers) [CKKAG97, Fer15]
- coherent J/ψ photo-production [A$^+$13c, Zha17a, ZKM$^+$18].

4.3.2 Hot medium effects

Hot medium effects cover effects on charmonium production caused by the presence of the QGP. Historically, the first reference to the formation of a QGP was introduced to explain J/ψ results from the NA50 collaboration in Pb–Pb collisions at $\sqrt{s_{\mathrm{NN}}} = 158\,\mathrm{GeV}/n$ [G$^+$96]. A strong suppression was observed that could not be explained by nuclear absorption, unlike previous measurements from smaller collision systems (see Fig. 4.4). A first approach [BO96] investigated the local energy density reached in the collision and proposed a critical value above which J/ψ are suppressed in the medium. An important assumption was that the associated time scale was short enough for the suppression to occur before the system expansion and before significant displacement of J/ψ through the medium. Because of the modest difference of maximum density reached in Pb–Pb and S–U collisions (~35 %), it was suggested that the origin of this larger suppression might lie in the different properties of the medium formed in the Pb–Pb system.

Color screening and sequential suppression

In 1986 Matsui and Satz predicted the suppression of quarkonium states as a **signature of the QGP formation** [MS86]. The main idea is that the range of the strong interaction binding the quarkonium pair is reduced in a diluted color-charge medium, analogous to the electromagnetic screening mechanism. A **sequential bound state dissociation** [KMS88]

is expected through the **melting of the** $Q\bar{Q}$ **pairs by color screening** in the medium.
A simplified treatment of how the presence of colour charges affects the dipole potential consists in introducing in the potential expression [4.1] a Debye screening term which depends on the screening radius $r_D = \frac{1}{\mu}$, as:

$$V = \sigma r \left(\frac{1 - e^{-\mu r}}{\mu r} \right) - \frac{\alpha}{r} e^{-\mu r}. \tag{4.2}$$

The Debye screening radius is inversely proportional to the color charge density, hence to the medium temperature. An enhancement of the QGP temperature would thus decrease r_D leading to a dissociation of the quarkonium pair if its radius is larger than r_D. The dissociation temperature T_d above which the state is completely melted can be estimated through lattice QCD calculations [DPS01]. A sequential suppression inside each quarkonia family should occur, corresponding to the different melting temperatures of the states due to their binding energy (illustrated on Fig. 4.3).

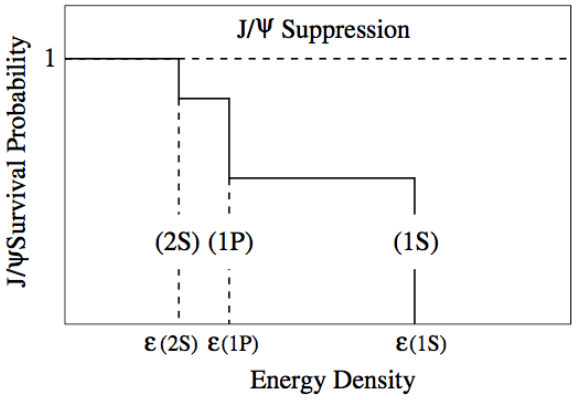

Figure 4.3 – Illustration of the sequential suppression for charmonium states as a function of the energy density ϵ

Expected dissociation temperatures and radii of the first charmonium states are summarised in Tab. 4.2.

state	J/ψ	χ_c	$\psi(2S)$	$\Upsilon(1S)$	$\Upsilon(2S)$	$\Upsilon(3S)$
ΔE [GeV]	0.64	0.20	0.05	1.1	0.54	0.20
radius[fm]	0.25	0.36	0.45	0.14	0.28	0.38
T/T_c	2.10	1.16	1.12	> 4.0	1.60	1.17

Table 4.2 – Binding energy, relative dissociation temperature and radius of charmonium and bottomonium resonances [Sat06]

Within this picture, the measurement of each quarkonium state production should provide an **estimation of the medium thermal properties**.
This suppression scenario framed the charmonium studies from SPS to RHIC energies. The first measurement of charmonium suppression was performed at the SPS [G+96]. J/ψ and $\psi(2S)$ production cross sections by the NA50 collaboration for different collision systems are presented in Fig. 4.4 as a function of the penetration length (L) in the nuclear matter. The latter variable is an indication of the collision centrality as it increases with the impact parameter. The observations are normalised by the cross sections of the Drell-Yan

(DY) electromagnetic process ($q + \bar{q} \rightarrow \gamma/Z \rightarrow \mu_+\mu_-$) which is not sensitive to hot medium effects. Cold nuclear matter behaviour is represented by the solid lines. On the left panel,

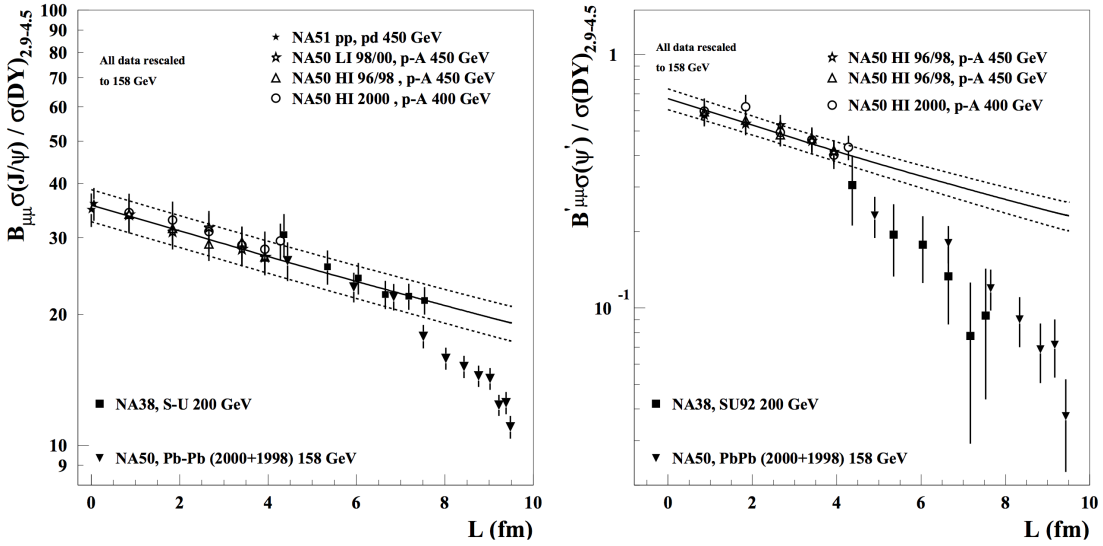

Figure 4.4 – Ratio of J/ψ and ψ(2S) to DY cross sections as a function of the penetration length L [G+96] at SPS

experimental data from small collision systems follow this linear dependence until L~ 8 fm where a sudden drop is observed for central Pb-Pb collisions at 158 GeV. This drastic deflection was interpreted as an anomalous suppression of J/ψ due to the formation of a QGP [A+07d, A+05f, B+06], although other interpretations, not involving a QGP, were also proposed [ABFP96, CFK00, KT06, AP14, BKCS04]. In addition to J/ψ observations, ψ(2S) measurements exhibit a similar pattern from a lower penetration length.
However, the comparison of RHIC results in Au-Au collisions at $\sqrt{s_{NN}} = 200$ GeV and SPS observations (see Fig. 4.5) reveals an equivalent suppression despite the factor 10 of the increased collision energy. A stronger suppression was expected at RHIC, and models describing J/ψ suppression in central collisions at SPS overestimate the suppression at RHIC. In addition, measurements at forward rapidity are more suppressed than at mid-rapidity, contrary to the expectations due to the lower energy density at forward rapidity. Two possible explanations were suggested at the time, either a very high J/ψ dissociation temperature (around $2T_c$, i.e. direct J/ψ 's are not suppressed), or the existence of a second J/ψ production source through $c\bar{c}$ pair recombination.

Bottomonium measurements by the CMS experiment are an excellent illustration of this sequential suppression (Fig. 4.6). The excited states are more suppressed than the ground state, with the Υ(3S) almost completely melted. An increased suppression is observed as a function of the centrality.

This initial picture of a QGP thermometer evolved as a yield enhancement of charmonium production with respect to pp collisions was observed from RHIC to LHC collision energies. It led to the introduction of the (re)generation mechanism.

(Re)generation

Due to the **enhanced charm-quark density** in the medium at higher collision energy, an additional source of quarkonium production was proposed. Charmonium pairs can also be **statistically** formed at a later stage of the collision through **charm-quark binding**. Higher

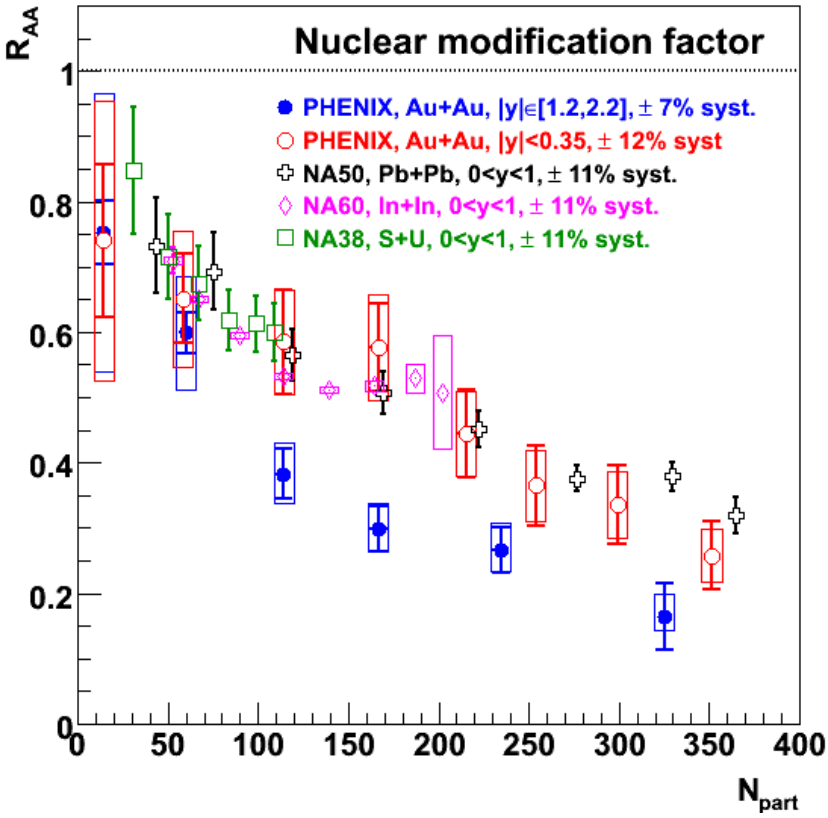

Figure 4.5 – Comparison of J/ψ nuclear modification factors as a function of the number of participants at RHIC and SPS for various collision systems [dC13]

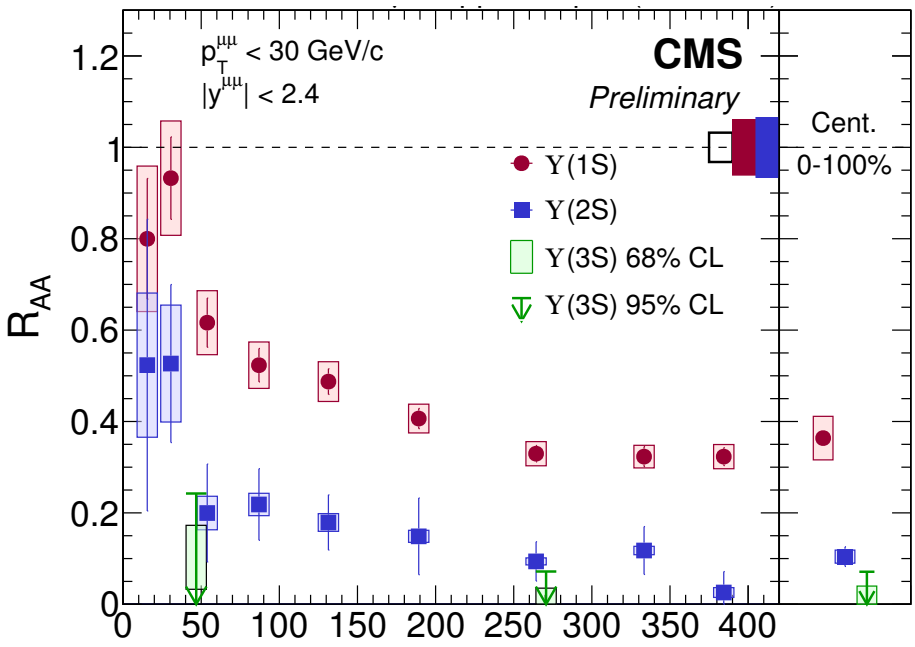

Figure 4.6 – Nuclear modification factor of Υ(1S), Υ(2S) and Υ(3S) states as a function of the number of participants measured by the CMS experiment at $\sqrt{s_{NN}} = 5.02$ TeV[S+18b]

collision energy induces an increased charm-anticharm production cross section relative to that coming from initial hard processes alone and leads to a higher density of charm quarks in the medium, thus to an increased probability to form $c\bar{c}$ pairs from initially uncorrelated charm quarks [BMS00]. The formation of the bound state can therefore

occur at a later stage of the medium evolution from charm quarks which interacted and potentially thermalised with the medium. (Re)generation should become stronger with increasing charm-quark density, and thus with increasing energy density. The effect increases with the collision energy but also with the number of binary nucleon-nucleon collisions $\langle N_{coll} \rangle$. This mechanism explains the higher J/ψ R_{AA} at the LHC compared to previous RHIC measurements (see Fig. 4.7). The rapidity dependence of the $c\bar{c}$ cross

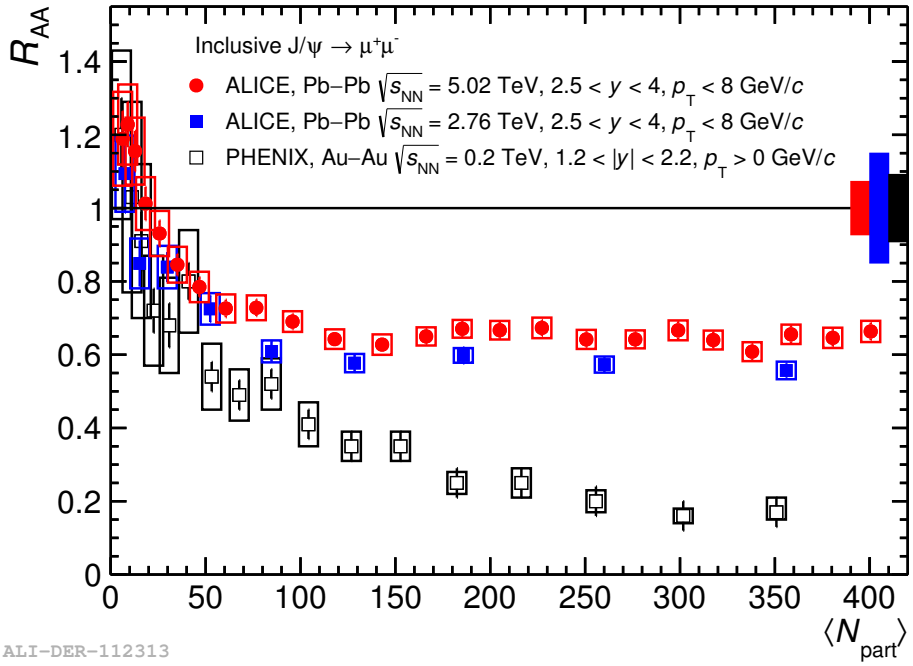

Figure 4.7 – Comparison of J/ψ nuclear modification factors as a function of the number of participants measured by PHENIX in Au–Au collisions at $\sqrt{s_{NN}} = 200$ GeV [A+11c] and ALICE in Pb–Pb collisions at $\sqrt{s_{NN}} = 2.76$ TeV [A+12c] and $\sqrt{s_{NN}} = 5.02$ TeV[A+17d]

section indicates that (re)combination effects should decrease with increasing rapidity. ALICE R_{AA} measurements as a function of rapidity (Fig.4.8) show a consistent evolution with the $c\bar{c}$ cross section decrease. (Re)generation process is expected to be more relevant for charmonium than bottomonium states due to a lower mass. Since the charm quark is much lighter than the bottom quark, the charm-production cross section is larger, hence the charm density is increased. Fig. 4.9 summarises the available measurements of J/ψ nuclear modification factor as a function of the collision energy for different centrality classes. Results from RHIC and the LHC are presented.

Because charm quarks interacted with the medium before (re)combinating into charmonium states, part of their initial momentum is lost. Therefore, (re)generated charmonium spectra is expected to be shifted towards the low-p_T region [MT05]. This is studied through the r_{AA} variable corresponding to the ratio of the mean squared transverse momentum $\langle p_T^2 \rangle$ measured in A–A collisions with respect to pp collisions:

$$r_{AA} = \frac{\langle p_T^2 \rangle_{A-A}}{\langle p_T^2 \rangle_{pp}}. \tag{4.3}$$

ALICE r_{AA} measurements at $\sqrt{s_{NN}} = 2.76$ TeV and $\sqrt{s_{NN}} = 5.02$ TeV (Fig.4.10) show actually that in the most central collisions the p_T spectra is shifted in Pb–Pb with respect to pp collisions, but their ratio is close to unity at low $\langle N_{part} \rangle$.

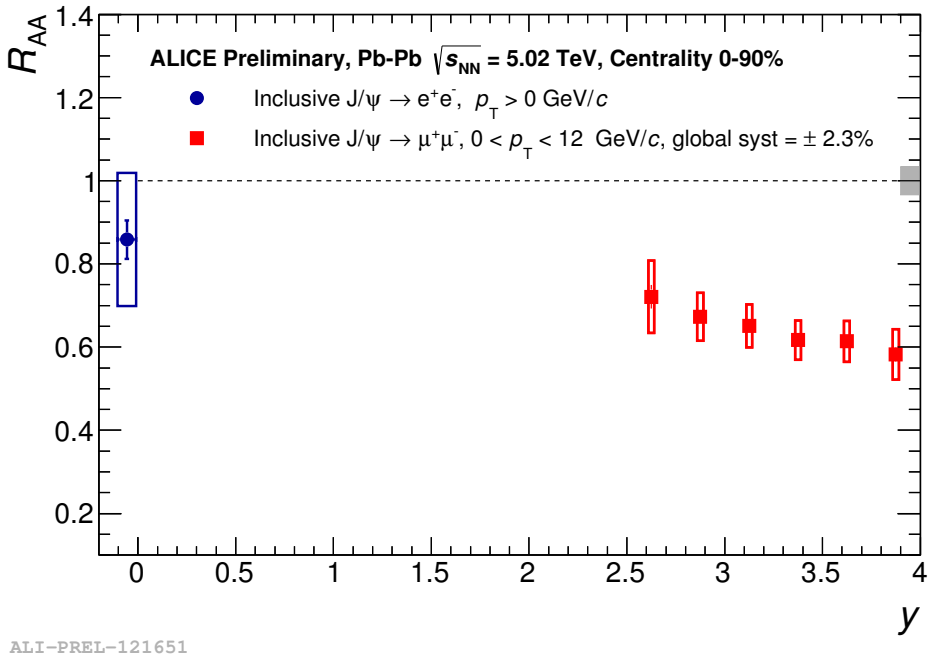

Figure 4.8 – Rapidity dependence of J/ψ modification factor measured by ALICE in Pb–Pb collisions at $\sqrt{s_{NN}} = 5.02$ TeV

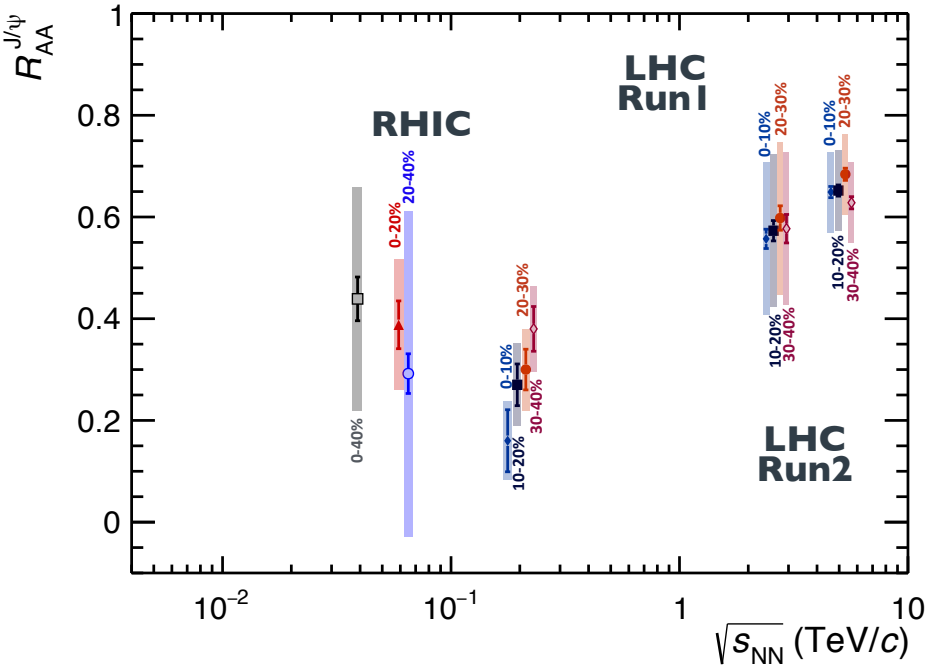

Figure 4.9 – J/ψ nuclear modification factor at forward rapidity as a function of the collision energy in different centrality ranges [A⁺11c, A⁺12e, A⁺12c, A⁺17d]

This second source of charmonium production predicts an enhancement of the observed yields and competes with the suppression mechanism. Both mechanisms need to be considered to describe charmonium production, their relevance depending on the kinematics and energy of the collision system. The J/ψ R_{AA} evolution with p_T (Fig. 4.11)

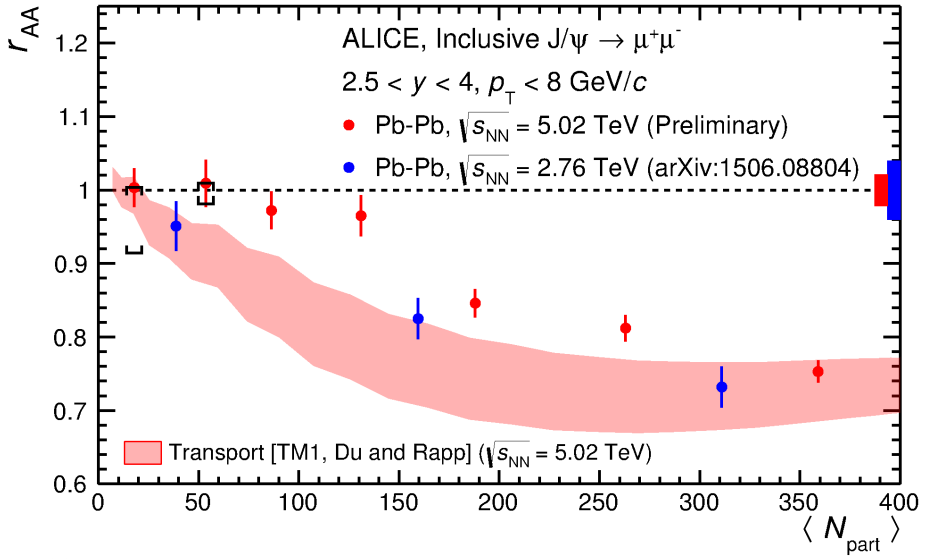

ALI-PREL-120574

Figure 4.10 – J/ψ r_{AA} as a function of the number of participants measured by ALICE in Pb–Pb collisions at $\sqrt{s_{NN}} = 2.76\,\text{TeV}$ and $\sqrt{s_{NN}} = 5.02\,\text{TeV}$. A comparison to a transport model is proposed [ZR11]

shows also evidence of (re)generation. (Re)generated J/ψ are produced predominantly at low p_T, compensating J/ψ suppression in the most central collisions, as expected from transport model predictions [DR15].

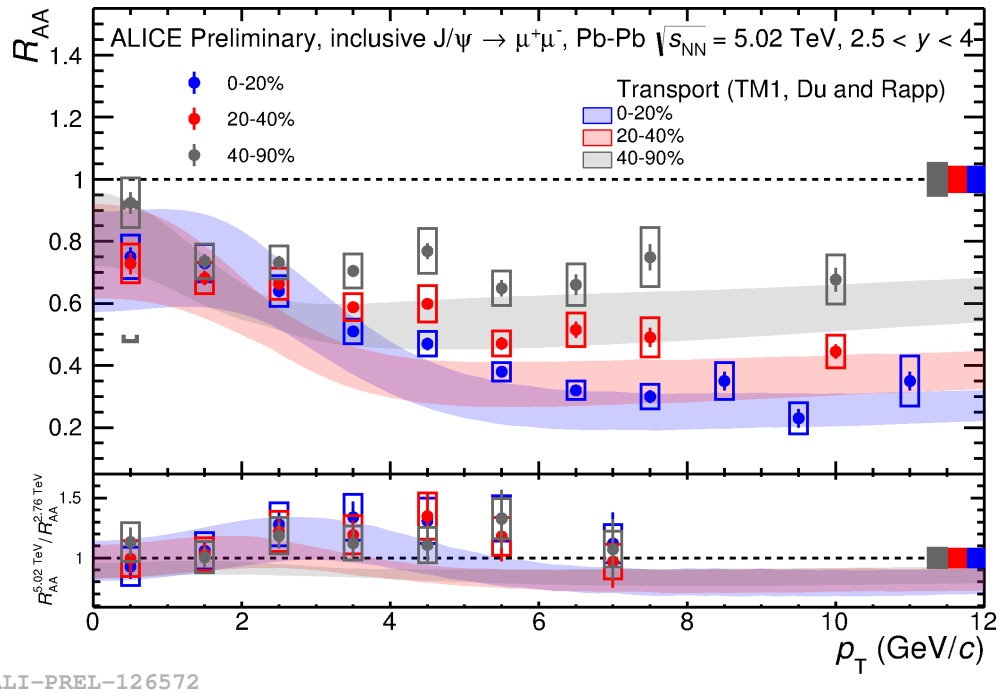

ALI-PREL-126572

Figure 4.11 – J/ψ R_{AA} as a function of p_T measured by ALICE in Pb–Pb collisions at $\sqrt{s_{NN}} = 5.02\,\text{TeV}$ for three centrality ranges. A comparison to a transport model is proposed [DR15]

4.4 Charmonium elliptic flow

The flow of quarkonium states is rather complex to predict since **several mechanisms can affect the states at different stages**. Both $c\bar{c}$ pairs and formed quarkonia can lose or gain energy in the medium. Their energy loss might potentially differ and both could contribute to the final state anisotropy. Details on studies about charm quark flow in the medium are given in Sec.3.3. The expected main contribution to J/ψ flow is from (re)combined charm quarks in the medium if charm quarks thermalised. The status of what is known in the literature on J/ψ v_2 is discussed in this section, based on the previous measurements performed for different collision systems and energies.

4.4.1 RHIC results

The J/ψ azimuthal anisotropy measured with the PHENIX [Sil08] or STAR [A+13d] experiments is compatible with zero(see Fig. 4.12 and Fig. 4.13), although a positive elliptic flow coefficient cannot be excluded since the statistical uncertainties are quite large. The

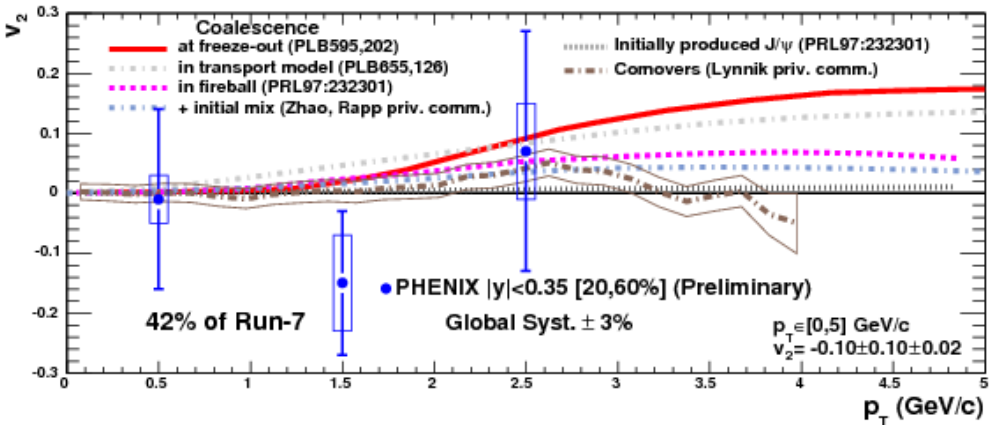

Figure 4.12 – J/ψ v_2 at $\sqrt{s_{NN}}$ = 200 GeV measured by PHENIX and compared to several theoretical predictions [Sil08]

PHENIX measurement (Fig. 4.12) was performed at mid-rapidity (y<0.35) via the J/ψ di-electron decay channel and for semi-central collisions 20–60 %. The results are compared to several transport models either considering only primordial J/ψ [YZX06] or including a (re)generation component with partial or full charm thermalisation and occuring at different collision stages [GKR04, RR07, YZX06, ZR08b]. Predictions from the comovers approach are also available [LBC08]. In addition, arguments were raised to interpret the negative value of J/ψ elliptic flow at intermediate p_T as a signature of charm-quark thermalisation [KB09].

The same measurement was performed with the STAR detector. The analysis was also performed by reconstructing J/ψ through the di-electron decay channel at mid-rapidity ($|y|$<1). Fig.4.13 represents the azimuthal anistropy for the 0–80 % centrality range. Differential results in centrality can be found in [A+13d]. The highest v_2 value is reached for the first p_T bin and remaining data (2<p_T< 10 GeV/c) are compatible with zero. The non-flow estimation is represented by a green band. Whereas charged-hadron [A+04a] and ϕ-meson [A+07b] results show a significant azimuthal anisotropy, the J/ψ v_2 is low in comparison. Theoretical calculations [YZX06, GKR04, ZR08a, LXZ10] predict much greater v_2 from p_T> 2 GeV/c.

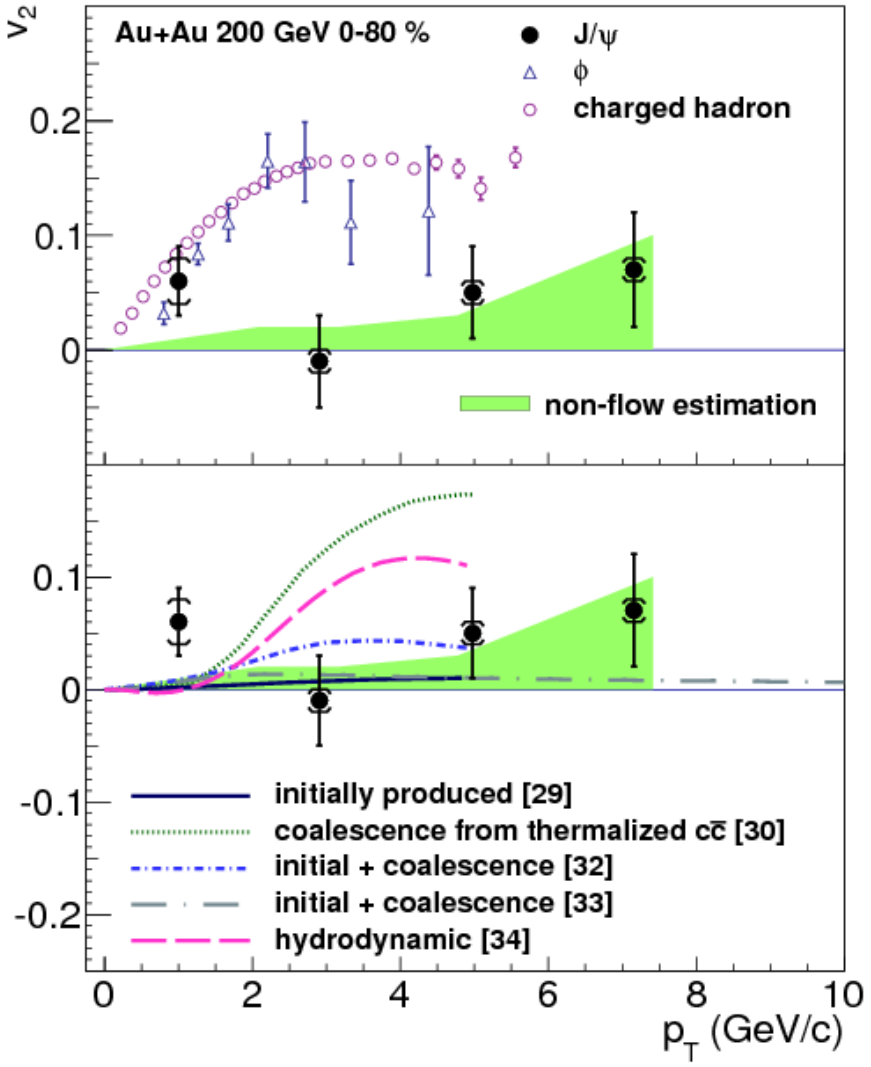

Figure 4.13 – J/ψ v_2 at $\sqrt{s_{NN}} = 200\,GeV$ measured by STAR and compared to theoretical predictions and other particle measurements [A+13d]

More recently, the J/ψ elliptic flow was measured in U–U collisions at $\sqrt{s_{NN}} = 193\,GeV$ (see Fig. 4.14) with the STAR detector [Zha17b]. The observations are compatible with observations in Au–Au collisions and do not allow to conclude on J/ψ azimuthal anisotropy at RHIC.

4.4.2 LHC results at $\sqrt{s_{NN}} = 2.76\,TeV$

First hints of a positive J/ψ v_2 were observed in the dimuon decay channel at $\sqrt{s_{NN}} = 2.76\,TeV$ by the ALICE [A+13a] experiment and confirmed by the observations of the CMS [K+17] collaboration in a different kinematic region. The ALICE measurement was performed for inclusive J/ψ at forward rapidity for several centrality classes and in the transverse momentum range $0 < p_T < 10\,GeV/c$. The elliptic flow was obtained from the Event Plane method (see Sec. 5.1) using the V0A as Event Plane detector, whose the rapidity gap with the muon spectrometer is 5.3 units. The J/ψ v_2 was extracted from the dimuon v_2 with the $\langle v_2 \rangle$ technique (see Sec. 5.2.3), and the detector resolution was calculated with the 3 sub-event methods using the V0A, V0C and TPC detectors. The highest flow value

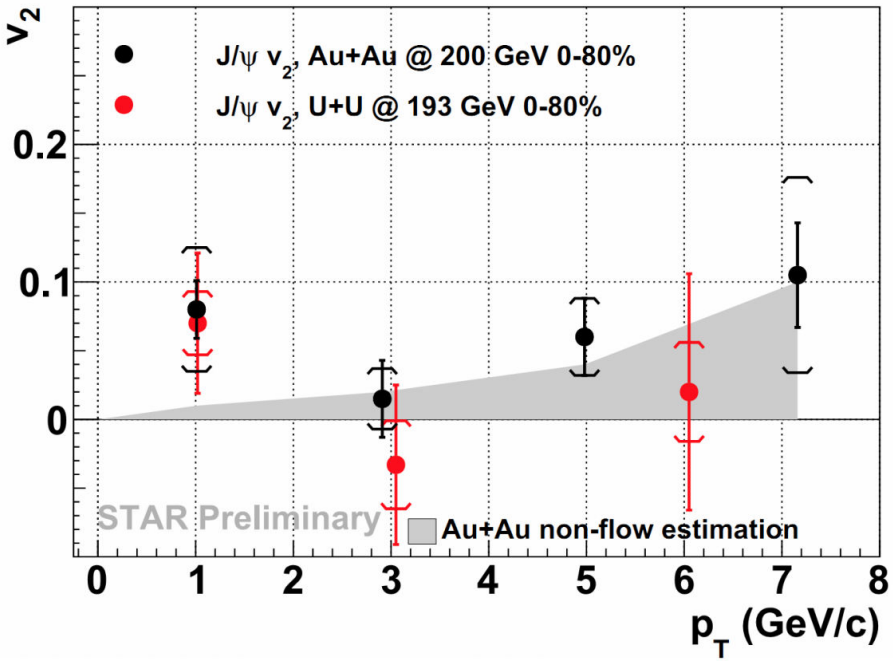

Figure 4.14 – J/ψ v_2 in U–U collisions at $\sqrt{s_{\mathrm{NN}}} = 193$ GeV measured by STAR and compared to Au–Au collisions at $\sqrt{s_{\mathrm{NN}}} = 200$ GeV[Zha17b] (combined data from several data taking periods)

$v_2 = 0.116 \pm 0.046(\mathrm{stat.}) \pm 0.029(\mathrm{syst.})$ was observed in semi-central collisions for $2 < p_{\mathrm{T}} < 4$ GeV/c. A maximum significance of 2.9σ is reached by combining several p_{T} bins. Theory predictions are compared to the results obtained in the 20–60 % centrality class (Fig. 4.15 Left). Two transport models [LXZ10, ZER13] are shown including a regeneration component around ~ 30 %. The model from Y.Liu et al. [LXZ10] is plotted with (full line) and without (dashed line) the hypothesis of thermalisation of b quarks.

The centrality dependence of the J/ψ v_2 was studied in the transverse momentum range $1.5 < p_{\mathrm{T}} < 10$ GeV/c (see Fig. 4.15 Right). For peripheral collisions, the J/ψ v_2 is compatible with zero and the highest significance is reached for semi-central collisions. The analysis was also performed with the $\Delta\varphi$ and the gapped correlation [BDO01b, BDO01a, A$^+$05e] methods with similar results. A similar technique to the $\langle v_2 \rangle$ extraction was used to extract the uncorrected (for detector acceptance and efficiency) average transverse momentum of the reconstructed J/ψ . The values are plotted for each centrality bins to locate the v_2 values.

The elliptic flow of prompt J/ψ was measured by CMS in the 10–60 % centrality class and for the transverse momentum range $6.5 < p_{\mathrm{T}} < 30$ GeV/c. A positive $v_2 = 0.066 \pm 0.014$ (stat) ±0.014 (syst) ±0.002 (global) was observed with a 3.3σ significance using the event plane method and the $\Delta\varphi$ technique (see Sec. 5.2.2). The resolution of the event plane detector is ~ 0.8 and the rapidity gap is 3 units. The v_2 dependence on p_{T}, centrality and rapidity is shown on Fig. 4.16, together with the R_{AA} results. The J/ψ v_2 measured by the CMS experiment is consistent with the ALICE results and does not exhibit significant dependence on the kinematic variables. For comparison, the J/ψ R_{AA} measured by CMS is also featured.

The non-prompt contribution from B-hadron decays reflects the energy loss of b quarks in the medium. The non-prompt J/ψ elliptic flow was also measured by CMS in two kinematic regions: $6.5 < p_{\mathrm{T}} < 30$ GeV/c for $|y| < 2.4$, and $3 < p_{\mathrm{T}} < 6.5$ GeV/c and $1.6 < |y| < 2.4$ (Fig. 4.17). Because of the large uncertainties, the measurements remain

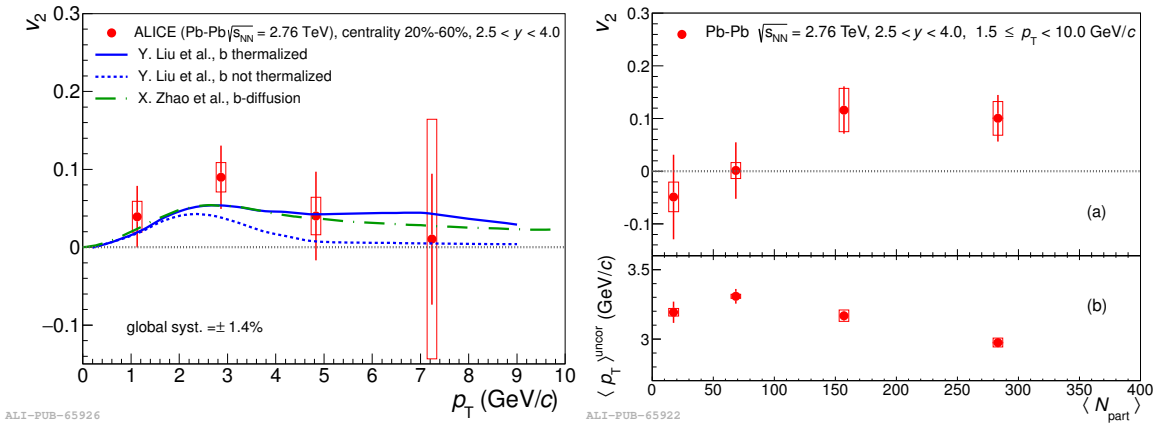

Figure 4.15 – (Left) J/ψ v_2 as a function of p_T for the centrality class 20–40 %, (Right) J/ψ v_2 and $\langle p_T \rangle$ vs centrality for $1.5 < p_T < 10\,\text{GeV}/c$ at $\sqrt{s_{NN}} = 2.76\,\text{TeV}$[A+13a] measured by ALICE

compatible with zero. However, the results show the first signs that b quark might also (partially) thermalise in the medium,

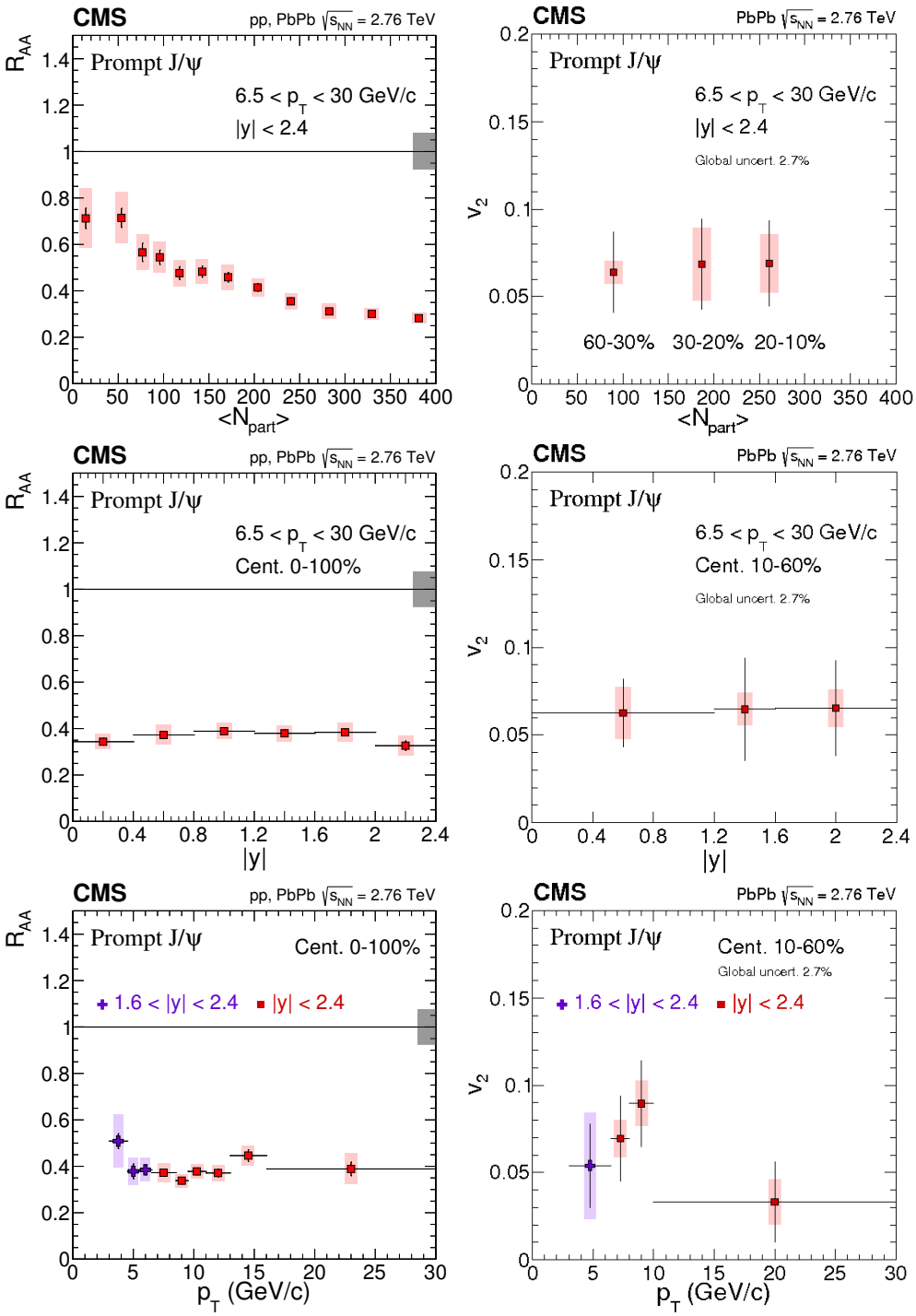

Figure 4.16 – Centrality (Top), rapidity (Middle) and p_T (Bottom) dependence of prompt J/ψ R_{AA} (Left) and v_2 (Right) measured with the CMS detector [K+17]

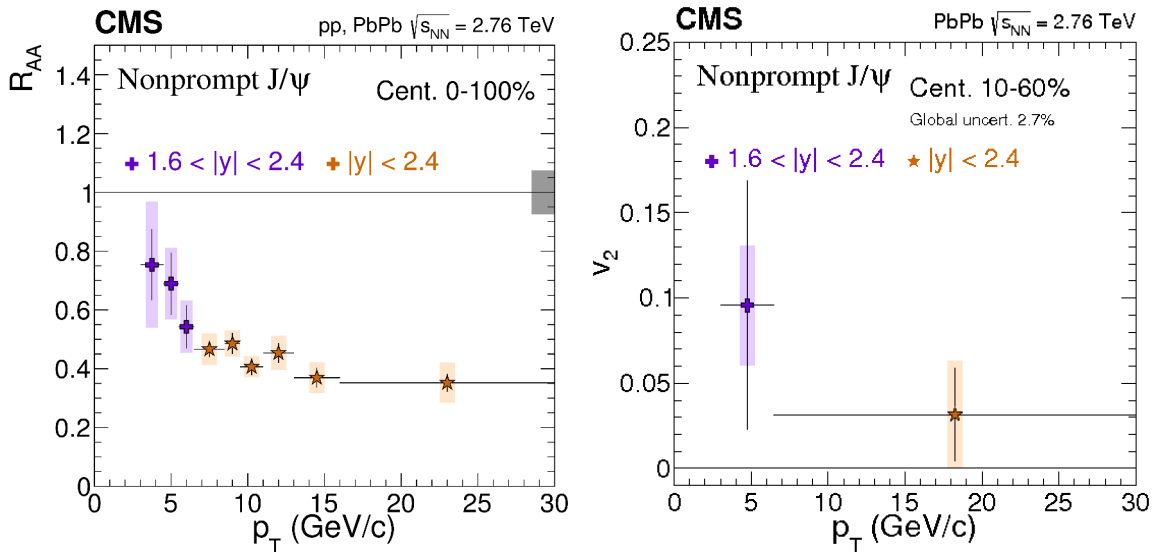

Figure 4.17 – p_T dependence of non-prompt J/ψ R_{AA} (Left) and v_2 (Right) measured with the CMS detector [K+17]

4.5 Theoretical models

Currently, three main theoretical approaches aim to describe charmonium production in nucleus-nucleus collisions: transport models, statistical hadronisation models and the comover model.

Transports models offer a description of the medium from the initial colliding nuclei until the final freeze-out. Quarkonium states are continuously dissociated and (re)combined throughout the deconfined state in an expanding and isotropic fireball. The space-time evolution is described through a relativistic Boltzmann equation [ZR11, ZXXZ14, DR15, The02] with a direct suppression and a (re)generation term. Cold nuclear matter effects (shadowing, nuclear absorption and Cronin effects) are included. The model also takes into account the feed-down contribution from higher excited states.

The statistical hadronisation model [ABMRS03] assumes a complete dissociation of $Q\bar{Q}$ pairs in the medium. Charm quarks reach a thermal equilibrium in the medium and combine statistically into open or closed heavy flavours at the phase boundary. The model was extended to heavy quarks from its success in the description of hadron abundances from AGS to LHC energies. The multiplicities of hadrons containing light quark (u,d,s) are described by the thermodynamical grand canonical ensemble with only thermal parameters, the chemical freeze-out temperature and the chemical potential, calculated for each collision system and energy [ABMS09]. The extension to charm quarks introduces a third parameter, the charm-production cross section $\sigma_{c\bar{c}}$. A direct consequence is that the relative yield of charmonium states only depends on the hadronisation temperature. The measurement of the J/ψ / ψ(2S) ratio is therefore a key observable to test the hadronisation model.

The comover approach [CBF+08, Fer14] interprets the cold and hot matter effects on quarkonium production as the result of the dynamical interactions between the bound state and the dense comoving medium. The model is based on rate equation similar to transport models and does not assume a medium equilibrium. It relies on an effective interaction cross section σ_{co} of J/ψ with a comoving medium of both partonic and hadronic origin. The model also contains a (re)generation component of J/ψ mesons through the (re)combination of charm quarks. Cold nuclear effects are included by considering nuclear shadowing and nuclear absorption.

The predictions from all models over the full centrality range are compared to ALICE measurements in Pb–Pb collisions at $\sqrt{s_{NN}} = 5.02$ TeV in Fig. 4.18. All models still contain many uncertainties. Some basic parameters are not ascertain yet, such as the medium temperature, others have a large impact on the predictions, e.g. the $c\bar{c}$ production cross section and CNM effects on quarkonium production which are not completely understood yet, and could substantially benefit from future precise experimental measurements.

Alternative theoretical approaches including other contributions might also give reasonable description of charmonium production. One of them considers thermal production of charm quarks via gluon fusion and quark and anti-quark annihilation [ZCGZ16]. The authors argue that thermal production becomes sizeable from $\sqrt{s_{NN}} = 5.02$ TeV and dominant at the Future Circular Collider (FCC) energies (39 TeV). The main consequence is an increased J/ψ production in the medium, in particular for central collisions. An intriguing prediction of the model is an enhancement of low-p_T J/ψ at the FCC.

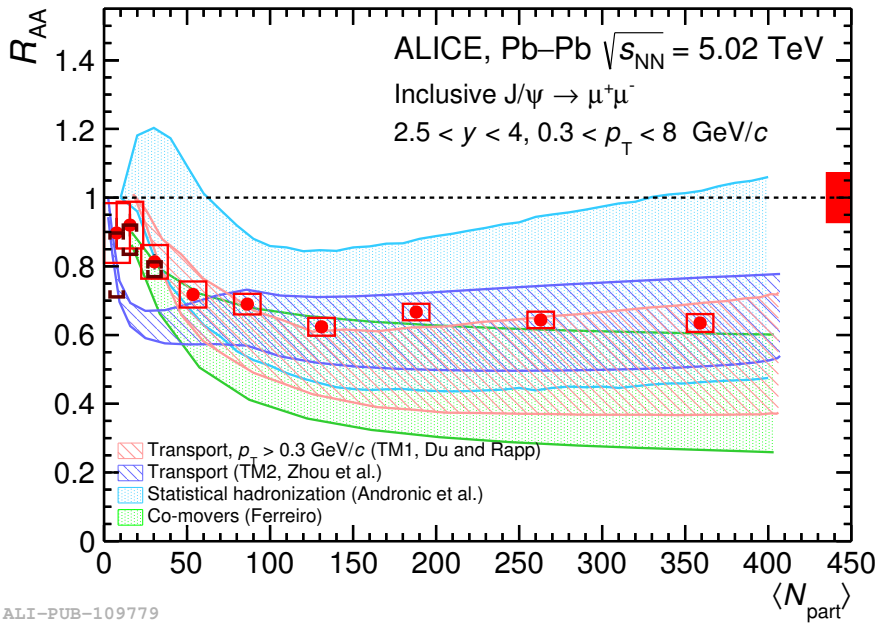

Figure 4.18 – Inclusive J/ψ R_{AA} in Pb–Pb collisions (in the 0–90 % centrality range) measured by ALICE at $\sqrt{s_{NN}} = 5.02$ TeV compared to several theoretical predictions [A+17d]

CHAPTER 5

ANALYSIS

"Half my life is an act of revision."

— John Irving

This chapter describes the analysis procedure. The J/ψ elliptic flow was measured using two methods based on the event plane estimation. The flow technique, the signal extraction, the systematic uncertainties and the results are presented. Additional cross checks are also featured. Data used in this thesis are from Pb-Pb collisions at $\sqrt{s_{\rm NN}} = 5.02$ TeV collected from October to November 2015 during LHC's second run. The results are compared to the previous Pb-Pb data campaign at $\sqrt{s_{\rm NN}} = 2.76$ TeV from LHC run 1 (November-December 2011). The complete list of runs can be found in the Appendix A. The analysis focused on three centrality ranges: 5–20 %, 20–40 %, and 40–60 %.

5.1 Azimuthal asymmetry analysis

The analysis is based on the event plane method. This method is built on the **estimation of the reaction plane** (see Sec. 3) from the flow vectors. For each event, the flow vectors Q_n are obtained from the angular distribution of a specific subset of particles produced in the collision. The unit vectors u_n are defined from the particle angles (ϕ) as $u_n = x_n + i\,y_n \equiv \cos n\phi + i \sin n\phi = \exp\{i\,n\phi\}$ and extracted from the detector multiplicities. The **reconstructed reaction plane** is called **event plane** (EP). The event flow vectors and their components in the event plane ($Q_{n,x}$ and $Q_{n,y}$) are defined for each harmonic and can be expressed in the complex plane. They are computed event by event by summing over all measured particles (N_p):

$$Q_{n,x} = \sum_{N_p} (w_i \cos n\phi_i) \tag{5.1}$$

$$Q_{n,y} = \sum_{N_p} (w_i \sin n\phi_i) \tag{5.2}$$

Several weights (w_i) can be applied. In most analyses the particle transverse momentum is used. In the case of a segmented detector, such as the V_0, the ϕ angles correspond to the centres of the detector sectors and the weights are taken as the corresponding channel amplitudes. The **event plane angle** corresponds to the rotation angle between the event plane axes and the detector frame. It is denoted as $\Psi_{\rm EP}$.

The flow vector can be expressed in the detector frame as:

$$Q_n \equiv Q_{n,x} + i Q_{n,y} = |Q_n| \exp\{i\,n\Psi_{{\rm EP},n}\}. \tag{5.3}$$

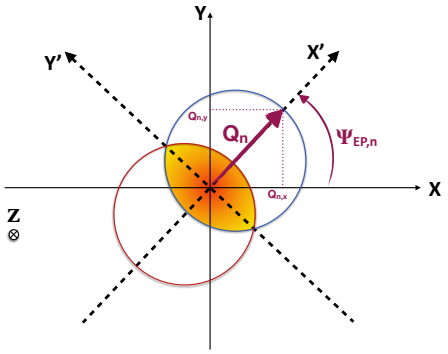

Figure 5.1 – Illustration of the event plane frame

For each harmonic n of the Fourier decomposition, the event plane angle is ascertained in $[-\frac{\pi}{n}, \frac{\pi}{n}]$ from the event vector coordinates as:

$$\Psi_{\mathrm{EP},n} = \frac{1}{n} \arctan \frac{\mathrm{Q}_{n,y}}{\mathrm{Q}_{n,x}} \tag{5.4}$$

The *observed* n^{th} flow coefficient (v_n) of the particle azimuthal distribution is computed from the n^{th} azimuthal angle $\Psi_{\mathrm{EP},n}$ as the average over all events of all particle angles (ϕ_i) in a given (p_{T},y) interval:

$$v_n^{obs}(\mathrm{p_T}, \mathrm{y}) = \langle \cos[n(\phi_i - \Psi_{\mathrm{EP},n}] \rangle. \tag{5.5}$$

The *final* value of the v_n coefficients is obtained by correcting the *observed* value with the event plane resolution σ_{plane} as:

$$\mathrm{v_n} = \frac{\mathrm{v_n^{obs}}}{\sigma_{\mathrm{plane}}}. \tag{5.6}$$

In the case of the elliptic flow (v_2) analysis, the azimuthal angle of the second harmonic $\Psi_{\mathrm{EP},2}$ is used to estimate the reaction plane angle Ψ_{R}.
To avoid auto-correlations and reduce the non-flow contribution, the pseudo-rapidity (η) gap between the event plane detector and the detector measuring the particles angles should be as large as possible. This allows to minimise the sample containing both particles of reference for the flow vector determination and particles of interest. The analysis was performed by using either the V0A or the SPD. The corresponding η gaps with the Muon Spectrometer are $\Delta\eta_{\mathrm{V0A}}$=5.3 and $\Delta\eta_{\mathrm{SPD}}$=1.1. Although the V0C share a common acceptance region with the spectrometer, it was also calibrated to compute the event plane resolution correction factor. Moreover, the results obtained with the V0C as event plane detector provide a good estimate of the non-flow contamination due to the η range overlap.

5.1.1 Dectector equalisation

Effects of non-uniform acceptance of the event plane detector are corrected through a so-called **equalisation procedure**. The method consists of correcting the measured flow vectors from detector effects through algebraic operations.

The calculation and calibration of the Q_n vectors was performed through the *FlowVectorCorrections* framework within the AliPhysics repository. The framework performs all

required calibrations to compensate detector effects and calculates the flow vectors. More details can be found in the FlowVectorCorrections TWiki page. Its implementation is based on the publication [SV08]. The corrections are calculated and applied iteratively for each harmonic. The procedure is performed independently for each event plane detector. It is applied on a run-per-run basis as a function of centrality and z-vertex position. The following steps are supported by the framework:

- *Gain equalisation of channel multiplicities*: to ensure that same multiplicities are detected in different channels and considered with the same weight, all channel multiplicities (M_c) are scaled by their averages. This step is applied only to the V0 detectors and is done separately for each ring to account for the different acceptances:

$$\mathrm{M}'_c = \frac{\mathrm{M}_c}{\langle \mathrm{M}_c \rangle} \tag{5.7}$$

- *Vector recentering*: flow vectors are corrected to be centered at zero (x and y components) and the width (σ_{Q_n}) is scaled to unity

$$\mathrm{Q}'_\mathrm{n} = \frac{\mathrm{Q}_\mathrm{n} - \langle \mathrm{Q}_\mathrm{n} \rangle}{\sigma_{\mathrm{Q}_\mathrm{n}}} \tag{5.8}$$

- *Detector alignment*: flow vectors are corrected from rotation by choosing a detector configuration as an alignment reference:

$$\mathrm{Q}'_n = \mathscr{R}(\Delta\phi)\mathrm{Q}_n. \tag{5.9}$$

  The rotation angle $\Delta\phi$ is determined from a given detector configuration A and an harmonic m

$$\Delta\phi_n = -\frac{1}{m}\tan^{-1}\left(\frac{\langle \mathrm{Q}_{n\mathrm{X}}\mathrm{Q}^{\mathrm{A}}_{m\mathrm{Y}}\rangle - \langle \mathrm{Q}_{n\mathrm{Y}}\mathrm{Q}^{\mathrm{A}}_{m\mathrm{X}}\rangle}{\langle \mathrm{Q}_{n\mathrm{X}}\mathrm{Q}^{\mathrm{A}}_{m\mathrm{X}}\rangle + \langle \mathrm{Q}_{n\mathrm{Y}}\mathrm{Q}^{\mathrm{A}}_{m\mathrm{Y}}\rangle}\right) \tag{5.10}$$

  where $\langle\cdots\rangle$ denote an average over all events in a given event class. This step is not performed for the SPD.

- *Vector twist and rescaling*: Averages of unit vectors over all events can be expressed for a given reaction plane orientation as

$$\langle \mathrm{Q}_\mathrm{n}\rangle_{\Psi_{\mathrm{RP}}} = \langle \mathrm{X}_\mathrm{n}\rangle_{\Psi_{\mathrm{RP}}} + \mathrm{i}\langle \mathrm{Y}_\mathrm{n}\rangle_{\Psi_{\mathrm{RP}}} = v_n(\cos(n\Psi_{\mathrm{RP}}) + i\sin(n\Psi_{\mathrm{RP}})). \tag{5.11}$$

  Some effects of non-uniform acceptance are the apparition of residual terms in the expression of $\langle \mathrm{X}_\mathrm{n}\rangle_{\Psi_{\mathrm{RP}}}$ and $\langle \mathrm{Y}_\mathrm{n}\rangle_{\Psi_{\mathrm{RP}}}$. Vector twist results in sinus terms in the equation of $\langle \mathrm{X}_\mathrm{n}\rangle_{\Psi_{\mathrm{RP}}}$ and cosine terms for $\langle \mathrm{Y}_\mathrm{n}\rangle_{\Psi_{\mathrm{RP}}}$. Neglecting the contributions from other harmonics and after vector recentering, the expression of $\langle \mathrm{X}_\mathrm{n}\rangle_{\Psi_{\mathrm{RP}}}$ and $\langle \mathrm{Y}_\mathrm{n}\rangle_{\Psi_{\mathrm{RP}}}$ is:

$$\begin{aligned} \langle \mathrm{X}_\mathrm{n}\rangle_{\Psi_{\mathrm{RP}}} &= \mathrm{a}^+\{\cos(\mathrm{n}\Psi_{\mathrm{RP}}) + \Lambda^+\sin(\mathrm{n}\Psi_{\mathrm{RP}})\} \\ \langle \mathrm{Y}_\mathrm{n}\rangle_{\Psi_{\mathrm{RP}}} &= \mathrm{a}^-\{\sin(\mathrm{n}\Psi_{\mathrm{RP}}) + \Lambda^-\cos(\mathrm{n}\Psi_{\mathrm{RP}})\}. \end{aligned} \tag{5.12}$$

  Non-zero $\Lambda^{(+,-)}$ coefficients are corrected for through a diagonalisation procedure as:

$$\mathrm{Q}'_{n,(x,y)} = \frac{\mathrm{Q}_{n,(x,y)} - \Lambda^{(+,-)}\mathrm{Q}_{n,(x,y)}}{1 - \Lambda^-\Lambda^+}. \tag{5.13}$$

  An additional rescaling step accounts for acceptance coefficients ($a^{(+,-)}$):

$$\mathrm{Q}''_{n,(x,y)} = \frac{\mathrm{Q}'_{n,(x,y)}}{a^{(+,-)}}. \tag{5.14}$$

5.1.2 Event selection and implementation

The *FlowVectorCorrections* framework ran over the 137 QA selected LHC15o runs (A) with the following selections:

- events must pass the physics selection
- events must be validated for the centrality calibration and within the 0–90 % centrality class
- to improve the flattening quality of the event plane, a cut on the vertex position along the beam axis ($|z_{vertex}| \leqslant 10$ cm) was applied
- one of the following triggers was required: kMB, kINT7 or kMUSPB (see 2.2.7). The last trigger was added with respect to the standard selections of the *FlowVectorCorrections* framework (including kMB or KIN7 only) to increase the statistics of minimum bias events.

Tab. 5.1 lists the various Q vector calibration steps for the SPD, V0A and V0C detectors. Channelised detector configurations require additional corrections with respect to tracking detectors. The impact of the calibration on vector flattening is more striking for the first

Step	SPD	V0A(C)
0	no calibration	no calibration
1	recentering	gain equalisation
2	twist and rescaling	recentering
3	-	alignment
4	-	twist and rescaling

Table 5.1 – Calibration steps of the Q_n vector for the SPD, V0A and V0C with the QnVectorCorrections framework

correction steps, while the last ones are more nuanced.

The EP angle distributions of each calibration step for several centrality ranges are given in Fig. 5.2 and Fig. 5.3. The distributions are fitted to constant functions. A clear flattening improvement of the event-plane angle distribution is observed for the SPD. The V0A event plane distributions are also greatly improved by the first two steps. The third one enhances slightly more the flattening but the last one does not bring additional improvement, its effect seems even to deteriorate the results. The situation is similar for the V0C (see Fig. B.1 in the Appendix), with an effect of the third step mainly significant for peripheral collisions (70–80 % and 80–90 %). Consequently, the analysis was performed with the flow vectors after the third equalisation step (*alignment*) for both V0 detectors and after the second one (*twist and rescaling*) for the SPD.

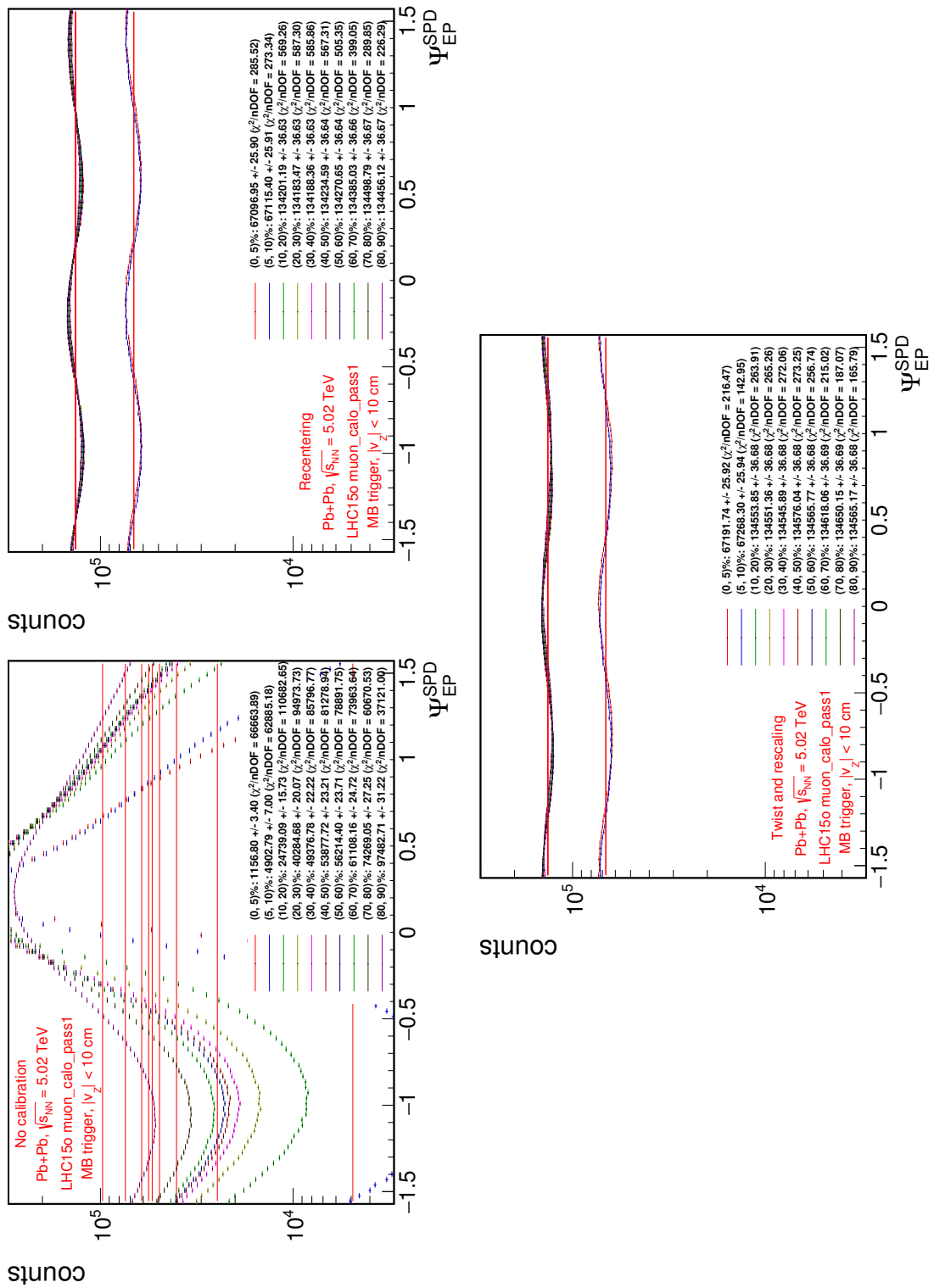

Figure 5.2 – Distributions of the SPD EP angles in centrality ranges after each calibration step (from Left to Right: no calibration, recentering and twist/rescaling)

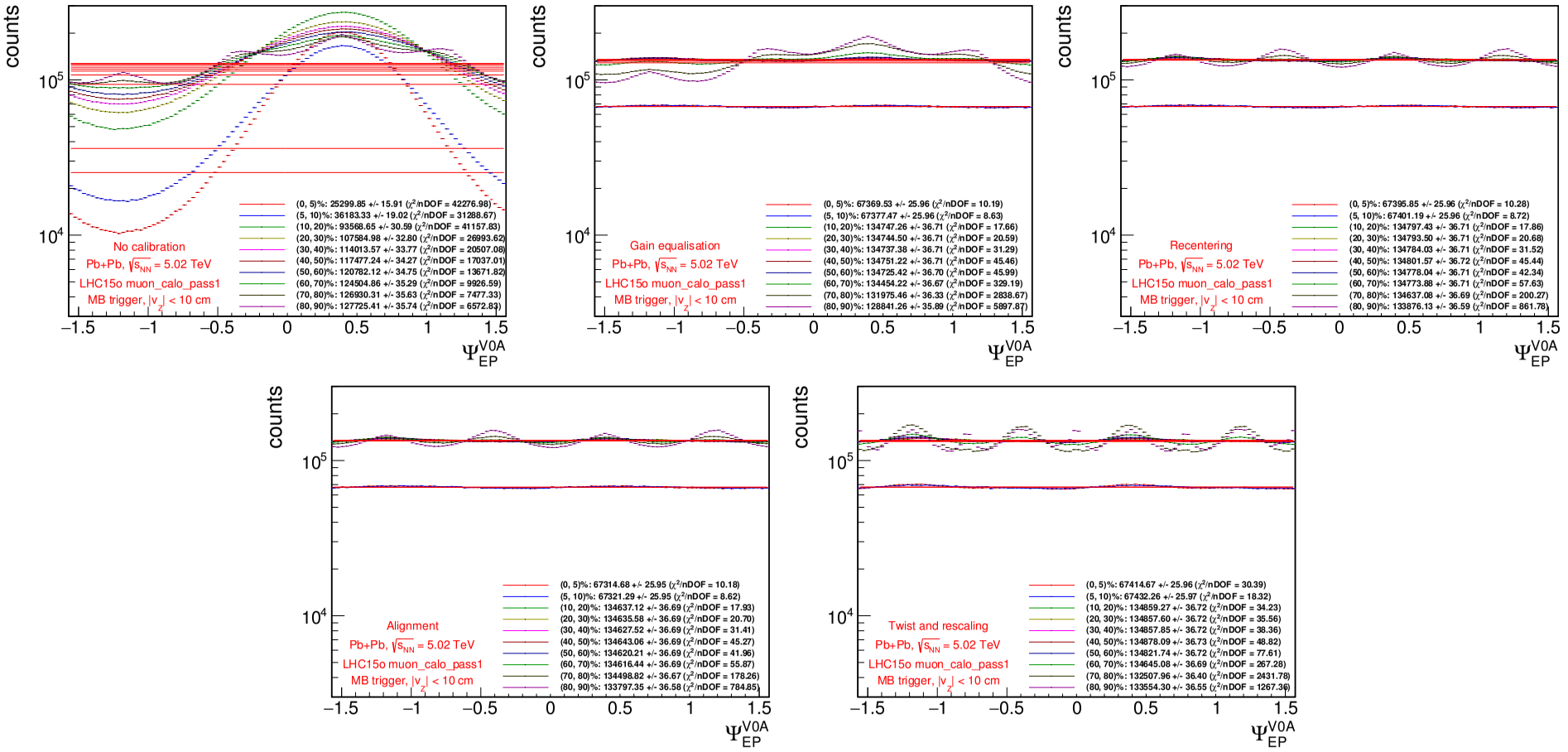

Figure 5.3 – Distributions of the V0A EP angles in centrality ranges after each calibration step (from Top Left to Bottom Right: no calibration, gain equalisation, recentering, alignment, twist/rescaling)

The comparison of the event plane angles obtained with the different detectors after the equalisation procedure is presented on Fig. 5.4. A clear correlation is observed, supporting the validity of the event plane measurement.

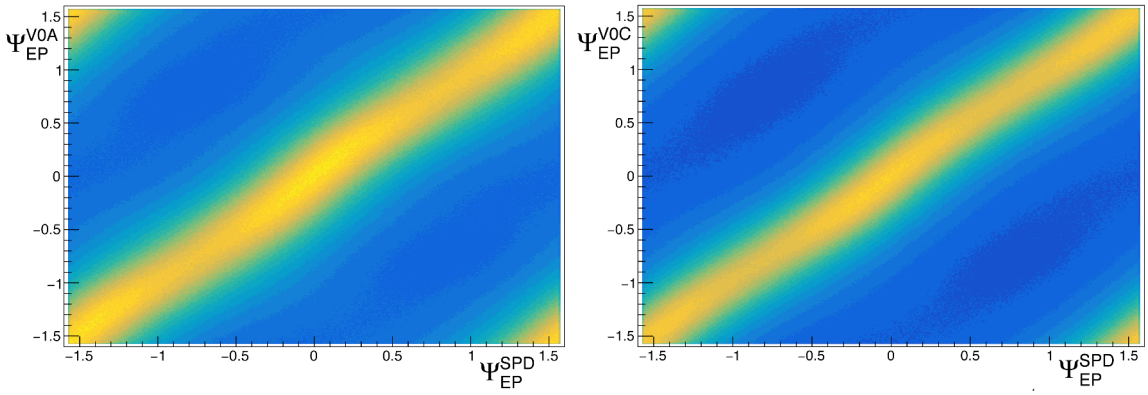

Figure 5.4 – Comparison the EP angle distributions for (Left) V0A vs SPD and (Right) V0A vs SPD

5.1.3 Resolution determination

The determination of the event plane is limited by the finite number of particles measured by the detector and the fluctuations in the particle multiplicity distributions [PV98]. This effect introduces a smearing in the determination of the event plane angle as estimator of the true reaction plane angle. The resolution can be defined for each harmonic n as:

$$\sigma_{\text{plane,n}} = \langle \cos\left[n(\Psi_{\text{EP,n}} - \Psi_{\text{RP}})\right] \rangle. \tag{5.15}$$

In order to take into account this difference, a correction of the observables referring to the event plane is required. The raw (before correction) and corrected (after correction) observables are respectively denoted *observed* and *corrected* and are related by the event plane resolution σ_{plane} as:

$$X^{\text{corr}} = \frac{X^{\text{obs}}}{\sigma_{\text{plane}}}. \tag{5.16}$$

The resolution of the event plane determination was evaluated with the **3 sub-event technique**. The event plane resolution of a sub-detector a can be obtained by using two other sub-detectors b and c [PV98] from the estimated harmonic event plane Ψ_{n} as:

$$\sigma^{\text{a}}_{\text{plane,n}} = \langle \cos\left[n(\Psi^{\text{a}}_{\text{n}} - \Psi_{\text{RP}})\right] \rangle = \sqrt{\frac{\langle \cos\left[n(\Psi^{\text{a}}_{\text{n}} - \Psi^{\text{b}}_{\text{n}})\right] \rangle \langle \cos\left[n(\Psi^{\text{a}}_{\text{n}} - \Psi^{\text{c}}_{\text{n}})\right] \rangle}{\langle \cos\left[n(\Psi^{\text{b}}_{\text{n}} - \Psi^{\text{c}}_{\text{n}})\right] \rangle}}. \tag{5.17}$$

This analysis uses the SPD, V0A, and V0C as sub-detectors. The relative pseudo-rapidity gaps are $\Delta\eta_{\text{V0A-SPD}}$=1.6, $\Delta\eta_{\text{SPD-V0C}}$=0.5, and $\Delta\eta_{\text{V0A-V0C}}$=4.5.

Since the resolution scales with the multiplicity, it is determined in small centrality bins. The resolutions for the SPD, V0A, and V0C as a function of centrality are shown in Fig. 5.5. The highest resolution is reached for the SPD, consequently it was used as event plane detector for the main results of this analysis.

After the resolution is obtained in fine centrality bins, average values over the wider bins of the J/ψ v_2 analysis must be computed. Because the analysis is performed on dimuon-triggered data, and in order to reflect the event distribution containing J/ψ particles

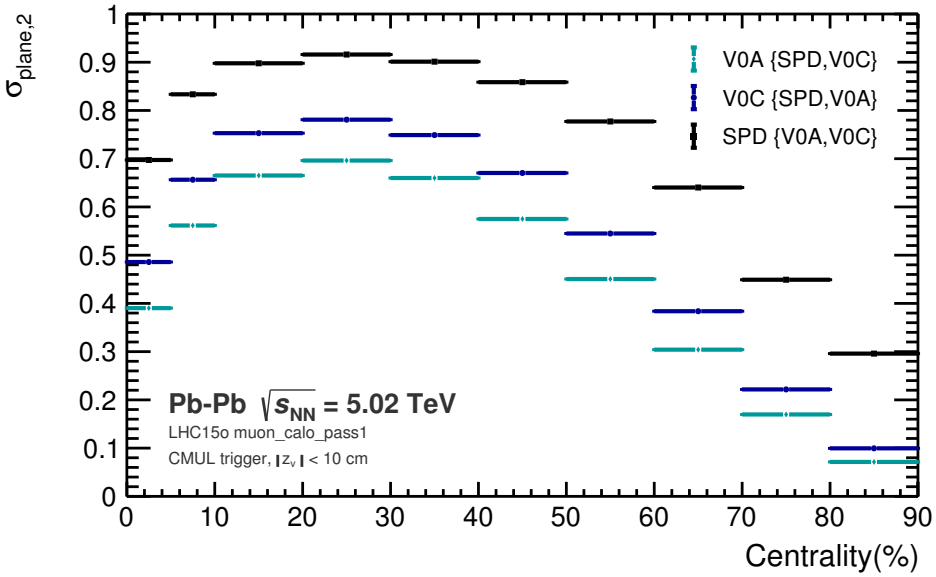

Figure 5.5 – Event plane resolution of SPD, V0A, and V0C sub-detectors as a function of centrality

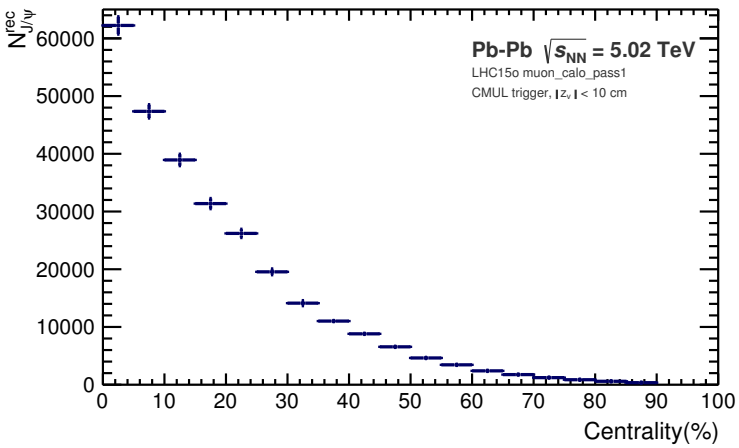

Figure 5.6 – Number of reconstructed J/ψ used as weight for the event plane resolution as a function of centrality

(Fig. 5.6), this average is weighted by the number of reconstructed J/ψ in each centrality class. The final event plane resolutions are listed in Tab. 5.2 for the various centrality intervals considered in this analysis.

Centrality	V0A	SPD
0–90 %	0.57010 ± 0.00010	0.83283 ± 0.00019
0–5 %	0.39296 ± 0.00036	0.70185 ± 0.00064
5–20 %	0.62400 ± 0.00014	0.87252 ± 0.00019
20–40 %	0.68269 ± 0.00010	0.91036 ± 0.00014
40–60 %	0.53348 ± 0.00014	0.83202 ± 0.00022
60–90 %	0.22916 ± 0.00033	0.55374 ± 0.00327

Table 5.2 – $N_{J/\psi}$ -weighted EP resolutions of SPD and V0A detectors for the various centrality ranges considered in this analysis.

5.2 J/ψ elliptic flow extraction

The J/ψ v_2 extraction was performed using two different techniques, each based either on the **event plane** or on the **scalar product** determination. Both analysis techniques were applied in several p_{T}, rapidity, and centrality bins. For the event plane method, the second harmonic event plane ($\Psi_{\mathrm{EP},2}$) is computed and corrected using the *FlowVectorCorrections* framework. This procedure is described in Sec. 5.1 of the present manuscript. The analysis was performed using either the V0A or the SPD as event plane detector. For the scalar product, the second harmonic of the flow vectors is used (see Sec. 5.5.1). The J/ψ is reconstructed through the dimuon decay channel. Muon tracks are measured in the Muon Spectrometer, and dimuon pairs are formed by associating two muons of opposite sign. Pair transverse momentum, rapidity, invariant mass, and v_2 can then be computed.

5.2.1 Event and track selections

Event selection

The analysis focused on three centrality ranges: 5–20 %, 20–40 % and 40–60 %. More details on centrality estimation with the ALICE detector and the corresponding produced number of particles can be found in the Appendix (Sec. 5.6.2). Only events passing the physics selection are included in the analysis sample. The trigger classes used in the analysis are CMUL7-B-NOPF-MUFAST and CMLL7-B-NOPF-MUFAST (more details are found in Sec. 2.2.7).

Track cuts:

Tracks not passing the following selection criteria were rejected :

- pseudo-rapidity within the Muon Spectrometer range $-4 < \eta < -2.5$, to be in the detector acceptance
- radial coordinate at the exit of the front hadron absorber located within the angular acceptance of the spectrometer ($2 \leq \theta_{\mathrm{A}bs} \leq 10\,\mathrm{deg}$), this condition being translated into a cut on the radial transverse position of the muon track ($17.6\,\mathrm{cm} < \mathrm{R}_{abs} < 89.5\,\mathrm{cm}$), to reject tracks undergoing multiple Coulomb scatterings in the high-Z materials of the front absorber
- match of the reconstructed track in the tracking chambers with a reconstructed segment in the trigger system and estimated transverse momentum by the trigger above the trigger threshold, to ensure that the selected dimuons triggered the muon trigger and to limit the contribution from muonic π and K decays.

Dimuon pair cuts

Dimuon pairs are measured over the transverse momentum range $0 < p_{\mathrm{T}} < 12\,\mathrm{GeV}/c$ and in the rapidity interval $-4 < y < -2.5$. The later will be referred to using the corresponding positive interval within the rest of the document. The so-called $p \times \mathrm{DCA}$ cut (where p is the track momentum and Distance of Closest Approach (DCA) is the distance between the vertex and track extrapolated to the vertex transverse plane) was not applied in this analysis since its effect was previously shown to be negligible for the J/ψ yield extraction.

5.2.2 The $dN/d\Delta\phi$ method

The first method for the J/ψ v_2 extraction consists of fitting the distribution of the number of reconstructed J/ψ as a function of the relative angle to the event plane in various p_T and centrality bins. This method is quite intuitive as it shows the variation of the particle production as a function of the emission angle with respect to the Event Plane (EP) angle around the collision.

Description

The relative angle $\Delta\varphi = \varphi_{\mu\mu} - \Psi_{EP,2}$ of each opposite sign dimuon pair is computed, and the sample is divided into $\Delta\varphi$ bins comprised in the $[0,\pi]$ range. Considering the statistics, 6 $\Delta\varphi$ bins were used. In each $\Delta\varphi$ bin, the number of J/ψ is extracted by fitting the invariant mass distribution of opposite sign dimuons with the sum of a signal and a background function. First, the $\Delta\varphi$ integrated distribution corresponding to the considered p_T and centrality bin is fitted. Then the mass and width parameters of the signal are fixed in each $\Delta\varphi$ bin according to the values obtained in the integrated range. Fig. 5.7 shows an example of a fit performed in the 6 $\Delta\varphi$ bins.

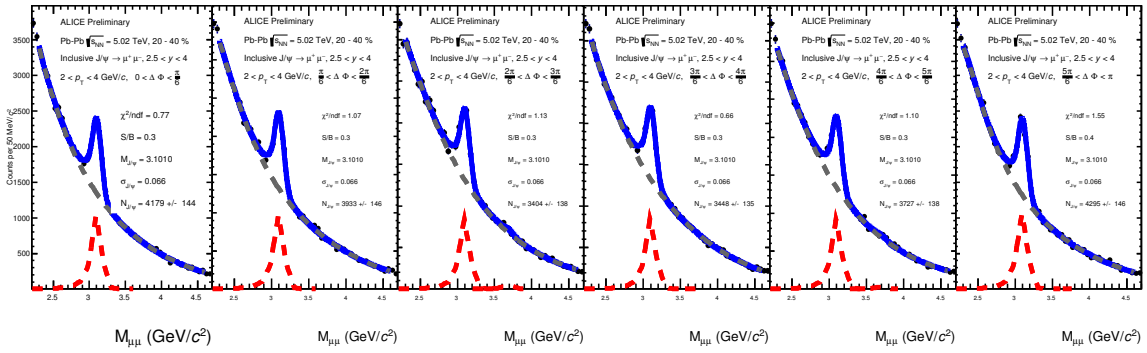

Figure 5.7 – Example of J/ψ invariant mass distributions for $2 < p_T < 4$ GeV/c and $2.5 < y < 4$ in the 20–40 % centrality range for 6 $\Delta\varphi$ bins

Signal and background parametrisation

Three different functions have been considered to describe the signal form:

- an extended Crystal-ball(B.2.1) with the tails fitted to the results obtained in proton-proton collisions (integrated in p_T)
- an extended Crystal-ball(B.2.1) with the tails fitted as a function of p_T to the embedding [1] of pure Monte Carlo (MC) J/ψ in real MB triggered events
- an NA60 function(B.2.1) with the tail fitted as a function of p_T to the embedding of pure MC J/ψ in real MB triggered events

The fit parameters can be found in the Appendix (5.2.2). Each signal function was combined with two different background functional forms: a polynomial ratio (2nd order polynomial divided by a 3rd order polynomial) and a quadratic variable-width Gaussian (B.2.1).

[1] The embedding technique consists of simulating particles (in this case J/ψ) and embedding the detector response into the event before analysing the data.

Each combination of background and signal form was declined into 3 invariant mass ranges (GeV/c) : [2.2–4.5], [2.3–4.6], and [2.4–4.7]. This results in (2 backgrounds x 3 signals x 3 ranges =) 18 tests of the signal extraction. The result of each fit test was validated by requiring good fit and covariance-matrix status. The final v_2 values and their statistical uncertainties were obtained as the average of all successful tests for a given p_{T} and centrality bin. The systematic uncertainty due to the signal extraction was calculated as the Root Mean Square (RMS)[2] of all the successful tests. In addition, the results with both event plane detectors were compared.

Extraction of the v_2 coefficient

The J/ψ v_2 can be extracted as the modulation of the $\mathrm{N}_{\mathrm{J/\psi}}$ distribution versus the relative angle to the event plane $\Delta\varphi$. Therefore the J/ψ distribution as a function of $\Delta\varphi$ is fitted with:

$$\mathrm{N}_0 \times [1 + 2\mathrm{v}_2^{\mathrm{obs}} \times \cos(2\Delta\varphi)]. \tag{5.18}$$

An example of J/ψ v_2 extraction is presented in Fig. 5.8. The J/ψ elliptic flow measurements

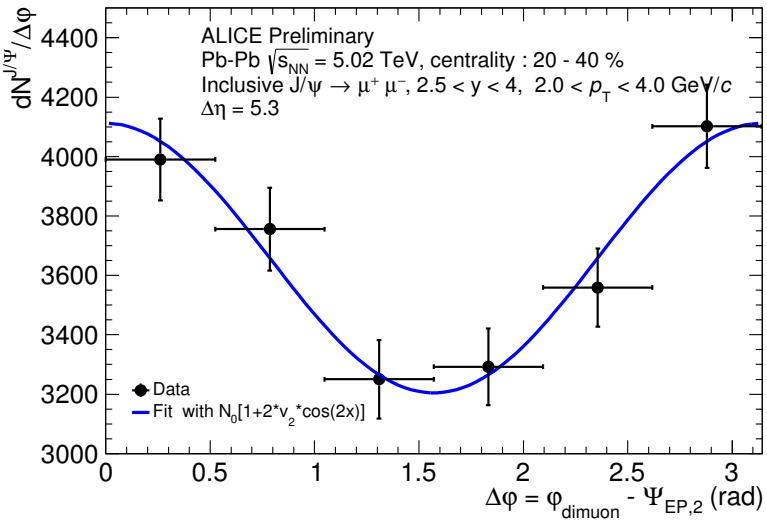

Figure 5.8 – Example of J/ψ v_2 extraction with the event plane method (SPD) for $2 < p_{\mathrm{T}} < 4$ GeV/c and $2.5 < y < 4$ in the centrality range 20–40 % (the horizontal error bars stand for the bin widths)

from the $d\mathrm{N}/d\Delta\varphi$ technique are presented as a function of the transverse momentum in three centrality classes (5–20 %, 20–40 %, 40–60 %) in Fig. 5.9 where the SPD is the event plane detector. Similar results with the V0A can be found in the appendix (Fig. B.2). The elliptic flow coefficients are given before (*observed* values) and after (*corrected* values) resolution correction. In both cases the first three plots correspond to a given centrality range and the last one compares the *corrected* v_2 values from the various centrality ranges.

For all measurements the elliptic flow coefficient rises with p_{T}, reaching a maximum value for intermediate transverse momentum range ($2 < p_{\mathrm{T}} < 8$ GeV) and decreases or saturates for higher p_{T} values. Since the detector resolution is lower than one, corrected values are higher than the observed ones. The difference between both sets of values is different for each centrality range as the resolution factor is taken as a function of centrality. Comparison of the results for different centrality classes shows that semi-central collisions

[2]The RMS is calculated as the arithmetic mean of the squares of a set of numbers.

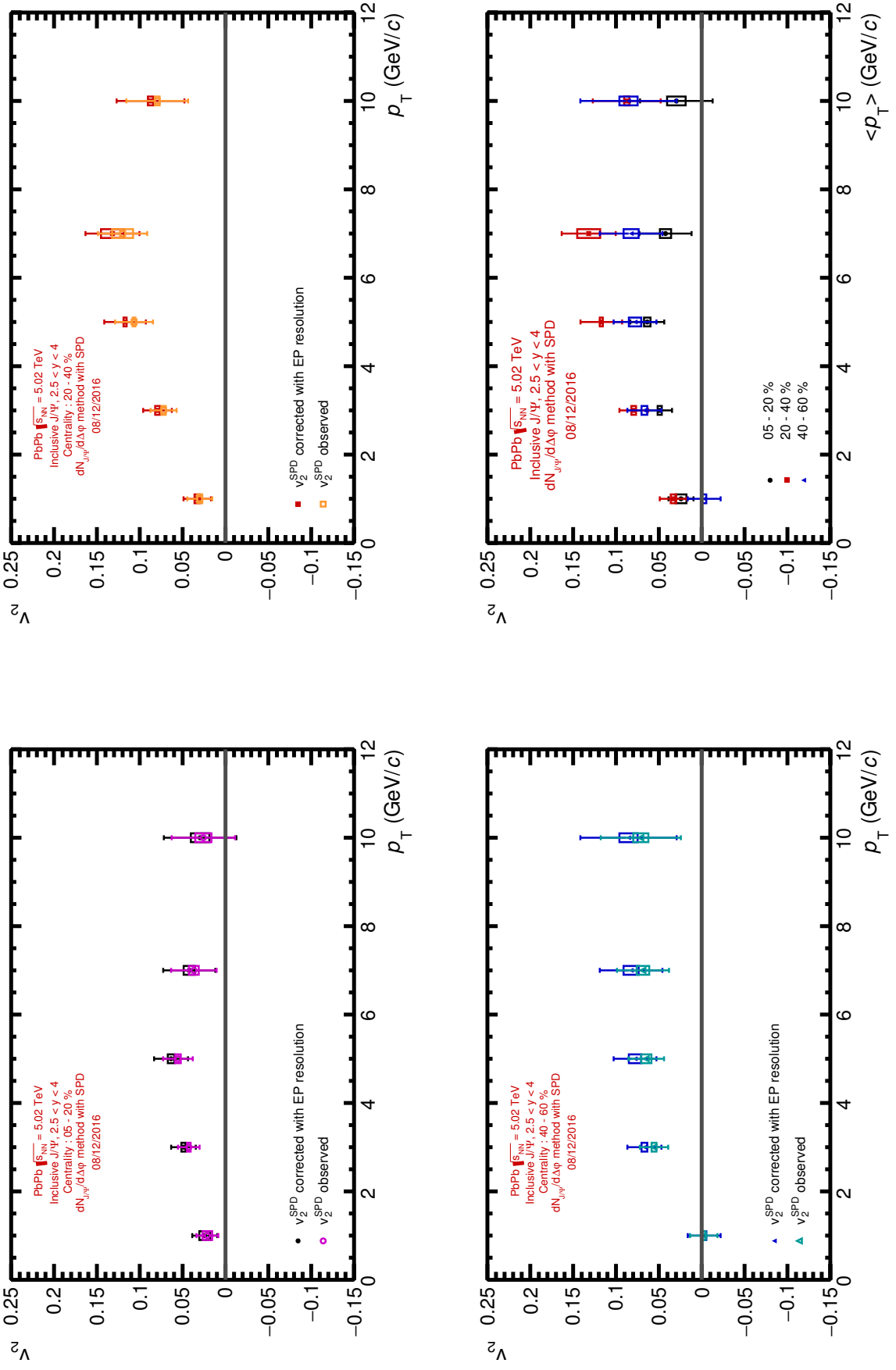

Figure 5.9 – Inclusive J/ψ v_2 as a function of p_T in the rapidity range $2.5 < y < 4$ in 3 centrality classes using the $dN/d\Delta\phi$ method and the SPD as event plane detector. Boxes represent the systematic uncertainty from the signal extraction. The last plot compares the *corrected* v_2 values from the various centrality ranges

(20-40%) exhibit the largest elliptic flow amplitudes. However, the p_{T} evolution is similar for all centrality classes. Values from Fig. 5.9 are summarized in Tab. 5.3.

p_{T} bin (GeV/c)	[0–2]	[2–4]	[4–6]	[6–8]	[8–12]
v_2^{obs} 5–20 %	0.0193	0.0380	0.0493	0.0332	0.0231
Stat. error 5–20 %	0.0125	0.0125	0.0163	0.0240	0.0329
Syst. error 5–20 %	0.0062	0.0062	0.0065	0.0074	0.0095
v_2^{obs} 20–40 %	0.0290	0.0660	0.0970	0.1158	0.0726
Stat. error 20–40 %	0.0146	0.0151	0.0209	0.0272	0.0333
Syst. error 20–40 %	0.0064	0.0062	0.0062	0.0073	0.0064
v_2^{obs} 40–60 %	0.0064	0.0462	0.0567	0.0566	0.0587
Stat. error 40–60 %	0.0152	0.0150	0.0183	0.0260	0.0398
Syst. error 40–60 %	0.0062	0.0064	0.0062	0.0074	0.0093

Table 5.3 – Table of data points shown in Fig. 5.3 : J/ψ v_2 (*corrected* values) in centrality classes 5–20 %, 20–40 %, and 40–60 % in the rapidity range $2.5 < y < 4$ from the $d\mathrm{N}/d\Delta\phi$ method with the SPD as event plane detector

An interesting cross-check of the results obtained with this method is the extraction of the background elliptic flow. Counting the number of dimuon pairs outside the J/ψ mass range in the various $\Delta\phi$ and fitting it with the cosinus distribution of equation 5.18 allows to compare the amplitude of the J/ψ v_2 with the dimuon background. Two side bands were defined at lower and larger invariant mass ranges [1.5–2.0 GeV/c^2] and [6.0–8.0 GeV/c^2] to avoid other resonance regions. The variation of the number of dimuons as a function of $\Delta\phi$ in both side bands was lower than in the J/ψ mass regions. This was observed for all p_{T} bins. An example is illustrated on Fig. 5.10 for $2 < p_{\mathrm{T}} < 4$ GeV/c in semi-central collisions.

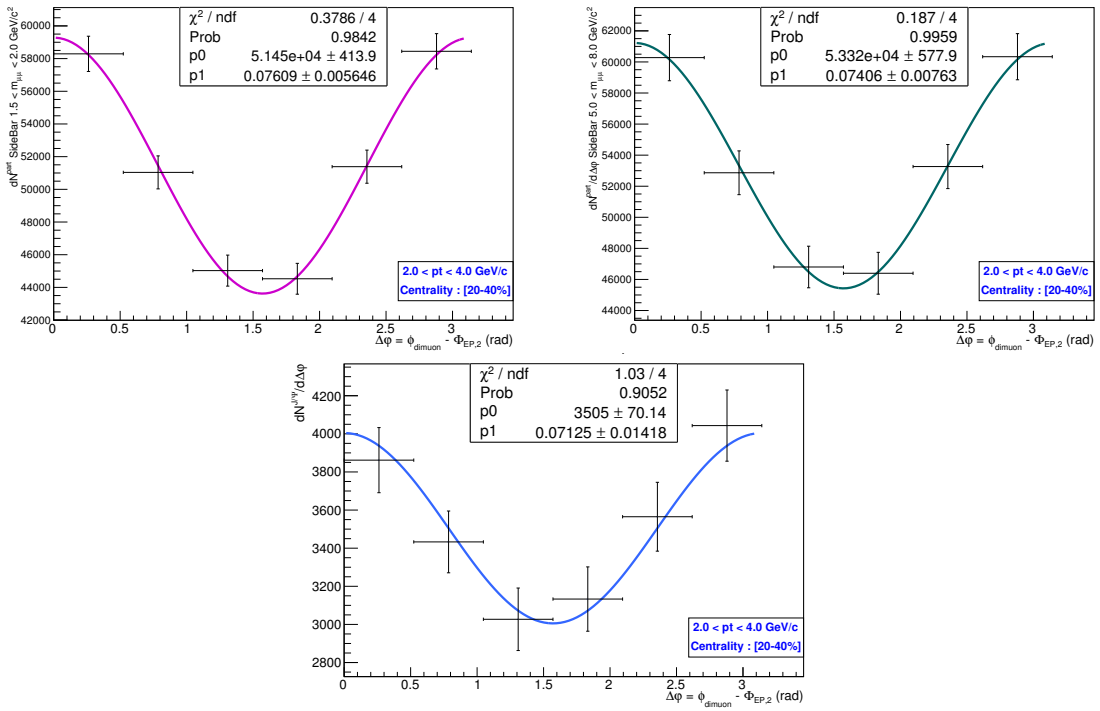

Figure 5.10 – Example of background v_2 extraction with the event plane method (SPD) for $2 < p_T < 4\,\mathrm{GeV}/c$ and $2.5 < y < 4$ in the centrality range 20–40 % and the invariant mass ranges (Top Left) [1.5–2.0 GeV/c^2] and (Top Right) [6.0–8.0 GeV/c^2] compared to (Bottom) the [2.2–4.5 GeV/c^2] J/ψ invariant mass range

5.2.3 The mean v_2 method

The J/ψ v_2 can also be extracted by fitting the total v_2 of the opposite-sign dimuon pairs as a function of the reconstructed invariant mass [BO04].

Description

For each p_T and centrality bin, the observed flow is computed as $v_2^{obs} = \langle \cos[2(\varphi_{\mu\mu} - \Psi_{EP,2})] \rangle$ where $\varphi_{\mu\mu}$ is the angle of the dimuon pair and $\Psi_{EP,2}$ is the event plane angle for the second harmonic. The total flow is the combination of the signal (S) and the background (B) contributions and can be therefore expressed as

$$v_2(\text{total}, M_{\mu\mu}) = \frac{f(S, M_{\mu\mu}) \times v_2^S + f(B, M_{\mu\mu}) \times v_2^B(M_{\mu\mu})}{N_{S+B}(M_{\mu\mu})}, \tag{5.19}$$

where v_2^S and v_2^B correspond respectively to the elliptic flow of the signal and the background, and $f(S, M_{\mu\mu})$ and $f(B, M_{\mu\mu})$ describe the dimuon invariant mass distributions, i.e. the fractions of signal and background in the total dimuon spectrum. This expression can be rearranged as :

$$v_2(\text{total}, M_{\mu\mu}) = \alpha(M_{\mu\mu}) \times v_2^S + [1 - \alpha(M_{\mu\mu})] \times v_2^B(M_{\mu\mu}), \tag{5.20}$$

where the fraction of signal $\alpha(M_{\mu\mu}) = \frac{S(M_{\mu\mu})}{[S(M_{\mu\mu})+B(M_{\mu\mu})]}$ is extracted from fits to the invariant mass distribution.

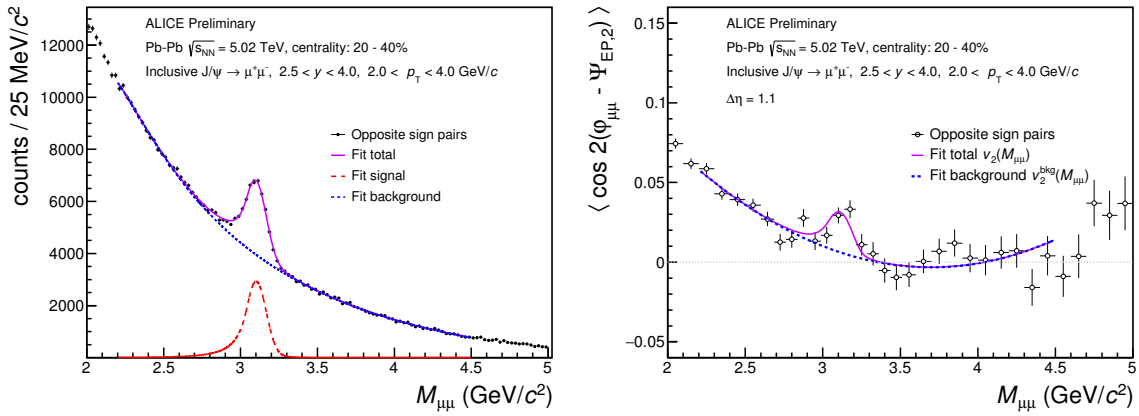

Figure 5.11 – J/ψ (Left) invariant mass and (Right) corresponding $\langle v_2 \rangle$ extraction with $2 < p_T < 4$ GeV/c in the centrality range 20–40 %

Signal and background parametrisation

Various signal and background functions were used for fitting the dimuon invariant mass distribution to extract $\alpha(m_{\mu\mu})$. For the **signal**, the same signal forms as for the $dN/d\Delta\phi$ method were used (more details can be found in 5.2.2):

- extended Crystal-ball (B.2.1) with the tails fitted to the results obtained in proton-proton collisions
- extended Crystal-ball (B.2.1) with the tails fitted to the embedding of pure MC J/ψ in real MB triggered events

- NA60 function (B.2.1) with the tail fitted to the embedding of pure MC J/ψ in real MB triggered events

For the **dimuon invariant mass background** the following forms were used:

- quadratic variable width Gaussian (B.2.1)
- polynomial ratio (2nd order polynomial divided by a 3rd order polynomial)
- Chebyshev polynomials of order 6

The **background flow** $v_2^B(M_{\mu\mu})$ was described by the following ad-hoc functions:

- polynomial of order 2
- polynomial of order 2 multiplied by an exponential function,
- Chebyshev polynomials of order 4

For each combination of signal, invariant mass background, and v_2 background, three invariant mass fit ranges were used, [2.2–4.4], [2.3–4.6], and [2.4–4.7] (GeV/c). In total (3 backgrounds x 3 signals x 3 v_2 backgrounds x 3 ranges =)81 tests were used. Again, the result of each fit test was validated by requiring good fit and covariance-matrix status.

The final v_2 values and their statistical uncertainties were obtained as the average of all successful tests for a given p_T and centrality bin. An example is shown on Fig. 5.11 and details on the signal-extraction systematic uncertainty can be found in Sec. 5.3. The same method is also used to extract the average transverse momentum $\langle p_T \rangle_{uncorr}$ and rapidity $\langle y \rangle_{uncorr}$ of reconstructed J/ψ , uncorrected for detector acceptance and efficiency.

The J/ψ v_2 results obtained with the mean v_2 method are presented in Fig. 5.12 and Fig. 5.13. Similar observations can be made from the mean v_2 results as from the $dN/d\Delta\phi$ method. The values are summarised in Tab. 5.4 and Tab. 5.5.

p_T bin (GeV/c)	[0–2]	[2–4]	[4–6]	[6–8]	[8–12]
v_2^{corr} 5–20 %	0.0122	0.0295	0.342	0.0289	0.0161
Stat. error 5–20 %	0.0110	0.0104	0.0154	0.0240	0.0359
Syst. error 5–20 %	0.0040	0.0017	0.0022	0.005	0.0085
v_2^{corr} 20–40 %	0.0265	0.0915	0.1026	0.0991	0.0595
Stat. error 20–40 %	0.0183	0.0153	0.0201	0.0297	0.0456
Syst. error 20–40 %	0.00748	0.00684	0.00802	0.00652	0.00687
v_2^{corr} 40–60 %	0.0115	0.0214	0.0325	0.0011	0.0427
Stat. error 40–60 %	0.0156	0.0139	0.0190	0.0292	0.0425
Syst. error 40–60 %	0.0018	0.0012	0.0038	0.0112	0.0048

Table 5.4 – (Table of data points shown in Fig. 5.12) J/ψ v_2 (*corrected* values) in centrality classes 5–20 %, 20–40 %, and 40–60 %, in the rapidity range $2.5 < y < 4$ from the mean v_2 method with the V0A as event plane detector

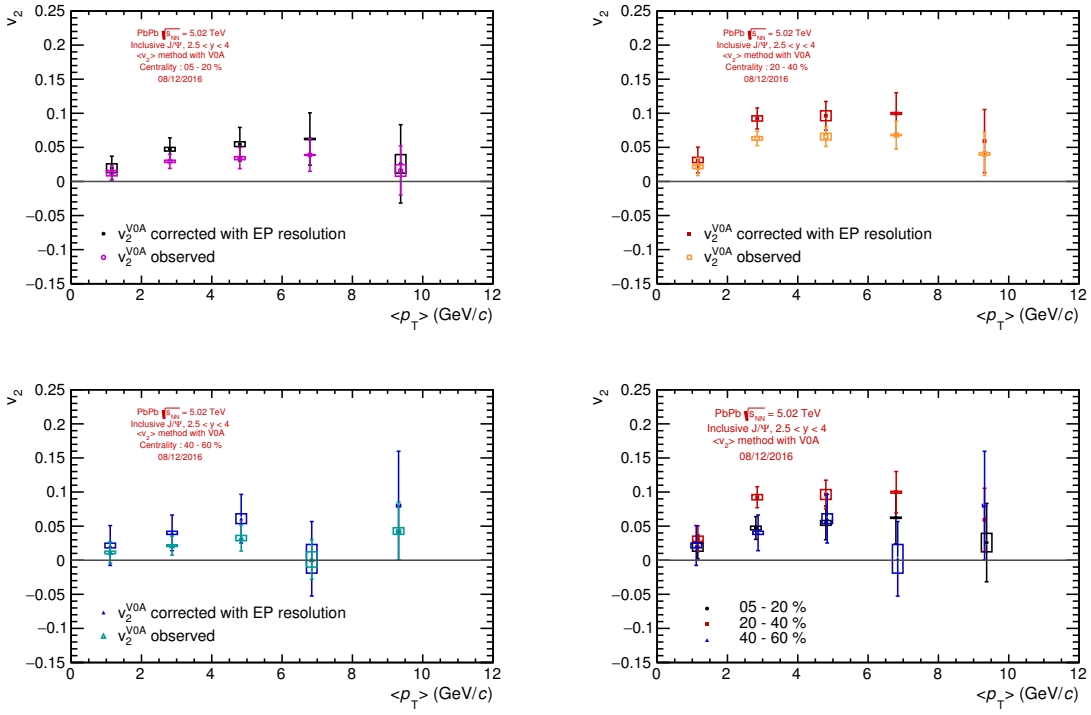

Figure 5.12 – Inclusive J/ψ v_2 as a function of p_T in the rapidity range $2.5 < y < 4$ in 3 centrality classes using the mean v_2 method and the V0A as event plane detector. Boxes represent the systematic uncertainty from the signal extraction.

p_T bin (GeV/c)	[0–2]	[2–4]	[4–6]	[6–8]	[8–12]
v_2^{corr} 5–20 %	0.0136	0.0493	0.0577	0.0406	0.0265
Stat. error 5–20 %	0.0110	0.0104	0.0157	0.0243	0.0342
Syst. error 5–20 %	0.0055	0.0013	0.0039	0.003	0.0018
v_2^{corr} 20-40%	0.0299	0.0732	0.1147	0.1153	0.0973
Stat. error 20–40 %	0.0134	0.0117	0.0151	0.0230	0.0340
Syst. error 20–40 %	0.00732	0.00753	0.00698	0.00862	0.00704
v_2^{corr} 40–60 %	-0.0005	0.0540	0.0640	0.0688	0.0455
Stat. error 40–60 %	0.0154	0.0143	0.0189	0.0284	0.0419
Syst. error 40–60 %	0.0016	0.0023	0.0017	0.0014	0.0018

Table 5.5 – (Table of data points shown in Fig. 5.13) J/ψ v_2 (*corrected* values) in centrality classes 5–20 %, 20–40 %, and 40–60 %, in the rapidity range $2.5 < y < 4$ from the mean v_2 method with the SPD as event plane detector

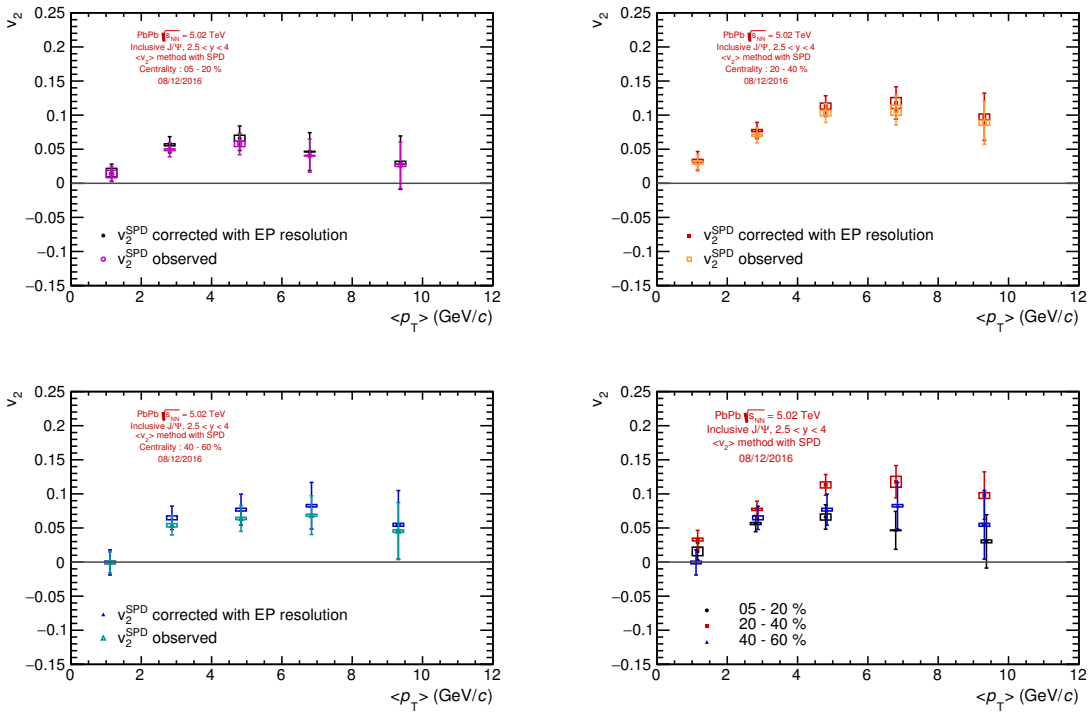

Figure 5.13 – Inclusive J/ψ v_2 as a function of p_{T} in the rapidity range $2.5 < y < 4$ in 3 centrality classes using the mean v_2 method and the SPD as event plane detector. Boxes represent the systematic uncertainty from the signal extraction.

5.2.4 Acceptance and efficiency corrections

Measurements are affected by various effects due to **detector limitations** (finite geometrical acceptance, detection efficiency) and the **efficiency of the reconstruction algorithm**. The various cuts and selections on single-muon and pair tracks can also affect the results. Raw numbers must therefore be corrected not to depend on the experimental setup and conditions. The purpose of this correction is to get the actual number of produced particles from the measured one. It is performed by calculating a single factor, known as the **Acceptance*Efficiency** (Aε) correction. However, in the case of correlation measurements, such as the elliptic flow, the absolute efficiency should not affect the measurement as long as it does not vary within the probed region. The Aε term is detector-related, and since the Event Plane angle is randomly distributed for each collision, the detector response should be averaged over the dimuon azimuthal distribution with respect to the Event Plane. For consistency, the impact on the J/ψ v_2 measurement was investigated. The correction is also required for p_{T}-integrated results.
The Aε is calculated through MC simulations to reproduce detector conditions and performances during the data taking. For a given process, it is computed as the ratio of reconstructed over generated particles:

$$A\varepsilon(p_{\mathrm{T}}, y) = \frac{N_{\mathrm{rec}}(p_{\mathrm{T}}, y)}{N_{\mathrm{gen}}(p_{\mathrm{T}}, y)} \tag{5.21}$$

MC simulations are performed following a three-step procedure:

- Primary particles are generated and decayed using parametrised (p_{T},y) distributions for generated input functions. Generation functions are estimated through a data-driven method which is based on the replication of the real (p_{T},y) distributions.
- Particle propagation is simulated through the detectors. The simulation is performed through transport models (GEANT3 [BBC+94], GEANT4 [A+03c]) where the geometry and material properties of the apparatus are implemented. Particle hits in the active parts of the detectors are created and the trigger response is recorded. To take into account variations of the detector status, MC simulations are performed on a run-by-run basis. In the case of Pb–Pb collisions, the detector response to a signal is embedded into raw data from a real event. This embedding technique aims to reproduce the occupancy of the detector and the corresponding efficiency losses for different event centralities.
- Particle tracks are reconstructed from generated hits in the detectors using the same reconstruction procedure as for real data.

The accuracy of the Aε correction is estimated through the associated systematic errors from the input generation functions, the tracking efficiency, the trigger efficiency, and the matching efficiency between the tracker and the trigger. More details on the procedure, associated systematic uncertainty determination, and simulations codes can be found at [A+16d].

The Aε correction was applied in this thesis for analyses integrated over the full p_{T} range, $0 < p_{\mathrm{T}} < 12$ GeV/c, and for rapidity-differential studies. The effect of the Aε correction was also investigated for the p_{T}-differential analysis integrated in rapidity, and it shows a negligible impact. The comparison is presented on Fig. 5.14. It is important to note that the Aε correction affects the v_2 value but also the p_{T} distribution of the dimuon pairs. For a deeper comparison, the results should therefore be plotted as a function of the $\langle p_{\mathrm{T}} \rangle$ of

the corresponding bins. However, the v_2 values with or without the Aε are very close and the comparison only serves here as a cross check.

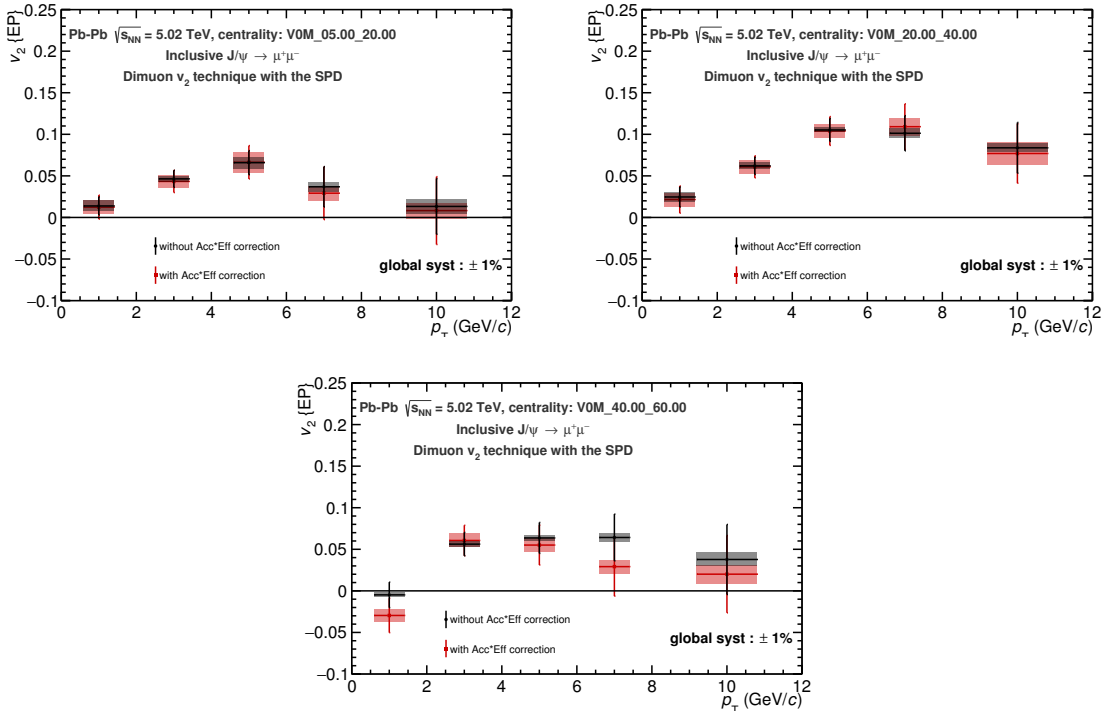

Figure 5.14 – Effect of the Aε correction on results obtained with the mean v_2 method using the SPD as EP detector for different centrality ranges (from left to right: 5–20 %, 20–40 %, and 40–60 %). Boxes for systematic uncertainty contain signal extraction only.

5.3 Systematic uncertainties

Different sources of systematic uncertainties on the measurement were investigated and are summarised in Tab. 5.6. Other systematics uncertainties affecting the measurement

Source	Value	Type
Signal extraction	0.003–0.008	correlated with p_{T}, y and centrality
Reconstruction efficiency	0.006	absolute, uncorrelated
Flow equalisation	1 %	global
EP resolution	1 %	uncorrelated

Table 5.6 – Summary of systematic uncertainties for the methods based on the event plane estimation

independently of the relative dimuon angles should a priori not impact the measured anisotropy. To check for any additional biases an event mixing method was implemented (see Sec. 5.3.5).

5.3.1 Signal extraction

Various combinations of signal and background forms over several fit ranges were studied (see example on Fig. 5.7). For each method, the systematic uncertainty due to the signal extraction was calculated as the RMS of all the successful tests. Full test results can be found in the Appendix in Fig. B.3 for the $d\mathrm{N}/d\Delta\varphi$ method and in Fig. B.5 and Fig. B.4 for the mean v_2 method.

5.3.2 J/ψ reconstruction

The non-uniform detector occupancy created by the particle anisotropy could bias the measurement since the detector efficiency varies with the detector occupancy. Large efficiency differences due to different occupancy levels in the spectrometer could induce an additional spurious variation of detected particles. This particle distribution would be correlated to the real event anisotropy and thus undistinguishable in the data analysis. Therefore the effect must be properly estimated and corrected for if necessary in the analysis. The effect on the reconstruction efficiency was studied through embedded MC simulations. J/ψ decays were simulated with an azimuthally isotropic distribution and embedded into real events with preserved characteristics, including event plane orientation and track density distribution in the detector. Since the simulated J/ψ distribution is isotropic and uncorrelated from the real event plane, the reconstructed v_2 should be null. Any deviation would indicate a residual v_2 arising from the non-uniform detector occupancy.
The analysis was performed using embedding productions [3] in the same p_{T} and centrality classes as the real data analysis. The same event reconstruction and signal extraction steps were performed using the mean v_2 method. Most values are compatible with zero but few intervals show J/ψ v_2 deviations by more than 1σ. The largest deviation is obtained in the 20–40 % centrality class and is illustrated on Fig. 5.15, measured either using the V0A(left) or SPD(right) as EP detector. The most significant deviation measured with the

[3] LHC16$e2$ and LHC16e2$_{\mathrm{plus}}$ samples

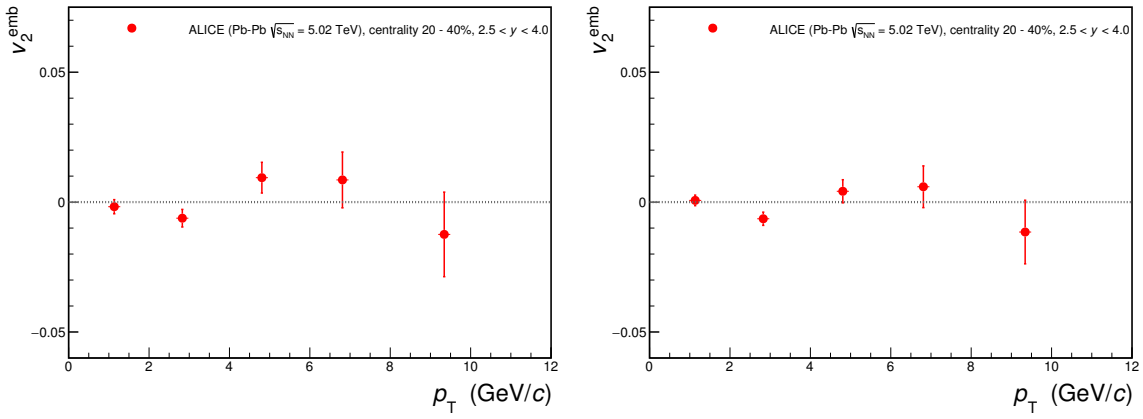

Figure 5.15 – J/ψ v_2 as a function of p_T measured in embedded MC events in the 20–40 % centrality range using the V0A (Left) or the SPD (Right) as EP detector

SPD is $v_2 = -0.0058 \pm 0.0023$(stat.) and was obtained in the range $2 < p_T < 4$ GeV/c. The largest one observed using the V0A as EP detector is $v_2 = 0.0064 \pm 0.0040$(stat.) in the range $4 < p_T < 6$ GeV/c. To be conservative, an absolute systematic uncertainty of 0.006 was assigned for all p_T and centrality ranges and considered as uncorrelated.

5.3.3 Flow vector equalisation

A first evaluation of the flattening quality can be performed by fitting the event plane angle distributions with a constant function. The result for each distribution at every calibration step is given on Fig. 5.2, Fig. 5.3, and Fig. B.1. Additional cross-checks were performed by controlling the (x,y) coordinates of the flow vectors:

- A self consistency check consists in comparing the abscissa product of the flow vector $\langle Q^a_{n,x} \times Q^b_{n,x} \rangle$ with the ordinate product $\langle Q^a_{n,y} \times Q^b_{n,y} \rangle$ for two detectors a and b. The averages of the products provide two independent measurements of the correlation between two detectors. Fig. 5.16 compares the product averages as a function of centrality. The difference between the two measurements is quite significant before any correction is applied and quite stable as a function of centrality. The first correction brings them closer (the differences are always below 5 %) but the effect of the next correction steps is negligible.

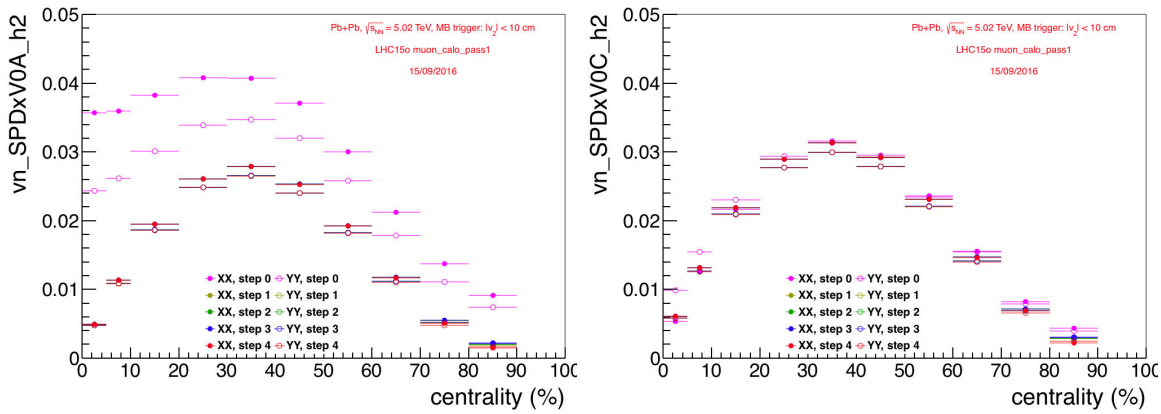

Figure 5.16 – (Left) $\langle Q^{SPD}_{2,x} Q^{V0A}_{2,x} \rangle$ and $\langle Q^{SPD}_{2,y} Q^{V0A}_{2,y} \rangle$ as a function of centrality after each calibration pass. (Right) $\langle Q^{SPD}_{2,x} Q^{V0C}_{2,x} \rangle$ and $\langle Q^{SPD}_{2,y} Q^{V0C}_{2,y} \rangle$ as a function of centrality after each calibration pass.

- The cross-terms of the flow vector coordinates between two detectors $\langle Q^a_{n,x} \times Q^b_{n,y} \rangle$ and $\langle Q^a_{n,y} \times Q^b_{n,x} \rangle$ are expected to be zero. Deviations originate from non-flow contributions and provide an estimate of the systematic uncertainty on the event plane determination. Fig. 5.17 shows the cross-terms between the SPD and V0A or V0C.

Here again the most significant improvement comes from the first correction step. A gradual enhancement is observed up to the third step for the SPD/V0C cross-terms. Looking a the SPD/V0A cross-terms, the next step also enhances the quality of the flattening.

The largest value reached by the ratio does not exceed 1 %, therefore this value was assigned as a global systematic uncertainty on the v_2 analysis from the EP determination.

5.3.4 Event plane resolution

As part of the J/ψ v_2 analysis through the dimuon electron channel, the event plane resolution for the V0A was also calculated using the V0C and TPC detectors instead of the V0C and SPD. The dataset (full reconstruction pass 1 (A)) is slightly different than the one in this analysis but allows the comparison of the detector resolutions. Fig. 5.19 shows the ratio of the V0A event plane resolution obtained with the SPD and V0C with respect to that obtained with the TPC and V0C as a function of centrality. For the centrality classes

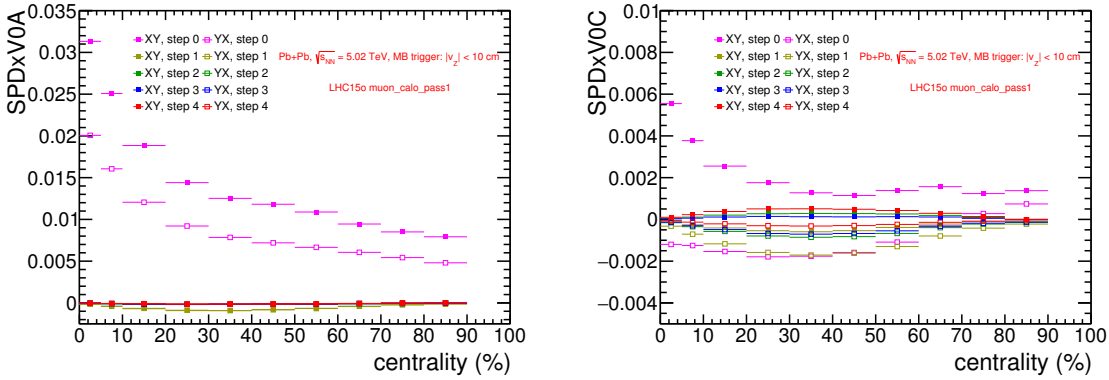

Figure 5.17 – (Left) $\langle Q_{2,x}^{SPD} Q_{2,y}^{V0A} \rangle$ and $\langle Q_{2,y}^{SPD} Q_{2,x}^{V0A} \rangle$ as a function of centrality after each calibration pass. (Right)$\langle Q_{2,x}^{SPD} Q_{2,y}^{V0C} \rangle$ and $\langle Q_{2,y}^{SPD} Q_{2,x}^{V0C} \rangle$ as a function of centrality after each calibration pass.

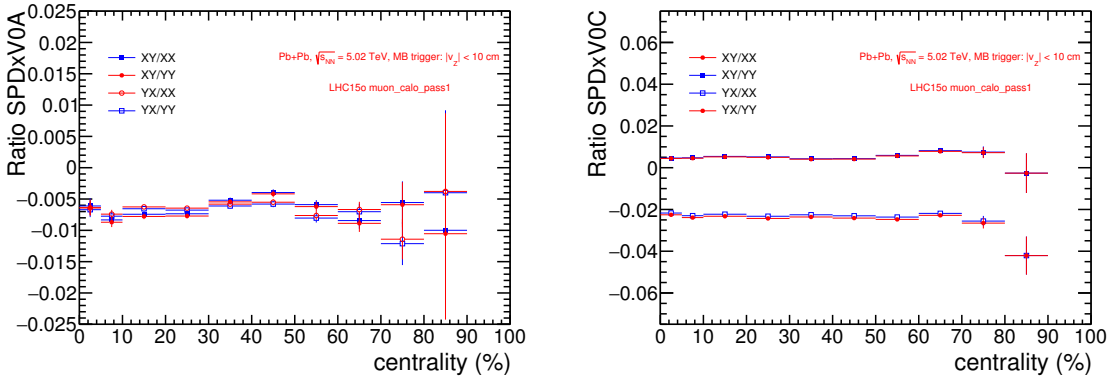

Figure 5.18 – (Left) Ratio of $\langle Q_{2,x}^{SPD} Q_{2,y}^{V0A} \rangle$ and $\langle Q_{2,y}^{SPD} Q_{2,x}^{V0A} \rangle$ by $\langle Q_{2,x}^{SPD} Q_{2,x}^{V0A} \rangle$ and $\langle Q_{2,y}^{SPD} Q_{2,y}^{V0A} \rangle$,(Right) Ratio of $\langle Q_{2,x}^{SPD} Q_{2,y}^{V0C} \rangle$ and $\langle Q_{2,y}^{SPD} Q_{2,x}^{V0C} \rangle$ by $\langle Q_{2,x}^{SPD} Q_{2,x}^{V0C} \rangle$ and $\langle Q_{2,y}^{SPD} Q_{2,y}^{V0C} \rangle$ as a function of centrality

below 70 % the ratio does not deviate from 1 by more than 1 %. It was assumed that this variation should be similar for the SPD event plane resolution. Therefore a 1 % systematic uncertainty was assigned to the v_2 analysis from the event plane reconstruction.

5.3.5 Event plane mixing

To check the presence of any effects that would induce a preferred direction, arising either from the detectors or the analysis, the analysis was performed by mixing dimuon pairs from one event with event plane angles from other events. The J/ψ signal was extracted from real data but to each event was assigned another event plane angle, from a different event with similar characteristics. For this purpose, event pools were created containing 100 events within the same centrality class (10 %-wide). Then for each event, the event plane of another event from its pool is used to compute the J/ψ relative angle. Therefore the correlation between the dimuon pair and the event plane angles is suppressed and no anisotropy should be measured.

Fig. 5.20 shows the comparison of the J/ψ v_2 coefficients obtained by mixing event planes with respect to the unbiased sample in the 20–40 % centrality class. The J/ψ v_2 values from the event plane mixing are negligible. Other sources of systematic uncertainties

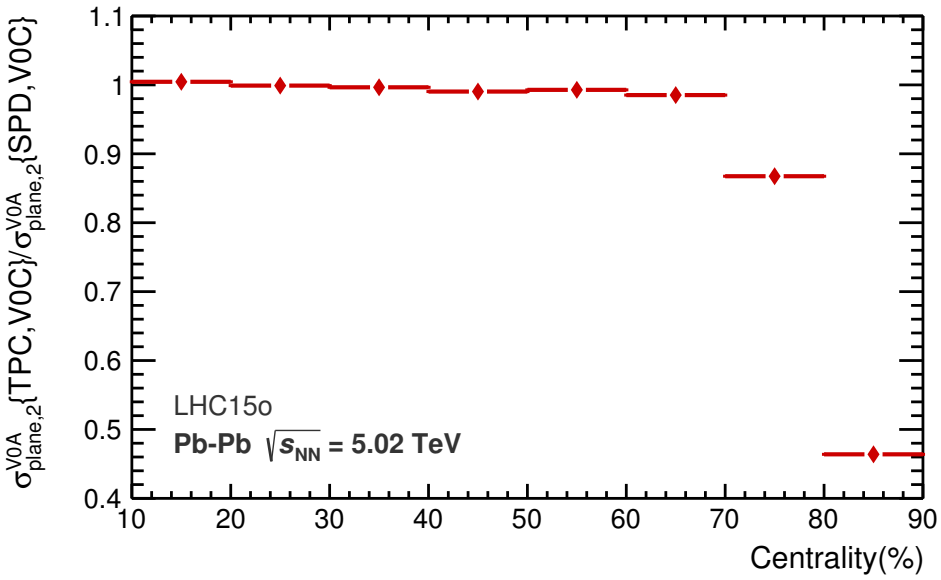

Figure 5.19 – Ratio of the V0A-EP resolution obtained with the SPD and V0C with respect to that obtained with the TPC and V0C as a function of centrality

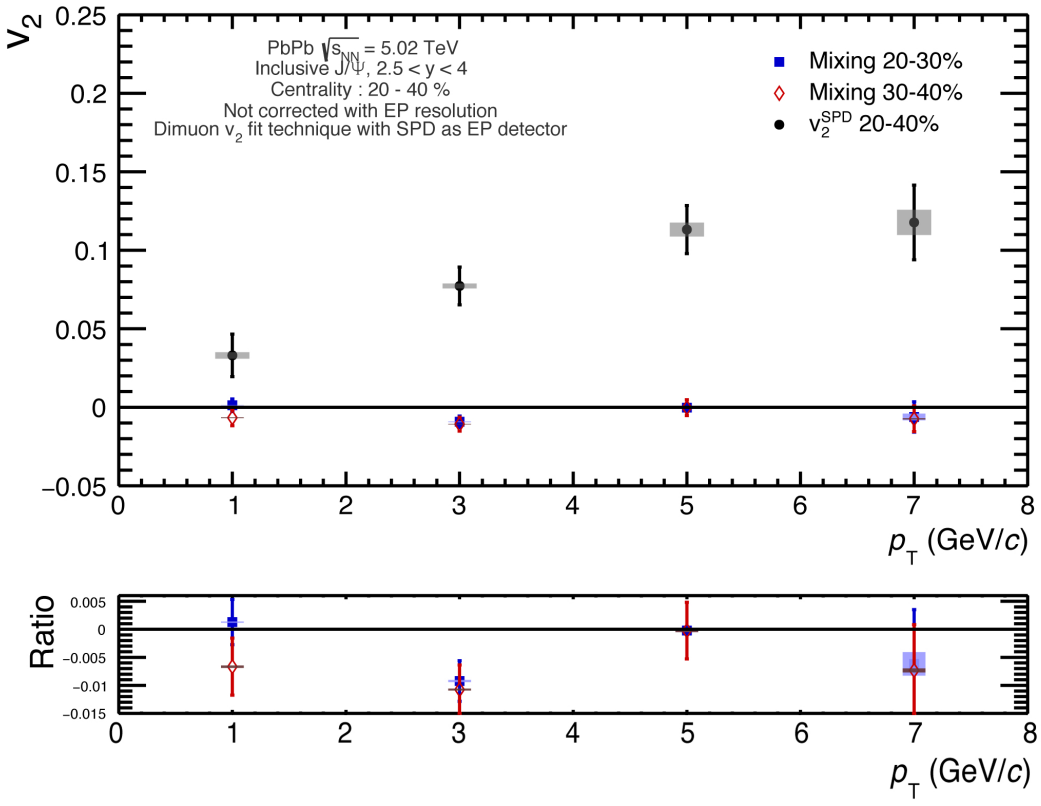

Figure 5.20 – (Top) J/ψ v_2 (*observed* values) from event mixing technique as a function of p_T for the 20–40 % centrality class using the mean v_2 method and the SPD as EP detector, (Bottom) ratio of v_2 results from mixing to real data. Boxes contain systematic uncertainty from signal extraction

on the measurement can therefore be neglected.

5.4 Results

This section describes the analysis results and the influence of several parameters. A discussion on the physical interpretations is proposed in the next chapter.

5.4.1 Method comparison for v_2 extraction

The J/ψ v_2 results obtained with the $dN/d\Delta\phi$ method or the mean v_2 were compared for each centrality class. The comparison is presented on Fig. 5.21. Measurements from both event plane detectors are presented and discussed. Both v_2 extraction methods give

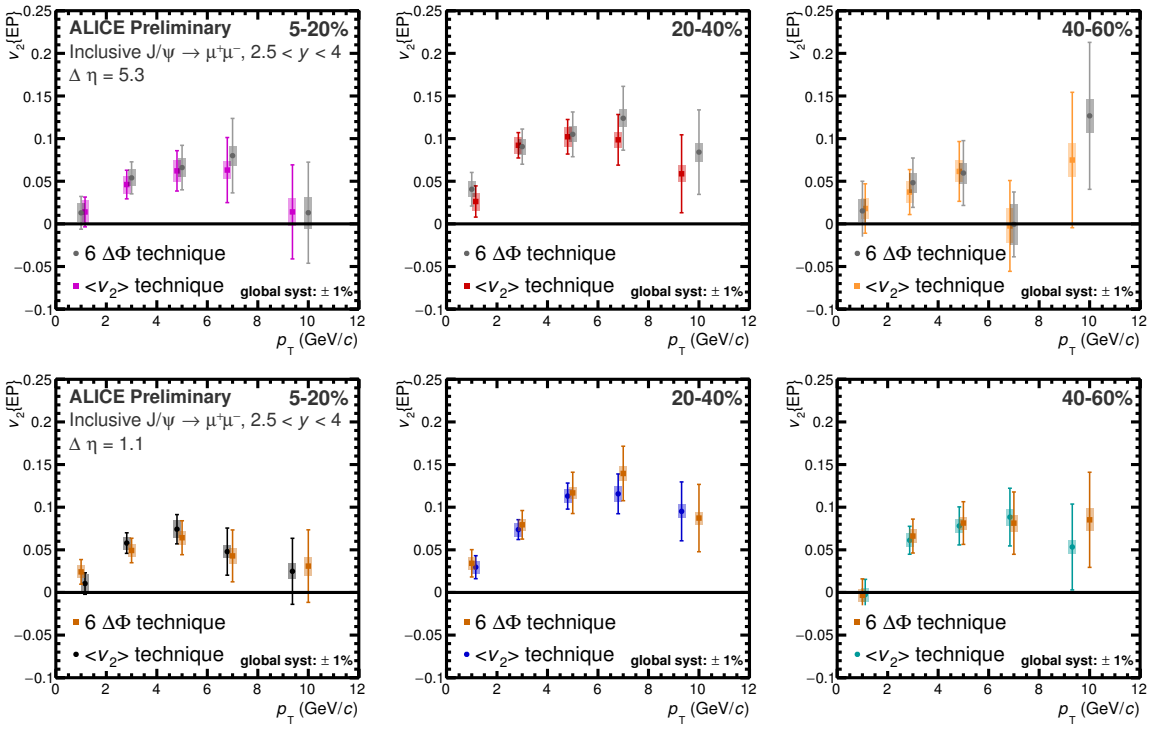

Figure 5.21 – Method comparison for J/ψ v_2 extraction for all centrality class (5–20 %, 20–40 % and 40–60 %) and each event plane detector (top: V0A, bottom: SPD). The point abscissas are slightly shifted to improve legibility

compatible values. The statistical and systematic uncertainties are very similar. The mean v_2 method was selected for the final results.

5.4.2 Impact of the detector η gap on the measurement

Two detectors were available to measure the event plane for the analysis: the V0A and the SPD. The comparison of the J/ψ v_2 coefficients obtained with each detector is presented for each centrality class on Fig. 5.22 using the mean v_2 method. All p_T and centrality ranges show very similar measurements. The largest difference is observed in the 40–60 % centrality class for the $6 < p_T < 8\,\text{GeV}/c$ interval but the difference is not statistically significant. Therefore the analyses performed either with the V0A or the SPD are compatible. Since the SPD detector has a better resolution than the V0A for the EP determination, it was used for the final results in the publication. To avoid auto-correlations the relative pseudo-rapidity gap between the detector used as event plane and the Muon Spectrometer should be as

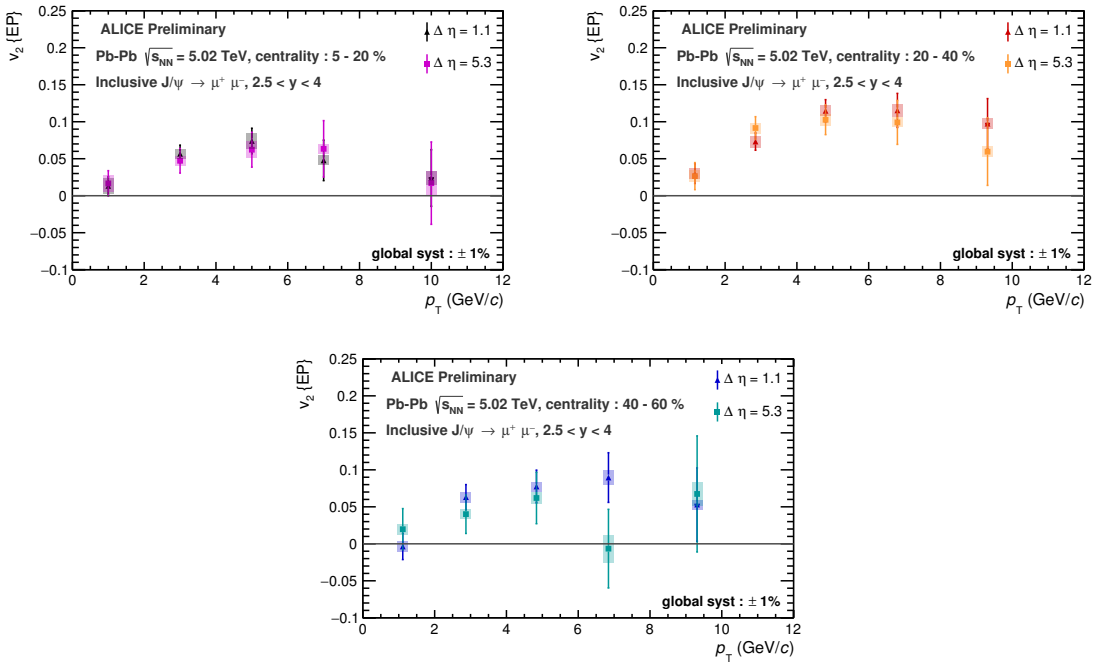

Figure 5.22 – Comparison of the results obtained with the mean v_2 method (from left to right: in the centrality classes 5–20 %, 20–40 % and 40–60 %) using the V0A ($\Delta\eta = 5.3$) and the SPD ($\Delta\eta = 1.1$) as event plane detector and the mean v_2 method. Boxes for systematic uncertainty contain signal extraction only.

large as possible. In the case of the V0A, the detector is spaced by 5.3 units of pseudo-rapidity from the spectrometer. However, the η gap between the SPD and the spectrometer falls to 1.1 pseudo-rapidity units. The v_2 values obtained with the two event plane detectors differ slightly and non-flow effects were therefore investigated. The analysis was performed using this time the V0C as event plane detector. The pseudo-rapidity overlap between the V0C ($-3.7 < \eta < -1.7$) and the Muon Spectrometer ($-4. < \eta < -2.5$) being of 1.2 units of pseudo-rapidity, there is no doubt that some tracks are used both for the event plane determination and for the J/ψ reconstruction. The comparison of the v_2 measurement with the three event plane detectors is given on Fig. 5.23 using the $dN/d\Delta\phi$ method for centrality bin 20–40 %. The V0C resolution was estimated at $\sigma^{\mathrm{V0C}} = 0.76843 \pm 0.00011$ for this centrality bin using the 3 sub-event method as described in Sec. 5.1.3. The v_2 values given by the three detectors are relatively close and the size of the systematic uncertainties does not allow to draw clear conclusions. For this analysis the SPD can therefore be used safely without fearing non-flow effects from the smaller pseudo-rapidity gap.

5.4.3 Centrality dependence of the J/ψ v_2

The comparison of the results obtained in the different centrality classes is illustrated on Fig.5.24 as a function of the transverse momentum using the SPD as event plane detector. All classes show a similar evolution of the v_2 coefficient versus p_T.

Integrating the v_2 results over the full p_T range allows for a centrality comparison. The p_T-integrated results are presented on Fig. 5.25 as a function of centrality. The values are corrected with the Aε. The highest anisotropy is reached for semi-central collisions. More central (5–20 %) collisions give a similar amplitude.

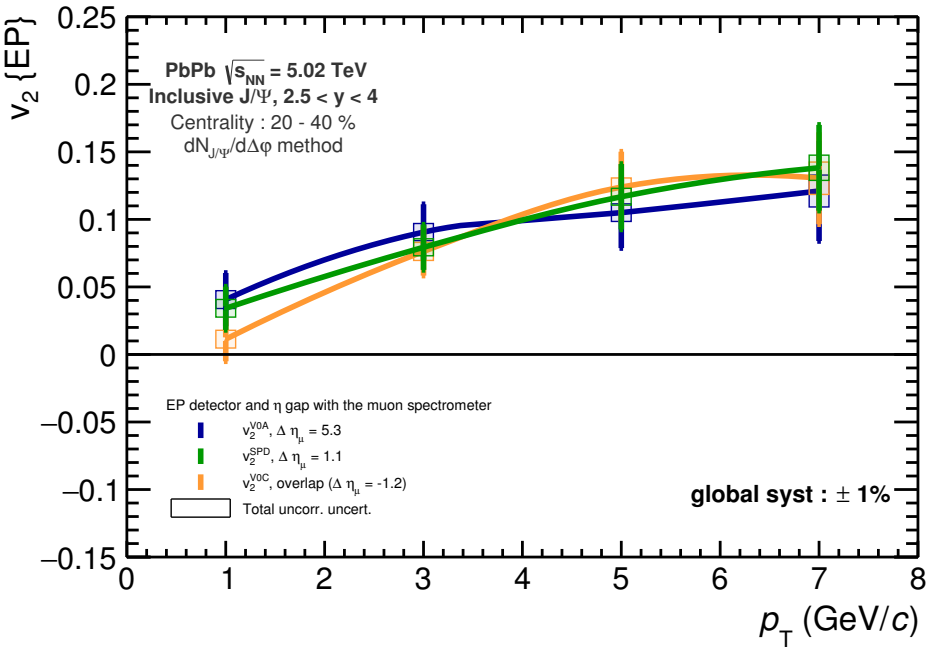

Figure 5.23 – Comparison of the results obtained for the $dN/d\Delta\varphi$ method in the centrality 20-40% using the V0A, the SPD or the V0C as event plane detector. Boxes for systematic uncertainty contain signal extraction and J/ψ reconstruction.

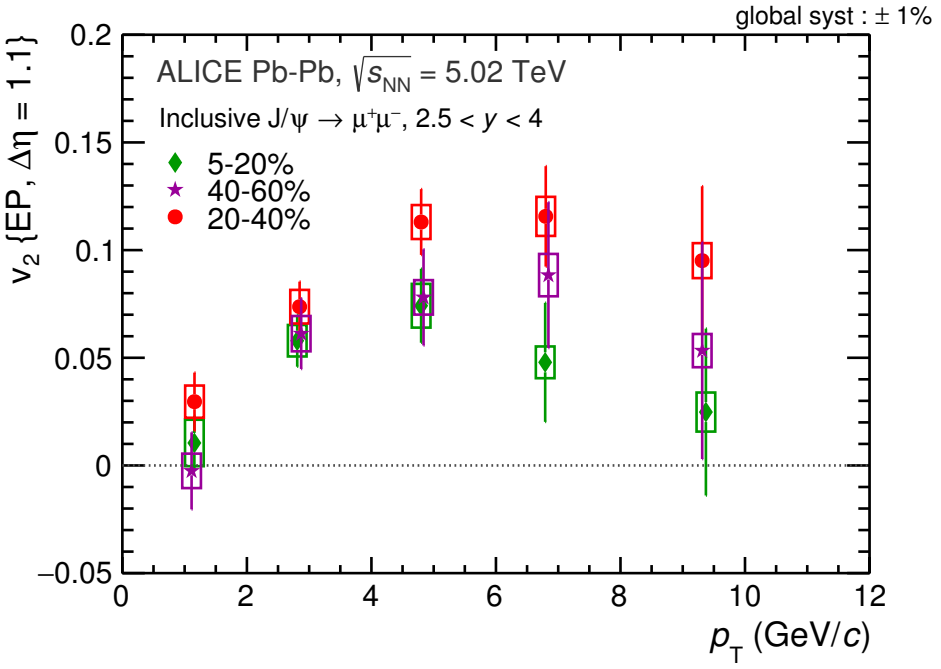

Figure 5.24 – J/ψ v_2 as a function of p_T for all centrality classes

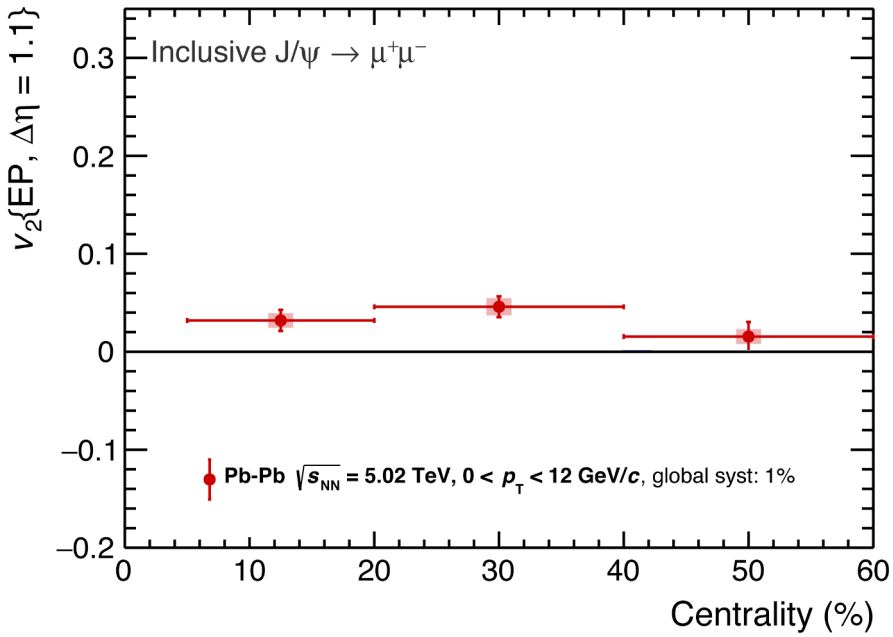

Figure 5.25 – J/ψ v_2 as a function of centrality integrated in p_T and corrected for Aε effects

5.4.4 Rapidity dependence of the J/ψ v_2

The charged-hadron elliptic flow decreases slightly with the rapidity. The J/ψ R_{AA} at forward rapidity seems also to increase at low rapidity ($2.5 < y < 3.25$) which could indicate that more recombination occurs in this rapidity region, although all the measurements are compatible within uncertainties. To investigate any rapidity dependence of the J/ψ v_2 the analysis was also performed by dividing the sample into two rapidity regions: $2.5 < y < 3.25$ and $3.25 < y < 4$. The results were computed in the same centrality bins (5–20 %, 20–40 % and 40–60 %) as a function of p_T (see Fig.5.26) and integrated in p_T (see Fig. 5.27). The data are corrected for Aε effects. The difference is not significant between the two bins as a function of p_T. The p_T-integrated v_2 as a function of the centrality also does not show significant differences between the two rapidity bins. The values are higher for the most forward region but data are compatible within uncertainty (only systematic uncertainties from the signal extraction are represented on the figures). The limited statistics do not allow to draw clear conclusions on a possible rapidity dependence of the J/ψ elliptic flow.

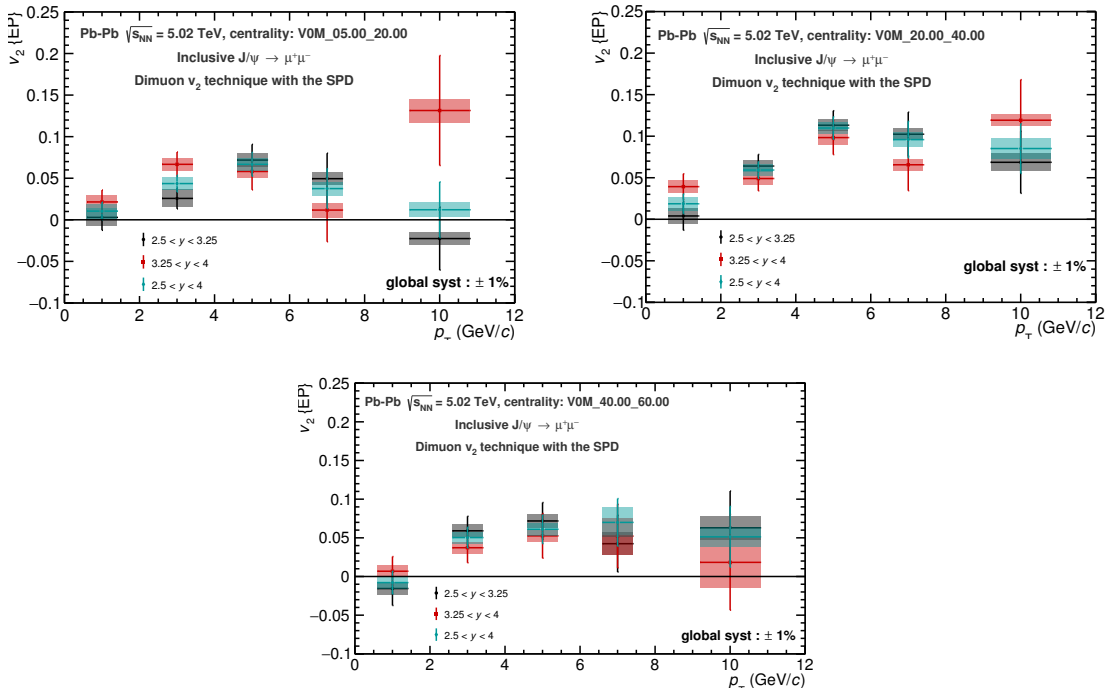

Figure 5.26 – J/ψ v_2 as a function of p_T in two rapidity bins for the centrality classes (left to right) 5–20 %, 20–40 % and 40–60 % using the dimuon v_2 fit technique and the SPD as event plane detector. Boxes for systematic uncertainty contain signal extraction only

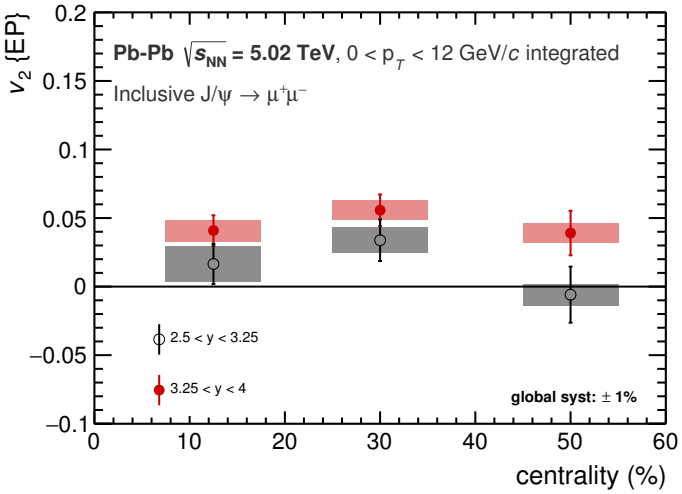

Figure 5.27 – J/ψ v_2 as a function of centrality in two rapidity bins using the dimuon v2 fit technique and the SPD as event plane detector. Boxes for systematic uncertainty contain signal extraction only

5.5 Flow method comparison

5.5.1 Description of the scalar product method

The Scalar Product (SP) method is a more sophisticated variation of the event plane method [VPS10, LO13]. The main criticism addressed to the event plane method is the imprecision on the the measured v_2 value, as it lies between the mean value of the coefficient averaged over all events $\langle v_2 \rangle$ and the square root of the squared coefficient mean value $\sqrt{\langle v_2^2 \rangle}$. This effect was demonstrated to be more significant for higher flow coefficients. In contrast, the scalar product method is always measuring the $\sqrt{\langle v_2^2 \rangle}$ value and provides therefore less ambiguous results. The technique does not require the reconstruction of the event plane and is based on the correlation of two particles. The observed flow coefficients are estimated from the scalar product of the particle unit flow vectors $\mathbf{u_n} \equiv e^{in\phi}$ with the flow vectors $\mathbf{Q_n}$. The $\mathbf{Q_n}$ flow vectors are constructed following the same method as in the event plane case. The detector equalisation procedure is also applied. To remove most of the multiplicity dependence, reduced flow vector are used in the analysis by scaling it with square root of the detector multiplicity (M) of the event:

$$\mathbf{q_n} = \frac{\mathbf{Q_n}}{\sqrt{M}}. \tag{5.22}$$

The average of the scalar products is calculated over all events and all particles in a given (p_T,y) range:

$$v_n(p_T, y)^{obs} = \langle \mathbf{q_n} \mathbf{u^*_{n,i}} . \rangle \tag{5.23}$$

These coefficients are corrected for the flow resolution σ_{SP} to obtain the final values:

$$v_n = \frac{v_n^{obs}}{\sigma_{SP}}. \tag{5.24}$$

Resolution determination

The resolution is computed using a similar method to the three sub-event technique for the event plane resolution. For a sub-detector a, the flow resolution (σ^a_{SP}) for the n^{th} harmonic measured with the scalar product method can be computed as:

$$\sigma^a_{SP} = \sqrt{\frac{\langle \mathbf{q_n^a q_n^{b*}} \rangle \langle \mathbf{q_n^a q_n^{c*}} \rangle}{\langle \mathbf{q_n^b q_n^{c*}} \rangle}}. \tag{5.25}$$

The resolution is computed in 5 %–wide centrality class (see Fig. 5.28) and the average is taken in the wider centrality class of the analysis by weighting with the number of reconstructed J/ψ for each interval. The values for the SPD and V0A detectors are given in Tab. 5.7 for the 20–40 % centrality class.

Centrality	V0A	SPD
20–40 %	0.036	0.077

Table 5.7 – $N_{J/\psi}$ –weighted SP resolutions of SPD and V0A detectors for the 20–40 % centrality class

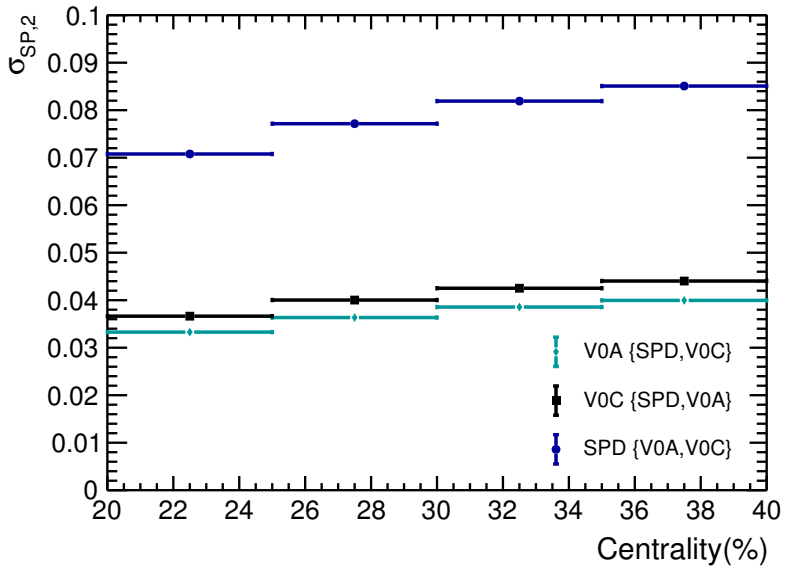

Figure 5.28 – Flow vector resolution of SPD, V0A,and V0C sub-detectors as a function of centrality in the 20–40 % class

5.5.2 Comparison to the event plane method

The v_2 results obtained with the scalar product and the event plane methods are compared for the 20–40 % centrality class on Fig. 5.29. All the values are compatible.

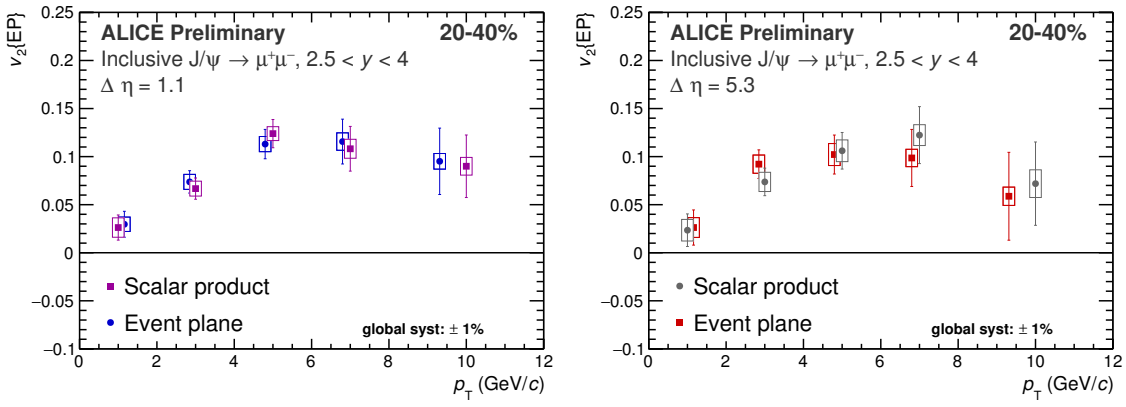

Figure 5.29 – Comparison of the $\langle v_2 \rangle$ results obtained with the event plane and the scalar product methods for semi-central collisions using (Left) the SPD or (Right) the V0A as EP/SP detector. Boxes for systematic uncertainty contain signal extraction and J/ψ reconstruction. Numerical values can be found in Tab. B.5 and Tab. B.6

The event plane and scalar product methods are differently affected by non-flow effects and flow fluctuations. Details on each method sensitivity are summarised in [VPS10]. More refined methods can be found in the literature [OPV09]. In the J/ψ v_2 analysis, the measurement uncertainty is dominated by the signal extraction. This study is therefore not yet sensitive enough to the differences of flow methods.

5.6 Angular dependence of the nuclear modification factor

The elliptic shape of the fireball can be used to study effects of the medium on the J/ψ production as a function of the path length. Particles traverse a **different path length** depending on their **azimuthal emission angle** and the longer their path length, the more they should experience effects of the medium. Dividing the system into regions with different path lengths allows to further investigate interactions of J/ψ particles with the system. Therefore a complementary measurement of flow analysis consists of studying the production ratio between the two directions.

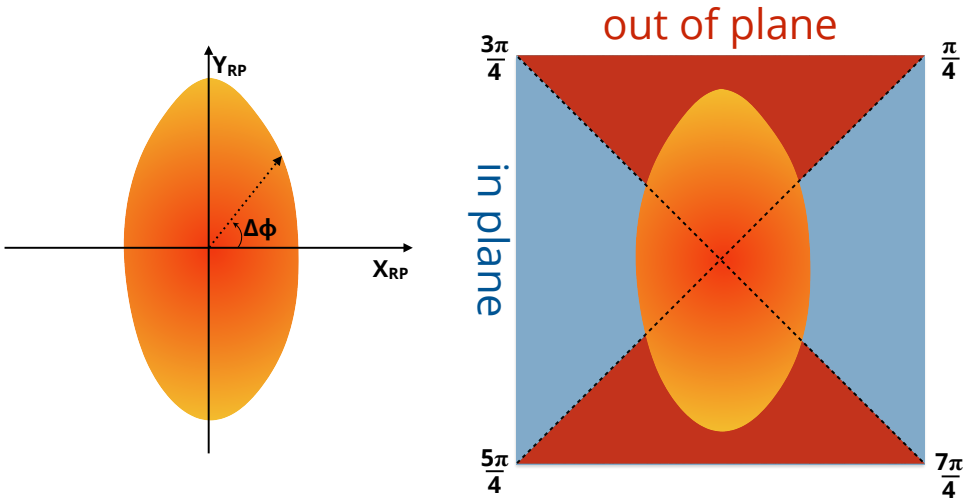

Figure 5.30 – Illustration of the in- and out-of-plane regions around the collision

The analysis principle is similar to the $dN/d\Delta\phi$ method. The transverse plane of the collision is divided in 2 complementary regions as illustrated on Fig. 5.30. For each region, a nuclear modification factor was computed and compared.

5.6.1 Data sample and selections

The same Pb–Pb data sample from LHC15o was analysed as for the J/ψ v_2 analysis, the event and track cuts are identical (see Sec. 5.2.1). The selections are also shared by the published R_{AA} analysis [A+16f] except for the additional cut on the position of the reconstructed collision vertex along the beam axis: $|z_{vertex}| < 10$cm.
The analysis was performed in three centrality classes: 5–20 %, 20–40 %, and 40–60 %. To ease the comparison with the published R_{AA} results, similar p_T bins were adopted (0–1, 1–2, 2–3, 3–4, 4–5, 5–6, 6–7, 7–8 and 8–12 GeV/c). An additional binning was added from the emission region of the dimuon pair. Two complementary space regions are defined, whether the relative emission angle of the dimuon pair with respect to the event plane angle ($\Delta\phi$) is in-plane ($\Delta\phi \in \left[-\frac{\pi}{4}, \frac{\pi}{4}\right] \cup \left[\frac{3\pi}{4}, \frac{5\pi}{4}\right]$) or out-of-plane ($|\Delta\phi| \in \left[\frac{\pi}{4}, \frac{3\pi}{4}\right]$). The full data sample is referred to as *integrated* and the derived $\Delta\phi$ regions are referred to as *in-plane* and *out-of-plane*. The azimuthal angle from the second harmonic event plane $\Psi_{EP,2}$ was used to estimate the reaction plane angle Ψ_{RP} using the SPD detector with the FlowVectorCorrections framework to calibrate and calculate the Q_n vectors (see Sec. 5.1).

5.6.2 R_{AA} measurement

The nuclear modification factor for each $\Delta\phi$ region was obtained from the measured J/ψ yields following the same analysis steps as the previous J/ψ R_{AA} publications [A+16d, A+17d]. The general expression for the R_{AA} is the following:

$$R_{AA}^{i,\Delta\phi}(\Delta p_T, \Delta y) = \frac{N_{J/\psi}^{i,\Delta\phi}(\Delta\phi, \Delta p_T, \Delta y)}{BR \cdot A\varepsilon^i(\Delta p_T, \Delta y) \cdot N_{MB}^i \cdot \langle T_{AA}^i \rangle \cdot \sigma_{J/\psi}^{pp}(\Delta p_T, \Delta y)} \tag{5.26}$$

where

$N_{J/\psi}^i(\Delta\phi, \Delta p_T, \Delta y)$ is the extracted number of J/ψ in a given Δp_T and Δy bin for the centrality class i and the defined $\Delta\phi$ region

BR is the branching ratio of J/ψ into the dimuon decay channel BR = (5.96±0.03)% [eaPDGte]

$A\varepsilon^i$ is the acceptance×efficiency term

N_{MB}^i is the number of equivalent minimum bias collisions for the centrality class i

$\langle T_{AA}^i \rangle$ is the average of the nuclear overlap function in the centrality class i

$\sigma_{J/\psi}^{pp}(\Delta p_T, \Delta y)$ is the J/ψ cross section in pp collisions at the same energy

Additional details on the equation terms are given in the next paragraphs.

Signal extraction

The number of J/ψ is extracted by fitting the invariant mass distribution of opposite sign dimuons in each p_T bin and centrality class. The mass and width parameters of the fit functions are fixed for the $\Delta\phi$-differential samples to the integrated results. Several fits are tested, combining a function describing the signal form and a second function for the background description, in three invariant mass ranges. The functions are the same as for the elliptic flow analysis and are described in Sec. 5.2.2. For each fit function, the integrated distribution is fitted in each p_T and centrality class. The mass and width of the signal function are extracted to be fixed in the corresponding bins of the $\Delta\phi$-differential histograms. The final numbers of J/ψ and their statistical uncertainties were obtained as the average of all successful tests for a given p_T and centrality bin. The systematic uncertainty due to the signal extraction was calculated as the RMS of all the successful tests. The extracted numbers of J/ψ as a function of p_T is illustrated on Fig. 5.31 for the three centrality classes.

Acceptance × efficiency

The Acceptance × efficiency (Aε) term accounts for detector limitations (see Sec. 5.2.4). The values used in this analysis are taken from the previous J/ψ R_{AA} study [A+17d]. The effect of the z_{vertex} can be neglected since the Aε term does not depend significantly on the vertex position. Since this analysis introduces an additional selection from the $\Delta\phi$ binning, the shape of the measured yields as a function of p_T and rapidity in all centrality bins was compared to the integrated results. The comparison can be found in Appendix on Fig. B.14. The yield evolutions are very similar and the differences fall within the systematic uncertainties of the Aε term. Therefore the measurements do not depend on the $\Delta\phi$ angle of the dimuon pair. These observations are consistent with an isotropic distribution of the event plane angle of the collisions since the acceptance of the detector does not depend on $\Delta\phi$.

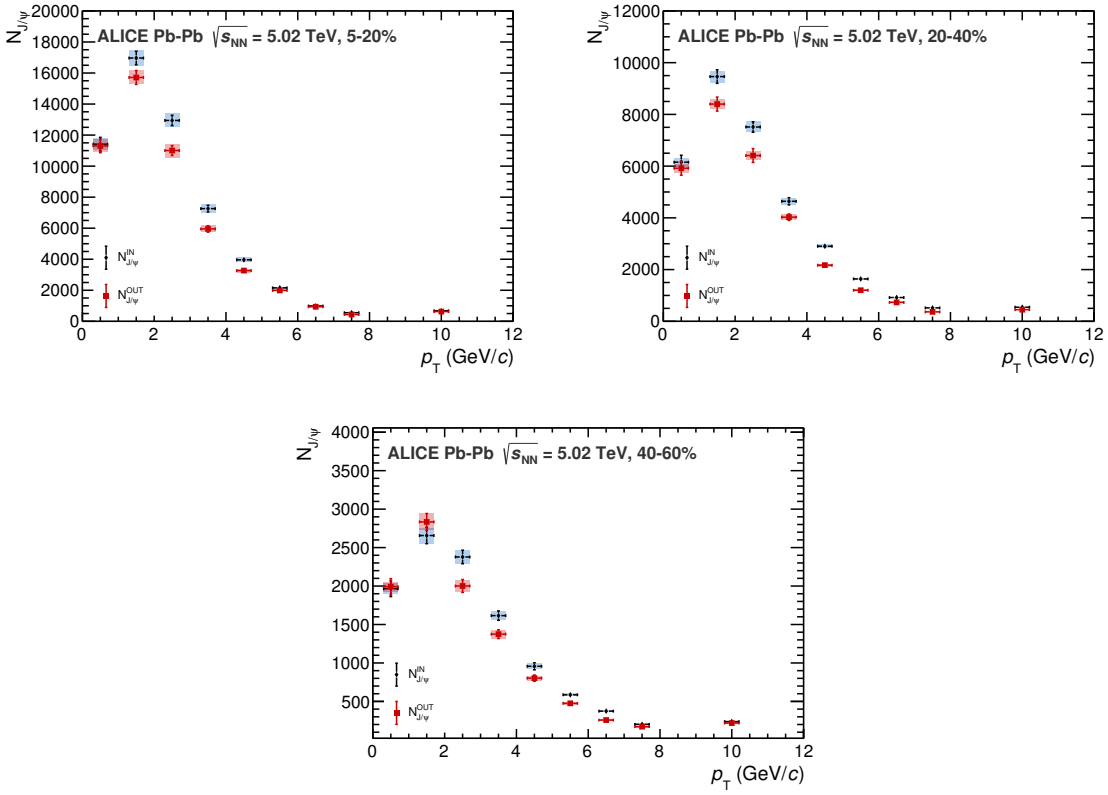

Figure 5.31 – In- and out-of-plane numbers of J/ψ as a function of p_T for each centrality class

Normalisation

Using the dimuon trigger introduces a bias in the data sample that is corrected for through the so-called *normalisation* procedure. The number of events in the R_{AA} equation (5.26) is obtained from the number of selected events. The number of equivalent minimum bias collisions (N^{eq}_{MB}) is computed from the number of triggered unlike-sign muon events (N_{CMUL}) multiplied by a normalisation factor by summing over all runs as:

$$N^{eq}_{MB} = \sum_{run=i} F^{i}_{norm} N^{i}_{CMUL}. \tag{5.27}$$

The normalisation factor was computed through several methods. The final F_{norm} value is computed as the weighted average of all methods and the differences are considered as a systematic uncertainty on the final result [AMGP17]. The value is taken from previous J/ψ R_{AA} analysis as both analysis selections only differ by the z_{vertex} cut and the latter influences the normalisation factor: $F_{NORM} = 11.84 \pm 0.06\%(stat.) \pm 0.5\%(sys.)$). Details can be found at [A+17d]. The number of CMUL events is computed with the event and pair selections corresponding to the present analysis in the [0–90 %] centrality class, and comes to $N_{CMUL} = 1.16 \times 10^8$ events.

Nuclear overlap function

The nuclear overlap function, denoted T_{AB}, represents the effective overlap area for which a nucleon from the nucleus A can interact with a given nucleon in a nucleus [d'E03, MRSS07]. It is computed as the integral:

$$T_{AB}(b) = \int d^2 s T_A(s) T_B(s-b). \tag{5.28}$$

Centrality (%)	$\langle N_{part} \rangle$	$\langle T_{AA} \rangle$
5–20 %	304.2	16.98 ± 0.56
20–40 %	159.6	6.754 ± 0.33
40–60 %	69.97	1.949 ± 0.081

Table 5.8 – Averages of the nuclear overlap function $\langle T_{AA} \rangle$ and number of participating nucleons $\langle N_{part} \rangle$ for the centrality classes of the analysis

The T_X function correspond to the thickness function of the nucleus X evaluated from the nuclear density ρ_X for an impact parameter b:

$$T_X(b) = \int dz \rho_X(b,z). \tag{5.29}$$

It is estimated through Monte-Carlo simulations based on the Glauber model [A+16c].

The nuclear overlap function of two nuclei A and B is related to the number of binary collisions N_{coll} through the inelastic nucleon-nucleon cross section (σ_{in}^{NN}) and the number of nucleons (A_X) for a given impact parameter b as $N_{coll}(b) = \sigma_{in}^{NN} A_A A_B T_{AB}(b)$. The values of the $\langle T_{AA} \rangle$ are given in Tab. 5.8 for the centrality ranges investigated in this analysis.

Resolution

Because of the finite resolution of the event plane detector, the extracted numbers of J/ψ values need to be corrected by a factor depending on the flow value for the considered bin. The number of particles in a given bin is related to the v_2 value as :

$$N(\Delta\varphi_{\mu\mu}) = N_0[1 + 2v_2 \cos(2\Delta\varphi_{\mu\mu})], \tag{5.30}$$

N_0 being the total number of particles in the $\Delta\phi$ integrated bin. The observed v_2 values are corrected by the detector resolution $\sigma_{plane,2}$ (see Sec. 5.1.3) as :

$$v_2^{corr} = \frac{v_2^{obs}}{\sigma_{plane,2}}. \tag{5.31}$$

The following relation between the observed and corrected number of particles can be extracted:

$$N^{corr}(\Delta\phi) = N^{obs}(\Delta\varphi_{\mu\mu}) \frac{1 + 2v_2^{obs}\cos(2\Delta\varphi_{\mu\mu})}{1 + 2v_2^{corr}\cos(2\Delta\varphi_{\mu\mu})} = N^{obs}(\Delta\varphi_{\mu\mu}) \frac{1 + 2\sigma_{plane,2}v_2^{corr}\cos(2\Delta\phi)}{1 + 2v_2^{corr}\cos(2\Delta\varphi_{\mu\mu})}. \tag{5.32}$$

The resolution factors for the in- and out-of-plane number of particles are computed as:

$$res = \frac{1 + 2v_2^{corr}\cos(2\Delta\phi)}{1 + 2v_2^{corr}\sigma_{plane,2}\cos(2\Delta\phi)} \tag{5.33}$$

Tab. 5.9 summarises the calculated resolution factor in- (taking $\Delta\phi = 0$) and out-of-plane (taking $\Delta\phi = \pi/2$) for each centrality and p_T ranges.

The sum of in- and out-of-plane yields should be constant before and after the resolution correction. The difference of the yield sums falls below 0.26 %.

p_T(GeV/c)	Resolution factor					
Centrality	5–20 %		20–40 %		40–60 %	
Region	IN	OUT	IN	OUT	IN	OUT
[0;2]	1.0025	0.9974	1.0051	0.9943	0.9993	1.0007
[2;4]	1.0134	0.9835	1.0117	0.9847	1.0120	0.9851
[4;6]	1.0167	0.9783	1.0168	0.9745	1.0149	0.98023
[6;8]	1.0113	0.9866	1.0172	0.9736	1.0166	0.9772
[8;12]	1.0061	0.9933	1.0145	0.9794	1.0105	0.9872

Table 5.9 – Resolution factor to the yields for each centrality range

Systematic uncertainties

This paragraph discusses the different sources of systematic uncertainties on the R_{AA} measurement. Some of them are common to the J/ψ v_2 analysis. Tab.5.10 summarises all sources of systematic uncertainties. The same value is considered for both plane regions as no variation is expected with $\Delta\phi$. Therefore these systematic uncertainties are considered as correlated when comparing in- and out-of-plane results.

- The **signal extraction** systematic uncertainty is estimated by using different signal and background functions to fit the dimuon distribution in different invariant-mass ranges (see Sec. 5.6.2)
- The **estimation of the centrality limits** can introduce a variation in the number of J/ψ for a given centrality class. The corresponding uncertainty is mostly significant for central collisions (reaching up to ~ 1 %) and negligible for peripheral collisions [AMGP17]
- The systematic uncertainties from the **tracking, trigger, and matching efficiencies, and from the Monte-Carlo input functions** are included in the systematic uncertainty of the Aε term and are considered for the R_{AA} dependence as uncorrelated with p_T and correlated with the centrality
- The F_{norm} systematic uncertainty is estimated from the calculation differences between an online method using the trigger inputs from the detectors and an offline method based on the recorded trigger classes
- The systematic uncertainty on the determination of the **J/ψ cross section** is estimated from the pp reference. It contains a statistical, an uncorrelated, and a correlated uncertainty originating from the branching ratio and the luminosity
- The **nuclear overlap function estimation** is associated to a systematic uncertainty varying with the collision centrality between ~ 3 % and ~ 6 %
- The uncertainty on the **event plane determination** is taken as correlated with the centrality

Sources	vs centrality	vs p_{T}
Signal ex.	[1.4–6]%	[1.4–6]%
MC input	2%	2–3 %
Centrality det.	0.1–3.5%	0–1.4%*
$\mathrm{F_{norm}}$	0.5%*	0.5%*
$\langle \mathrm{T_{AA}} \rangle$	3.1–6%	3.2–4.5%*
Tracking efficiency	3%* $\oplus$ 1%	3% $\oplus$ 1%*
Int. trigger eff.	1.5%*	1.5%
Trigger response	[0–2.2]%* $\oplus$ [0–1]%	[0–3.8]% $\oplus$ [0–1]%*
Matching efficiency	1%*	1%
pp ref.	[1.4–10]%* $\oplus$ [3.5–4.5]%* $\oplus$ 2.1%*	[2.5–20]%* [3–9]% $\oplus$ 2.1%*
EP determination	1%*	1%*.

Table 5.10 – Summary of systematic uncertainties on the $\mathrm{R_{AA}}$ measurement. Values with an asterisk are considered as fully correlated with the corresponding variable.

5.6.3 Cross-checks with integrated sample results

Comparison to the $\Delta\phi$-integrated results

To check for any bias originating from the $\Delta\phi$ binning, the analysis was performed without dividing dimuon candidates in function of their emission angle. The results for this *unbiased* sample show intermediate $\mathrm{R_{AA}}$ values between the in- and -out-of-plane observations. The comparison is illustrated on Fig. 5.32.
Counting the number of J/ψ measured in each analysis bin also gives consistent results since the difference between the number of J/ψ measured in the unbiased analysis and the sum of in- and out-of-plane numbers is negligible. Since the cut on the vertex position should not affect the analysis, a cross-check was performed by comparing the $\mathrm{R_{AA}}$ values without the $\Delta\phi$ binning to previous integrated analysis (released as preliminary results by the ALICE Collaboration [Tar17]), see Fig. 5.33. Both analyses only differ by the $\mathrm{z_{vertex}}$ cut and the centrality classes. For semi-central collisions, the same centrality class is considered and both analyses agree. The other centrality classes are different (5–20% vs 0–20% and 40–60% vs 40–90%) but the comparison shows compatible results.

Computation from combining $\mathrm{R_{AA}}$ and v_2 results

The nuclear modification factor can also be computed for different azimuthal angles by combining integrated $\mathrm{R_{AA}}$ and elliptic flow results. Since the only term from the $\mathrm{R_{AA}}$ (see eq. 5.26) depending on the $\Delta\phi$ variable is the number of J/ψ as:

$$\mathrm{N}(\Delta\phi, \Delta\mathrm{p_T}, \Delta\mathrm{y}) = \mathrm{N^{int}}(\Delta\mathrm{p_T}, \Delta\mathrm{y})(1 + 2\mathrm{v_2}(\Delta\mathrm{p_T}, \Delta\mathrm{y}))\cos(2\Delta\phi)) \tag{5.34}$$

this equation can be directly transferred to the $\mathrm{R_{AA}}$. The J/ψ elliptic flow analysis was performed using 2 GeV/c -wide p_{T} bins. The calculation is therefore limited to this binning. Fig. 5.34 shows the comparison between the results obtained with this method (in 2 GeV/c -wide bins) and the values obtained from the analysis in 2 $\Delta\phi$ bins for semi-central collisions. All the values are compatible.

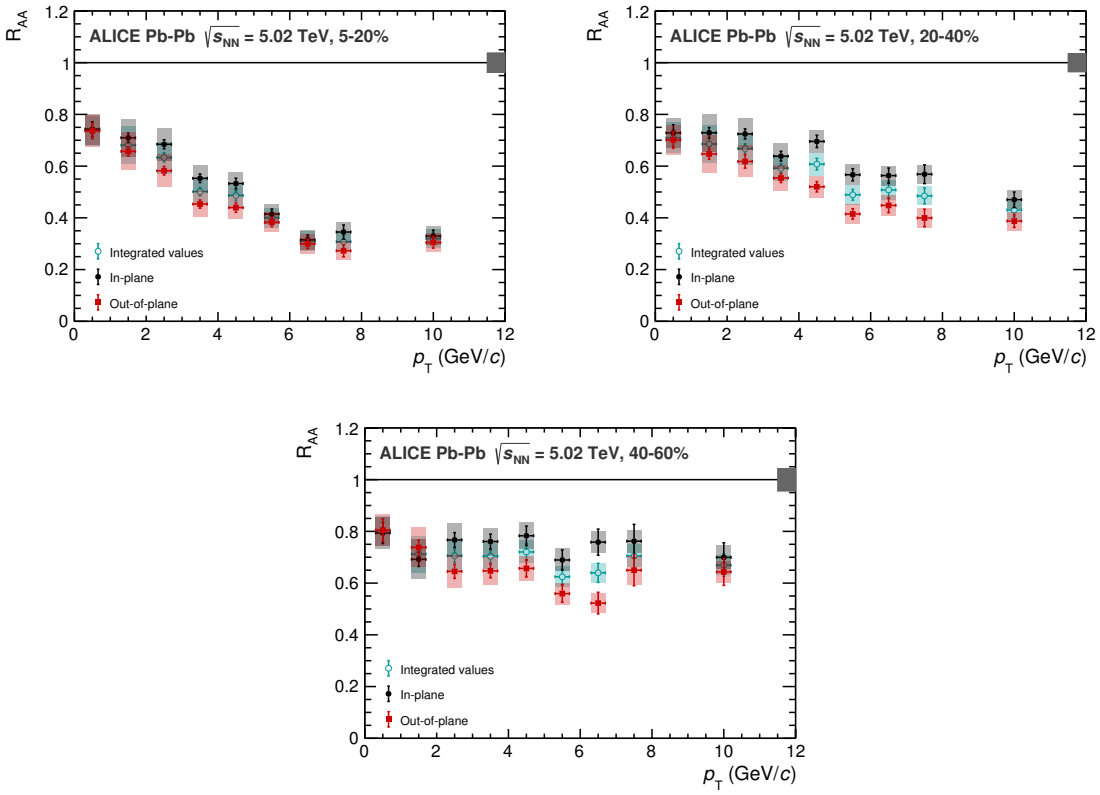

Figure 5.32 – Comparison of nuclear modification factor values from the in- and out-of-plane binning to the $\Delta\phi$-integrated analysis

Results

For each p_T bin of the analysis, the R_{AA} dependence with the centrality of the in- and out-of-plane samples is represented on Fig.5.35. The centrality dependence is similar for both regions. As expected, the R_{AA} is higher in-plane than out-of-plane for a given p_T and centrality range. Depending on the J/ψ p_T the R_{AA} evolution is different. For p_T below 2 GeV/c, the R_{AA} is flattened and does not seem to depend on the collision centrality. However, for higher p_T ranges, the R_{AA} increases strongly with decreasing centrality.

5.6.4 Investigating path-length scaling

Azimuthal studies of particles interacting mainly with the medium through energy loss show a characteristic scaling of the nuclear modification factor with respect to the mean path length traversed by the particle. This is the case of jets or other high-p_T probes (see π^0 at RHIC for example [A$^+$09a]) where the path-length dependence is predicted as $\propto$ L for elastic energy loss and as $\propto$ L^2 for collisional energy loss. A similar study for J/ψ particles is here performed.
In this respect, the mean path length was estimated for each centrality and $\Delta\phi$ bin. The estimation was performed using the Trento model [MBB15] to compute the initial condition of the collision. For a given centrality, the in- and out-of-plane averages of the path length from several events are computed. For each event, several probes are simulated with an isotropic distribution of their azimuthal direction, and the path length is calculated as the line integral of the entropy density distribution along that direction. The nuclear modification factor dependence with centrality from Fig. 5.35 can be also studied through

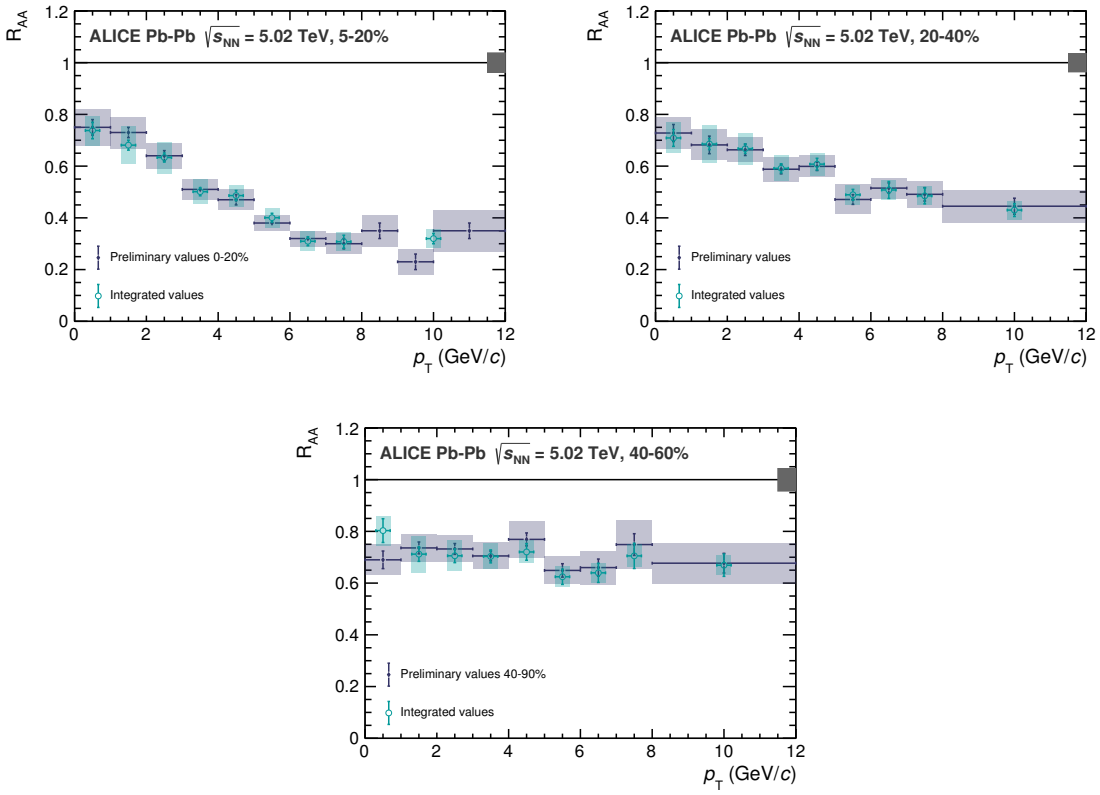

Figure 5.33 – Comparison of R_{AA} values integrated in $\Delta\phi$ from this analysis with $z_{vertex} < 10$cm cut (*integrated values*) to results from previous analysis without z_{vertex} cut (*preliminary values [Tar17]*)

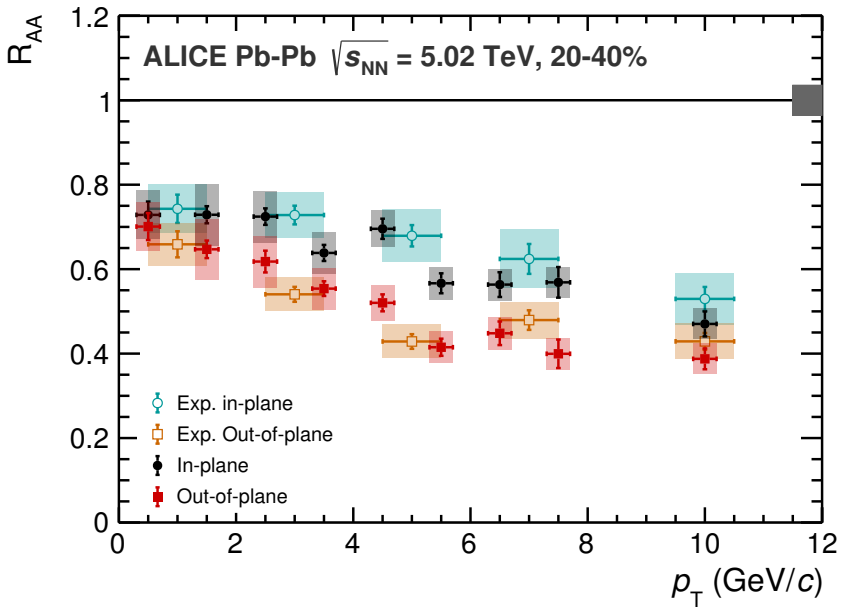

Figure 5.34 – Comparison of nuclear modification factor values from the in- and out-of-plane binning analysis to the computed values from integrated R_{AA} and v_2 results for the 20–40% centrality class

the mean path length (L) for each p_T bin. The result is shown on Fig. 5.36 where the blue and black symbols correspond to the in-plane region and the orange and red symbols

correspond to the out-of-plane regions. A similar evolution to the centrality dependence is observed at low- and high-p_{T}. In- and out-of-plane values seem to align as a function of L for the highest p_{T} regions.

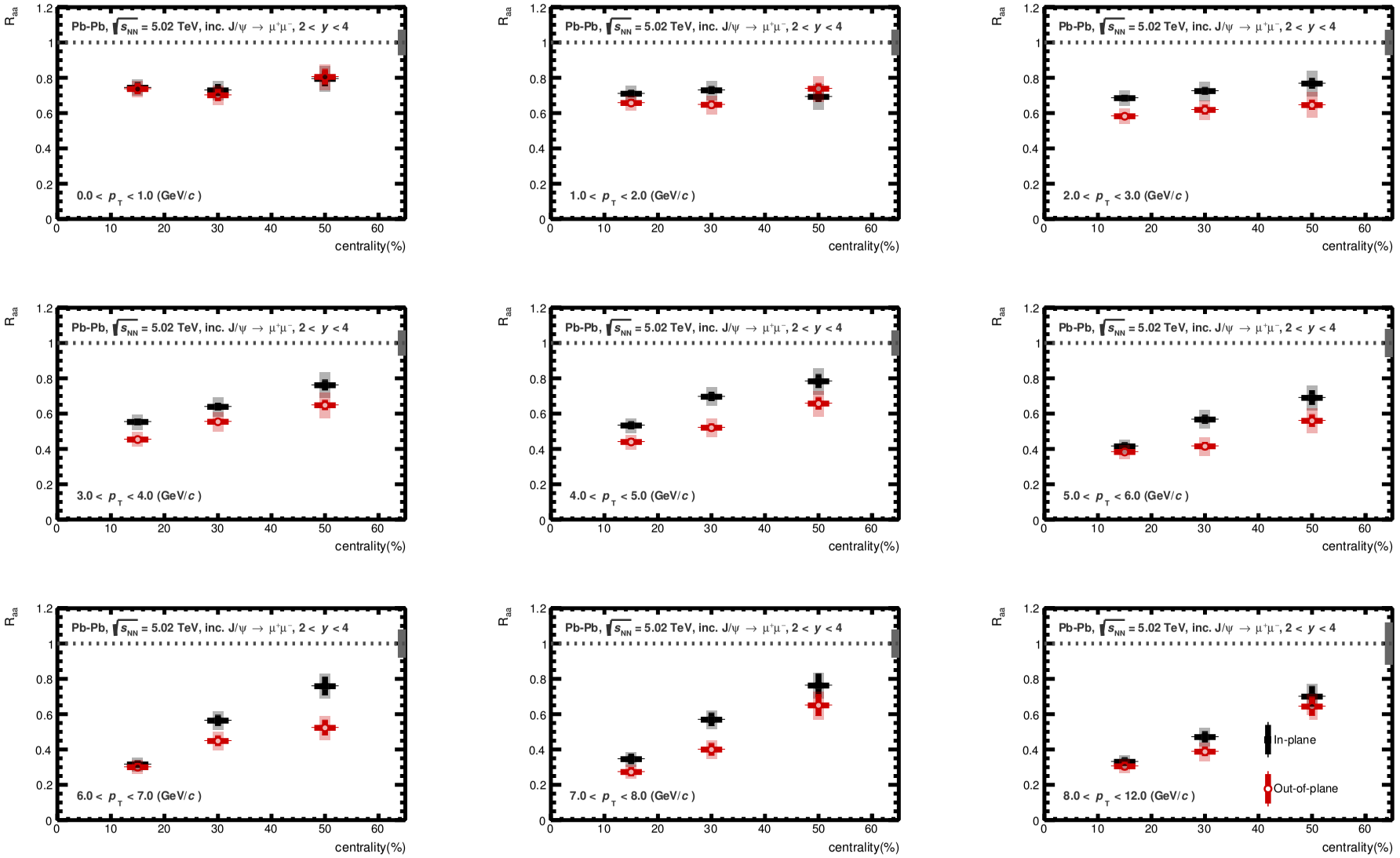

Figure 5.35 – Nuclear modification factor in- and out-of-plane as a function of the event centrality for different p_T bins. Numerical values can be found in Tab. B.7)

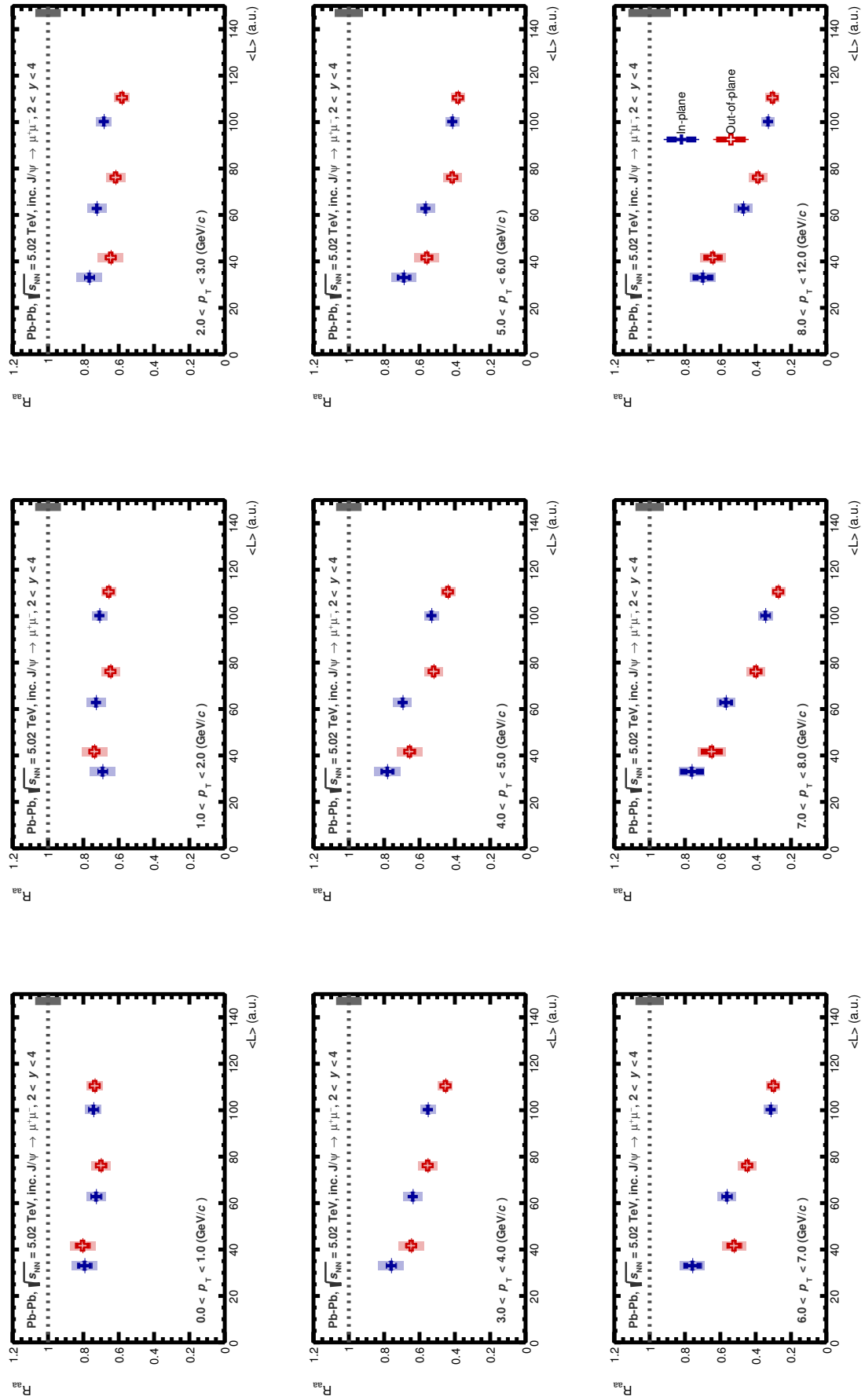

Figure 5.36 – Nuclear modification factor in- and out-of-plane as a function of the mean path length for different p_T bins

CHAPTER 6

DISCUSSION

"As a matter of fact, I rather feel like expressing myself now."

— Audrey Hepburn

This final chapter discusses the results obtained in this thesis and provides some thinking about consequences on charm and charmonium physics as well as future prospectives at the LHC. The first section is dedicated to results overview and comparison to other available measurements and theoretical predictions. The second part focuses on charm quarks and their possible thermalisation in the medium in both Pb–Pb and p–Pb collisions. The last section addresses short- and long-term prospectives for heavy quarks studies with the ALICE experiment at the LHC.

6.1 J/ψ elliptic flow at forward rapidity

The J/ψ v_2 analysis was performed in three centrality classes (5–20 %, 20–40 %, and 40–60 %) as a function of the transverse momentum. Fig. 6.1 shows the comparison between the three measurements. For all centralities, a significant positive elliptic flow is observed in several p_{T} ranges. First of all, these new measurements confirm the hints of non-zero J/ψ elliptic flow observed in Pb–Pb collisions at $\sqrt{s_{\mathrm{NN}}} = 2.76\,\mathrm{TeV}$ [A+13a], with single bin significances up to 6σ. So the first conclusion is that **J/ψ flows in** Pb–Pb **collisions at** $\sqrt{s_{\mathrm{NN}}} = 5.02\,\mathrm{TeV}$ and exhibits a positive v_2 . Qualitatively the scenario of cc̄ **(re)generation in the medium is favoured**. Yet theoretical models are not fully compatible with the experimental results. This could imply the presence of underlying effects or other interactions that are not considered yet.

The measurements display a similar evolution as a function of transverse momentum:

- In the lowest p_{T} region (0–2 GeV/c) the elliptic flow coefficient is very low or compatible with zero. This observation is common to other particle and flow coefficient measurements.
- Intermediate p_{T} ranges (2–6 GeV/c) demonstrate an increasing v_2 up to a maximum value (around ~ 0.07–0.12) that decreases afterwards.
- In the highest p_{T} bin ($8 < p_{\mathrm{T}} < 12\,\mathrm{GeV}/c$), the v_2 coefficient is compatible with zero for the 5–20 % and 40–60 % centrality classes. However, in semi-central collisions the v_2 is significantly positive (>2.6σ).

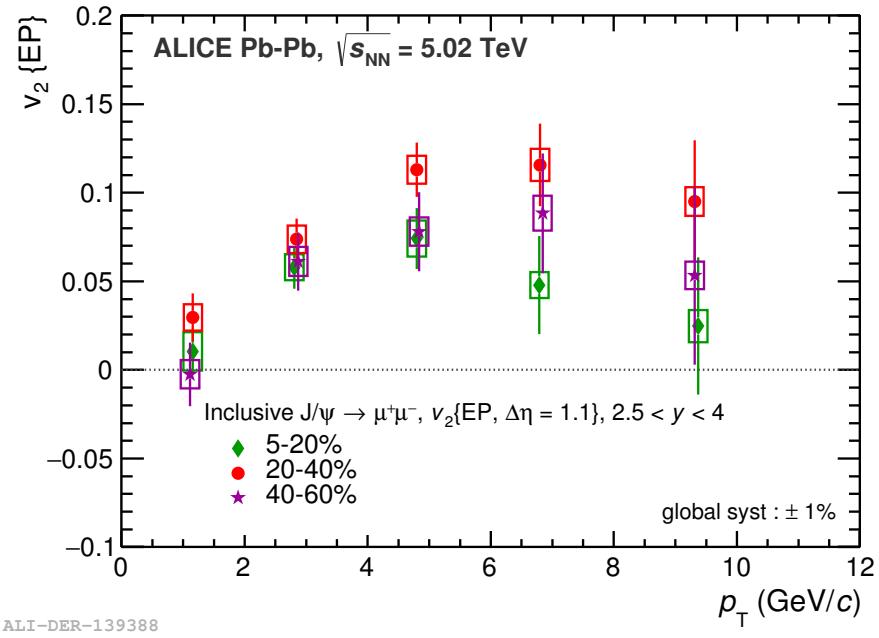

Figure 6.1 – J/ψ v_2 in Pb–Pb collisions at $\sqrt{s_{NN}} = 5.02$ TeV at forward rapidity for three centrality classes. Numerical values can be found in Tab. 5.5 and Tab. 5.4

Semi-central collisions, corresponding to the 20–40 % centrality class, exhibit the highest values with a maximum $v_2 = 0.113 \pm 0.015(\text{stat}) \pm 0.008(\text{syst})$ at $4 < p_T < 6$ GeV/c. Other centrality classes show lower v_2 values which are compatible between them. This observation can be easily interpreted since the geometry of more central collisions is associated to a weaker anisotropy (the overlap region has a lower eccentricity) and less (re)generation is expected for more peripheral regions. The centrality class with the highest flow corresponds thus to a compromise between initial geometry and (re)generation.

6.1.1 Azimuthal dependence of J/ψ production

R_{AA} measurements in- and out-of-plane for different centrality ranges are presented in Fig. 6.2. The results are plotted as a function of the mean path length in medium, calculated in- and out-of-plane for each centrality class, for several p_T bins. Two polynomial fits are proposed since no theoretical predictions are available.
Charmonia are not expected to exhibit a similar energy loss in the medium as high-p_T particles but a dependence of the suppression is observed with the traversed mean path length in the medium. **A hint of linear scaling** with ⟨L⟩ is observed, suggesting energy loss of J/ψ or charm quarks in medium. For $p_T < 2$ GeV/c, the J/ψ dependence is rather flat. Similarly to J/ψ R_{AA} vs centrality results, this observation could be attributed to the (re)generation component. Above this value a decrease is observed with ⟨L⟩. The evolution differs from a jet-like behaviour but is not incompatible with the suppression scheme.

Previous measurements were performed for high-p_T π^0 at RHIC [A+09a] to investigate the interplay between collective flow and jet-quenching effects. This analysis is the first study of azimuthal angular dependency for J/ψ production.

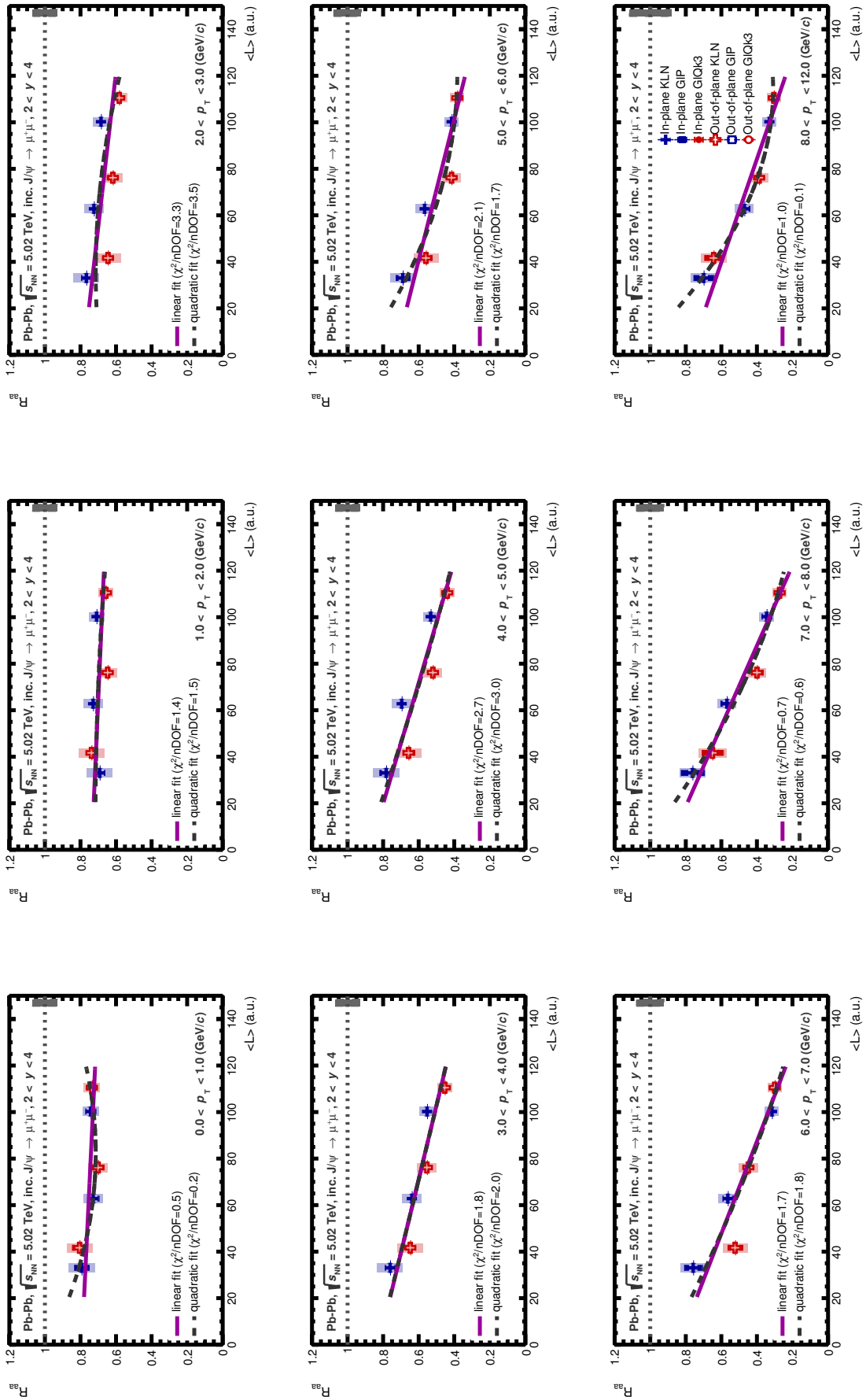

Figure 6.2 – J/ψ R_{AA} in- and out-of-plane as a function of the mean path length for different p_T bins in Pb–Pb collisions at $\sqrt{s_{NN}}$ = 5.02 TeV fitted with linear and quadratic polynomials

6.1.2 Comparison with ALICE measurements at mid-rapidity

The ALICE detector can also measure J/ψ at mid-rapidity through the di-electron decay channel: $J/\psi \rightarrow e^+e^-$ in the central barrel. The comparison of the measured J/ψ v_2 between both rapidity regions is presented in Fig. 6.3 for the 20–40% centrality class [A+17b]. The two measurements are compatible given the large dielectron uncertainties. The most significant value $v_2 = 0.129 \pm 0.080(\text{stat}) \pm 0.040(\text{sys})$ is measured for the p_T range $2 < p_T < 6\,\text{GeV}/c$. This pioneer measurement is the first hint of a positive J/ψ at mid-rapidity down to zero p_T and is very promising for the next LHC data taking of Pb–Pb collisions. Al-

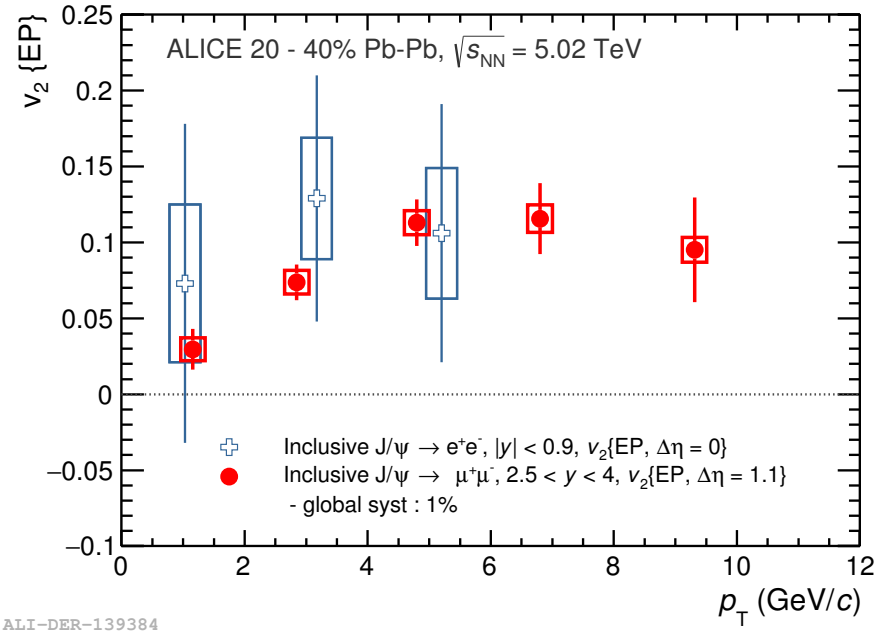

Figure 6.3 – Comparison of rapidity measurement for J/ψ v_2 in Pb–Pb collisions at $\sqrt{s_{NN}} = 5.02\,\text{TeV}$

though no rapidity dependence can be observed with the current precision, a higher v_2 is expected at mid-rapidity since more (re)generation should occur. Differential measurements in rapidity with the Muon Spectrometer (Sec. 5.4.4) are neither precise enough to exhibit this feature. More precise observations would allow to highlight a rapidity dependence. The rapidity dependence obtained by the comparison of ALICE and CMS results at $\sqrt{s_{NN}} = 2.76\,\text{TeV}$ does not allow to draw any conclusion.

6.1.3 Comparison to other experiments and lower beam energies

Previous results in A–A collisions at RHIC energies and at the LHC at $\sqrt{s_{NN}} = 2.76\,\text{TeV}$ allow for a comparison of the measured anisotropy coefficients. Fig. 6.4 compares the different measurements at the LHC from ALICE and CMS [K+17]. Both the CMS and ALICE detectors measured the J/ψ elliptic flow coefficient at $\sqrt{s_{NN}} = 2.76\,\text{TeV}$. The values are compatible but still have large uncertainties. The CMS detector allows to disentangle prompt and non-prompt contributions of J/ψ production. Prompt J/ψ measurements from CMS show compatible results with inclusive J/ψ results from ALICE. The non-prompt component also shows hints of positive v_2. Fig. 6.5 compares the J/ψ elliptic flow measurements in Pb–Pb collisions of ALICE at $\sqrt{s_{NN}} = 2.76\,\text{TeV}$ and $\sqrt{s_{NN}} = 5.02\,\text{TeV}$ with results from STAR at RHIC in Au–Au collisions at $\sqrt{s_{NN}} = 200\,\text{GeV}$. The measured J/ψ v_2 coefficient at LHC energies is larger than the v_2 at RHIC energies, which is compatible with zero. R_{AA} measurements at RHIC are described by models including very small regeneration [ZER13]

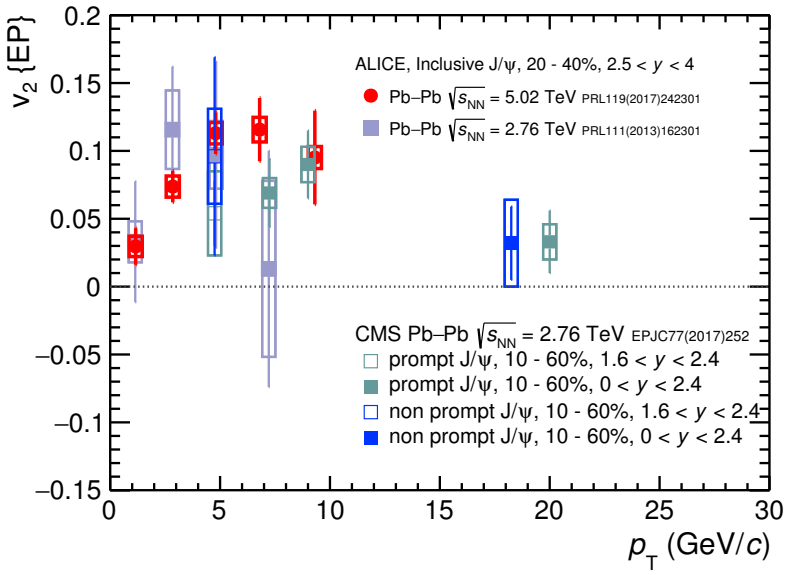

Figure 6.4 – Comparison of J/ψ v_2 measurements at $\sqrt{s_{\mathrm{NN}}} = 5.02\,\mathrm{TeV}$ with $\sqrt{s_{\mathrm{NN}}} = 2.76\,\mathrm{TeV}$ results by ALICE and CMS

and the measured v_2 in Au–Au and U–U collisions seems to support this statement. LHC's first Pb–Pb collisions at $\sqrt{s_{\mathrm{NN}}} = 2.76\,\mathrm{TeV}$ show the first hint of positive J/ψ v_2, measured both by ALICE and CMS but with quite large uncertainties. Even if measurements at RHIC

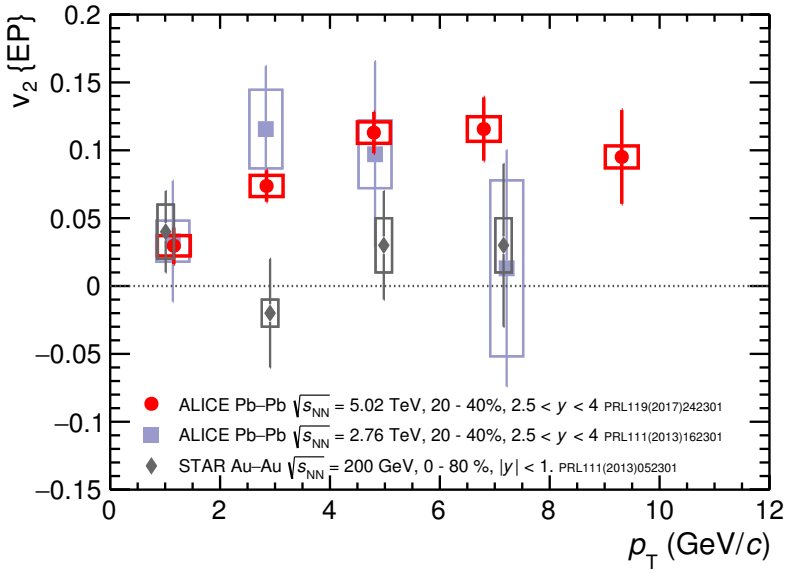

Figure 6.5 – Comparison of J/ψ v_2 measurements at the LHC by ALICE and at RHIC by STAR

energies seem to indicate a zero J/ψ flow, the large uncertainties leave it compatible with results at $\sqrt{s_{\mathrm{NN}}} = 2.76\,\mathrm{TeV}$. Higher statistics is needed to draw clear conclusions on charm thermalisation and quarkonium formation through (re)combination at RHIC.
In Pb–Pb collisions at $\sqrt{s_{\mathrm{NN}}} = 5.02\,\mathrm{TeV}$, the positive v_2 at high p_{T} was confirmed by the measurements up to 30 GeV/c of ATLAS for prompt and non-prompt J/ψ [A+18a]. Previous results of CMS also show a non-zero elliptic flow for prompt J/ψ at $\sqrt{s_{\mathrm{NN}}} = 2.76\,\mathrm{TeV}$. The

highest values correspond to the prompt contribution and are compatible with ALICE data in the matching p_T bins (Fig. 6.6). ATLAS and ALICE results show a consistent evolution of J/ψ v_2 as a function of p_T in different centrality ranges.

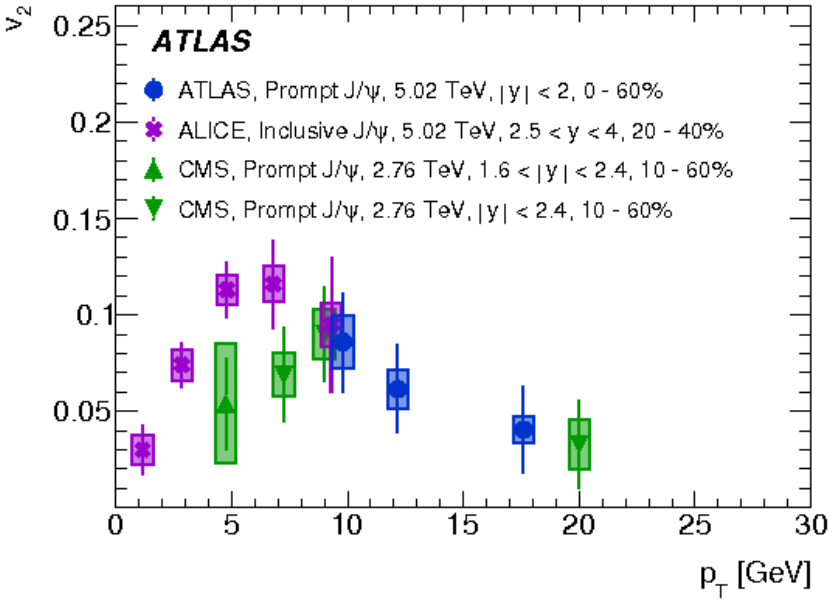

Figure 6.6 – Elliptic flow as a function of p_T for inclusive J/ψ at $p_T < 12$ GeV measured by ALICE at $\sqrt{s_{NN}} = 5.02$ TeV compared with prompt J/ψ measured by ATLAS ($9 < p_T < 30$ GeV) at $\sqrt{s_{NN}} = 5.02$ TeV and CMS ($6.5 < p_T < 30$ GeV) at $\sqrt{s_{NN}} = 2.76$ TeV

6.1.4 Theoretical predictions

Theoretical predictions from two transport models [DR15, ZER13] and [ZXXZ14, GSX+15] are compared to the observations in semi-central collisions. The elliptic flow observable is complementary to the nuclear modification factor and provides further constraints on model predictions. Since primordial J/ψ are not expected to exhibit a strong azimuthal dependence and (re)generated J/ψ should inherit the flow of charm quarks, J/ψ v_2 is a determinant observable to address the interplay between suppression and (re)generation mechanisms.
Both models incorporate J/ψ from (re)combined and thermalised charm quarks, primordial J/ψ experiencing path-length effects through the medium (this prompt contribution includes direct J/ψ and feed-down from higher mass sates) and the contribution from B hadron decays (assuming full b quark thermalisation in the medium).

TM1 The calculations [1] are based on the transport model [ZR10] of Xingbo Zhao and Ralf Rapp extended to Pb–Pb collisions at the LHC in [ZR11] and [DR15]. The J/ψ v_2 is computed as a function of p_T as the weighted average of primordial-suppressed J/ψ (estimated from Υ(2S) calculations at $\sim 1/3 p_T$), (re)generated J/ψ (using hydrodynamics results from [HFR14] and QGP temperature of 180 MeV) and the non-prompt J/ψ contribution from B feed-down [HFR14]. The predictions from this model are able to reproduce ALICE R_{AA} measurements for the same collision system (see Fig. 6.7). The hashed band represents the

[1] pre-dictions

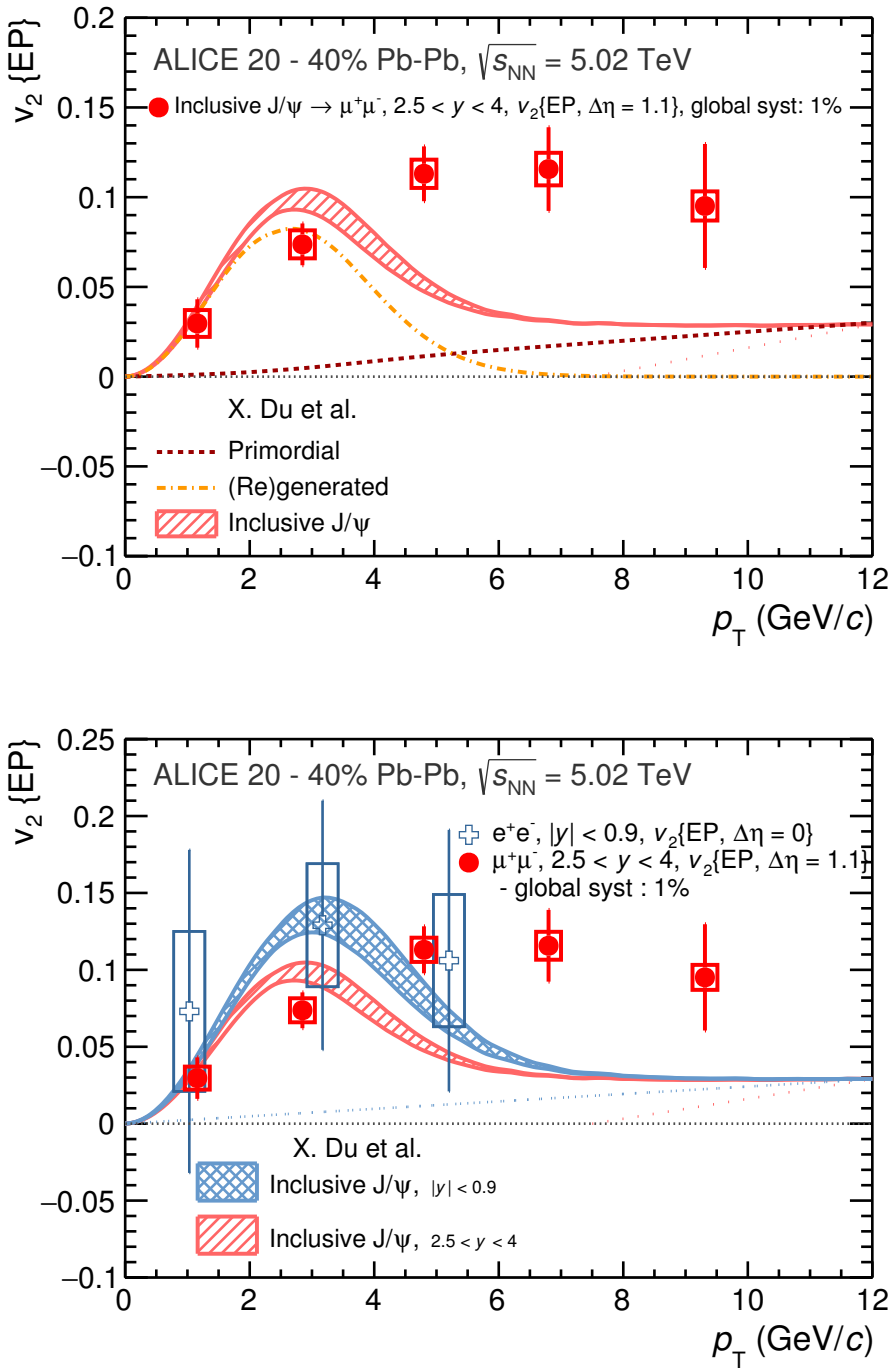

Figure 6.7 – Inclusive J/ψ v_2 in semi-central Pb–Pb collisions at $\sqrt{s_{NN}} = 5.02$ TeV compared to TM1 [DR15] predictions: (Top) Contribution details at forward rapidity, (Bottom) Comparison of forward and mid-rapidity predictions

total inclusive J/ψ v_2 prediction for the kinematic range measured by ALICE at forward rapidity. The band width stands for the uncertainty from shadowing effects (estimated from p–Pb and EPS09 between 0–20 %). The (re)generation component is drawn in yellow to highlight its significant contribution. The dashed red line emphasizes the minor role of the primordial component. The evolution at low and intermediate p_T (up to 4 GeV/c) is compatible with the measurements (red circles on the plot). The amplitude is only achieved by including a strong (re)generation contribution, reaching up to ~50% in semi-central

collisions. Above p_T>4 GeV/c, the calculated J/ψ v_2 originates mainly from the primordial contribution and does not agree with our data. Tab. 6.1 gives the corresponding fractions of primordial and (re)generated contributions from R_{AA} predictions. From the predictions, it

pt (GeV/c)	primordial(%)	(re)generated(%)
0	0.36	0.64
2	0.49	0.51
4	0.86	0.14
6	0.99	0.01
>7	1	0

Table 6.1 – Fractions of primordial and (re)generated J/ψ at forward rapidity in different p_T bins from R_{AA} calculations of TM1 [DR15] in Pb–Pb collisions at $\sqrt{s_{NN}}$ = 5.02 TeV for the 20–40 % centrality class

is clear that the (re)combination is the main contributor while the primordial component plays a subordinate role. (Re)generation and suppression mechanisms have antagonist effects on the R_{AA} value. Since J/ψ elliptic flow originates mostly from (re)combined charm quarks, this observable offers an additional test of transport models and a quantitative evaluation of the (re)combination input. Mid-rapidity calculations (in blue) are compatible with the data and predict a higher maximum than at forward rapidity due to the increased (re)generation component (see Sec. 4.3.2).

TM2 The calculations [2] from the second model are based on the transport approach detailed in [ZXXZ14]. In addition to TM1 components, charm quark interactions with electromagnetic fields during the charmonium formation at early stages is taken into account. The basic idea is that the magnetic field orientation creates a preferred direction and breaks the system symmetry [GSX+15]. Calculation details are shown with data comparison on Fig. 6.8. The prompt J/ψ v_2 evolution is shown as a dotted yellow line and the primordial contribution is in dark red. The pink dashed line is the total inclusive J/ψ calculations (prompt charmonia and B decay contribution) but without magnetic field effect (and assuming no shadowing). The calculations including all contributions (both collective and non-collective) are represented by the yellow band, the width standing for shadowing impact. Similar conclusions can be drawn from data comparison as for the previous model. At low p_T, the v_2 amplitude is reproduced assuming a strong (re)generation component but a large discrepancy is observed at hight p_T between the calculations and the measurements. At high p_T, the total v_2 originates from magnetic field effects and B decays. The latter contribution remains the most important one at forward rapidity. Adding the magnetic contribution enlarges the v_2 value but it remains much below the experimental data.

Both models require a **large contribution from (re)generation** to reproduce the measured amplitude at low p_T. This observation favours the (re)generation scenario of J/ψ and constitutes a **strong case for charm quark thermalisation** in the medium. However, theoretical predictions **fail to describe intermediate p_T measurement**. The amplitude is largely underestimated in this kinematic range, even when adding an additional contribution of the magnetic field as suggested by [ZXXZ14]. A tension is observed between

[2] post-dictions

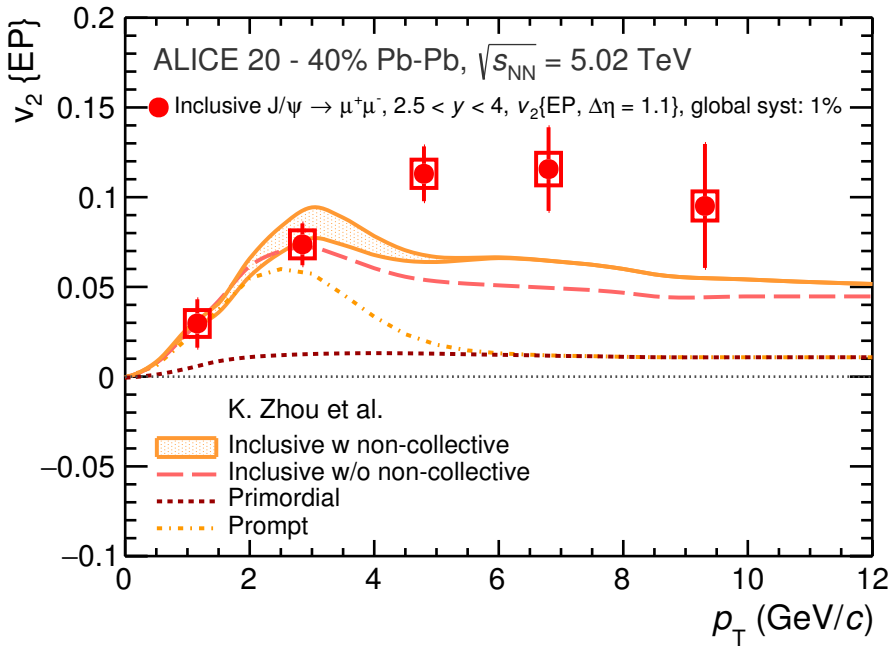

Figure 6.8 – Inclusive J/ψ v_2 at forward rapidity in semi-central Pb–Pb collisions at $\sqrt{s_{NN}} = 5.02$ TeV compared to TM2 [ZXXZ14] predictions

experimental results and theory in the $4 < p_T < 8$ GeV/c. Higher p_T values measured by ALICE and also by ATLAS are compatible with the calculations.
The measured J/ψ v_2 is interpreted within the transport model approach as the result of several effects:

- flow inheritance from (re)combined charm quarks, depending on:
  - the bulk flow if charm quarks thermalised (event partially) in the medium
  - the proportion of (re)generated J/ψ since most of the flow is expected to originate from charm quarks in the medium that (re)combined later to form $c\bar{c}$ pairs
- path-length effects as primordial J/ψ traverse a longer path through the medium when emitted out-of-plane than in-plane (mainly significant at high p_T), depending on:
  - the geometry of the initial system
  - the proportion of initially produced J/ψ and their formation region with respect to the QGP
- non-inclusive components might also have a large impact
  - Feed-down from higher excited states might lower the J/ψ v_2 if less (re)combination occurs
  - B meson contribution if bottom flow differs from charm

This picture is adopted by transport models but other effects might also lead to an azimuthal J/ψ anisotropy. Within this approach, the tension at intermediate p_T could be

imputed on a primordial contribution (possibly not fully understood in terms of azimuthal distribution) or on (re)combination occurring to larger p_T than currently considered. Another contribution from the medium may also impact J/ψ production and azimuthal distribution. Different models reproduce J/ψ R_{AA} measurements without introducing a (re)generation component. For example thermal production of charm quarks and/or $c\bar{c}$ pairs in the QGP phase offers a different approach of charmonium production in the medium, assuming charm and beauty hadrons production during the hadronisation stage and in thermal equilibrium with the medium. Measurements of ψ(2S) **elliptic flow** should significantly improve the global picture as a larger (re)combination is expected for higher mass states. Equally important, **ϒ flow** results would bring valuable information on quarkonium physics, as less/negligible (re)generation is expected.
Non-QGP effects could also contribute to the observed anisotropy without affecting the total production of J/ψ . In that case, these effects could also manifest in p–Pb collisions. This point is further discussed in the paragraph 6.2.2.
Magnetic fields created in the collision may have a larger intensity than predicted and the effects on final particle distributions may currently be underestimated or misunderstood. If this component is significant, J/ψ v_2 may also be a probe of magnetic effects. Direct flow (v_1) measurements for charged particles [GKR14] and in particular with charm content [DPC+17] are for now the best way to access magnetic field intensity. Polarisation studies in Pb–Pb and p–Pb collisions could also reveal key information on charmonium dynamics and interactions in the medium.

6.2 Does charm quark thermalise at the LHC?

Closed heavy flavour v_2 provides an opportunity to study charm-quark flow in the medium, in particular by comparing to open-heavy-flavour and light-meson results. The next section gives arguments from available measurements for charm-quark thermalisation at LHC energies.
Some questions are still open:

- Do charm quarks thermalise at the LHC?
- Do they follow the collective dynamics of the bulk? i.e. How does charm flow scales with lighter-quark flow?

6.2.1 What can be learned from the open charm comparison ?

Open heavy flavours show signs that charm quarks participate to the collective expansion dynamics. Yet both charm and light quarks contribute to their flow. If charm quarks (re)combine in the medium into $c\bar{c}$ pairs, produced J/ψ should inherit their flow. However, the comparison is not trivial between both particles since D mesons also carry a light quark that contributes to the final hadron flow and several contributions play a role in J/ψ production. The simplest case may be thus at high p_T where the primordial component should dominate J/ψ production. Despite this caveat, flow comparison of both open and closed heavy flavours should make a strong statement for charm thermalisation and (re)combination in the medium. To go further, since flow corresponds to particle expansion, the mass scaling of the meson p_T was investigated. In the coalescence picture, similar constituent velocities are required to bound together [LM03]. As a consequence, in the D meson case, the light quark p_T is much smaller than that of its hadron, carrying

a momentum fraction $z_q = \frac{p_{\mathrm{T},l}}{p_{\mathrm{T,D}}} \sim \frac{m_l}{m_{\mathrm{D}}}$. In order to scale accordingly the particle momentum, the x-axis was scaled by the number of heavy quarks (n_{Q}) (Fig. 6.9, Right). A mass scaling should be equivalent. The v_2 evolution of both particles follows a similar trend and the scaling seems adequate. At low p_{T} the agreement seems better when scaling the p_{T} but not at intermediate p_{T}. This very qualitative statement would greatly benefit from J/ψ measurements at higher p_{T}. Large-p_{T} J/ψ results from ATLAS seem to agree with D-meson data. In spite of the centrality and rapidity differences of the measurements,

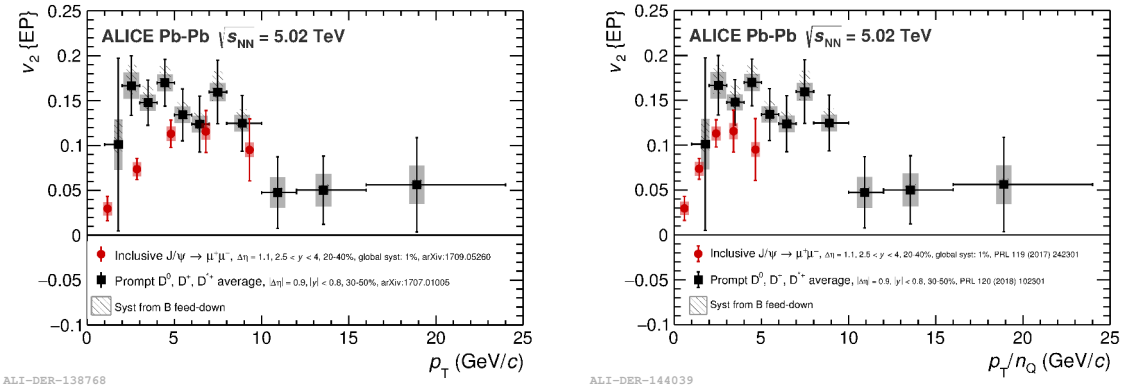

Figure 6.9 – Comparison of J/ψ and D mesons elliptic flow in semi-central (20–40 %) Pb–Pb collisions at $\sqrt{s_{\mathrm{NN}}} = 5.02$ TeV as a function of p_{T} (Left) and p_{T} scaled by the meson number of heavy quarks (Right)

the similar flow amplitude measured for both D mesons and J/ψ is a strong hint that charm quarks reach locally a thermal equilibrium in the medium. It also supports the (re)generation mechanism at the LHC. The comparison of charmed mesons (J/ψ and D mesons) to light mesons allows to study the scaling of charm flow with the bulk one and to investigate the asymmetric momentum configuration of open heavy flavours. The large mass imbalance in the D meson constituents and the uncertainties on both J/ψ and D mesons results prevent from investigating flow scaling originating from the particle mass or from the number of constituent quarks. Since only a fraction of J/ψ originates from the (re)combination of charm quarks and the observed flow is the average of all contributions, a direct comparison cannot drive to a quantitative scale study. Drawing clear conclusions from the comparison of D mesons and J/ψ elliptic flow is also challenging since charm quarks from dissociated J/ψ carry the properties of the previously bound state and will contribute to form D mesons. Nevertheless the azimuthal anisotropy from primordial J/ψ is expected to be rather minor and the fraction of charm quarks in the medium from dissociated charmonium states should also be negligible.
A message can still be extracted from these comparisons: **charm quarks interact with the expanding medium** and **J/ψ production through (re)generation is assessed at** $\sqrt{s_{\mathrm{NN}}} = 5.02$ TeV. For a precise investigation of charm flow in the medium, further studies are necessary. The (re)generation component of J/ψ needs to be accurately calculated and the flow of J/ψ should be perfectly understood and reproduced, up to high p_{T}. If the charm density is very high, charmed hadrons could just inherit the flow contribution from charm quarks [LM03]. To investigate the relation between partonic and hadronic flow of charm, more precise results for D mesons and charmed baryons are required. In addition, a **theoretical model describing simultaneously open heavy flavours and charmonium** would be very valuable as no uniform approach is currently available for the treatment of particle production and dynamics in the medium.

6.2.2 Results in p–Pb collisions

Studies in p–Pb collisions provide valuable references to disentangle effects from the hot medium, due to the formation of the QGP, and effects, caused by the presence of the nuclei, as both are affecting particle production in Pb–Pb collisions. While D meson production is strongly suppressed in Pb–Pb collisions, it is much less affected by Cold Nuclear Matter (CNM) effects, particularly at high p_{T}. However, measurements of charmonium R_{AA} indicate a strong sensitivity to CNM effects. High-multiplicity p–Pb collisions demonstrate signs of collective behaviour (cf. 3.4). These QGP-like effects are also found in the heavy flavour sector and measurements of J/ψ azimuthal anisotropy exhibit positive values. Correlations between charged hadrons and inclusive J/ψ at forward rapidity measured by ALICE in p–Pb collisions at $\sqrt{s_{\mathrm{NN}}} = 5.02\,\mathrm{TeV}$ and $\sqrt{s_{\mathrm{NN}}} = 8.16\,\mathrm{TeV}$ indicate significant v_2 coefficients [A+18b]. The results in both beam directions (p–Pb and Pb–p) combining data from $\sqrt{s_{\mathrm{NN}}} = 5.02\,\mathrm{TeV}$ and $\sqrt{s_{\mathrm{NN}}} = 8.16\,\mathrm{TeV}$ collisions are compared to Pb–Pb measurements and model predictions on Fig. 6.10. **No J/ψ (re)generation nor suppression is expected in** p–Pb **collisions** and because of the smaller system size, independently of the formation of a QGP, **path-length effects should be negligible**. Similar amplitudes are yet observed between p–Pb and central (5–20 %)) Pb–Pb collisions. A clear anisotropy is observed up to ~6 GeV/c and the uncertainties on the measurement after become too large to have a clear statement. An unknown mechanism might be the origin of the J/ψ elliptic flow both in p–Pb collisions and in high-p_{T} Pb–Pb collisions. It might also be originating from early magnetic fields.

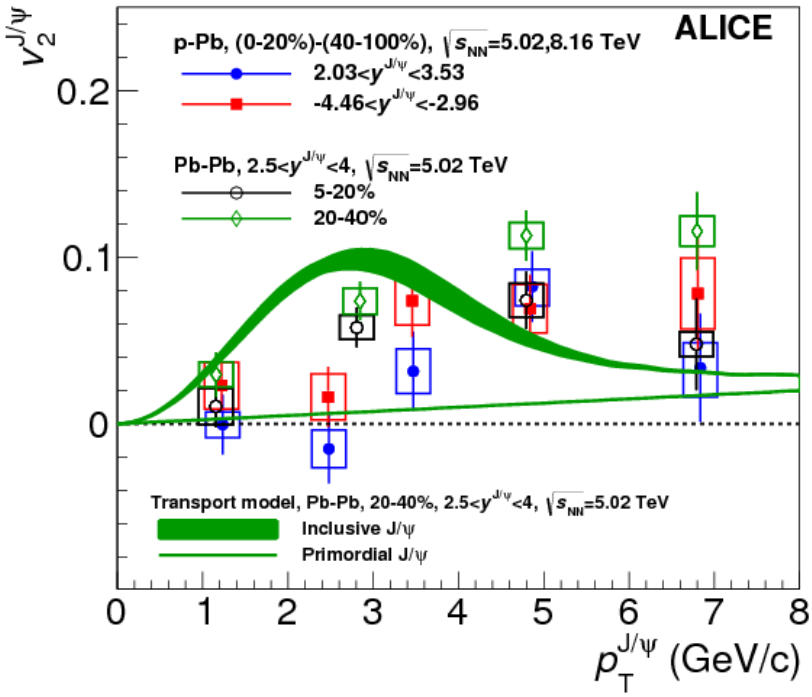

Figure 6.10 – Combined ($\sqrt{s_{\mathrm{NN}}} = 5.02\,\mathrm{TeV}$ and $\sqrt{s_{\mathrm{NN}}} = 8.16\,\mathrm{TeV}$) J/ψ v_2 coefficients in p–Pb and Pb–p collisions compared to central and semi-central Pb–Pb collisions at $\sqrt{s_{\mathrm{NN}}} = 5.02\,\mathrm{TeV}$ and transport model calculations for semi-central Pb–Pb collisions at $\sqrt{s_{\mathrm{NN}}} = 5.02\,\mathrm{TeV}$ from [DR15]

The measurement of J/ψ anisotropy in p–Pb collisions was complemented by open heavy-flavour particles at mid-rapidity via azimuthal correlations of electrons from charm- and beauty-hadron decays, and charged particles. A positive muon v_2 was also observed at forward and backward rapidity in high-multiplicity p–Pb collisions [A+16g], muons being

predominantly produced by heavy-flavour decays for p_{T} greater than 2 GeV/c (cf Fig. 6.11). Several results provide evidence that heavy quarks interact with the bulk also in the p–Pb

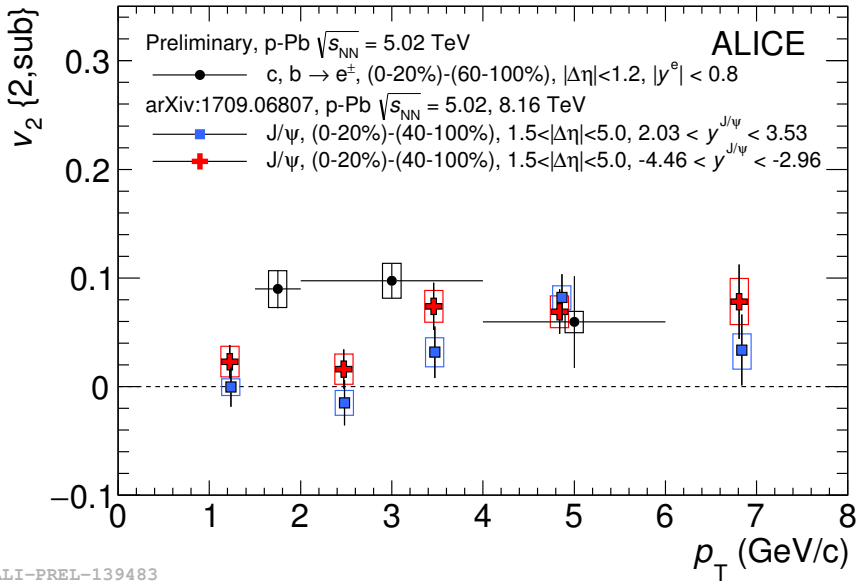

Figure 6.11 – Elliptic flow of HF-decay electrons in p–Pb at $\sqrt{s_{\mathrm{NN}}}$ = 5.02 TeV compared to J/ψ average at $\sqrt{s_{\mathrm{NN}}}$ = 5.02 TeV and at $\sqrt{s_{\mathrm{NN}}}$ = 8.16 TeV

system. The collectivity of charm quarks can be compared to other flavours by comparing different hadron species. The v_2 measurements of J/ψ , D^0 and K^0_s mesons by CMS in p–Pb collisions at $\sqrt{s_{\mathrm{NN}}}$ = 8.16 TeV [S+18a, CMS18b] suggest a lower anisotropy for charm with respect to strangeness. The elliptic coefficients are shown as a function of p_{T} and the transverse kinetic energy scaled by the number of constituent quarks on Fig. 6.12. At low kinetic energy, the elliptic flow of J/ψ and D^0 mesons is consistent with K^0_s results but above $\mathrm{KE_T}/n_q$ >1 GeV/c, both charmed mesons exhibit smaller anisotropies than the K^0_s. This difference between strange and charm quarks could be attributed to a weaker coupling of charm to the medium formed during p–Pb collisions.

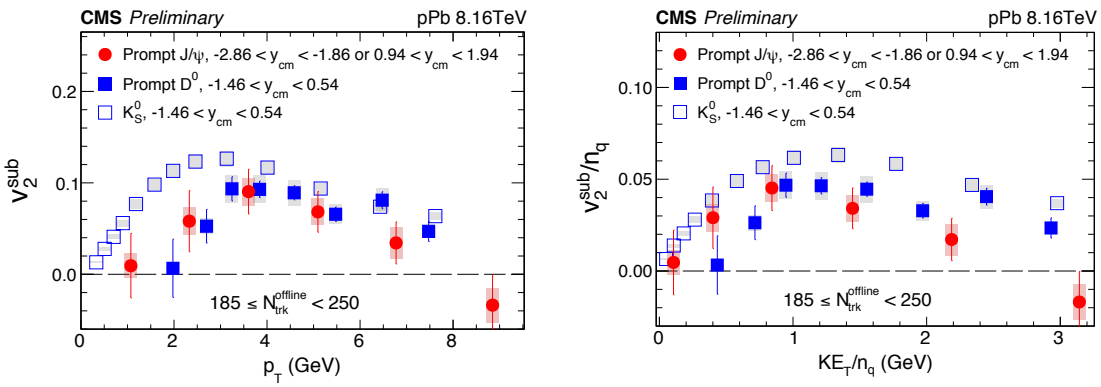

Figure 6.12 – (Top) Measurement of J/ψ elliptic flow in high-multiplicity p–Pb collisions at $\sqrt{s_{\mathrm{NN}}}$ = 8.16 TeV by CMS compared to D^0 and $\mathrm{K_s}$ mesons, (Bottom) values as a function of the transverse kinetic energy ($\mathrm{KE_T}$) and scaled by the number of constituent quarks n_q

6.3 Prospectives at the LHC

6.3.1 Short term: LHC run3

The next LHC Pb–Pb data campaign (2018) will provide new collisions at $\sqrt{s_{\rm NN}} = 5.02\,\text{TeV}$ with an integrated luminosity $\mathscr{L} = 1\,\text{nb}^{-1}$. Fig. 6.13 illustrates the expected J/ψ v_2 and uncertainties on the measurement combining the Pb–Pb periods from 2015 and 2018. The

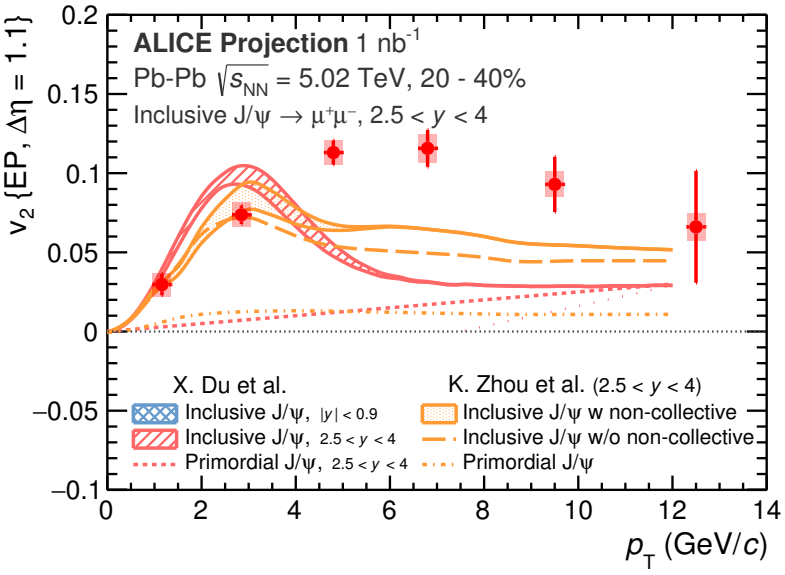

Figure 6.13 – Projection for J/ψ v_2 measurements with ALICE in Pb–Pb collisions at $\sqrt{s_{\rm NN}} = 5.02\,\text{TeV}$ for the full run 2 period. Calculations from [DR15] and [ZXXZ14] are shown

statistical gain is expected to reduce the uncertainties on the measurement and extend the $p_{\rm T}$ range up to 15 GeV/c. This projection assumes similar J/ψ v_2 values as the 2015 results with reduced statistical uncertainties by a factor 2 (from the luminosity increase). The last $p_{\rm T}$ bin was extrapolated from the previous points. First measurements of ψ(2S) and ϒ elliptic flow might also become accessible with the additional statistics. Results from other experiments in different kinematic regions will allow a deeper investigation of quarkonium elliptic flow.

6.3.2 Expected improvements with the ALICE upgrade

The ALICE experiment is preparing for a major detector upgrade during the second long shutdown for Run3 and Run4. The upgraded detectors will improve the current capabilities of the apparatus and allow to investigate new observables. Technical details on the systems can be found in Sec. 2.3. The next paragraphs summarize the expectations for flow measurements of heavy flavours. Simulations for projected results of quarkonium states, open-charm hadrons and B mesons from the , the , the Muon Spectrometer and the upgrades are presented.

The **luminosity increase** of the beams is expected to reach an integrated value of $10\,\text{nb}^{-1}$ for Pb–Pb collisions at $\sqrt{s_{\rm NN}} = 5.5\,\text{TeV}$ with an interaction rate of 50 kHz. Precision measurements would thus be possible. The improvement on the J/ψ elliptic flow measurement from the statistical gain is illustrated on Fig. 6.14 for Pb–Pb collisions up to $p_{\rm T}$=7 GeV/c (although measurements up to 15 GeV/c are expected) at both forward- and mid-rapidity.

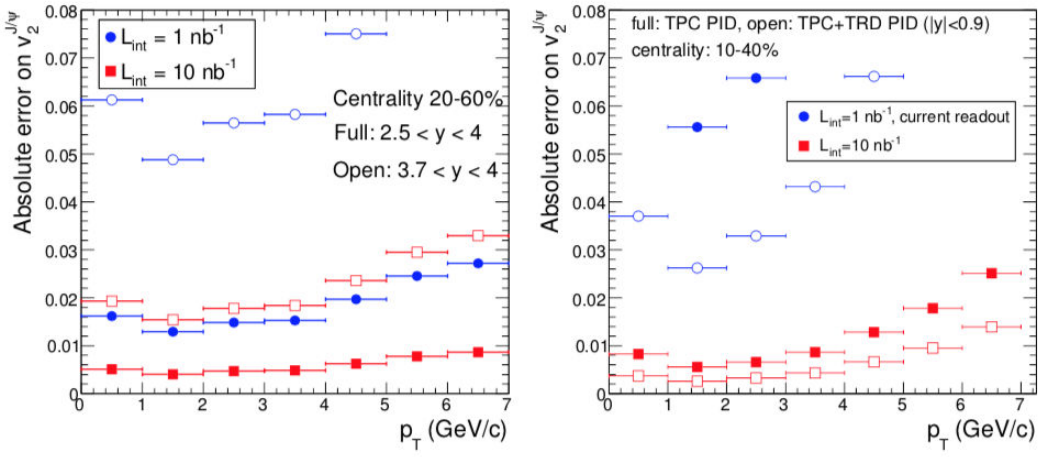

Figure 6.14 – Expected absolute statistical uncertainty on the measurement of J/ψ v_2 by ALICE as a function of p_T with the Muon Spectrometer (left panel, centrality range 20–60 %) and with the Central Barrel (right panel, centrality range 10–40 %)

Measurements in p–Pb collisions will also reach a higher precision (Fig. 6.15) with the expected 500 nb^{-1} integrated-luminosity scenario.

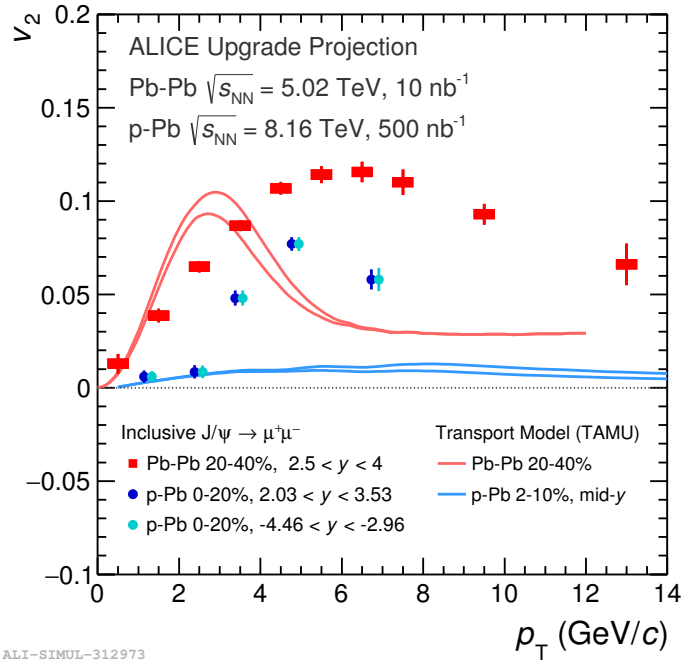

Figure 6.15 – Expected results at forward rapidity with statistical uncertainties for J/ψ v_2 in Pb–Pb and p–Pb collisions with the ALICE detector compared to calculations from [DR15]

The **extraction of the** ψ(2S) **signal** will also significantly benefits from this new detector. In particular, the signal over background ratio (around 0.2–0.5 % with the current Muon Spectrometer) is expected to improve by a factor up to 10. The background suppression should enable a p_T-differential measurements and larger significances, in particular in semi-central collisions where the ψ(2S) might be completely suppressed. A precise measurement of the ψ(2S) will also contribute to J/ψ results since the contribution from higher mass charmonium states to the J/ψ v_2 is not fully understood yet. Higher mass decays could either originate from (re)generated charmonium or initially produced states

and the fraction is unknown. Even if one could assume that the flow from decayed χ_c and $\psi(2S)$ will be passed on to the generated J/ψ , no quantitative v_2 estimations are available for any of these states.

With the Muon Forward Tracker (MFT) upgrade, ALICE will be capable of measuring **muons coming from displaced vertices**. This option is opening the way for both **prompt charmonium studies** and **b-hadron measurements** through muon and J/ψ decays. Current charmonium measurements with the Muon Spectrometer include a combinatorial background of semi-muonic decays from light hadrons and non-prompt correlated sources. Precise results of the prompt J/ψ component will be possible, allowing to study more specifically J/ψ production by removing the unknown contribution of the b-hadron to the charmonium measurements. However, the comparison of inclusive (by ALICE) and prompt (CMS and ATLAS) J/ψ v_2 measurements at $\sqrt{s_{\rm NN}} = 2.76$ TeV (Fig. 6.5) and $\sqrt{s_{\rm NN}} = 5.02$ TeV (Fig. 6.6) suggests that the non-prompt contribution has a rather low impact on the inclusive result.

The MFT will also provide a valuable tool for the **production study of beauty mesons** in heavy-ion collisions. Bottomonium studies will benefit from the larger collected data and potentially enable the measurement of Υ flow. The secondary vertex of the B decay is around 500 µm from the primary vertex and the measurement of displaced J/ψ production is not possible without a high-precision vertex tracker. The open beauty reference will be measured through the B $\rightarrow$ J/ψ +X channel. The measurement of the J/ψ v_2 from b-hadron decays could also become feasible with the Time Projection Chamber (TPC) upgrade and the TRD electron identification. Beauty measurements through non-prompt D^0 will also be accessed down to low $p_{\rm T}$. The expected elliptic flow results for B hadrons from D^0 and J/ψ channels are presented on Fig. 6.16 as a function of $p_{\rm T}$. These results will provide valuable insights on bottom energy loss in the medium.

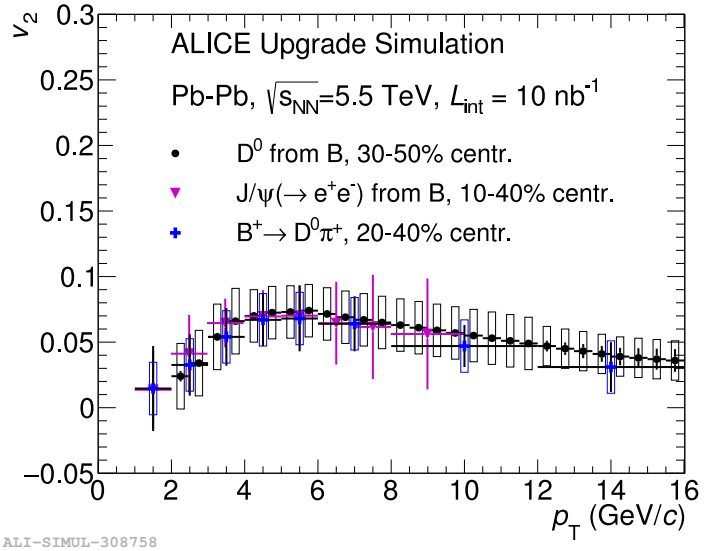

Figure 6.16 – ALICE projections for the elliptic flow of B mesons from different decays: $B^+ \rightarrow D^0\pi^+$, non-prompt D^0 and J/ψ from B decays at mid-rapidity with estimated statistical uncertainties

More precise results are also expected for **open charm** as well as **new measurements**. Increased signal-to-background ratios and direct measurements of the prompt fraction for D mesons will represent strong improvements. $p_{\rm T}$-differential studies will be both be extended to higher $p_{\rm T}$ and performed down to $p_{\rm T} = 0$, thanks to the better tracking of

low-momentum decay π. The first observation of the Λ_c elliptic flow and the comparison to charmed mesons (D^0 and D_s^+ on Fig. 6.17) will considerably help the study of charm quark thermalisation.

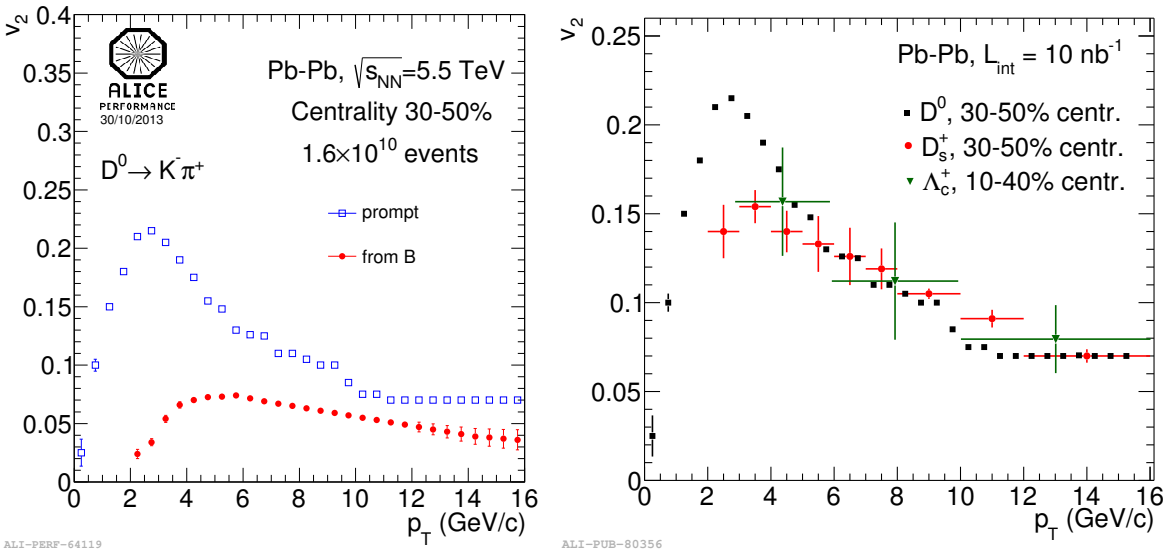

Figure 6.17 – ALICE projections for (Left) prompt and non-prompt D^0 v_2 in semi-central 30–50 % Pb-Pb collisions and (Right) D^0, D_s^+ and Λ_c v_2 with estimated statistical uncertainties at $\sqrt{s_{NN}} = 5.5\,\text{TeV}$

CHAPTER 7

CONCLUSION

"I imagined it. I wrote it. But I guess I never thought I'd see it."

— Ken Follett, The Pillars of the Earth

Quarkonium states have been for long considered as a probe and a thermometer of the quark gluon plasma. Production and dynamics inside the medium are described by transport models through two antagonist mechanisms. Since the initial production occurs before the formation of the QGP, the dissociation of $c\bar{c}$ states by Debye screening attests the formation of a deconfined state. At LHC energies, the higher charm density creates a second source of production by (re)combination of charm quarks, also in the case of a QGP formation. The combination of both mechanisms reproduces simply but satisfyingly J/ψ nuclear modification factor dependencies in comparison to experimental measurements.

In parallel to quarkonium production studies, flow results provide a complementary outlook on heavy bound states. Collective phenomena studies are one of the major source of information on the expanding system. Light-quark hadrons have shown numerous results, with flow coefficient measurements up the 6th harmonic for some species. Complex and precise experimental methods have been developed. Fewer measurements are available from heavy quarks. A major question is their degree of thermalisation in the medium. Whereas light quarks lose all information about their interactions prior to the hadronisation stage, the longer relaxation time of heavy quarks should allow to access the early evolution of the medium. Several positive elliptic flow coefficients are observed for D mesons and heavy-flavour decays at various energies. In the quarkonium case, (re)combined states are expected to inherit the flow of charm quarks that evolved with the medium. The first hint of positive J/ψ flow was observed by ALICE and CMS through the dimuon decay channel in Pb–Pb collisions at $\sqrt{s_{\mathrm{NN}}} = 2.76\,\mathrm{TeV}$.

This thesis focused on the second heavy-ion data taking of the LHC of Pb–Pb collisions at $\sqrt{s_{\mathrm{NN}}} = 5.02\,\mathrm{TeV}$. The increased energy and collected statistics enabled a very precise measurement of J/ψ v_2 as a function of p_{T} for different centrality ranges with the Muon Spectrometer at forward rapidity. The coefficient exhibits the largest significance in semi-central collision where a pioneering measurement was also performed through the di-electron decay channel at mid-rapidity. The comparison of D–meson and J/ψ flow is a strong case for charm thermalisation in the medium and quarkonium production through the (re)generation mechanism. The amplitude of the J/ψ flow is expected and reproduced by theoretical models when adding a significant fraction of (re)generation. However, a rapid decrease is predicted from intermediate p_{T} ($\sim 4\,\mathrm{GeV}/c$) up to a small anisotropy arising from the primordial component, while data do not show such a drop, remaining with a similar value of v_2 up to about $8\,\mathrm{GeV}/c$. The measurement was performed using

several methods and two different detectors. The first study of azimuthal dependence of J/ψ production is also presented here, with a hint of path-length dependence. Additionally, this thesis work includes the characterisation of silicon MAPS sensors for the future Muon Forward Tracker by testing full-scale prototypes. The detector upgrade will add new capabilities to the ALICE apparatus for dimuon studies at forward rapidity.

The study of smaller systems (e.g. pp and p–Pb at the LHC) have revealed unexpected results for flow and several characteristics previously associated to the heavy-ion physics are found. These features are also present in the heavy-flavour sector. New questions about the origin of collective effects and their precise definition – and part associated to hydrodynamics – are therefore raised. Understanding how to describe all systems and multiplicities is very important for the description – and the definition – of what we call *medium* in heavy-ion collisions. The observations of a positive J/ψ elliptic flow in p–Pb collisions at $\sqrt{s_{\rm NN}} = 5.02\,\text{TeV}$ and $\sqrt{s_{\rm NN}} = 8.16\,\text{TeV}$ by ALICE and CMS are also interrogating previous certitudes on quarkonium physics. The energy density should be too low for charm quark (re)combination and any path-length contribution should be much more negligible than in the Pb–Pb system, yet the amplitudes are comparable. The magnetic field created during the collision might contribute to these observations.

In summary, the current description of quarkonium production in the medium by transport models includes the initial production of quarkonium states, their dissociation in the QGP and a second source through (re)combination of charm quarks. The measurement of the J/ψ elliptic flow was expected to give access to the (re)generation fraction but the results reassess our understanding of charmonium production in the medium. The unexpected amplitude at intermediate $p_{\rm T}$ and the unexplained non-zero coefficient observed in the p–Pb system indicate that a least a mechanism is missing or misinterpreted. The picture of charmonia as QGP thermometer does not seem to hold any more and considering the unsettled production mechanism already in pp collisions, many directions could be accessible.

On the experimental side, several measurements would help understanding the picture. At the LHC, the next Pb–Pb run at $\sqrt{s_{\rm NN}} = 5.02\,\text{TeV}$ and in the future the upgrade of the ALICE detector and the high-luminosity LHC will give access to new and more precise observations: prompt J/ψ , ψ(2S) and Υ elliptic flow coefficients in pp, p–Pb and Pb–Pb collisions. Precise results at RHIC energies would also be extremely valuable. Results at intermediate energy between RHIC and the LHC or with different collision systems would allow to investigate deeper the interplay between suppression and (re)generation.

APPENDIX A

DATA SAMPLE

The data sample analysed in this work corresponds to the LHC15o period: Pb–Pb collisions at $\sqrt{s_{\mathrm{NN}}} = 5.02\,\mathrm{TeV}$. The detectors used in this analysis are the Muon Tracker, the Muon Trigger, the SPD, the V0, the T0, and the ZDC.

The following 137 runs from the 2015Pb–Pb period (LHC15o muon calo pass1) were validated by the quality analysis and used in this analysis:
246994,246991,246989,246984,246982,246980,246949,246948,246945,246942,246937,246930,
246871,246867,246865,246864,246859,246855,246851,246847,246846,246845,246844,246809,
246808,246807,246806,246805,246804,246765,246763,246760,246759,246758,246757,246755,
246751,246750,246676,246675,246495,246493,246488,246487,246434,246433,246431,246428,
246,24,246392,246391,246390,246276,246275,246272,246225,246222,246220,246217,246182,
246181,246178,246153,246152,246151,246148,246115,246113,246089,246087,246053,246049,
246048,246042,246037,246036,246012,246003,246001,245996,245963,245954,245952,245949,
245833,245831,245829,245793,245785,245775,245766,245759,245752,245738,245731,245729,
245705,245700,245692,245683,245554,245543,245542,245540,245535,245507,245505,245504,
245501,245496,245450,245446,245410,245409,245407,245401,245353,245347,245346,245345,
245343,245259,245253,245233,245232,245231,245152,245151,245146,245145,245068,245066,
245064,244983,244982,244980,244918.
Further information can be found on the TWiki page: electronic logbook link

APPENDIX B

ANALYSIS

B.1 Flow vector equalisation for the V0C

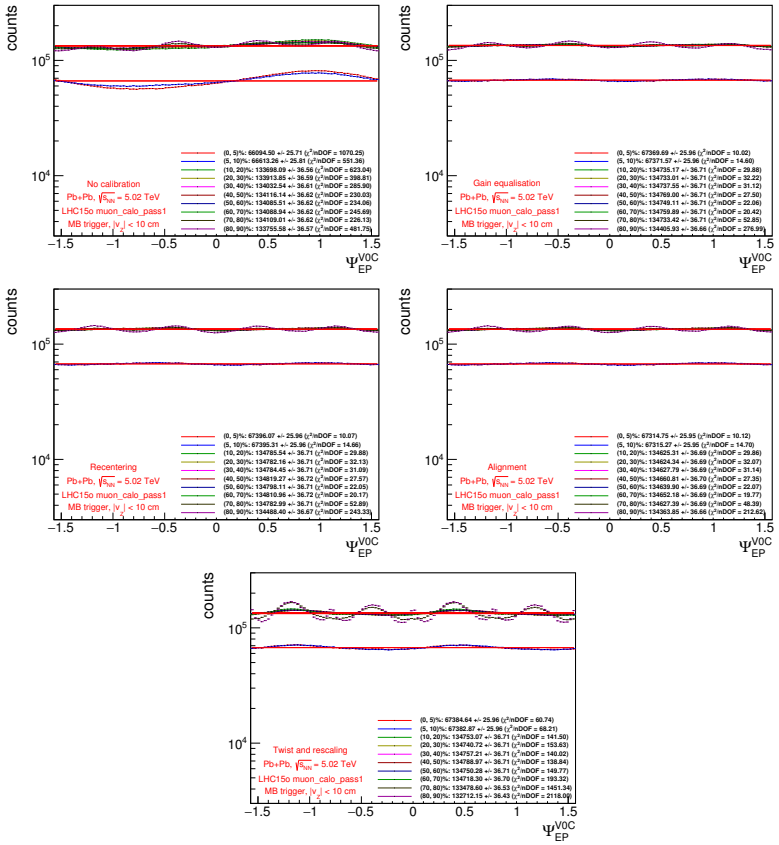

Figure B.1 – Distributions of the V0C EP angles in centrality ranges after each calibration step (from Step0 to Step4) from left to right and top to bottom.

B.2 Signal extraction

B.2.1 Fit function definitions

Extended Crystal-ball (CB2) The function was introduced by the Crystal-Ball Collaboration and contains a Gaussian core with two tails. It is defined with a normalisation factor N, two Gaussian core parameters ($\bar{x}$ and σ) and four real parameters for the tails (α, n, α' and n') as:

$$f(x) = \mathrm{N} \cdot \begin{cases} \exp\left(\frac{-(x-\bar{x})^2}{2\sigma^2}\right) & \text{pour } \alpha' > \frac{x-\bar{x}}{\sigma} > -\alpha \\ \mathrm{A} \cdot \left(\mathrm{B} - \frac{x-\bar{x}}{\sigma}\right)^{-n} & \text{pour } \frac{x-\bar{x}}{\sigma} \leq -\alpha \\ \mathrm{C} \cdot \left(\mathrm{D} + \frac{x-\bar{x}}{\sigma}\right)^{-n'} & \text{pour } \frac{x-\bar{x}}{\sigma} \geq \alpha' \end{cases}$$

with

$$\mathrm{A} = \left(\frac{n}{|\alpha|}\right)^n \cdot \exp\left(-\frac{|\alpha|^2}{2}\right) \;\; ; \quad \mathrm{B} = \frac{n}{|\alpha|} - |\alpha|$$

$$\mathrm{C} = \left(\frac{n'}{|\alpha'|}\right)^{n'} \cdot \exp\left(-\frac{|\alpha'|^2}{2}\right) \;\; ; \quad \mathrm{D} = \frac{n'}{|\alpha'|} - |\alpha'|$$

NA60 The NA60 function is also defined as a Gaussian core with two tails. The form features a normalisation factor N, two Gaussian core parameters ($\bar{x}$ and σ) but eight real parameters corresponding to the left and right tails (α^{L}, p_1^{L}, p_2^{L}, p_3^{L}, α^{R}, p_1^{R}, p_2^{R}, p_3^{R})

$$f(x) = \mathrm{N} \cdot \exp\left(-0.5\left(\frac{t}{t_0}\right)^2\right)$$

with

$$t = \frac{x-\bar{x}}{\sigma}$$

and

$$\begin{cases} t_0 = 1 + p_1^{\mathrm{L}}(\alpha^{\mathrm{L}} - t)^{(p_2^{\mathrm{L}} - p_3^{\mathrm{L}}\sqrt{\alpha^{\mathrm{L}} - t})} & \text{pour } t < \alpha^{\mathrm{L}} \\ t_0 = 1 & \text{pour } \alpha^{\mathrm{L}} < t < \alpha^{\mathrm{R}} \\ t_0 = 1 + p_1^{\mathrm{R}}(t - \alpha^{\mathrm{R}})^{(p_2^{\mathrm{R}} - p_3^{\mathrm{R}}\sqrt{t - \alpha^{\mathrm{R}}})} & \text{pour } t > \alpha^{\mathrm{R}} \end{cases}$$

Quadratic variable width Gaussian

A Gaussian function is expressed through an exponential form:

$$f(x) = \mathrm{N} \cdot \exp\left(\frac{-(x-\bar{x})^2}{2\sigma^2}\right)$$

where N is the normalisation factor, $\bar{x}$ is the position of the peak centre, and the σ parameter defines the width of the distribution and can be expressed as a function of two real parameters α and β as:

$$\sigma = \alpha + \beta\left(\frac{x-\bar{x}}{\bar{x}}\right)$$

In the *quadratic variable width* version, the definition of the σ parameter is modified by adding a quadratic term proportional to a third parameter γ.

$$\sigma = \alpha + \beta\left(\frac{x-\bar{x}}{\bar{x}}\right) + \gamma\left(\frac{x-\bar{x}}{\bar{x}}\right)^2$$

B.2.2 Fit function parameters

α	n	α′	n’
0.974323	7.36371	1.84248	16.0656

Table B.1 – CB2 parameters for J/ψ signal shape obtained from pp collisions for $0 < p_{\mathrm{T}} < 12\mathrm{GeV}/c$

p_{T} bin (GeV/c)	α	n	α′	n’
[0., 2.]	0.88	4.80	2.38	2.44
[2., 4.]	0.98	3.53	2.29	2.55
[4., 6.]	1.07	3.14	2.24	2.72
[6., 8.]	1.17	3.02	2.12	3.07
[8., 12.]	1.26	3.02	1.91	3.42
[0., 12.]	0.95	3.94	2.32	2.53

Table B.2 – p_{T}-dependence of CB2 parameters for J/ψ signal shape obtained from J/ψ embedding sample for centrality 0-90% and $-4 < y < -2.5$

p_{T} bin (GeV/c)	α^{L}	p_1^{L}	p_2^{L}	p_3^{L}	α^{L}	p_1^{L}	p_2^{L}	p_3^{L}
[0., 2.]	-0.389	0.225	1.158	0.042	2.275	0.189	1.293	0.062
[2., 4.]	-0.728	0.238	1.096	0.025	2.194	0.190	1.291	0.062
[4., 6.]	-0.910	0.237	1.119	0.028	2.168	0.186	1.267	0.051
[6., 8.]	-1.098	0.233	1.119	0.028	2.011	0.184	1.339	0.076
[8., 12.]	-1.127	0.226	1.094	0.019	1.406	0.172	1.484	0.094
[0., 12.]	-0.668	0.233	1.100	0.028	2.225	0.189	1.291	0.061

Table B.3 – p_{T}-dependence of NA60 parameters for J/ψ signal shape obtained from J/ψ embedding sample for centrality 0-90% and $-4 < y < -2.5$

B.3 Test results and numerical values

B.3.1 Results with the Event Plane method

p_{T} bin (GeV/c)	[0.,2.]	[2.,4.]	[4.,6.]	[6.,8.]	[8.,12.]
v_2 5–20 %	0.0129652	0.0539739	0.0660315	0.0800134	0.0131028
Stat. unc. 5–20 %	0.0192097	0.0187735	0.0260936	0.0436621	0.059289
Syst. unc. 5–20 %	0.0106551	0.00990476	0.0110827	0.0112789	0.0187165
v_2 20–40 %	0.0406169	0.090584	0.105	0.123861	0.0841397
Stat. unc. 20–40 %	0.0197043	0.0206206	0.0262324	0.0374332	0.049548
Syst. unc. 20–40 %	0.00921203	0.00904498	0.00915174	0.0100799	0.0109835
v_2 40–60 %	0.0151947	0.0482966	0.059613	-0.000623966	0.126702
Stat. unc. 40–60 %	0.0348091	0.0289469	0.0380045	0.0380045	0.086171
Syst. unc. 40–60 %	0.0132554	0.0116865	0.0117759	0.0240241	0.0195482

Table B.4 – Table of data points shown in Fig. B.2 : J/ψ v_2 (*corrected* values) in centrality classes 5–20 % , 20–40 % and 40–60 % in rapidity range $-4 < y < -2.5$ from the $d\mathrm{N}/d\Delta\phi$ method with the V0A as event plane detector

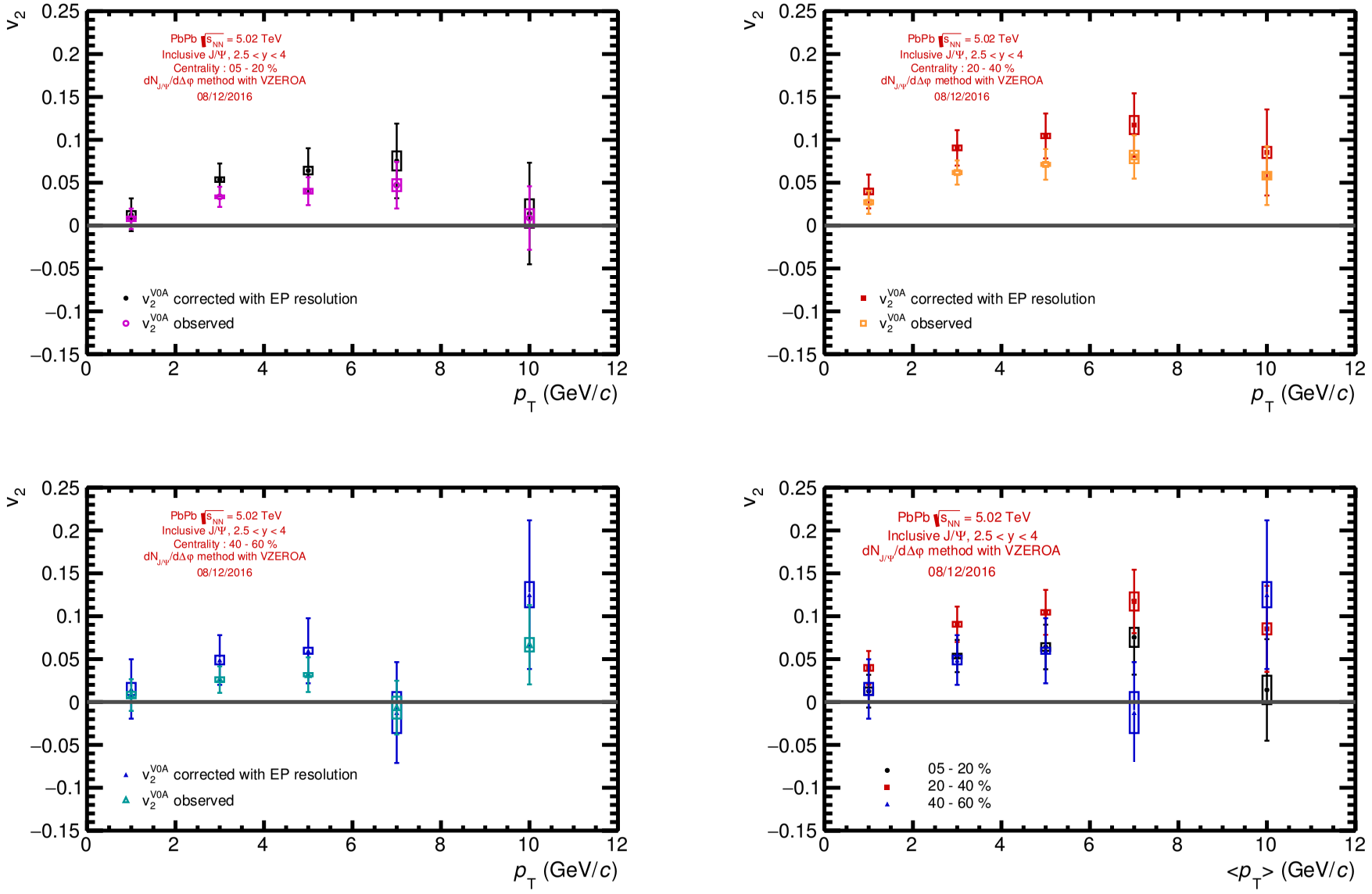

Figure B.2 – Inclusive J/ψ v_2 as a function of p_T in the rapidity range $2.5 < y < 4.0$ in 3 centrality classes using the $dN/d\Delta\phi$ method and the V0A as event plane detector. Boxes represent systematic uncertainty from the signal extraction.

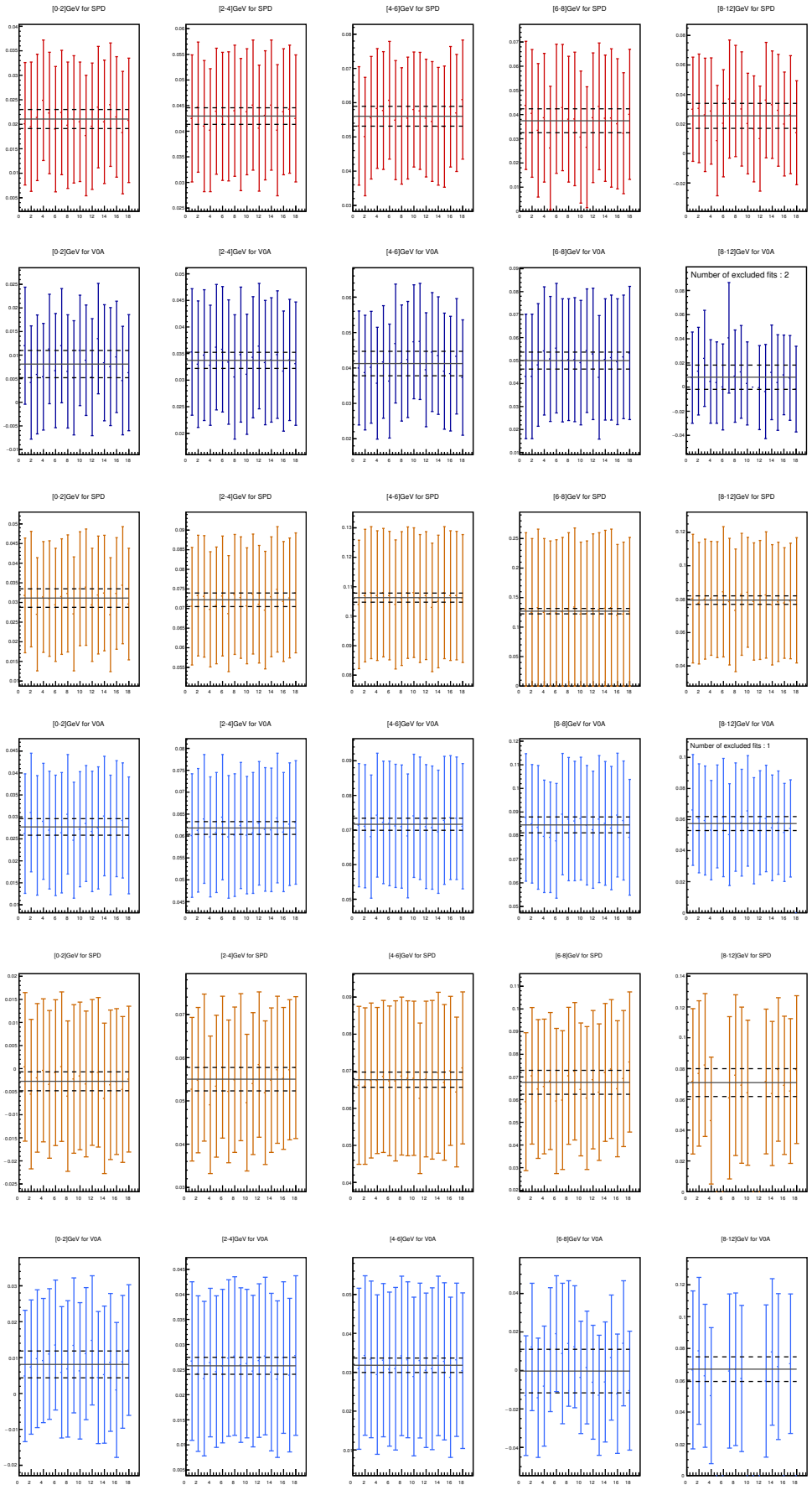

Figure B.3 – Systematics for J/ψ v_2 extraction in the centrality ranges 5–20 %, 20–40 % and 40–60 % using the $dN/d\Delta\phi$ technique with the SPD (red) or the V0A (blue) as EP detector

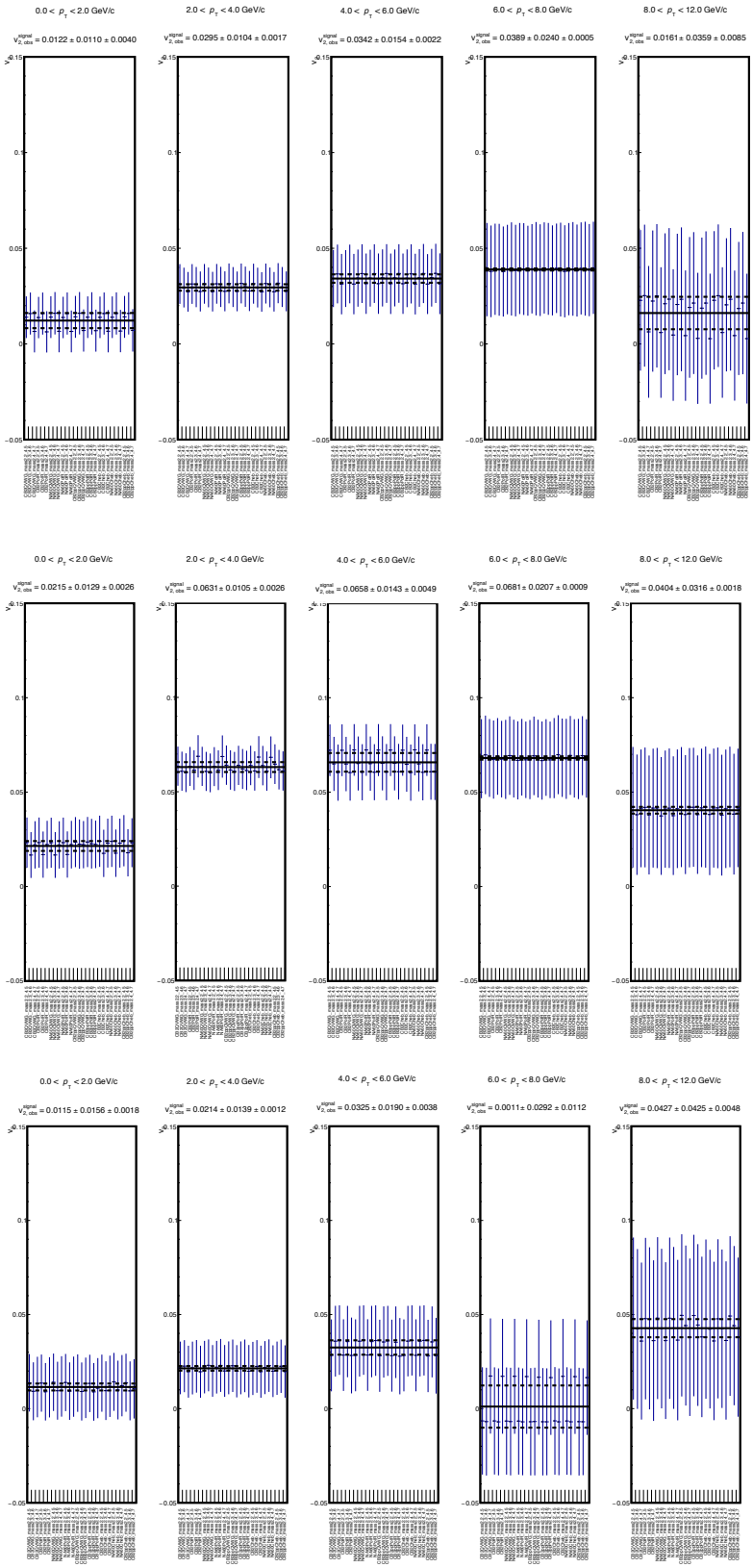

Figure B.4 – Systematics for J/ψ v_2 extraction in the centrality ranges 5-20%, 20-40% and 40-60% using the mean v_2 technique with the EP method and the V0A as EP detector

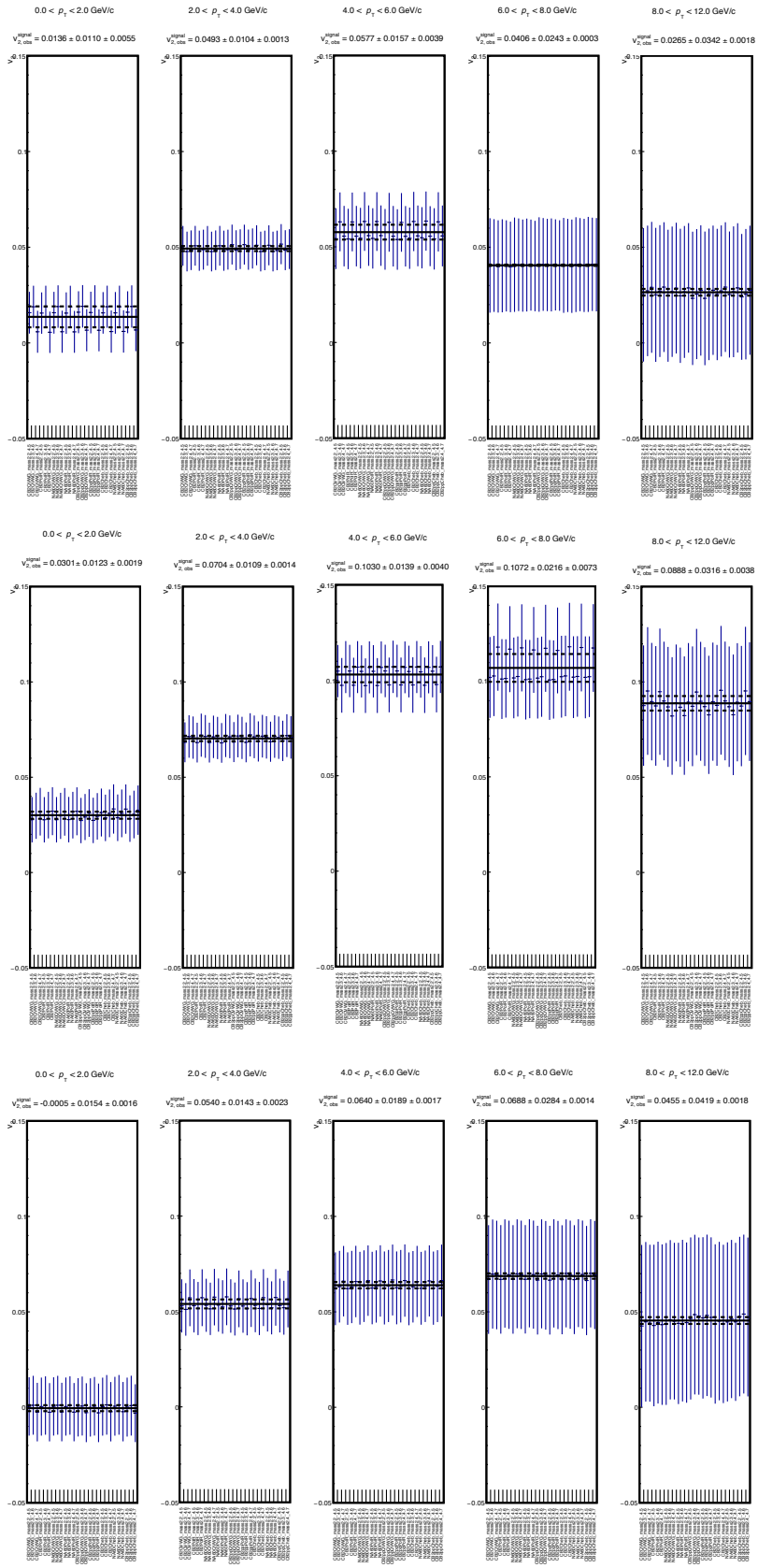

Figure B.5 – Systematics for J/ψ v_2 extraction in the centrality ranges 5-20%, 20-40% and 40-60% using the mean v_2 technique with the EP method and the SPD as EP detector

B.3.2 Results with the Scalar Product method

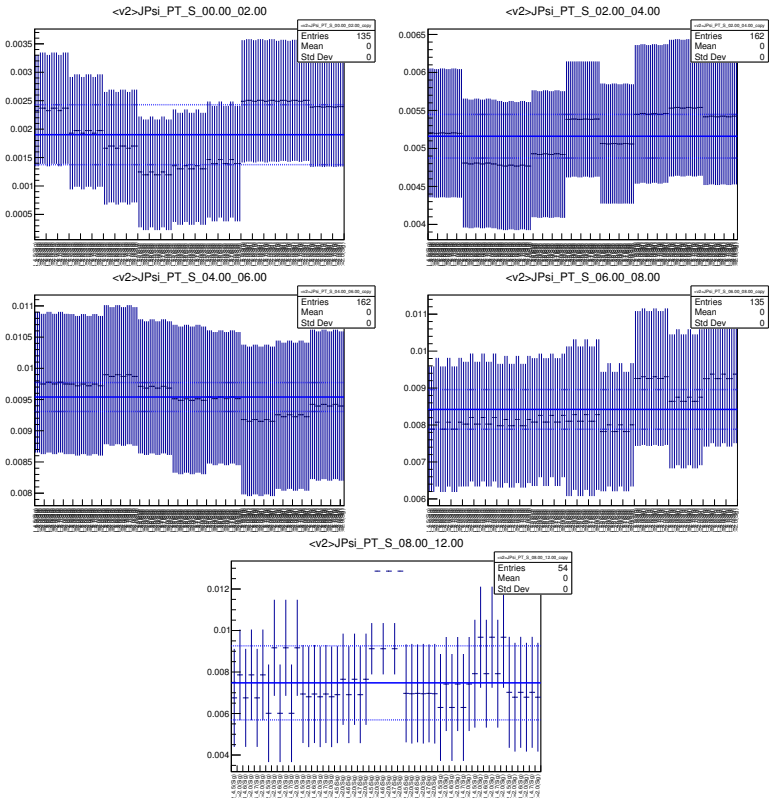

Figure B.6 – Systematics for J/ψ v_2 extraction in the centrality ranges 20-40% using the mean v_2 technique with the SP method and the SPD as EP detector

p_T bin (GeV/c)	[0.,2.]	[2.,4.]	[4.,6.]	[6.,8.]	[8.,12.]
v_2 (SPD)	0.0262161	0.0667095	0.123923	0.108164	0.0899637
Stat. unc. (SPD)	0.0130821	0.0110425	0.014693	0.0232542	0.0325298
Syst. unc. (SPD)	0.0100893	0.0077582	0.0072208	0.00986504	0.00920849

Table B.5 – Table of data points shown in Fig. 5.29 : J/ψ v_2 (*corrected* values) in the 20–40 % centrality range and in the rapidity range $-4 < y < -2.5$ from the $\langle v_2 \rangle$ method with the scalar product and the SPD as event plane detector

p_T bin (GeV/c)	[0.,2.]	[2.,4.]	[4.,6.]	[6.,8.]	[8.,12.]
v_2 (V0A)	0.023442	0.0736947	0.106083	0.122373	0.0718723
Stat. unc. (V0A)	0.0169534	0.0143303	0.0190242	0.029627	0.0433498
Syst. unc. (V0A)	0.0112316	0.00999393	0.0113007	0.0108477	0.0143983

Table B.6 – Table of data points shown in Fig. 5.29 : J/ψ v_2 (*corrected* values) in the 20–40 % centrality range and in the rapidity range $-4 < y < -2.5$ from the $\langle v_2 \rangle$ method with the scalar product and the V0A as event plane detector

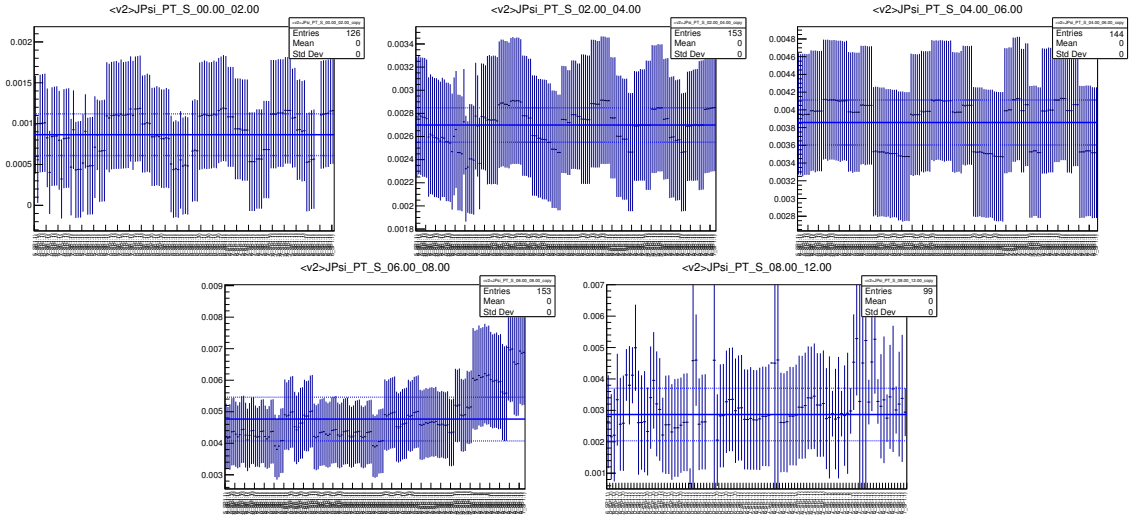

Figure B.7 – Systematics for J/ψ v_2 extraction in the centrality ranges 20-40% using the mean v_2 technique with the SP method and the V0A as EP detector

B.4 R_{AA} vs path length

B.4.1 5-20% centrality range

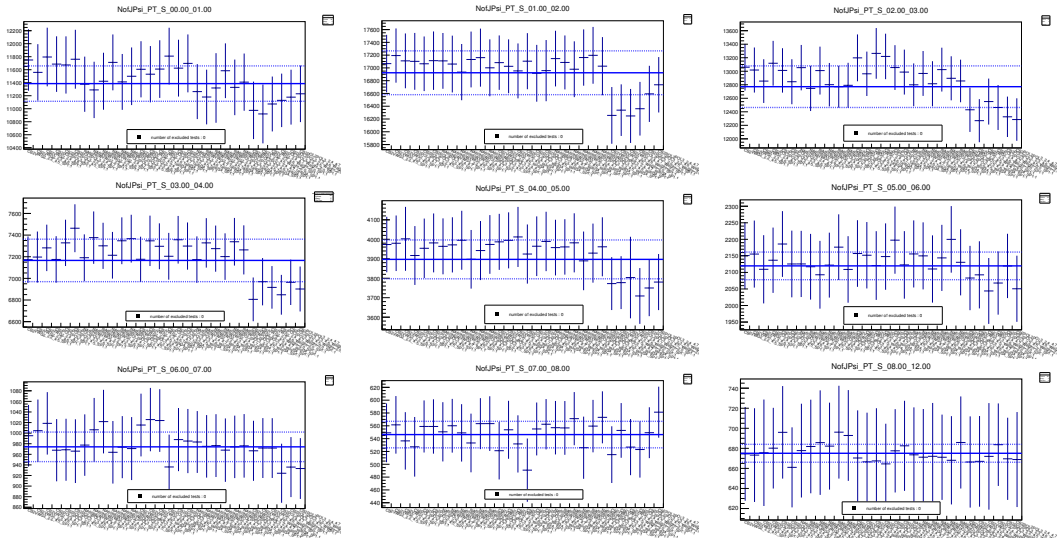

Figure B.8 – In-plane signal extraction tests for the 5-20% centrality class

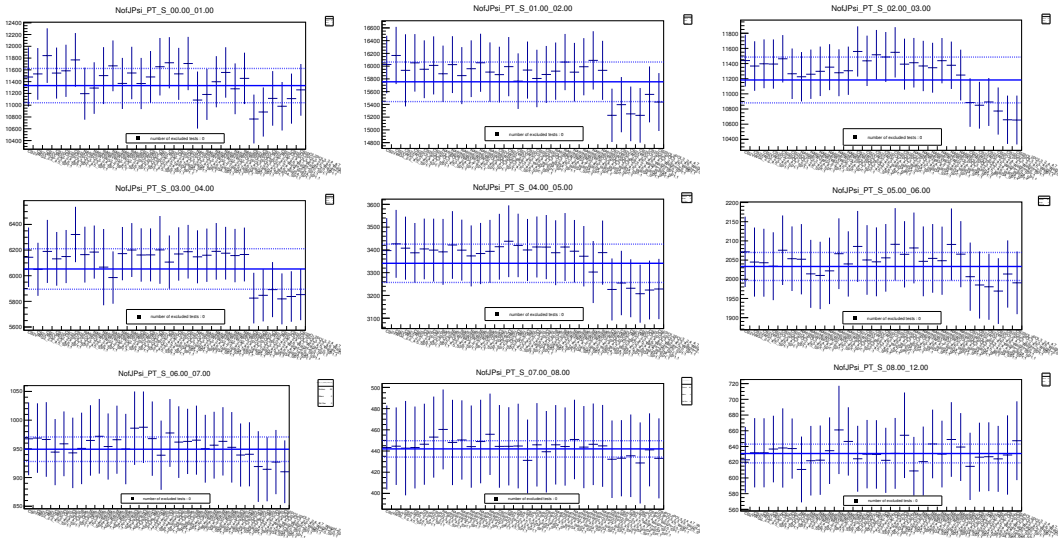

Figure B.9 – In-plane signal extraction tests for the 5-20% centrality class

B.4.2 20-40% centrality range

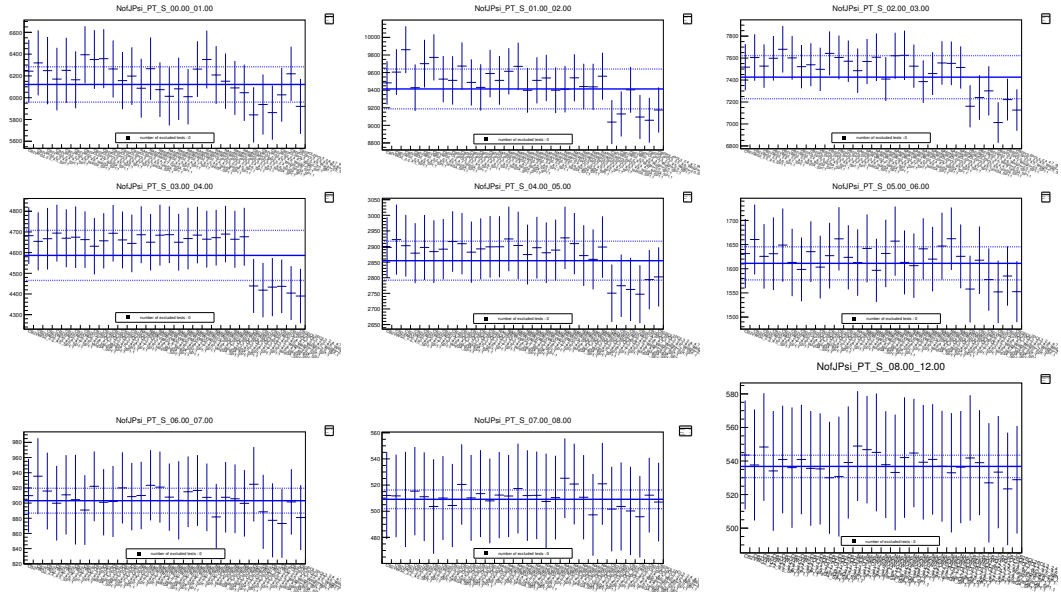

Figure B.10 – In-plane signal extraction tests for the 20-50% centrality class

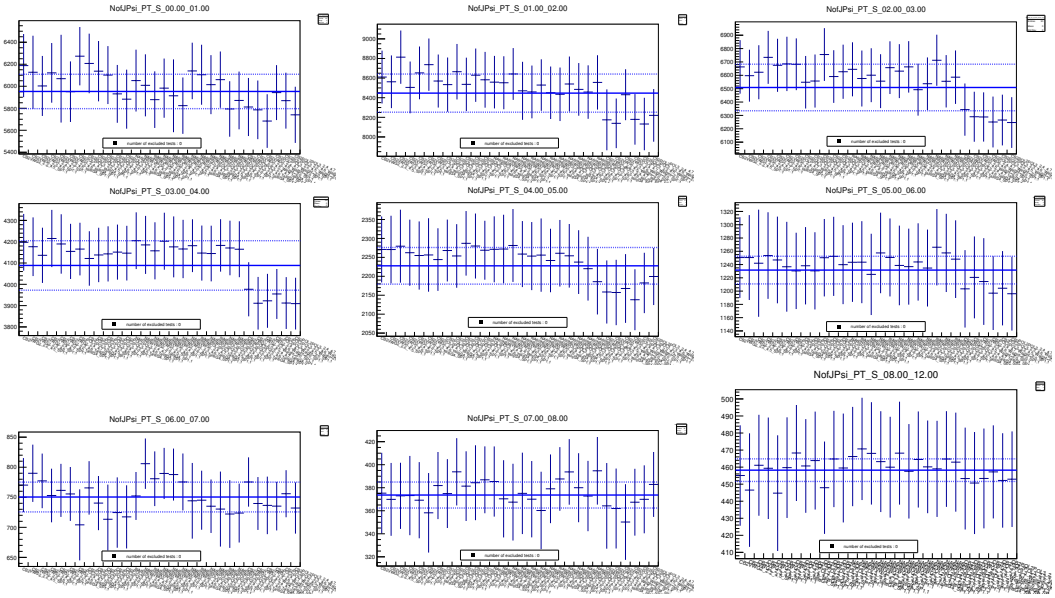

Figure B.11 – In-plane signal extraction tests for the 20-40% centrality class

B.4.3 40-60% centrality range

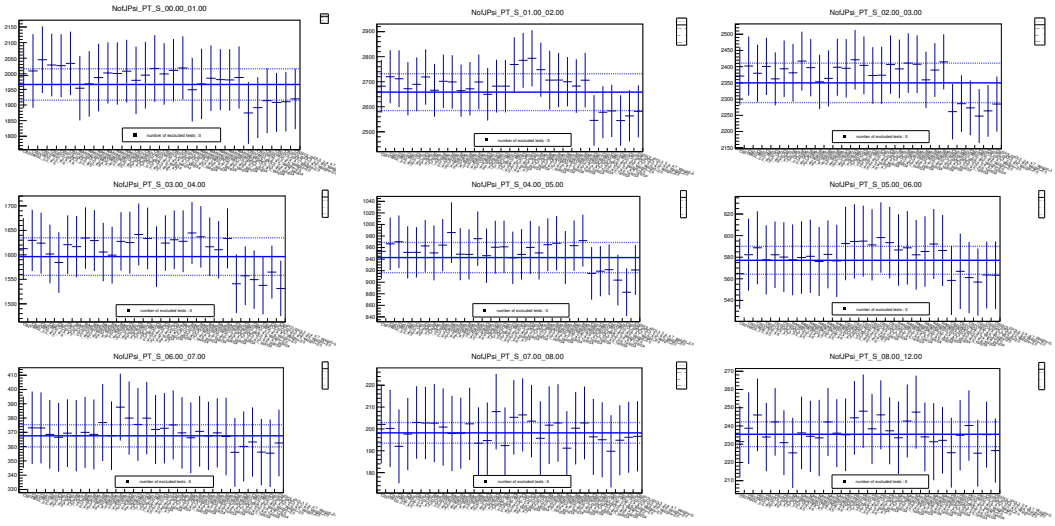

Figure B.12 – In-plane signal extraction tests for the 40-60% centrality class

	In-plane			Out-of-plane		
p_T(GeV/c)	5–20 %	20–40 %	40–60 %	5–20 %	20–40 %	40–60 %
0–1	0.743	0.729	0.794	0.736	0.701	0.805
stat.	0.029	0.032	0.04	0.029	0.032	0.042
sys.	0.045	0.055	0.073	0.0459	0.054	0.072
1–2	0.709	0.729	0.692	0.657	0.647	0.738
stat.	0.018	0.020	0.028	0.019	0.021	0.028
sys.	0.042	0.054	0.073	0.041	0.053	0.073
2–3	0.685	0.724	0.767	0.582	0.618	0.645
stat.	0.018	0.0120	0.028	0.017	0.026	0.027
sys.	0.043	0.055	0.073	0.044	0.0537	0.071
3–4	0.553	0.638	0.761	0.453	0.553	0.647
stat	0.017	0.019	0.029	0.016	0.017	0.0268
sys.	0.043	0.054	0.072	0.0401	0.053	0.072
4–5	0.533	0.696	0.783	0.439	0.520	0.657
stat.	0.021	0.024	0.037	0.018	0.020	0.033
sys.	0.042	0.053	0.074	0.040	0.052	0.072
5–6	0.415	0.567	0.689	0.383	0.415	0.559
stat.	0.020	0.024	0.039	0 .017	0.0203	0.033
sys.	0.039	0.052	0.071	0.0389	0.052	0.070
6–7	0.315	0.563	0.758	0.300	0.028	0.522
stat.	0.019	0.029	0.051	0.019	0.053	0.042
sys.	0.039	0.052	0.071	0.038	0.448	0.069
7–8	0.345	0.569	0.762	0.273	0.400	0.650
stat.	0.027	0.036	0.065	0.023	0.034	0.060
sys.	0.042	0.052	0.072	0.038	0.052	0.079
8–12	0.330	0.470	0.699	0.305	0.388	0.643
stat.	0.022	0.030	0.058	0.022	0.025	0.052
sys.	0.038	0.051	0.073	0.038	0.052	0.071

Table B.7 – (Table of data points shown in Fig.5.35) In- and out-of-plane R_{AA} values for each centrality and p_T bin

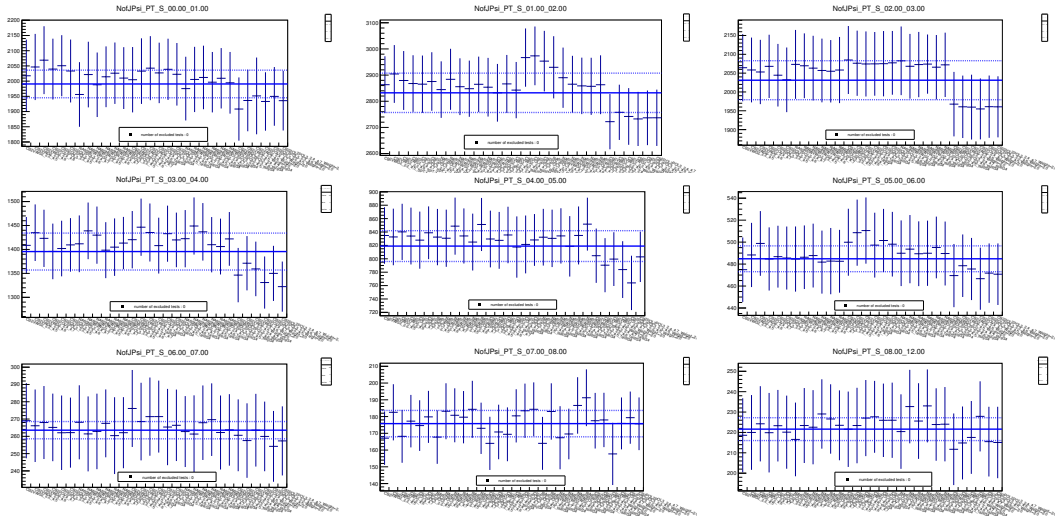

Figure B.13 – In-plane signal extraction tests for the 40-60% centrality class

B.5 Acceptance Efficiency

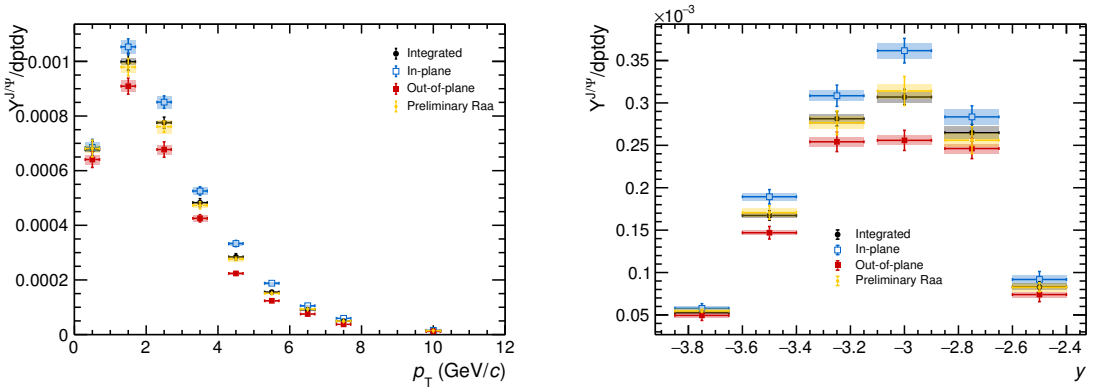

Figure B.14 – Yields comparison between in-, out-of-plane and integrated samples and previous analysis as a function of (Left) p_T and (Right) rapidity

B.6 Systematics

p_{T} (GeV/c)	Trigger efficiency (%)
0–1	0.08
1–2	0.01
2–3	0.01
3–4	0.009
4–5	0.007
5–6	0.006
6–7	0.004
7–8	0.004
8–12	0.003

Table B.8 – Systematic uncertainty from the trigger efficiency as a function of p_{T}

ACRONYMS

AdS/CFT anti-de Sitter/conformal field theory.

AERD Address Encoder Reset Decoder.

AGS AGS Alternating Gradient Synchrotron.

ALICE A Large Ion Colliding Experiment.

ALPIDE ALICE PIxel DEtector.

ATLAS A Toroidal Lhc ApparatuS.

BNL Brookhaven National Laboratory.

BTF Beam Test Facility.

CERN Centre Européen pour la Recherche Nucléaire.

CMOS Complementary Metal–Oxide–Semiconductor.

CMS Compact Muon Solenoid.

CNM Cold Nuclear Matter.

CTP Central Trigger Processor.

DAQ Data AcQuisition.

DCA Distance of Closest Approach.

DESY Deutsches Elektronen-Synchrotron.

DUT Device Under Test.

DY Drell-Yan.

EMCal ElectroMagnetic Calorimeter.

EP Event Plane.

FCC Future Circular Collider.

GEM Gas Electron Multiplier.

HLT High Level Trigger.

IP Interaction Point.

ITS Inner Tracking System.

LEIR Low-Energy Injector Ring.

LHC Large Hadron Collider.

LHCb Large Hadron Collider beauty.

LHCf Large Hadron Collider forward.

LINAC LINear ACcelerator.

MAPS Monolithic Active Pixel Sensor.

MB Minimum Bias.

MC Monte Carlo.

MFT Muon Forward Tracker.

MTR Muon Trigger.

MWPC Multi-Wire-Proportional Chambers.

NMOS n-channel Metal Oxide Semiconductor.

NRQCD Non Relativistic QCD.

PAL Pohang Accelerator Laboratory.

pALPIDE Prototype ALICE PIxel DEtector.

pALPIDE-1 Prototype ALPIDE-1.

pALPIDE-2 Prototype ALPIDE-2.

pALPIDE-3 Prototype ALPIDE-3.

pALPIDE-3b Prototype ALPIDE-3b.

PCB PCB Printed Circuit Board.

PDS Permanent Data Storage.

PHENIX Pioneering High Energy Nuclear Interaction eXperiment.

PHOS PHoton Spectrometer.

PMOS p-channel Metal Oxide Semiconductor.

pQCD perturbative QCD.

PS Proton Synchrotron.

PSB Proton Synchrotron Booster.

QCD Quantum ChromoDynamics.

QGP Quark Gluon Plasma.

RHIC Relativistic Heavy-Ion Collider.

RMS Root Mean Square.

RPC Resistive Plate Chamber.

SDD Silicon Drift Detector.

SLAC Stanford Linear Accelerator Center.

SLRI Synchrotron Light Research Institute.

SP Scalar Product.

SPD Silicon Pixel Detector.

SPS Super Proton Synchrotron.

SSD Silicon Strip Detector.

STAR Solenoidal Tracker At RHIC.

T0 TZERO.

TOF Time Of Flight.

TOTEM TOTal cross section, Elastic scattering and diffraction dissociation Measurement at the LHC.

TPC Time Projection Chamber.

TRD Transition Radiative Detector.

V0 VZERO.

V0A VZERO-A.

V0C VZERO-C.

ZDC Zero Degree Calorimeter.

List of Figures

List of Tables

BIBLIOGRAPHY

[A+74a] E598, J. J. Aubert et al. Experimental Observation of a Heavy Particle J. *Phys. Rev. Lett.*, 33:1404–1406, 1974. 44

[A+74b] SLAC-SP-017, J. E. Augustin et al. Discovery of a Narrow Resonance in e^+e^- Annihilation. *Phys. Rev. Lett.*, 33:1406–1408, 1974. [Adv. Exp. Phys.5,141(1976)]. 44

[A+01a] STAR, K. H. Ackermann et al. Elliptic flow in Au+Au collisions at $\sqrt{s_{\rm NN}}$ = 130 GeV. *Phys. Rev. Lett.*, 86:402–407, 2001, nucl-ex/0009011. 30

[A+01b] STAR, C. Adler et al. Identified particle elliptic flow in Au+Au collisions at $\sqrt{s_{\rm NN}}$ = 130 GeV. *Phys. Rev. Lett.*, 87:182301, 2001, nucl-ex/0107003. 30

[A+03a] STAR, C. Adler et al. Disappearance of back-to-back high $p_{\rm T}$ hadron correlations in central Au+Au collisions at $\sqrt{s_{\rm NN}}$ = 200 GeV. *Phys. Rev. Lett.*, 90:082302, 2003, nucl-ex/0210033. 7

[A+03b] PHENIX, S. S. Adler et al. Elliptic flow of identified hadrons in Au+Au collisions at $\sqrt{s_{\rm NN}}$ = 200 GeV. *Phys. Rev. Lett.*, 91:182301, 2003, nucl-ex/0305013. 38, XXIV

[A+03c] GEANT4, S. Agostinelli et al. GEANT4: A Simulation toolkit. *Nucl. Instrum. Meth.*, A506:250–303, 2003. 80

[A+03d] NA49, C. Alt et al. Directed and elliptic flow of charged pions and protons in Pb+Pb collisions at 40-A-GeV and 158-A-GeV. *Phys. Rev.*, C68:034903, 2003, nucl-ex/0303001. 30

[A+04a] STAR, J. Adams et al. Azimuthal anisotropy at RHIC: The First and fourth harmonics. *Phys. Rev. Lett.*, 92:062301, 2004, nucl-ex/0310029. 53

[A+04b] STAR, John Adams et al. Particle type dependence of azimuthal anisotropy and nuclear modification of particle production in Au+Au collisions at $\sqrt{s_{\rm NN}}$ = 200 GeV. *Phys. Rev. Lett.*, 92:052302, 2004, nucl-ex/0306007. 31

[A+05a] STAR, J. Adams et al. Azimuthal anisotropy in Au+Au collisions at $\sqrt{s_{\rm NN}}$ = 200 GeV. *Phys. Rev.*, C72:014904, 2005, nucl-ex/0409033. 31

[A+05b] STAR, John Adams et al. Experimental and theoretical challenges in the search for the quark gluon plasma: The STAR Collaboration's critical assessment of the evidence from RHIC collisions. *Nucl. Phys.*, A757:102–183, 2005, nucl-ex/0501009. 29

[A+05c] PHENIX, K. Adcox et al. Formation of dense partonic matter in relativistic nucleus-nucleus collisions at RHIC: Experimental evaluation by the PHENIX collaboration. *Nucl. Phys.*, A757:184–283, 2005, nucl-ex/0410003. 43

[A+05d] PHENIX, S. S. Adler et al. Measurement of single electron event anisotropy in Au+Au collisions at $\sqrt{s_{\mathrm{NN}}}$ = 200 GeV. *Phys. Rev.*, C72:024901, 2005, nucl-ex/0502009. 34

[A+05e] PHENIX, S. S. Adler et al. Saturation of azimuthal anisotropy in Au+Au collisions at $\sqrt{s_{\mathrm{NN}}}$ = 62 GeV to 200 GeV. *Phys. Rev. Lett.*, 94:232302, 2005, nucl-ex/0411040. 55

[A+05f] NA50, B. Alessandro et al. A New measurement of J/ψ suppression in Pb-Pb collisions at 158 GeV per nucleon. *Eur. Phys. J.*, C39:335–345, 2005, hep-ex/0412036. 48

[A+07a] STAR, B. I. Abelev et al. Mass, quark-number, and $\sqrt{s_{\mathrm{NN}}}$ dependence of the second and fourth flow harmonics in ultra-relativistic nucleus-nucleus collisions. *Phys. Rev.*, C75:054906, 2007, nucl-ex/0701010. 31

[A+07b] STAR, B. I. Abelev et al. Partonic flow and ϕ-meson production in Au+Au collisions at $\sqrt{s_{\mathrm{NN}}}$ = 200 GeV. *Phys. Rev. Lett.*, 99:112301, 2007, nucl-ex/0703033. 53

[A+07c] PHENIX, A. Adare et al. Scaling properties of azimuthal anisotropy in Au+Au and Cu+Cu collisions at $\sqrt{s_{\mathrm{NN}}}$= 200 GeV. *Phys. Rev. Lett.*, 98:162301, 2007, nucl-ex/0608033. 31

[A+07d] NA60, R. Arnaldi et al. J/ψ production in indium-indium collisions at 158-GeV/nucleon. *Phys. Rev. Lett.*, 99:132302, 2007. 48

[A+08] ALICE, K. Aamodt et al. The ALICE experiment at the CERN LHC. *JINST*, 3:S08002, 2008. 11, 2

[A+09a] PHENIX, S. Afanasiev et al. High-p_{T} π^0 Production with Respect to the Reaction Plane in Au+Au Collisions at $\sqrt{s_{\mathrm{NN}}}$ = 200 GeV. *Phys. Rev.*, C80:054907, 2009, 0903.4886. 101, 108

[A+09b] PHENIX, S. Afanasiev et al. Photoproduction of J/ψ and of high mass e^+e^- in ultra-peripheral Au+Au collisions at $\sqrt{s_{\mathrm{NN}}}$= 200 GeV. *Phys. Lett.*, B679:321–329, 2009, 0903.2041. 46

[A+10] ALICE, K Aamodt et al. Elliptic flow of charged particles in Pb-Pb collisions at 2.76 TeV. *Phys. Rev. Lett.*, 105:252302, 2010, 1011.3914. 31

[A+11a] LHCb, R. Aaij et al. Measurement of J/ψ production in pp collisions at $\sqrt{s}$ = 7 TeV. *Eur. Phys. J.*, C71:1645, 2011, 1103.0423. 45

[A+11b] PHENIX, A. Adare et al. Heavy Quark Production in $p+p$ and Energy Loss and Flow of Heavy Quarks in Au+Au Collisions at $\sqrt{s_{\mathrm{NN}}}$ = 200 GeV. *Phys. Rev.*, C84:044905, 2011, 1005.1627. 34, 35, XXIV

[A+11c] PHENIX, A. Adare et al. J/ψ suppression at forward rapidity in Au+Au collisions at $\sqrt{s_{\mathrm{NN}}}$ = 200 GeV. *Phys. Rev.*, C84:054912, 2011, 1103.6269. 50, 51, XXV

[A+12a] LHCb, R Aaij et al. Measurement of $\psi(2S)$ meson production in pp collisions at $\sqrt{s}$= 7 TeV. *Eur. Phys. J.*, C72:2100, 2012, 1204.1258. 45

[A+12b] LHCb, R Aaij et al. Measurement of the ratio of prompt χ_c to J/ψ production in pp collisions at $\sqrt{s}$ = 7 TeV. *Phys. Lett.*, B718:431–440, 2012, 1204.1462. 45

[A+12c] ALICE, Betty Abelev et al. J/ψ suppression at forward rapidity in Pb-Pb collisions at $\sqrt{s_{\rm NN}}$ = 2.76 TeV. *Phys. Rev. Lett.*, 109:072301, 2012, 1202.1383. 50, 51, XXV

[A+12d] PHENIX, A. Adare et al. Deviation from quark-number scaling of the anisotropy parameter v_2 of pions, kaons, and protons in Au+Au collisions at $\sqrt{s_{\rm NN}}$ = 200 GeV. *Phys. Rev.*, C85:064914, 2012, 1203.2644. 31

[A+12e] PHENIX, A. Adare et al. J/ψ suppression at forward rapidity in Au+Au collisions at $\sqrt{s_{\rm NN}}$ = 39 and 62.4 GeV. *Phys. Rev.*, C86:064901, 2012, 1208.2251. 51, XXV

[A+13a] ALICE, Ehab Abbas et al. J/ψ Elliptic Flow in Pb-Pb Collisions at $\sqrt{s_{\rm NN}}$ = 2.76 TeV. *Phys. Rev. Lett.*, 111:162301, 2013, 1303.5880. 54, 56, 107, XXV, 7

[A+13b] ALICE, Betty Abelev et al. Centrality determination of Pb-Pb collisions at $\sqrt{s_{\rm NN}}$ = 2.76 TeV with ALICE. *Phys. Rev.*, C88(4):044909, 2013, 1301.4361. 6

[A+13c] ALICE, Betty Abelev et al. Coherent J/ψ photoproduction in ultra-peripheral Pb-Pb collisions at $\sqrt{s_{\rm NN}}$ = 2.76 TeV. *Phys. Lett.*, B718:1273–1283, 2013, 1209.3715. 46

[A+13d] STAR, L. Adamczyk et al. Measurement of J/ψ Azimuthal Anisotropy in Au+Au Collisions at $\sqrt{s_{\rm NN}}$ = 200 GeV. *Phys. Rev. Lett.*, 111(5):052301, 2013, 1212.3304. 53, 54, XXV, 7

[A+13e] STAR, L. Adamczyk et al. Third Harmonic Flow of Charged Particles in Au+Au Collisions at $\sqrt{s_{\rm NN}}$ = 200 GeV. *Phys. Rev.*, C88(1):014904, 2013, 1301.2187. 31

[A+13f] PHENIX, A. Adare et al. Nuclear Modification of $\psi(2S)$, χ_c, and J/ψ Production in d+Au Collisions at $\sqrt{s_{\rm NN}}$ = 200 GeV. *Phys. Rev. Lett.*, 111(20):202301, 2013, 1305.5516. 46

[A+13g] PHENIX, A. Adare et al. Υ(1S+2S+3S) production in d+Au and $p+p$ collisions at $\sqrt{s_{\rm NN}}$ = 200 GeV and cold-nuclear matter effects. *Phys. Rev.*, C87(4):044909, 2013, 1211.4017. 46

[A+14a] LHCb, R Aaij et al. Study of J/ψ production and cold nuclear matter effects in p-Pb collisions at $\sqrt{s_{\rm NN}}$ = 5 TeV. *JHEP*, 02:072, 2014, 1308.6729. 46

[A+14b] LHCb, Roel Aaij et al. Study of Υ production and cold nuclear matter effects in p-Pb collisions at $\sqrt{s_{\rm NN}}$=5 TeV. *JHEP*, 07:094, 2014, 1405.5152. 46

[A+14c] ALICE, B Abelev et al. Technical Design Report for the Upgrade of the ALICE Inner Tracking System. *J. Phys.*, G41:087002, 2014. 16, 3

[A+14d] ALICE, B Abelev et al. Upgrade of the ALICE Experiment: Letter Of Intent. *J. Phys.*, G41:087001, 2014. 16, 19, XXIII, 3

[A+14e] ALICE, Betty Bezverkhny Abelev et al. Azimuthal anisotropy of D meson production in Pb-Pb collisions at $\sqrt{s_{\rm NN}}$ = 2.76 TeV. *Phys. Rev.*, C90(3):034904, 2014, 1405.2001. 35, 36, XXIV, 6

[A+14f] ALICE, Betty Bezverkhny Abelev et al. J/ψ production and nuclear effects in p-Pb collisions at $\sqrt{\rm S_{NN}}$ = 5.02 TeV. *JHEP*, 02:073, 2014, 1308.6726. 46

[A+14g] ALICE, Betty Bezverkhny Abelev et al. Performance of the ALICE Experiment at the CERN LHC. *Int. J. Mod. Phys.*, A29:1430044, 2014, 1402.4476. 11, 2

[A+14h] ALICE, Betty Bezverkhny Abelev et al. Suppression of ψ(2S) production in p-Pb collisions at $\sqrt{s_{\rm NN}}$ = 5.02 TeV. *JHEP*, 12:073, 2014, 1405.3796. 46

[A+14i] STAR, L. Adamczyk et al. J/ψ production at low $p_{\rm T}$ in Au+Au and Cu+Cu collisions at $\sqrt{s_{\rm NN}}$ = 200 GeV with the STAR detector. *Phys. Rev.*, C90(2):024906, 2014, 1310.3563.

[A+14j] STAR, L. Adamczyk et al. Suppression of Υ production in d+Au and Au+Au collisions at $\sqrt{s_{\rm NN}}$=200 GeV. *Phys. Lett.*, B735:127–137, 2014, 1312.3675. [Erratum: Phys. Lett.B743,537(2015)]. 46

[A+15a] LHCb, Roel Aaij et al. Measurement of the η_c(1S) production cross-section in proton-proton collisions via the decay $\eta_c(1S) \to p\bar{p}$. *Eur. Phys. J.*, C75(7):311, 2015, 1409.3612. 44

[A+15b] ALICE, Betty Bezverkhny Abelev et al. Elliptic flow of identified hadrons in Pb-Pb collisions at $\sqrt{s_{\rm NN}}$ 2.76 TeV. *JHEP*, 06:190, 2015, 1405.4632. 33, XXIV

[A+15c] ALICE, Betty Bezverkhny Abelev et al. Production of inclusive Υ(1S) and Υ(2S) in p-Pb collisions at $\sqrt{\mathbf{s}_{\rm NN}}$ = 5.02 TeV. *Phys. Lett.*, B740:105–117, 2015, 1410.2234. 46

[A+15d] ALICE, Jaroslav Adam et al. Rapidity and transverse-momentum dependence of the inclusive J/ψ nuclear modification factor in p-Pb collisions at $\sqrt{s_{\rm NN}}$= 5.02 TeV. *JHEP*, 06:055, 2015, 1503.07179. 46

[A+16a] Virgo, LIGO Scientific, B. P. Abbott et al. Observation of Gravitational Waves from a Binary Black Hole Merger. *Phys. Rev. Lett.*, 116(6):061102, 2016, 1602.03837. 5

[A+16b] ALICE, Jaroslav Adam et al. Anisotropic flow of charged particles in Pb-Pb collisions at $\sqrt{s_{\rm NN}}$=5.02 TeV. *Phys. Rev. Lett.*, 116(13):132302, 2016, 1602.01119. 31, 32, 39, XXIV

[A+16c] ALICE, Jaroslav Adam et al. Centrality dependence of the charged-particle multiplicity density at midrapidity in Pb-Pb collisions at $\sqrt{s_{\rm NN}}$ = 5.02 TeV. *Phys. Rev. Lett.*, 116(22):222302, 2016, 1512.06104. 98

[A+16d] ALICE, Jaroslav Adam et al. Differential studies of inclusive J/ψ and ψ(2S) production at forward rapidity in Pb-Pb collisions at $\sqrt{s_{\rm NN}}$ = 2.76 TeV. *JHEP*, 05:179, 2016, 1506.08804. 80, 96

[A+16e] ALICE, Jaroslav Adam et al. Elliptic flow of electrons from heavy-flavour hadron decays at mid-rapidity in Pb-Pb collisions at $\sqrt{s_{\rm NN}}$= 2.76 TeV. *JHEP*, 09:028, 2016, 1606.00321. 34, 35, XXIV, 6

[A+16f] ALICE, Jaroslav Adam et al. Elliptic flow of muons from heavy-flavour hadron decays at forward rapidity in Pb–Pb collisions at $\sqrt{s_{\rm NN}}$ =2.76 TeV. *Phys. Lett.*, B753:41–56, 2016, 1507.03134. 34, 35, 95, XXIV, 6, 8

[A+16g] ALICE, Jaroslav Adam et al. Forward-central two-particle correlations in p-Pb collisions at $\sqrt{s_{\rm NN}}$ = 5.02 TeV. *Phys. Lett.*, B753:126–139, 2016, 1506.08032. 118

[A+16h] ALICE, Jaroslav Adam et al. Higher harmonic flow coefficients of identified hadrons in Pb-Pb collisions at $\sqrt{s_{\rm NN}}$ = 2.76 TeV. *JHEP*, 09:164, 2016, 1606.06057. 31

[A+16i] ALICE, Jaroslav Adam et al. Production of light nuclei and anti-nuclei in pp and Pb-Pb collisions at energies available at the CERN Large Hadron Collider. *Phys. Rev.*, C93(2):024917, 2016, 1506.08951. 13, XXIII

[A+16j] ALICE, Jaroslav Adam et al. Pseudorapidity dependence of the anisotropic flow of charged particles in Pb-Pb collisions at $\sqrt{s_{\rm NN}}$ = 2.76 TeV. *Phys. Lett.*, B762:376–388, 2016, 1605.02035. 33, XXIV

[A+16k] A. Andronic et al. Heavy-flavour and quarkonium production in the LHC era: from proton–proton to heavy-ion collisions. *Eur. Phys. J.*, C76(3):107, 2016, 1506.03981. 43

[A+17a] LHCb, Roel Aaij et al. Observation of $\eta_c(2S) \to p\bar{p}$ and search for X(3872) $\to p\bar{p}$ decays. *Phys. Lett.*, B769:305–313, 2017, 1607.06446. 44

[A+17b] ALICE, Shreyasi Acharya et al. J/ψ elliptic flow in Pb-Pb collisions at $\sqrt{s_{\rm NN}}$ = 5.02 TeV. *Phys. Rev. Lett.*, 119(24):242301, 2017, 1709.05260. 110

[A+17c] ALICE, Jaroslav Adam et al. Enhanced production of multi-strange hadrons in high-multiplicity proton-proton collisions. *Nature Phys.*, 13:535–539, 2017, 1606.07424. 7

[A+17d] ALICE, Jaroslav Adam et al. J/ψ suppression at forward rapidity in Pb-Pb collisions at $\sqrt{s_{\rm NN}}$= 5.02 TeV. *Phys. Lett.*, B766:212–224, 2017, 1606.08197. 50, 51, 60, 96, 97, XXV, XXVI

[A+17e] STAR, L. Adamczyk et al. Energy dependence of J/ψ production in Au+Au collisions at $\sqrt{s_{\rm NN}}$ = 39, 62.4 and 200 GeV. *Phys. Lett.*, B771:13–20, 2017, 1607.07517.

[A+17f] STAR, L. Adamczyk et al. Measurement of D^0 Azimuthal Anisotropy at Midrapidity in Au+Au Collisions at $\sqrt{s_{\rm NN}}$=200 GeV. *Phys. Rev. Lett.*, 118(21):212301, 2017, 1701.06060. 36

[A+18a] ATLAS, Morad Aaboud et al. Prompt and non-prompt J/ψ elliptic flow in Pb+Pb collisions at $\sqrt{s_{\rm NN}}$ = 2 5.02 TeV with the ATLAS detector. *Eur. Phys. J.*, C78(9):784, 2018, 1807.05198. 111

[A+18b] ALICE, S. Acharya et al. Search for collectivity with azimuthal J/ψ-hadron correlations in high multiplicity p-Pb collisions at $\sqrt{s_{\rm NN}}$ = 5.02 and 8.16 TeV. *Phys. Lett.*, B780:7–20, 2018, 1709.06807. 118

[A+18c] ALICE, Shreyasi Acharya et al. Anisotropic flow of identified particles in Pb-Pb collisions at $\sqrt{s_{\rm NN}}$= 5.02 TeV. 2018, 1805.04390. 31

[A+18d] ALICE, Shreyasi Acharya et al. Azimuthal anisotropy of heavy-flavour decay electrons in p-Pb collisions at $\sqrt{s_{\rm NN}}$ = 5.02 TeV. 2018, 1805.04367. 41, XXV

[A+18e] ALICE, Shreyasi Acharya et al. D-meson azimuthal anisotropy in mid-central Pb-Pb collisions at $\sqrt{s_{\rm NN}}$ = 5.02 TeV. *Phys. Rev. Lett.*, 120(10):102301, 2018, 1707.01005. 35, 6

[A+18f] ALICE, Shreyasi Acharya et al. Energy dependence and fluctuations of anisotropic flow in Pb-Pb collisions at $\sqrt{s_{\rm NN}}$ = 5.02 and 2.76 TeV. 2018, 1804.02944. 32, 39, XXIV

[A+18g] ALICE, D. Adamová et al. J/ψ production as a function of charged-particle pseudorapidity density in p-Pb collisions at $\sqrt{s_{\rm NN}}$ = 5.02 TeV. *Phys. Lett.*, B776:91–104, 2018, 1704.00274. 46

[ABFP96] N. Armesto, M. A. Braun, E. G. Ferreiro, and C. Pajares. Percolation approach to quark - gluon plasma and J/ψ suppression. *Phys. Rev. Lett.*, 77:3736–3738, 1996, hep-ph/9607239. 48

[ABMRS03] A. Andronic, P. Braun-Munzinger, K. Redlich, and J. Stachel. Statistical hadronization of charm in heavy ion collisions at SPS, RHIC and LHC. *Phys. Lett.*, B571:36–44, 2003, nucl-th/0303036. 59, 7

[ABMS09] A. Andronic, P. Braun-Munzinger, and J. Stachel. Thermal hadron production in relativistic nuclear collisions: The Hadron mass spectrum, the horn, and the QCD phase transition. *Phys. Lett.*, B673:142–145, 2009, 0812.1186. [Erratum: Phys. Lett.B678,516(2009)]. 7, 59

[AEGH97] J. F. Amundson, Oscar J. P. Eboli, E. M. Gregores, and F. Halzen. Quantitative tests of color evaporation: Charmonium production. *Phys. Lett.*, B390:323–328, 1997, hep-ph/9605295. 45

[AFJ+11] N. Andersson, V. Ferrari, D. I. Jones, K. D. Kokkotas, B. Krishnan, J. S. Read, L. Rezzolla, and B. Zink. Gravitational waves from neutron stars: Promises and challenges. *Gen. Rel. Grav.*, 43:409–436, 2011, 0912.0384. 5

[AKPR13] François Arleo, Rodion Kolevatov, Stéphane Peigné, and Maryam Rustamova. Centrality and $p_{\rm T}$ dependence of J/ψ suppression in proton-nucleus collisions from parton energy loss. *JHEP*, 05:155, 2013, 1304.0901. 46

[AKR] P. Antonioli, A. Kluge, and W. Riegler. Upgrade of the ALICE Readout & Trigger System. Technical report. 16, 3

[AMGP17] Benjamin Audurier, Gines Martinez-Garcia, and Philippe Pillot. Étude de la production inclusive de J/ψ dans les collisions pp et Pb-Pb à $\sqrt{s_{\rm NN}}$ = 5.02 TeV avec le spectromètre à muons de l'expérience ALICE au LHC, 2017. Presented on 2017-10-05. 97, 99

[AP13] Francois Arleo and Stephane Peigne. Heavy-quarkonium suppression in p-A collisions from parton energy loss in cold QCD matter. *JHEP*, 03:122, 2013, 1212.0434. 46

[AP14] François Arleo and Stéphane Peigné. Quarkonium suppression in heavy-ion collisions from coherent energy loss in cold nuclear matter. *JHEP*, 10:073, 2014, 1407.5054. 48

[APS11] Francois Arleo, Stephane Peigne, and Taklit Sami. Revisiting scaling properties of medium-induced gluon radiation. *Phys. Rev.*, D83:114036, 2011, 1006.0818. 46

[Arm06] Nestor Armesto. Nuclear shadowing. *J. Phys.*, G32:R367–R394, 2006, hep-ph/0604108. 46

[ASRS08] Mark G. Alford, Andreas Schmitt, Krishna Rajagopal, and Thomas Schäfer. Color superconductivity in dense quark matter. *Rev. Mod. Phys.*, 80:1455–1515, 2008, 0709.4635. 5

[AT08] Francois Arleo and Vi-Nham Tram. A Systematic study of J/ψ suppression in cold nuclear matter. *Eur. Phys. J.*, C55:449–461, 2008, hep-ph/0612043. 46

[B$^+$94] E877, J. Barrette et al. Observation of anisotropic event shapes and transverse flow in Au+Au collisions at AGS energy. *Phys. Rev. Lett.*, 73:2532–2535, 1994, hep-ex/9405003. 30

[B$^+$97] E877, J. Barrette et al. Energy and charged particle flow in a 10.8-A Au+Au collisions. *Phys. Rev.*, C55:1420–1430, 1997, nucl-ex/9610006. [Erratum: Phys. Rev.C56,2336(1997)]. 30

[B$^+$99] E877, J. Barrette et al. Directed flow of light nuclei in Au+Au collisions at AGS energies. *Phys. Rev.*, C59:884–888, 1999, nucl-ex/9805006. 31

[B$^+$02] PHOBOS, B. B. Back et al. Pseudorapidity and centrality dependence of the collective flow of charged particles in Au+Au collisions at 130 GeV. *Phys. Rev. Lett.*, 89:222301, 2002, nucl-ex/0205021. 30

[B$^+$05] PHOBOS, B. B. Back et al. Centrality and pseudorapidity dependence of elliptic flow for charged hadrons in Au+Au collisions at $\sqrt{s_{\mathrm{NN}}}$= 200 GeV. *Phys. Rev.*, C72:051901, 2005, nucl-ex/0407012. 33, XXIV

[B$^+$06] NA50, G. Borges et al. Charmonia production at the CERN/SPS. *J. Phys.*, G32:S381–S390, 2006, hep-ex/0505065. 48

[B$^+$16] Sz. Borsanyi et al. Calculation of the axion mass based on high-temperature lattice quantum chromodynamics. *Nature*, 539(7627):69–71, 2016, 1606.07494. 38, 39, XXIV

[BAB16] Cristina Bedda, Michelangelo Agnello, and Elena Bruna. The ALICE experiment: D^+-meson production in heavy-ion collisions and silicon low noise sensors characterization for the ITS Upgrade., May 2016. Presented 06 May 2016. 25

[BBC$^+$94] René Brun, F. Bruyant, Federico Carminati, Simone Giani, M. Maire, A. McPherson, G. Patrick, and L. Urban. GEANT Detector Description and Simulation Tool. 1994. 80

[BBL95] Geoffrey T. Bodwin, Eric Braaten, and G. Peter Lepage. Rigorous QCD analysis of inclusive annihilation and production of heavy quarkonium. *Phys. Rev.*, D51:1125–1171, 1995, hep-ph/9407339. [Erratum: Phys. Rev.D55,5853(1997)]. 45

[BCL+04] Oliver S. Bruning, P. Collier, P. Lebrun, S. Myers, R. Ostojic, J. Poole, and P. Proudlock. LHC Design Report Vol.1: The LHC Main Ring. 2004. 9

[BDO01a] Nicolas Borghini, Phuong Mai Dinh, and Jean-Yves Ollitrault. A New method for measuring azimuthal distributions in nucleus-nucleus collisions. *Phys. Rev.*, C63:054906, 2001, nucl-th/0007063. 55

[BDO01b] Nicolas Borghini, Phuong Mai Dinh, and Jean-Yves Ollitrault. Flow analysis from multiparticle azimuthal correlations. *Phys. Rev.*, C64:054901, 2001, nucl-th/0105040. 55

[BFH+14] Szabocls Borsanyi, Zoltan Fodor, Christian Hoelbling, Sandor D. Katz, Stefan Krieg, and Kalman K. Szabo. Full result for the QCD equation of state with 2+1 flavors. *Phys. Lett.*, B730:99–104, 2014, 1309.5258. 38, 39, XXIV

[Bjo83] J. D. Bjorken. Highly Relativistic Nucleus-Nucleus Collisions: The Central Rapidity Region. *Phys. Rev.*, D27:140–151, 1983. 5

[BKCS04] E. L. Bratkovskaya, A. P. Kostyuk, W. Cassing, and Horst Stoecker. Charmonium chemistry in A+A collisions at relativistic energies. *Phys. Rev.*, C69:054903, 2004, nucl-th/0402042. 48

[BKVV15] P Buncic, M Krzewicki, and P Vande Vyvre. Technical Design Report for the Upgrade of the Online-Offline Computing System. Technical Report CERN-LHCC-2015-006. ALICE-TDR-019, Apr 2015. 16, 3

[BM07] P. Braun-Munzinger. Quarkonium production in ultra-relativistic nuclear collisions: Suppression versus enhancement. *J. Phys.*, G34:S471–478, 2007, nucl-th/0701093. 43

[BMS00] P. Braun-Munzinger and J. Stachel. (Non)thermal aspects of charmonium production and a new look at J/ψ suppression. *Phys. Lett.*, B490:196–202, 2000, nucl-th/0007059. 49, 7

[BO96] Jean-Paul Blaizot and Jean-Yves Ollitrault. J/ψ suppression in Pb Pb collisions: A Hint of quark - gluon plasma production? *Phys. Rev. Lett.*, 77:1703–1706, 1996, hep-ph/9606289. 46

[BO04] N. Borghini and J. Y. Ollitrault. Azimuthally sensitive correlations in nucleus-nucleus collisions. *Phys. Rev.*, C70:064905, 2004, nucl-th/0407041. 76

[BR81] R. Baier and R. Ruckl. Hadronic Production of J/ψ and Υ: Transverse Momentum Distributions. *Phys. Lett.*, 102B:364–370, 1981. 45

[But06] Sergey A. Butsyk. PHENIX results on open heavy flavor production and flow in Au+Au collisions at $\sqrt{s_{\mathrm{NN}}}$ = 200 GeV. *Nucl. Phys.*, A774:669–672, 2006, nucl-ex/0510010. 34

[C+14] CMS, Serguei Chatrchyan et al. Event activity dependence of Υ(nS) production in $\sqrt{s_{\rm NN}}$= 5.02 TeV p-Pb and $\sqrt{s}$= 2.76 TeV pp collisions. *JHEP*, 04:103, 2014, 1312.6300. 46

[CBF+08] A. Capella, L. Bravina, E. G. Ferreiro, A. B. Kaidalov, K. Tywoniuk, and E. Zabrodin. Charmonium dissociation and recombination at RHIC and LHC. *Eur. Phys. J.*, C58:437–444, 2008, 0712.4331. 59, 7

[CER93] Letter of Intent for A Large Ion Collider Experiment [ALICE]. Technical Report CERN-LHCC-93-016. LHCC-I-4, CERN, Geneva, 1993. 11

[CER96] *The forward muon spectrometer of ALICE: addendum to the technical proposal for a Large Ion Collider experiment at the CERN LHC.* LHC Tech. Proposal. CERN, Geneva, 1996. 11

[CER99] ALICE Collaboration. *ALICE Zero-Degree Calorimeter (ZDC): Technical Design Report.* Technical Design Report ALICE. CERN, Geneva, 1999. 11

[CER00] ALICE Collaboration. *ALICE time projection chamber: Technical Design Report.* Technical Design Report ALICE. CERN, Geneva, 2000. 12

[CER04] ALICE Collaboration. *ALICE forward detectors: FMD, TO and VO: Technical Design Report.* Technical Design Report ALICE. CERN, Geneva, 2004. Submitted on 10 Sep 2004. 12

[CER13a] Addendum of the Letter of Intent for the upgrade of the ALICE experiment : The Muon Forward Tracker. Technical Report CERN-LHCC-2013-014. LHCC-I-022-ADD-1, CERN, Geneva, Aug 2013. 13, 16, 17, XXIII, 3

[CER13b] Upgrade of the ALICE Time Projection Chamber. Technical Report CERN-LHCC-2013-020. ALICE-TDR-016, Oct 2013. 16, 3

[CER15] Technical Design Report for the Muon Forward Tracker. Technical Report CERN-LHCC-2015-001. ALICE-TDR-018, Jan 2015. 16, 17, 18, XXIII, XXXI, 3

[CFK00] A. Capella, E. G. Ferreiro, and A. B. Kaidalov. Nonsaturation of the J/ψ suppression at large transverse energy in the comovers approach. *Phys. Rev. Lett.*, 85:2080–2083, 2000, hep-ph/0002300. 48

[CKKAG97] A. Capella, A. Kaidalov, A. Kouider Akil, and C. Gerschel. J/ψ and ψ(2S) suppression in heavy ion collisions. *Phys. Lett.*, B393:431–436, 1997, hep-ph/9607265. 46

[CL96] Peter L. Cho and Adam K. Leibovich. Color octet quarkonia production. 2. *Phys. Rev.*, D53:6203–6217, 1996, hep-ph/9511315. 45

[CMS18a] CMS. Elliptic flow of charm and strange hadrons in high-multiplicity p-Pb collisions at $\sqrt{s_{\rm NN}}$ = 8.16 TeV. 2018. 41, XXV

[CMS18b] CMS. Observation of prompt J/ψ meson elliptic flow in high-multiplicity p-Pb collisions at $\sqrt{s_{\rm NN}}$ = 8.16 TeV. 2018. 119

[CP75a] N. Cabibbo and G. Parisi. Exponential Hadronic Spectrum and Quark Liberation. *Phys. Lett.*, 59B:67–69, 1975. 4

[CP75b] John C. Collins and M. J. Perry. Superdense Matter: Neutrons Or Asymptotically Free Quarks? *Phys. Rev. Lett.*, 34:1353, 1975. 4, 5

[Cre11] Sera Cremonini. The Shear Viscosity to Entropy Ratio: A Status Report. *Mod. Phys. Lett.*, B25:1867–1888, 2011, 1108.0677. 34

[dC13] R. Granier de Cassagnac. Heavy flavour and quarkonium experimental overview. *Talk at Strangeness in Quark Matter*, 2013. 49, XXV, 7

[d'E03] David G. d'Enterria. Hard scattering cross-sections at LHC in the Glauber approach: From pp to p-A and A-A collisions. 2003, nucl-ex/0302016. 97

[DPC+17] Santosh K. Das, Salvatore Plumari, Sandeep Chatterjee, Jane Alam, Francesco Scardina, and Vincenzo Greco. Directed Flow of Charm Quarks as a Witness of the Initial Strong Magnetic Field in Ultra-Relativistic Heavy Ion Collisions. *Phys. Lett.*, B768:260–264, 2017, 1608.02231. 116

[DPS01] S. Digal, P. Petreczky, and H. Satz. Quarkonium feed down and sequential suppression. *Phys. Rev.*, D64:094015, 2001, hep-ph/0106017. 47

[DR15] Xiaojian Du and Ralf Rapp. Sequential Regeneration of Charmonia in Heavy-Ion Collisions. *Nucl. Phys.*, A943:147–158, 2015, 1504.00670. 52, 59, 112, 113, 114, 118, 120, 121, XXV, XXVIII, XXXI, 7, 9

[eaPDGte] Particle Data Group, C. Patrignani et al. (Particle Data Group). Review of Particle Physics. *Chin. Phys. C*, 40(10):100001, 2016 and 2017 update. 4, 96, XXIII

[EPS09] K. J. Eskola, H. Paukkunen, and C. A. Salgado. EPS09: A New Generation of NLO and LO Nuclear Parton Distribution Functions. *JHEP*, 04:065, 2009, 0902.4154. 46

[Esu03] PHENIX, ShinIchi Esumi. Identified charged particle azimuthal anisotropy in PHENIX at RHIC. *Nucl. Phys.*, A715:599–602, 2003, nucl-ex/0210012. 38, XXIV

[Fer14] E. G. Ferreiro. Charmonium dissociation and recombination at LHC: Revisiting comovers. *Phys. Lett.*, B731:57–63, 2014, 1210.3209. 59, 7

[Fer15] E. G. Ferreiro. Excited charmonium suppression in proton–nucleus collisions as a consequence of comovers. *Phys. Lett.*, B749:98–103, 2015, 1411.0549. 46

[FJ16] Panagiota Foka and Małgorzata Anna Janik. An overview of experimental results from ultra-relativistic heavy-ion collisions at the CERN LHC: Bulk properties and dynamical evolution. *Rev. Phys.*, 1:154–171, 2016, 1702.07233. 5

[FK04] Z. Fodor and S. D. Katz. Critical point of QCD at finite T and μ, lattice results for physical quark masses. *JHEP*, 04:050, 2004, hep-lat/0402006. 5

[Fri77] Harald Fritzsch. Producing Heavy Quark Flavors in Hadronic Collisions: A Test of Quantum Chromodynamics. *Phys. Lett.*, 67B:217–221, 1977. 45

[FW13a] Hirotsugu Fujii and Kazuhiro Watanabe. Heavy quark pair production in high energy p-A collisions: Open heavy flavors. *Nucl. Phys.*, A920:78–93, 2013, 1308.1258. 46

[FW13b] Hirotsugu Fujii and Kazuhiro Watanabe. Heavy quark pair production in high energy p-A collisions: Quarkonium. *Nucl. Phys.*, A915:1–23, 2013, 1304.2221. 46

[G+96] NA50, M. Gonin et al. Anomalous J/ψ suppression in Pb+Pb collisions at 158-A-GeV/c. *Nucl. Phys.*, A610:404C–417C, 1996. 46, 47, 48, XXV, 7

[GKR04] V. Greco, C. M. Ko, and R. Rapp. Quark coalescence for charmed mesons in ultrarelativistic heavy ion collisions. *Phys. Lett.*, B595:202–208, 2004, nucl-th/0312100. 34, 35, 38, 53, XXIV

[GKR14] Umut Gursoy, Dmitri Kharzeev, and Krishna Rajagopal. Magnetohydrodynamics, charged currents and directed flow in heavy ion collisions. *Phys. Rev.*, C89(5):054905, 2014, 1401.3805. 116

[GKS+89] H. H. Gutbrod, B. W. Kolb, H. R. Schmidt, Arthur M. Poskanzer, H. G. Ritter, and K. H. Kampert. A New Component of the Collective Flow in Relativistic Heavy Ion Collisions. *Phys. Lett.*, B216:267–271, 1989. 31

[GSX+15] Xingyu Guo, Shuzhe Shi, Nu Xu, Zhe Xu, and Pengfei Zhuang. Magnetic Field Effect on Charmonium Production in High Energy Nuclear Collisions. *Phys. Lett.*, B751:215–219, 2015, 1502.04407. 112, 114, 9

[Gu13] PHENIX, Yi Gu. PHENIX Measurements of Higher-order Flow Harmonics for Identified Charged Hadrons in Au+Au collisions at $\sqrt{s_{\mathrm{NN}}}$ = 39–200 GeV. *Nucl. Phys.*, A904-905:353c–356c, 2013, 1211.4009. 31

[GW73] D. J. Gross and Frank Wilczek. Asymptotically Free Gauge Theories - I. *Phys. Rev.*, D8:3633–3652, 1973. 3

[GW74] D. J. Gross and Frank Wilczek. Asymptotically Free Gauge Theories. 2. *Phys. Rev.*, D9:980–993, 1974. 3

[Hal77] F. Halzen. Cvc for Gluons and Hadroproduction of Quark Flavors. *Phys. Lett.*, 69B:105–108, 1977. 45

[HFR13] Min He, Rainer J. Fries, and Ralf Rapp. D_s-Meson as Quantitative Probe of Diffusion and Hadronization in Nuclear Collisions. *Phys. Rev. Lett.*, 110(11):112301, 2013, 1204.4442. 35

[HFR14] Min He, Rainer J. Fries, and Ralf Rapp. Heavy Flavor at the Large Hadron Collider in a Strong Coupling Approach. *Phys. Lett.*, B735:445–450, 2014, 1401.3817. 112

[HLPS10] K. Hebeler, J. M. Lattimer, C. J. Pethick, and A. Schwenk. Constraints on neutron star radii based on chiral effective field theory interactions. *Phys. Rev. Lett.*, 105:161102, 2010, 1007.1746. 5

[HLPS13] K. Hebeler, J. M. Lattimer, C. J. Pethick, and A. Schwenk. Equation of state and neutron star properties constrained by nuclear physics and observation. *Astrophys. J.*, 773:11, 2013, 1303.4662. 5

[Huo03] Pasi Huovinen. Hydrodynamical description of collective flow. Chapter 1. pages 600–633, 2003, nucl-th/0305064. 34

[K+10] CMS, Vardan Khachatryan et al. Observation of Long-Range Near-Side Angular Correlations in Proton-Proton Collisions at the LHC. *JHEP*, 09:091, 2010, 1009.4122. 39

[K+17] CMS, Vardan Khachatryan et al. Suppression and azimuthal anisotropy of prompt and nonprompt J/ψ production in Pb-Pb collisions at $\sqrt{s_{\mathrm{NN}}}$ = 2.76 TeV. *Eur. Phys. J.*, C77(4):252, 2017, 1610.00613. 54, 57, 58, 110, XXV, 7

[KB09] Daniel Krieg and Marcus Bleicher. Negative Elliptic Flow of J/ψ 's: A Qualitative Signature for Charm Collectivity at RHIC. *Eur. Phys. J.*, A39:1–4, 2009, 0806.0736. 53

[KH03] Peter F. Kolb and Ulrich W. Heinz. Hydrodynamic description of ultrarelativistic heavy ion collisions. pages 634–714, 2003, nucl-th/0305084. 30, XXIV

[Kla02] Michael Klasen. Theory of hard photoproduction. *Rev. Mod. Phys.*, 74:1221–1282, 2002, hep-ph/0206169. 46

[KMS88] F. Karsch, M. T. Mehr, and H. Satz. Color Screening and Deconfinement for Bound States of Heavy Quarks. *Z. Phys.*, C37:617, 1988. 46

[KSS05] P. Kovtun, Dan T. Son, and Andrei O. Starinets. Viscosity in strongly interacting quantum field theories from black hole physics. *Phys. Rev. Lett.*, 94:111601, 2005, hep-th/0405231. 33

[KT06] Dmitri Kharzeev and Kirill Tuchin. Signatures of the color glass condensate in J/ψ production off nuclear targets. *Nucl. Phys.*, A770:40–56, 2006, hep-ph/0510358. 48

[LBC08] O. Linnyk, E. L. Bratkovskaya, and W. Cassing. Evidence for non-hadronic interactions of charm degrees of freedom in heavy-ion collisions at relativistic energies. *Nucl. Phys.*, A807:79–104, 2008, 0801.4282. 53

[LFLHA16] A. Le Fevre, Y. Leifels, C. Hartnack, and J. Aichelin. On the Origin of the Elliptic Flow and its Dependence on the Equation of State in Heavy Ion Reactions at Intermediate Energies. 2016, 1611.07500. 32

[LM03] Zi-wei Lin and Denes Molnar. Quark coalescence and elliptic flow of charm hadrons. *Phys. Rev.*, C68:044901, 2003, nucl-th/0304045. 34, 36, 37, 116, 117, XXIV

[LO13] Matthew Luzum and Jean-Yves Ollitrault. Eliminating experimental bias in anisotropic-flow measurements of high-energy nuclear collisions. *Phys. Rev.*, C87(4):044907, 2013, 1209.2323. 93

[LR08] Matthew Luzum and Paul Romatschke. Conformal Relativistic Viscous Hydrodynamics: Applications to RHIC results at $\sqrt{s_{\mathrm{NN}}}$ = 200 GeV. *Phys. Rev.*, C78:034915, 2008, 0804.4015. [Erratum: Phys. Rev.C79,039903(2009)]. 34

[LVW09] Carlos Lourenco, Ramona Vogt, and Hermine K. Woehri. Energy dependence of J/ψ absorption in proton-nucleus collisions. *JHEP*, 02:014, 2009, 0901.3054. 46

[LXZ10] Yunpeng Liu, Nu Xu, and Pengfei Zhuang. J/ψ elliptic flow in relativistic heavy ion collisions. *Nucl. Phys.*, A834:317C–319C, 2010, 0910.0959. 53, 55

[Mal99] Juan Martin Maldacena. The Large N limit of superconformal field theories and supergravity. *Int. J. Theor. Phys.*, 38:1113–1133, 1999, hep-th/9711200. [Adv. Theor. Math. Phys.2,231(1998)]. 33

[MBB15] J. Scott Moreland, Jonah E. Bernhard, and Steffen A. Bass. Alternative ansatz to wounded nucleon and binary collision scaling in high-energy nuclear collisions. *Phys. Rev.*, C92(1):011901, 2015, 1412.4708. 101

[MG02] Denes Molnar and Miklos Gyulassy. Saturation of elliptic flow and the transport opacity of the gluon plasma at RHIC. *Nucl. Phys.*, A697:495–520, 2002, nucl-th/0104073. [Erratum: Nucl. Phys.A703,893(2002)]. 36, 37, XXIV

[Mol04] Denes Molnar. Elliptic flow form quark coalescence: Mass ordering or quark number scaling? 2004, nucl-th/0408044. 31

[Mol07] Denes Molnar. Heavy quarks at RHIC from parton transport theory. *Eur. Phys. J.*, C49:181–186, 2007, nucl-th/0608069. 34

[MP08] Agnes Mocsy and Peter Petreczky. Can quarkonia survive deconfinement? *Phys. Rev.*, D77:014501, 2008, 0705.2559. 44

[MRSS07] Michael L. Miller, Klaus Reygers, Stephen J. Sanders, and Peter Steinberg. Glauber modeling in high energy nuclear collisions. *Ann. Rev. Nucl. Part. Sci.*, 57:205–243, 2007, nucl-ex/0701025. 6, 97

[MS86] T. Matsui and H. Satz. J/ψ Suppression by Quark-Gluon Plasma Formation. *Phys. Lett.*, B178:416–422, 1986. 46, 6

[MT05] Guy D. Moore and Derek Teaney. How much do heavy quarks thermalize in a heavy ion collision? *Phys. Rev.*, C71:064904, 2005, hep-ph/0412346. 50, 7

[NBZ11] James L. Nagle, Ian G. Bearden, and William A. Zajc. Quark-Gluon Plasma at RHIC and the LHC: Perfect Fluid too Perfect? *New J. Phys.*, 13:075004, 2011, 1102.0680. 34

[NEPT16] H. Niemi, K. J. Eskola, R. Paatelainen, and K. Tuominen. Predictions for 5.023 TeV Pb+Pb collisions at the CERN Large Hadron Collider. *Phys. Rev.*, C93(1):014912, 2016, 1511.04296. 32, XXIV

[NHLO16] Jacquelyn Noronha-Hostler, Matthew Luzum, and Jean-Yves Ollitrault. Hydrodynamic predictions for 5.02 TeV Pb-Pb collisions. *Phys. Rev.*, C93(3):034912, 2016, 1511.06289. 32, XXIV

[NHR18] Jacquelyn Noronha-Hostler and Claudia Ratti. Signatures of thermalized charm quarks in all charged flow observables. 2018, 1804.10661. 38, 39, XXIV

[NS02] Silvia Necco and Rainer Sommer. The N(f) = 0 heavy quark potential from short to intermediate distances. *Nucl. Phys.*, B622:328–346, 2002, hep-lat/0108008. 44

[Oll92] Jean-Yves Ollitrault. Anisotropy as a signature of transverse collective flow. *Phys. Rev.*, D46:229–245, 1992. 29

[Oll08] Jean-Yves Ollitrault. Relativistic hydrodynamics for heavy-ion collisions. *Eur. J. Phys.*, 29:275–302, 2008, 0708.2433. 34

[OPV09] Jean-Yves Ollitrault, Arthur M. Poskanzer, and Sergei A. Voloshin. Effect of flow fluctuations and nonflow on elliptic flow methods. *Phys. Rev.*, C80:014904, 2009, 0904.2315. 94

[Pac18] Vojtech Pacik. Elliptic flow coefficients of identified hadrons in pp and p–Pb collisions measured with ALICE. *Talk at Quark Matter*, 2018. 39

[PK15] Stéphane Peigné and Rodion Kolevatov. Medium-induced soft gluon radiation in forward dijet production in relativistic proton-nucleus collisions. *JHEP*, 01:141, 2015, 1405.4241. 46

[PSS01] G. Policastro, Dan T. Son, and Andrei O. Starinets. The Shear viscosity of strongly coupled N=4 supersymmetric Yang-Mills plasma. *Phys. Rev. Lett.*, 87:081601, 2001, hep-th/0104066. 33, 5

[PV98] Arthur M. Poskanzer and S. A. Voloshin. Methods for analyzing anisotropic flow in relativistic nuclear collisions. *Phys. Rev.*, C58:1671–1678, 1998, nucl-ex/9805001. 67

[RM82] Johann Rafelski and Berndt Muller. Strangeness Production in the Quark - Gluon Plasma. *Phys. Rev. Lett.*, 48:1066, 1982. [Erratum: Phys. Rev. Lett.56,2334(1986)]. 7

[RR07] L. Ravagli and R. Rapp. Quark Coalescence based on a Transport Equation. *Phys. Lett.*, B655:126–131, 2007, 0705.0021. 53

[RSM16] Felix Reidt, Johanna Stachel, and Luciano Musa. Studies for the ALICE Inner Tracking System Upgrade, Feb 2016. Presented 28 Apr 2016. 25

[RvH10] Ralf Rapp and Hendrik van Hees. Heavy Quarks in the Quark-Gluon Plasma. In *Quark-gluon plasma 4*, pages 111–206, 2010, 0903.1096. 34

[RZ06] M. Riordan and W. A. Zajc. The first few microseconds. *Sci. Am.*, 294N5:24–31, 2006. [Spektrum Wiss.2006N11,36(2006)]. 29

[S+17] CMS, Albert M Sirunyan et al. Pseudorapidity and transverse momentum dependence of flow harmonics in p-Pb and Pb-Pb collisions. 2017, 1710.07864. 33, XXIV

[S+18a] CMS, A. M. Sirunyan et al. Elliptic flow of charm and strange hadrons in high-multiplicity p-Pb collisions at $\sqrt{s_{\mathrm{NN}}}$ =8.16 TeV. *Phys. Rev. Lett.*, 121(8):082301, 2018, 1804.09767. 119

[S+18b] CMS, Albert M Sirunyan et al. Suppression of Excited Υ States Relative to the Ground State in Pb-Pb Collisions at $\sqrt{s_{\mathrm{NN}}}$= 5.02 TeV. *Phys. Rev. Lett.*, 120(14):142301, 2018, 1706.05984. 49, XXV

[Sat06] Helmut Satz. Colour deconfinement and quarkonium binding. *J. Phys.*, G32:R25, 2006, hep-ph/0512217. 44, 47, XXXI

[SHHS11] Chun Shen, Ulrich Heinz, Pasi Huovinen, and Huichao Song. Radial and elliptic flow in Pb+Pb collisions at the Large Hadron Collider from viscous hydrodynamic. *Phys. Rev.*, C84:044903, 2011, 1105.3226. 34

[Shu78] Edward V. Shuryak. Quark-Gluon Plasma and Hadronic Production of Leptons, Photons and Psions. *Phys. Lett.*, 78B:150, 1978. [Yad. Fiz.28,796(1978)]. 4, 5

[Shu02] E. V. Shuryak. The Azimuthal asymmetry at large p_{T} seem to be too large for a 'jet quenching'. *Phys. Rev.*, C66:027902, 2002, nucl-th/0112042. 34

[Sil08] PHENIX, Catherine Silvestre. PHENIX first measurement of the J/ψ elliptic flow parameter v(2) in Au+Au collisions at $\sqrt{s_{\mathrm{NN}}}$ = 200 GeV. *J. Phys.*, G35:104136, 2008, 0806.0475. 53, XXV, 7

[Sne11] Raimond Snellings. Elliptic Flow: A Brief Review. *New J. Phys.*, 13:055008, 2011, 1102.3010. 29

[SV08] Ilya Selyuzhenkov and Sergei Voloshin. Effects of non-uniform acceptance in anisotropic flow measurement. *Phys. Rev.*, C77:034904, 2008, 0707.4672. 63, 8

[Szc16] ALICE, A. Szczepankiewicz. Readout of the upgraded ALICE-ITS. *Nucl. Instrum. Meth.*, A824:465–469, 2016. 22, XXIII

[Tar17] Mohamad Tarhini. Measurement of charmonium production at forward rapidity in Pb–Pb collisions at $\sqrt{s_{\mathrm{NN}}}$ = 5.02 TeV with ALICE. In *QM2017*, 2017. 100, 102, XXVII

[The02] R. L. Thews. Quarkonium formation at high-energy. *Nucl. Phys.*, A702:341–345, 2002, hep-ph/0111015. 59, 7

[vHGR06] Hendrik van Hees, Vincenzo Greco, and Ralf Rapp. Heavy-quark probes of the quark-gluon plasma at RHIC. *Phys. Rev.*, C73:034913, 2006, nucl-th/0508055. 35, XXIV

[vHKR15] Jacobus Willem van Hoorn, Manfred Krammer, and Petra Riedler. Study and Development of a novel Silicon Pixel Detector for the Upgrade of the ALICE Inner Tracking System, Oct 2015. Presented 24 Nov 2015. 25

[vHMGR08] H. van Hees, M. Mannarelli, V. Greco, and R. Rapp. Nonperturbative heavy-quark diffusion in the quark-gluon plasma. *Phys. Rev. Lett.*, 100:192301, 2008, 0709.2884. 35, XXIV

[VKSGO17] Monika Varga-Kofarago, Raimond Snellings, and Jan Fiete Grosse-Oetringhaus. Anomalous Broadening of Jet-Peak Shapes in Pb-Pb Collisions and Characterization of Monolithic Active Pixel Sensors for the ALICE Inner Tracking System Upgrade, Oct 2017. Presented 19 Feb 2018. 25

[Vog10] R. Vogt. Cold Nuclear Matter Effects on J/ψ and Υ Production at the LHC. *Phys. Rev.*, C81:044903, 2010, 1003.3497. 46

[VPS10] Sergei A. Voloshin, Arthur M. Poskanzer, and Raimond Snellings. Collective phenomena in non-central nuclear collisions. *Landolt-Bornstein*, 23:293–333, 2010, 0809.2949. 93, 94

[VZ96] S. Voloshin and Y. Zhang. Flow study in relativistic nuclear collisions by Fourier expansion of Azimuthal particle distributions. *Z. Phys.*, C70:665–672, 1996, hep-ph/9407282. 29

[Y+15] P. Yang et al. Low-power priority Address-Encoder and Reset-Decoder data-driven readout for Monolithic Active Pixel Sensors for tracker system. *Nucl. Instrum. Meth.*, A785:61–69, 2015. 21, XXIII

[YZX06] Li Yan, Pengfei Zhuang, and Nu Xu. Competition between J/ψ suppression and regeneration in quark-gluon plasma. *Phys. Rev. Lett.*, 97:232301, 2006, nucl-th/0608010. 53

[ZCGZ16] Kai Zhou, Zhengyu Chen, Carsten Greiner, and Pengfei Zhuang. Thermal Charm and Charmonium Production in Quark Gluon Plasma. *Phys. Lett.*, B758:434–439, 2016, 1602.01667. 59

[ZCK05] Bin Zhang, Lie-Wen Chen, and Che-Ming Ko. Charm elliptic flow at RHIC. *Phys. Rev.*, C72:024906, 2005, nucl-th/0502056. 35, XXIV

[ZER13] Xingbo Zhao, Andrew Emerick, and Ralf Rapp. In-Medium Quarkonia at SPS, RHIC and LHC. *Nucl. Phys.*, A904-905:611c–614c, 2013, 1210.6583. 55, 110, 112, 9

[Zha17a] STAR, Wangmei Zha. Excess of J/ψ yield at very low transverse momenta in Au+Au collisions at $\sqrt{s_{\rm NN}}$ and U+U at $\sqrt{s_{\rm NN}}$ with STAR. *J. Phys. Conf. Ser.*, 779(1):012039, 2017. 46

[Zha17b] Wangmei Zha. Recent highlights from STAR. *Talk at Strangeness in Quark Matter*, 2017. 54, 55, XXV

[ZKL08] Ben-Wei Zhang, Che-Ming Ko, and Wei Liu. Thermal charm production in a quark-gluon plasma in Pb-Pb collisions at $\sqrt{s_{\rm NN}}$= 5.5 TeV. *Phys. Rev.*, C77:024901, 2008, 0709.1684. 43

[ZKM+18] W. Zha, S. R. Klein, R. Ma, L. Ruan, T. Todoroki, Z. Tang, Z. Xu, C. Yang, Q. Yang, and S. Yang. Coherent J/ψ photoproduction in hadronic heavy-ion collisions. *Phys. Rev.*, C97(4):044910, 2018, 1705.01460. 46

[ZR08a] Xingbo Zhao and Ralf Rapp. Charmonium Production at High p(t) at RHIC. In *24th Winter Workshop on Nuclear Dynamics (WWND 2008) South Padre Island, Texas, April 5-12, 2008*, 2008, 0806.1239. 53

[ZR08b] Xingbo Zhao and Ralf Rapp. Transverse Momentum Spectra of J/ψ in Heavy-Ion Collisions. *Phys. Lett.*, B664:253–257, 2008, 0712.2407. 53

[ZR10] Xingbo Zhao and Ralf Rapp. Charmonium in Medium: From Correlators to Experiment. *Phys. Rev.*, C82:064905, 2010, 1008.5328. 112

[ZR11] Xingbo Zhao and Ralf Rapp. Medium Modifications and Production of Charmonia at LHC. *Nucl. Phys.*, A859:114–125, 2011, 1102.2194. 52, 59, 112, XXV, 7

[ZXXZ14] Kai Zhou, Nu Xu, Zhe Xu, and Pengfei Zhuang. Medium effects on charmonium production at ultrarelativistic energies available at the CERN Large Hadron Collider. *Phys. Rev.*, C89(5):054911, 2014, 1401.5845. 59, 112, 114, 115, 120, XXVIII, 7, 9

Introduction aux collisions d'ions lourds

L'étude des collisions d'ions lourds vise à une meilleure compréhension de la matière hadronique, en particulier dans des conditions de densités d'énergie extrêmes. Dans ce régime, la théorie de l'interaction forte, la chromodynamique quantique (QCD), prédit une transition de la matière hadronique vers un état déconfiné : le plasma de quarks et de gluons (PQG). La nature et l'ordre de cette transition de phase ne sont pas encore déterminés à l'heure actuelle. Cet état aurait été celui de l'Univers quelques micro-secondes après le Big-Bang mais on suppose que cet état chaud et dense n'existe plus aujourd'hui qu'au cœur des étoiles à neutrons.

Un PQG peut cependant être reproduit à une échelle infiniment plus petite en collisionnant des noyaux lourds accélérés à des vitesses ultra-relativistes. Cela est rendu possible au sein d'accélérateurs de particules tels que le Super Proton Synchrotron (SPS, CERN, Genève, Suisse), le Relativistic Heavy Ion Collider (RHIC, Brookhaven National Laboratory, New York, États-Unis) ou encore le Large Hadron Collider (LHC, CERN, Genève, Suisse). Dans le cas où la température et la densité d'énergie atteintes lors de la collision sont suffisantes, un état déconfiné se forme dans lequel les quarks et les gluons ne sont plus confinés au sein des hadrons mais évoluent asymptotiquement libres. L'évolution de la collision est décrite en plusieurs étapes successives dans le scénario de Bjorken. Avant la collision, les noyaux peuvent être représentés comme deux disques plats perpendiculaires à la direction du faisceau dus à la contraction de Lorentz. Après le croisement des noyaux, des interactions partoniques multiples impliquant de grands transferts d'énergie ont lieu. Le système formé se trouve dans un état de pré-équilibre où les collisions inélastiques qui y ont lieu peuvent éventuellement conduire à une thermalisation du système. Le système évolue vers un état déconfiné si la densité d'énergie dans un volume donné est assez importante. La taille du PQG formé est estimé autour de 10–20 fm et son temps de vie autour de 5–10 fm/c. Assez rapidement le système s'étend et se refroidit tandis que les partons se recombinent pour former des hadrons, c'est l'hadronisation. Lorsque la densité de particules est suffisamment faible, les interactions inélastiques et élastiques cessent, c'est le freeze-out, les particules se déplacent alors dans le vide et seront mesurées au sein des détecteurs de l'expérience.

Plusieurs propriétés de la collision affectent la formation et l'évolution du système. En particulier l'énergie de la collisions (dénotée $\sqrt{s_{\mathrm{NN}}}$ dans le centre de masse) affecte la densité d'énergie initiale du PQG. La nature des noyaux (proton, Pb et Xe au LHC) modifie le nombre de nucléons participants dans la collisions. Ce dernier est généralement plus communément référé via l'observable centralité qui est liée au paramètre d'impact des noyaux. De part la durée de vie extrêmement courte du PQG, aucune observation directe ne peut être réalisée et ses propriétés doivent être extraites à partir des particules de l'état

final qui sont détectées par l'expérience. Cette spécificité créée une forte inter-dépendance entre la théorie et l'expérience car aucune conclusion ne peut être obtenue à partir des seules données expérimentales. De plus, une observable unique ne peut pas permettre de conclure à la formation d'un PQG car un résultat donné peut être expliqué indépendamment par plusieurs modèles dont les interprétations divergent. Seul un ensemble de résultats concomitants peut permettre la compréhension du milieu formé lors de la collision. Les sondes molles correspondent à des interactions associés à des impulsions relativement faible et sont les plus abondamment produites. Elles reflètent les propriétés globale de la collision et fournissent des informations sur la collectivité et les propriétés thermodynamique du milieu. A l'opposé les sondes dites dures correspondent à des interactions impliquant de larges impulsions et qui, de fait, ont lieu durant les interactions les plus énergétiques durant les premiers instants de la collision. Parmi les sondes dures, les saveurs lourdes et en particulier les quarkonia sont un outil précieux pour la caractérisation du milieu formé.

Étudier le PQG avec l'expérience ALICE

Le détecteur actuel

Le LHC est le plus grand et le plus puissant accélérateur de particules depuis 2009. Des aimants supraconducteurs jalonnent l'anneau de 27 km situé à 100 m sous la surface et créent un puissant champ magnétique qui guide les faisceaux de particules de haute énergie dans des tubes sous ultra-vide. Un système cryogénique à base d'hélium liquide est nécessaire au fonctionnement des aimants en les maintenant à une température de 1.9 K. Deux faisceaux circulent dans des directions opposées contenant des paquets d'environ 200 millions d'ions de plomb qui collisionnent jusqu'à 4000 fois par seconde. Plusieurs expériences sont situés sur l'année du LHC.
L'expérience ALICE est la seule entièrement dédiée à l'étude du PQG via les collisions d'ions lourds. Elle est composée de plusieurs sous-systèmes [A$^+$08] afin de mesurer et caractériser les différentes particules produites lors de la collision (voir [A$^+$14g] pour une revue complète de ses performances). L'appareil est constitué d'une partie centrale et d'un spectromètre à muons à l'avant. Les sous-détecteurs principalement impliqués dans l'analyse présentée dans ce manuscrit sont le trajectographe interne (Inner Tracking System (ITS)), le détecteur VZERO et le spectromètre à muons. L'ITS est composé de six couches cylindriques autour du faisceau centré autour du point d'interaction et couvre la région de rapidité $|\eta| < 0.9$. Le Silicon Pixel Detector (SPD) correspond aux deux couches les plus internes de l'ITS et est composé de pixels en silicone. Il joue un rôle majeur dans la détermination du vertex primaire de la collision. Le détecteur VZERO est composé de deux disques de scintillateurs perpendiculaires à la direction du faisceau et situés de part et d'autre du point d'interaction (le VZEROA à z = 340 cm et le VZEROC à z = -90 cm). Les deux disques sont divisés en quatre anneaux qui sont chacun segmentés en huit secteurs. Il permet notamment l'estimation de la centralité de la collision et la mesure du plan de réaction de la collision à partir des multiplicités de particules mesurées. Le spectromètre à muons est situé à rapidité avant ($-4 < \eta < -2.5$) et permet de mesurer les muons émis avec un angle polaire $171° < \theta < 178°$ par rapport à l'axe du faisceau. Il est composé d'un absorbeur frontal, de 10 plans de détection regroupés deux par deux en 5 chambres proportionnelles multifilaires (MWPC), d'un aimant dipolaire autour de la troisième station et d'un déclencheur à muons précédé d'un filtre à muons.

Le futur Muon Forward Tracker

L'expérience ALICE se prépare pour une mise à niveau majeure de plusieurs sous-systèmes durant le prochain arrêt du LHC [A+14d]. Ces plans sont alignés avec l'augmentation en luminosité du LHC dont le futur taux d'interaction atteindra 50 kHz pour les collisions Pb–Pb (ce qui correspond à une luminosité instantanée de $\mathscr{L} = 6\,\mathrm{cm}^{-1}\,\mathrm{s}^{-2} \times 10^{27}\,\mathrm{cm}^{-1}\,\mathrm{s}^{-2}$) et 200 kHz pour les collisions pp et p–Pb. Afin d'exploiter au maximum ces conditions expérimentales sans précédent et permettre la lecture de toutes les interactions, plusieurs améliorations et modifications du détecteur actuel s'imposent. Les systèmes concernés sont:

- La réduction du tube du faisceau de 29.8 mm à 19.2 mm
- L'installation de deux trajectographes en silicium basés sur des capteurs CMOS :
  - le détecteur à vertex actuel (ITS) dans la région de rapidité centrale sera remplacé par sept couches de capteurs pour une meilleure efficacité de trajectographie et résolution, notamment à basse impulsion transverse et une augmentation de la vitesse de lecture [A+14c]
  - un nouveau trajectographe sera installé à rapidité avant afin de rajouter une fonctionnalité de trajectographie au spectromètre à muons : le MFT [CER13a, CER15]
- La chambre à projection temporelle sera remplacée avec des chambres GEM et sa nouvelle électronique permettra d'opérer en lecture continue [CER13b]
- L'électronique de plusieurs systèmes sera également améliorée : le TRD, le TOF et le spectromètre à muons [AKR]
- Un nouveau système de computing pour gérer le flux de données attendu de 3.4 TB/s [BKVV15].

Le programme de physique du MFT se focalise sur la dynamique des quarkonia, la thermalisation des quarks lourds et leur perte d'énergie au sein du PQG, la physique de la beauté et l'étude de la brisure de symétrie chirale et sa restauration via les mesures de vecteurs de basse masse. Le MFT va permettre d'exploiter pleinement l'intervalle cinématique du spectromètre à muons en répondant à plusieurs de ses limitations intrinsèques. Le détecteur sera installé entre le point d'interaction et l'absorbeur frontal du spectromètre à muons. Il consiste en deux demi-cônes autour du tube-faisceau constitué de cinq demi-disques le long de l'axe du faisceau. Son acceptance en pseudo-rapidité couvre l'intervalle $3.6 < \eta < 2.45$. L'ajout du MFT va conduire à une réduction significative du bruit de fond dans les canaux muons et dimuons en rejetant les muons provenant des désintégrations semi-muoniques des pions et kaons, provenant majoritairement des interactions multiples dans l'absorbeur frontal. Il permettra une séparation fiable des J/ψ prompts et non-prompts, jusqu'à impulsion transverse nulle. Les contributions ouvertes et celles provenant de mésons B des saveurs lourdes ouvertes pourront également être séparées sans dépendre de modèles théoriques. La résolution angulaire de mésons de basse masse sera également améliorée. Afin de répondre à ce programme ambitieux, les futurs capteurs du MFT doivent permettre au détecteur de satisfaire plusieurs spécifications techniques. Étant donné les besoins proches du futur ITS, les mêmes capteurs seront utilisés pour les deux détecteurs. Ils devront notamment permettre d'atteindre une résolution spatiale

de 5 µm, une efficacité de détection de 99.5 %, un temps d'intégration de 20 µs et une dissipation énergétique inférieure à 150 mW/cm^2.

Les capteurs choisis se basent sur la technologie CMOS qui présente des caractéristiques intéressantes en termes de granularité, d'épaisseur de matériau, de vitesse de lecture, de consommation de puissance et de résistance aux radiations. Les capteurs de type MAPS permettent d'aller plus loin en intégrant à la fois le volume de détection et l'électronique de lecture sur un unique composant, permettant ainsi l'optimisation de la surface entre le volume sensible et l'électronique. Leur avantage principal par rapport aux capteurs hybrides est le faible budget de matière et la consommation de puissance moindre mais ils présentent une résistance limitée à l'irradiation (qui permet néanmoins de répondre aux besoins des futurs détecteurs). Les pixels CMOS Imaging Sensor Process de 0.18 µm de TowerJazz ont été sélectionnés pour le futur capteur. Ils présentent plusieurs intérêts : une couche épitaxiale de type p de haute résistivité (> 1 kΩcm) qui permet une collecte efficace des charges et une meilleure tolérance à l'irradiation via la possibilité d'appliquer une tension à la diode de collection. Lors du passage d'une particule chargée à travers la couche épitaxiale, des paires électrons-trous sont créées et sont ensuite collectées par une diode en surface. Des couches profondes de type p ainsi que les six couches de métal en surface permettent d'intégrer un circuit électronique de lecture en surface du pixel. Ce circuit intégré réalise l'amplification et la numérisation du signal. Une nouvelle architecture du circuit de lecture de la matrice de pixels a été développée afin d'optimiser la lecture des pixels, le stockage et la compression des informations. L'acquisition des données peut être réalisé soit en mode déclenchement soit en mode continu. Ce capteur final est le résultat de plusieurs années de R&D et le résultat d'une vaste campagne de caractérisation. Une partie de cette thèse a été dédiée à la caractérisation de plusieurs versions de prototypes de pixels (les trois familles de prototypes pleine échelle) à travers des tests en laboratoire et sous faisceaux. Chaque prototype présente différents secteurs avec des propriétés différentes. Les différences entre les prototypes et/out les secteurs ont permis de tester plusieurs formes et tailles de la diode de collection, plusieurs épaisseurs de couches épitaxiales, plusieurs mécanismes de ré-initialisation du pixel et d'optimiser l'électronique du pixel. Après production, les pixels ont été testés et caractérisés afin de trouver leur points de fonctionnement optimaux. Les capteurs sont connectés à une carte d'acquisition (DAQ board) qui permet l'échange d'information avec le capteur. Les tests en laboratoires ont été réalisés au niveau d'un pixel, d'un secteur comportant plusieurs pixels ou sur la matrice complète d'un capteur via un logiciel dédié:

- Le seuil, le bruit de fond temporel et la forme du signal ont été mesurés en faisant varier différents paramètres du circuit électronique
- Le bruit de fond d'un ensemble de pixel a été étudié en masquant les pixels les plus bruyants
- L'efficacité de collecte des charges a été mesurée en utilisant des sources radioactives.

Les performances des capteurs ont ensuite été testées via des tests sous faisceaux dans plusieurs installations (au BTF à Frascati (faisceau d'électrons de 450 MeV), au DESY à Hambourg (faisceau d'électrons de 5 GeV), au PAL à Pohang (faisceau d'électrons de 60 MeV), au SLRI à Nakhon Ratchasima (faisceau d'électrons de 1 GeV), au PS au CERN (faisceau de pions de 6 GeV), au SPS au CERN (faisceau de pions de 120 GeV) et au U—120M à Řež (faisceau de protons de 300 MeV). A chaque fois, sept capteurs ont été installés au sein d'un dispositif fixe et traversés par le faisceau. Les trois capteurs du milieu ont ainsi été caractérisés et les autres ont permis d'établir l'alignement du faisceau. Les données ont

ensuite été analysées afin d'extraire l'efficacité de détection, le niveau de bruit, la résolution spatiale et la taille des groupes de pixels. Plusieurs études systématiques ont été réalisées à la fois en laboratoire et lors des tests sous faisceaux afin d'obtenir une description la plus réaliste possible du fonctionnement des capteurs, notamment via l'étude des fluctuations entre les différents capteurs, la dépendance en température de la réponse du signal, l'impact des pixels morts dans la matrice, l'influence de l'application d'une tension inverse et l'impact de plusieurs niveaux et types d'irradiation sur ses performances globales. Le capteur final a ainsi été obtenu au travers d'une caractérisation et d'une compréhension approfondies du fonctionnement du pixel et de la matrice de pixels. Le choix final a porté sur une version d'un des derniers prototypes qui présente une grande marge d'opération avec un longueur du signal entre 8–10 µs et un très faible niveau de bruit.

Le flot elliptique

L'étude des phénomènes collectifs a énormément contribué à la description du système créé lors des collisions de noyaux. Dans le cas où le système interagit, un état d'équilibre thermique peut être établi et maintenu tel que l'évolution de la boule de feu peut être décrite comme l'expansion d'un fluide dans un mouvement collectif avec un court temps de termalisation. Cette expansion collective se développe à partir des gradients de pression initiaux et dépend fortement des interactions entre les constituants du milieu. L'une des découvertes majeures les plus surprenantes est le succès de l'hydrodynamique relativiste pour décrire quantitativement l'évolution d'une collision d'ions lourds. Le rapport viscosité sur densité d'entropie $\frac{\eta}{s}$ extrait est très proche de la limite inférieure théorique $\frac{\hbar}{4\pi}$ [PSS01], le PQG se comporte donc quasiment comme un fluide parfait.

Le flot anisotropique est la réponse du système à la géométrie initiale de la collision lors de la rencontre des noyaux. Dans le cas de collisions non-centrales, la géométrie initiale est en forme d'amande mais les gradients de pression importants vont rapidement faire évoluer le système vers une géométrie circulaire. Les anisotropies azimutales des distributions d'impulsions finales se développent à travers les interactions multiples au sein des constituants du milieu à un stade précoce de l'évolution du système. La zone de recouvrement des noyaux lors de la collision étant influencée par leur paramètre d'impact, le flot anisotropique dépend fortement de la centralité de la collision. Le plan de symétrie du système initial est appelé plan de réaction et est défini par le vecteur du paramètre d'impact des noyaux et la direction du faisceau. La distribution finale en impulsion des particules par rapport au plan de réaction est décomposable en une série de Fourrier selon : $\mathrm{E}\frac{d^3\mathrm{N}}{d^3p} = \frac{1}{2\pi}\frac{d^2\mathrm{N}}{p_\mathrm{T}dp_\mathrm{T}dy}\{1+\sum_{n=1}^{\infty}2v_n\cos(\mathrm{n}(\phi-\Psi_\mathrm{RP}))\}$. Pour chaque harmonique, le n^{ieme} coefficient de flot peut être accédé expérimentalement comme la moyenne du coefficient $v_n = \langle\cos[n(\phi-\Psi_\mathrm{RP})]\rangle$ sur toutes les particules et tous les évènements. Chaque coefficient permet d'accéder à des informations spécifiques sur le système. Le deuxième harmonique est appelé flot elliptique. Il est positif dans le cas où plus de particules sont mesurées dans le plan que hors du plan de la collision.

Les collisions d'ions lourds manifestent des coefficients d'anisotropie azimutale significatifs, typiquement attribués aux phénomènes collectifs. Les études de flot se focalisent généralement sur la dépendance en centralité, en l'impulsion transverse ou en masse des particules mesurées. Les valeurs maximales de flot elliptique sont obtenues dans le cas de collisions semi-centrales, qui correspond à un compromis entre l'asymétrie de la zone de recouvrement des noyaux et le nombre de participants dans la collision. Les

résultats en fonction de l'impulsion montrent deux comportements distincts : à bas p_{T} (en dessous de 2–3 GeV/c), le flot de différentes particules s'ordonne en fonction de leurs masses et à p_{T} intermédiaire, les particules se regroupent selon leur nombre de quarks. Initialement associées aux saveurs légères, ces observations ont récemment été étendues au secteur des saveurs lourdes. Les quarks lourds sont dans le même milieu que les quarks légers mais leur masse plus importante peut restreindre leur flot. Un des points clés de la physique des quarks lourds serait de savoir s'ils atteignent un équilibre local dans le milieu et s'ils suivent la même évolution hydrodynamique que les quarks légers. Parce que les constituants légers thermalisent dans le milieu, le spectre des hadrons composés de quarks légers reflète les propriétés d'expansion du milieu. Cependant les informations sur l'historique de leurs interactions ne sont plus accessibles. A l'opposé, les quarks lourds transportent ces informations et les conservent lors de l'hadronisation. En comparaison aux abondances des saveurs légères produites dans le PQG, seul un faible nombre de quark charmés sont produits lors d'une collision. L'étude du flot des hadrons formés de quarks lourds est particulièrement important afin d'extraire les degrés d'interaction et de thermalisation des quarks lourds dans le milieu afin d'accéder à leurs coefficients de transports et à la quantification de leurs interactions partoniques au sein de la boule de feu en expansion. Plusieurs observations de flot elliptique positif ont été réalisées au LHC dans les collisions Pb–Pb pour les décroissances semi-leptoniques de saveurs ouvertes à $\sqrt{s_{\mathrm{NN}}} = 2.76\,\mathrm{TeV}$ [A$^+$16f, A$^+$16e] et $\sqrt{s_{\mathrm{NN}}} = 5.02\,\mathrm{TeV}$ ainsi que pour les mésons D, également à $\sqrt{s_{\mathrm{NN}}} = 2.76\,\mathrm{TeV}$ [A$^+$14e] et $\sqrt{s_{\mathrm{NN}}} = 5.02\,\mathrm{TeV}$ [A$^+$18e].

Les quarkonia comme sonde du PQG

Les quarks lourds sont produits durant les premiers instants de la collisions lors de processus durs, avant la phase de déconfinement. Il est attendu que le même nombre de quarks lourds soit produits par collision binaire, à la fois dans les collisions pp et A–A. Ce nombre est conservé durant les phases partoniques et hadroniques de la collision car le taux d'annihilation des quarks lourds est supposé négligeable et et aucune production thermique n'est attendue aux énergies du LHC. Les états liés de quarks lourds $\mathrm{Q\bar{Q}}$ sont désignés sous le nom de quarkonia (charmonia pour $\mathrm{c\bar{c}}$ et bottomonia pour $\mathrm{b\bar{b}}$). Ils représentent une sonde privilégiée pour l'étude du QGP et sont étudiés depuis plus de quarante ans dans le contexte des collisions d'ions lourds. La large masse de leurs constituants permet de les traiter comme des systèmes non-relativistes et des approches théoriques effectives peuvent être appliquées pour décrire l'évolution de la paire $\mathrm{Q\bar{Q}}$ vers l'état quarkonium final. La première observation d'un charmonia a été celle de la particule J/ψ , l'état vecteur fondamental.

On distingue deux sources de production : les J/ψ issus d'une production directe et ceux non-provenant de la décroissance d'états excités. Ces deux contributions forment des J/ψ désignés sous le terme de prompts. D'autres processus non-prompts peuvent également contribuer à la production finale de charmonia, notamment les décroissances de hadrons b.

Lors des collisions d'ions lourds, la production de quarkonia est affectée par les effets dits chauds, dus à la présence de PQG mais également par d'autres effets, dits froids, causés par la présence des noyaux. Les collisions p–A offrent l'opportunité d'étudier ces derniers, dont la quantification est indispensable pour isoler la contribution des effets chauds dans les collisions A–A. Une suppression séquentielle des quarkonia a été initialement proposée comme signature de la formation d'un PQG [MS86]. Cette suppression est attribuée à un effet d'écrantage de couleur dans le milieu ou aux interactions dynamiques de la paire $\mathrm{Q\bar{Q}}$

avec les partons environnants. Plusieurs résultats au SPS [G$^+$96] et au RHIC [dC13] illustrent cette suppression dans les collisions Pb–Pb par rapport aux collisions pp. Plus tard, le taux de production important de J/ψ au LHC a conduit à l'introduction d'une deuxième source de production via (re)recombinaison statistique de quarks charmés [BMS00] dans le milieu à un stage ultérieur de la collision. Cet effet augmente avec la densité de quarks charmés dans le milieu, qui est reliée à la densité d'énergie. Il est donc d'autant plus significatif que l'énergie du système est importante mais également que le nombre de collisions binaires nucléon-nucléon augmente. Cet effet est plus significatif pour les charmonia que les bottomonia car la masse plus important du quark bottom réduit leur section efficace de production et donc leur densité au sein du PQG par rapport au charme. Les quarks lourds qui se (re)combinent ont précédemment interagi avec le milieu et perdu une partie de leur énergie. L'effet de (re)recombinaison a donc pour conséquence un décalage du spectre en impulsion transverse des J/ψ vers la région de bas-p_{T} [MT05, ZR11]. Plusieurs modèles théoriques existent pour décrire la production de quarkonia au sein du PQG. Le modèle d'hadronisation statistique [ABMRS03] suppose une dissociation complète des paires Q$\bar{\mathrm{Q}}$ dans le PQG et une (re)combinaison statistiques des quarks lourds à la limite des phases vers des saveurs lourdes ouvertes ou fermées. Le modèle des co-movers [CBF$^+$08, Fer14] interprète les effets chauds et froids du milieu comme le résultat d'interactions dynamiques entre la paire de quarks et l'environnement partonique qui l'entoure. Les modèles de transports offrent de leur côté une description de la production de quarkonia en supposant une dissociation et (re)génération continues tout au long de la phase de déconfinement et se basent sur une équation de Boltzmann relativiste [ZR11, ZXXZ14, DR15, The02].

Le flot elliptique des quarkonia est complexe à prédire en raison des différents mécanismes qui affectent la production des états lors des différentes étapes de l'évolution de la collision. Les quarks lourds, les paires c$\bar{\mathrm{c}}$ et les états quarkonia finaux peuvent gagner ou perdre de l'énergie dans le milieu, et toutes ces interactions peuvent impacter l'anisotropie de l'état final. Dans le cas du J/ψ , la contribution majeure attendue provient de la (re)combinaison des quarks charmés si ces derniers ont thermalisé au sein du milieu. Les mesures de flot elliptique du J/ψ réalisées au RHIC par les expériences PHENIX [Sil08] et STAR [A$^+$13d] montrent un coefficient compatible avec zéro mais les barres d'erreurs sont relativement importantes. Le premier indice de flot non nul pour le J/ψ a été mesuré par l'expérience ALICE à $\sqrt{s_{\mathrm{NN}}} = 2.76\,\mathrm{TeV}$ dans le canal dimuon à rapidité avant avec une signification statistique de 2.9σ [A$^+$13a]. Cette observation a également été réalisée par l'expérience CMS dans un intervalle cinématique différent [K$^+$17].

Analyse

Ce manuscrit présente l'analyse du flot elliptique des J/ψ avec le spectromètre à muons de l'expérience ALICE à $\sqrt{s_{\rm NN}} = 5.02$ TeV. Ces résultats sont la combinaison d'une méthode de mesure du flot avec l'extraction du signal du J/ψ .

Les résultats principaux ont été obtenus avec la méthode du plan d'évènement (event plane method). Celle-ci consiste à estimer le plan de réaction de la collision à partir des multiplicités de particules mesurées au sein des détecteurs, afin d'obtenir l'angle du plan d'évènement ($\Psi_{\rm EP}$) qui correspond à l'angle de rotation du plan de symétrie par rapport au référentiel du détecteur. Le plan d'évènement a été mesuré en utilisant soit le SPD soit le VZEROA. La résolution de la mesure de plan d'évènement a été obtenue via la méthode des 3 sous-détecteurs avec le VZEROA, le VZEROC et le SPD. Les vecteurs de flot obtenues à partir des multiplicités de particules mesurées ont été corrigés des effets dus à la non-homogénéité des détecteurs par la méthode d'equalisation [SV08]. Le flot elliptique a ensuite été extrait en utilisant deux procédures. Le J/ψ est mesuré en détectant deux muons de signes opposés avec le spectromètre à muons. L'angle relatif de la paire de dimuons par rapport au plan d'évènement ($\Delta\phi$) est calculé en soustrayant l'angle de ce dernier. La première méthode consiste à extraire le nombre de J/ψ dans différents intervalles d'angle relatif au plan d'évènement ($dN/d\Delta\phi$) et à extraire le coefficient de flot elliptique à partir de la variation observée sous la forme $N_0 \times [1 + 2v_2^{\rm obs} \times \cos(2\Delta\phi)]$. La seconde consiste à mesurer le flot elliptique total des paires dimuons mesurées et à isoler la contribution du signal en s'appuyant sur la forme du signal mesurée avec le spectre de masse invariante. Les incertitudes systématiques ont été évaluées à partir de l'extraction de signal, de l'impact de l'occupation non-homogène du détecteur sur l'efficacité de reconstruction du J/ψ , de l'équalisation des vecteurs du flot et de la résolution de l'angle du plan d'évènement. Les résultats obtenus en utilisant le SPD ou le VZEROA sont compatibles entre eux. L'effet de la correction d'acceptance-efficacité a été évaluée et ne montre pas d'impact significatif sur les résultats obtenus. Les mesures ont également été reproduites en se basant sur la méthode du produit scalaire et la comparaison des deux méthodes n'a pas révélé de différence significative. La dépendance en rapidité a été également étudiée en divisant l'échantillon en deux intervalles ($2.5 < \eta < 3.25$ et $3.25 < \eta < 4$) mais les barres d'erreurs ne permettent pas de tirer de conclusion.

La forme elliptique de la boule de feu peut être utilisée afin d'étudier en détail les effets du milieu sur la production du J/ψ en fonction du chemin parcouru. Les particules traversent un parcours plus long selon leur angle d'émission et plus ce parcours est long, plus elles subissent d'interactions avec les constituants du PQG. L'effet du PQG sur la production est mesuré via l'observable $R_{\rm AA}$, le facteur de modification nucléaire, qui correspond au ratio du taux de production mesuré dans les collisions Pb–Pb sur celui mesuré pour les collisions pp normalisé par le nombre de collisions binaires. L'analyse a été réalisée en mesurant le J/ψ via le canal dimuon avec le spectromètre à muons en reprenant les paramètres de la publication [A+16f] et en divisant l'échantillon selon l'angle relatif des dimuons mesurés par rapport au plan d'évènement (dans le plan de réaction qui correspond au petit axe de l'ellipse et hors du plan qui correspond à son grand axe). Trois centralités différentes ont été étudiées (5–20 %, 20–40 % et 40–60 %) avec des intervalles en impulsion transverse de 1 GeV/c. L'extraction de signal a été réalisée à partir de la distribution de masse invariante de muons de signe opposé avec les mêmes fonctions que celles utilisées dans l'analyse de flot elliptique. Les taux de production mesurés sont corrigés de l'effet d'acceptance-efficacité du détecteur et par la résolution du détecteur utilisé pour la détermination de l'angle du plan d'évènement. Les résultats ont été comparés à ceux

calculés avec le coefficient de flot elliptique mesuré et les valeurs de facteur modification nucléaire précédemment publiées. Les valeur du R_{AA} pour toutes les centralités et les régions du plan d'évènement ont ensuite été représentées en fonction du parcours moyen (ou du parcours moyen quadratique) dans le but de mettre en évidence une éventuelle dépendance.

Discussion des résultats

L'analyse du flot elliptique du J/ψ a été réalisée dans trois intervalles de centralité (5–20 %, 20–40 % et 40–60 %) et les résultats sont présentés en fonction de l'impulsion transverse. Dans les trois intervalles en centralité, un v_2 positif est observé pour le J/ψ dans plusieurs intervalles en p_T. Ces résultats confirment donc les indications précédentes d'un flot elliptique du J/ψ positif dans les collisions Pb–Pb à $\sqrt{s_{NN}} = 2.76$ TeV. La signification statistique maximale mesurée dépasse les 6σ dans les collisions semi-centrales. Les trois centralités manifestent une dépendance similaire en fonction de l'impulsion transverse. À bas p_T, le coefficient de flot elliptique est faible ou compatible avec zero. Cette observation se retrouve dans le cas d'autres particules et d'autres coefficients de flot. À p_T intermédiaire ($4 < p_T < 8$ GeV/c), un flot elliptique positif est observé et à haut p_T ($8 < p_T < 12$ GeV/c) le v_2 mesuré est compatible avec zéro pour les centralités 5–20 % et 40–60 % mais reste positif pour 20–40 %.

Les résultats sont compatibles avec les mesures réalisées dans le canal di-electron à rapidité centrale ainsi qu'avec les observations précédentes à plus basse énergie. L'amplitude du v_2 du J/ψ est également similaire à celle du flot elliptique mesuré pour les mésons D.

La comparaison avec les prédictions théoriques favorise qualitativement le scénario de (re)génération des paires $c\bar{c}$ dans le milieu mais les résultats ne sont pas totalement compris. Les résultats de deux modèles de transport sont proposés ([DR15, ZER13] et [ZXXZ14, GSX+15]). Le flot elliptique du J/ψ y est interprété comme le résultat du flot hérité des quarks charmés (re)recombinés qui dépend du flot du milieu si les quarks charmés y ont (partiellement ou totalement) thermalisé et la proportion de J/ψ (re)générés, des effets de longueur de parcours sur l'anisotropie des J/ψ primordiaux (s'ils traversent un chemin plus long s'ils sont émis hors du plan de réaction que dans le plan) qui dépend de la géométrie initiale du système, de la proportion de J/ψ initiaux et de leur zone de formation par rapport au PQG ainsi que d'autres contributions non-inclusives telles que les décroissances d'états excités et celles des mésons B. L'amplitude du flot elliptique du J/ψ est bien reproduit par les prédictions théoriques en incorporant une fraction importante de (re)génération qui est la contribution majeure au v_2 final mais la dépendance en moment transverse n'est pas encore comprise. Ceci pourrait impliquer la présence d'effets sous-jacents ou d'autres interactions qui ne sont pas considérés ou mal interprétées. La présence du champ magnétique puissant au début de la collision pourrait notamment contribuer à l'anisotropie observée.

Les mesures du R_{AA} dans et hors du plan de réaction ont été réalisées pour trois centralités différentes et sont comparées dans différents intervalles de moment transverse. Ces résultats constituent la première étude de dépendance angulaire azimutale de production du J/ψ et indiquent une possible dépendance avec le parcours moyen parcouru.

Conclusion

Les quarkonia ont longtemps été considérés comme une sonde et un thermomètre du plasma de quarks et de gluons formé lors des collisions d'ions lourds. Leur production et dynamique dans le milieu sont décrits par les modèles de transport au travers de deux mécanismes antagonistes. Parce que leur production initiale a lieu avant la formation de l'état déconfiné, leur dissociation par écrantage de couleur atteste de la formation d'un PQG. Aux énergies du LHC, la densité importante de quarks charmés est à l'origine d'une deuxième source de production par (re)combinaison de ces quarks à un stage plus avancé de la collision. L'association de ces deux mécanismes permet de reproduire simplement mais de façon satisfaisante les mesures expérimentales de facteur de modification nucléaire du J/ψ . En parallèle des mesures de production, les études de flot offrent une perspective complémentaire sur les états liés de quarks lourds. Les études de phénomènes collectifs sont une des sources majeures d'information sur le système en expansion et beaucoup de résultats ont été obtenus pour les hadrons formés de quarks légers. Moins de mesures sont disponibles pour les quarks lourds. Une question essentielle est leur degré de thermalisation au sein du milieu. Plusieurs observations de coefficients de flot elliptique positifs ont été réalisées pour les mésons D et les décroissances de saveurs lourdes à plusieurs énergies de collisions. Dans le cas des quarkonia, les états (re)combinés sont supposés hériter le flot des quarks lourds qui ont évolué dans PQG. Un premier indice de flot elliptique pour le J/ψ a été observé par ALICE et CMS à $\sqrt{s_{\rm NN}} = 2.76\,\text{TeV}$. Cette thèse porte sur la deuxième prise de données de collisions d'ions lourds Pb–Pb au LHC à $\sqrt{s_{\rm NN}} = 5.02\,\text{TeV}$. L'augmentation en énergie et la quantité de données plus importante a permis une nouvelle mesure très précise du v_2 du J/ψ avec le spectromètre à muons à rapidité avant, en fonction du moment transverse et dans différentes centralités de collisions. La signification statistique la plus importante a été observée dans les collisions semi-centrales (6σ) où une mesure pionnière a également été réalisée par la collaboration ALICE dans le canal di-électron à rapidité centrale. La comparaison des résultats obtenus pour le flot elliptique des mésons D et du J/ψ offre un argument solide pour la thermalisation du charme dans le milieu et la formation de J/ψ via le mécanisme de (re)génération. Les résultats ne sont reproduits qu'incomplètement par les modèles théoriques, remettant en question les certitudes précédentes sur la physique des quarkonia et laissant supposer qu'une ou plusieurs contributions sont manquantes ou incomprises. En parallèle, l'étude de systèmes plus petits (pp et p–Pb au LHC) a révélé des résultats inattendus pour l'anisotropie et en particulier plusieurs caractéristiques attribués à la physique des ions lourds y ont été observés. Ceci s'applique également au secteur des saveurs lourdes, notamment avec l'observation d'un flot elliptique positif pour le J/ψ dans les collisions p–Pb à $\sqrt{s_{\rm NN}} = 5.02\,\text{TeV}$ et $\sqrt{s_{\rm NN}} = 8.16\,\text{TeV}$ par ALICE et CMS où la densité d'énergie est supposée trop faible pour conduire à une production par (re)combinaison. La compréhension de ces systèmes est essentielle pour la description et la définition de ce qu'on appelle le *milieu* dans les collisions d'ions lourds. Plusieurs mesures expérimentales aideraient à clarifier la situation. Au LHC, la future prise de données de collisions Pb–Pb à $\sqrt{s_{\rm NN}} = 5.02\,\text{TeV}$ et la future amélioration du détecteur ALICE devraient donner accès à de nouvelles observables et à observations plus précises. Une partie de cette thèse à été consacrée à la caractérisation des capteurs de type MAPS du futur détecteur Muon Forward Tracker, un des éléments clés pour ces futures mesures à rapidité avant. Le flot elliptique des J/ψ prompt, du ψ(2S) et des Υ devrait notamment pouvoir être mesuré jusqu'à impulsion transverse nulle pour la première fois et apporter ainsi de nouveaux éléments pour la description de la dynamique des quarkonia dans le PQG.

UNIVERSITE / MATIERE
BRETAGNE \ MOLECULES
LOIRE / ET MATERIAUX

IMT Atlantique
Bretagne-Pays de la Loire
École Mines-Télécom

Titre : Mesure du flot elliptique du J/ψ dans les collisions Pb-Pb à avec le Spectromètre à Muons de l'expérience ALICE au LHC

Mots clés : LHC, Plasma de Quarks et de Gluons, ions-lourds, Pb-Pb, ALICE, charmonium, J/ψ, flot elliptique, charme

Résumé : Les conditions extrêmes de température et de densité d'énergie} créées lors des collisions d'ions lourds ultra-relativistes au sein du Grand collisionneur de hadrons (LHC) fournissent une occasion unique d'étudier les propriétés de la matière. Une transition de phase de la matière hadronique vers un milieu déconfiné de quarks et de gluons (PQG) est prédite par la chromodynamique quantique et des efforts théoriques et expérimentaux considérables ont été investis pour étudier ses propriétés. Parmis les sondes éminentes du PQG, les quarks lourds jouent un rôle prépondérant car ils sont créés lors des processus durs initiaux, avant la formation du PQG, et leur nombre est conservé durant les phases partoniques et hadroniques de la collision. Les états liés de quarks lourds – quarkonium (charmonium pour $c\bar{c}$ et bottomonium pour $b\bar{b}$), constituent des sondes remarquables du milieu. Les observations expérimentales de quarkonia aux énergies du LHC dans les collisions A-A sont reproduites au travers de deux mécanismes antagonistes : la suppression séquentielle, proposée très tôt comme signature du PQG, et la (re)génération de quarkonia par (re)combinaison de quarks déconfinés. Cependant des incertitudes importantes sont associées aux prédictions théoriques et de nombreuses inconnues demeurent. L'anisotropie azimuthale de l'espace des moments (désignée sous le terme de flot elliptique, v_2) de la production de charmonium devrait permettre d'avoir une meilleure vue d'ensemble et de contraindre davantage les paramètres des modèles théoriques. Si les quarks charmés se (re)combinent en paires $c\bar{c}$, les J/ψ produits devraient hériter de leur flot. Les études précédentes ont montré des premiers signes d'un v_2 positif du J/ψ dans les collisions Pb-Pb à $\sqrt{s_{NN}}$=2.76TeV.
Cette thèse porte sur la mesure de l'anisotropie azimuthale du J/ψ dans les collisions Pb-Pb à $\sqrt{s_{NN}}$=5.02TeV où une (re)combinaison légèrement plus importante est prédite par rapport aux énergies inférieures et une augmentation statistique d'un facteur 3 a été enregistrée. L'étude du flot elliptique du J/ψ fournit des informations clés sur la magnitude et la dynamique des mécanismes de suppression et de (re)génération de charmonia. Par ailleurs elle offre un regard unique sur l'évolution et les interactions des quarks charmés au sein du milieu en expansion.

Title : Measurement of the J/ψ elliptic flow in Pb-Pb collisions at $\sqrt{s_{NN}}$=5.02TeV with the muon spectrometer of ALICE at the LHC

Keywords: LHC, Quark-Gluon Plasma, heavy-ions, Pb–Pb, ALICE, charmonium, J/ψ, elliptic flow, charm

Abstract: Extreme temperatures and energy densities produced in ultra-relativistic heavy-ion collisions at the Large Hadron Collider provide a unique opportunity to study the properties of matter. A phase transition of the hadronic matter to a deconfined medium of quarks and gluons, the Quark-Gluon Plasma (QGP), is predicted by QuantumChromodynamics and considerable theoretical and experimental efforts have been invested to study its properties. Among the prominent probes of the QGP, heavy quarks play a crucial role since they are created in primary hard-scattering processes, before the QGP formation, and their number is conserved throughout the partonic and hadronic phases of the collision. Bound states of heavy quarks – quarkonium (charmonium for $c\bar{c}$ and bottomonium $b\bar{b}$) provide remarkable probes of the medium. At LHC energies, experimental observations of quarkonium in A-A collisions are reproduced through two antagonist mechanisms: a sequential suppression of the quarkonium states, early suggested as a signature of the QGP, and quarkonium (re)generation by (re)combination of deconfined quarks. However, theoretical predictions carry large uncertainties and many unknows remain. The momentum space azimuthal anisotropy of charmonium production (referred as elliptic flow v_2) should help to clarify the picture and to constrain the model parameters. If charm quarks (re)combine in the medium into $c\bar{c}$ pairs, the J/ψ originating from (re)combination should inherit their flow. Previous studies have shown first hints of a positive J/ψ v_2 in Pb-Pb collisions at $\sqrt{s_{NN}}$=2.76TeV.
This thesis focuses on the measurement of J/ψ azimuthal anisotropy in Pb-Pb collisions at $\sqrt{s_{NN}}$=5.02TeV where a slightly stronger (re)generation component is predicted with respect to lower collision energies, and a factor of 3 more data were collected. The study of J/ψ v_2 provides important information on the magnitude and dynamics of charmonium suppression and (re)generation mechanisms. In addition, it offers a unique insight on charm quark evolution and interactions in the expanding medium.